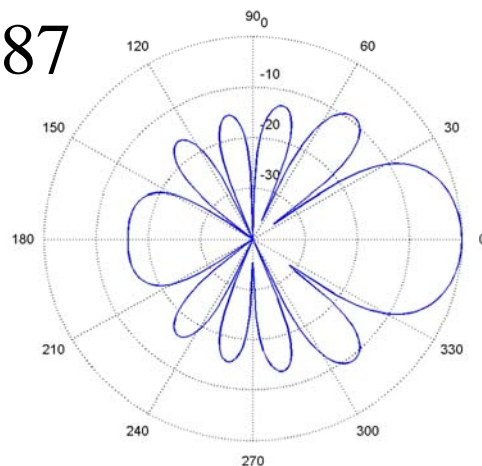
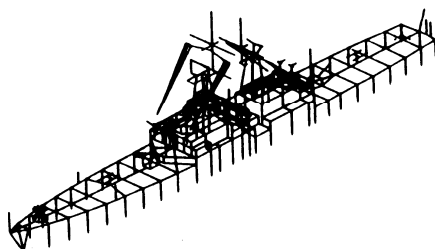
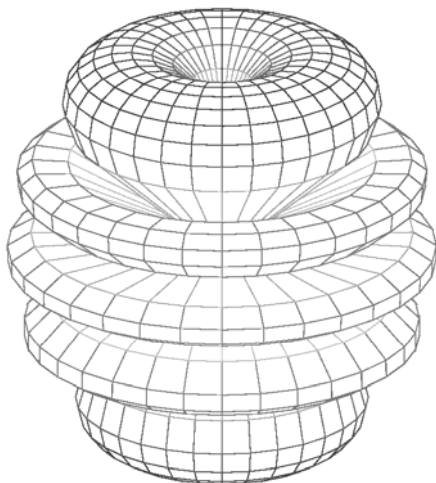
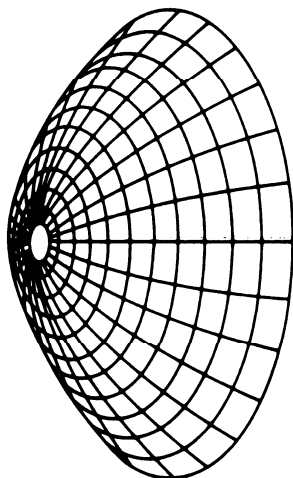
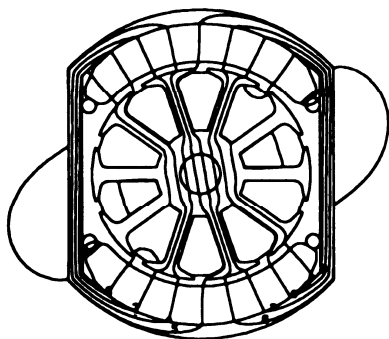
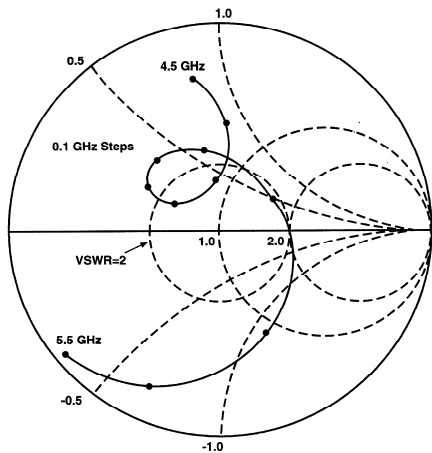


Applied Computational Electromagnetics Society Journal

Special Issue on
**Computational and Experimental
Techniques for RFID Systems and
Applications, Part I**

Guest Editors
**Lauri Sydänheimo, Fan Yang,
and Leena Ukkonen**

March 2010
Vol. 25 No. 3
ISSN 1054-4887



GENERAL PURPOSE AND SCOPE: The Applied Computational Electromagnetics Society (*ACES*) Journal hereinafter known as the *ACES Journal* is devoted to the exchange of information in computational electromagnetics, to the advancement of the state-of-the art, and the promotion of related technical activities. A primary objective of the information exchange is the elimination of the need to “re-invent the wheel” to solve a previously-solved computational problem in electrical engineering, physics, or related fields of study. The technical activities promoted by this publication include code validation, performance analysis, and input/output standardization; code or technique optimization and error minimization; innovations in solution technique or in data input/output; identification of new applications for electromagnetics modeling codes and techniques; integration of computational electromagnetics techniques with new computer architectures; and correlation of computational parameters with physical mechanisms.

SUBMISSIONS: The *ACES Journal* welcomes original, previously unpublished papers, relating to applied computational electromagnetics. Typical papers will represent the computational electromagnetics aspects of research in electrical engineering, physics, or related disciplines. However, papers which represent research in applied computational electromagnetics itself are equally acceptable.

Manuscripts are to be submitted through the upload system of *ACES* web site <http://aces.ee.olemiss.edu> See “Information for Authors” on inside of back cover and at *ACES* web site. For additional information contact the Editor-in-Chief:

Dr. Atef Elsherbeni

Department of Electrical Engineering
The University of Mississippi
University, MS 386377 USA
Phone: 662-915-5382 Fax: 662-915-7231
Email: atef@olemiss.edu

SUBSCRIPTIONS: All members of the Applied Computational Electromagnetics Society who have paid their subscription fees are entitled to receive the *ACES Journal* with a minimum of three issues per calendar year and are entitled to download any published journal article available at <http://aces.ee.olemiss.edu>.

Back issues, when available, are \$15 each. Subscriptions to *ACES* is through the web site. Orders for back issues of the *ACES Journal* and changes of addresses should be sent directly to *ACES*:

Dr. Allen W. Glisson

302 Anderson Hall
Dept. of Electrical Engineering
Fax: 662-915-7231
Email: aglisson@olemiss.edu

Allow four week’s advance notice for change of address. Claims for missing issues will not be honored because of insufficient notice or address change or loss in mail unless the Executive Officer is notified within 60 days for USA and Canadian subscribers or 90 days for subscribers in other countries, from the last day of the month of publication. For information regarding reprints of individual papers or other materials, see “Information for Authors”.

LIABILITY. Neither *ACES*, nor the *ACES Journal* editors, are responsible for any consequence of misinformation or claims, express or implied, in any published material in an *ACES Journal* issue. This also applies to advertising, for which only camera-ready copies are accepted. Authors are responsible for information contained in their papers. If any material submitted for publication includes material which has already been published elsewhere, it is the author’s responsibility to obtain written permission to reproduce such material.

APPLIED COMPUTATIONAL ELECTROMAGNETICS SOCIETY JOURNAL

Guest Editors

**Lauri Sydänheimo, Fan Yang,
and Leena Ukkonen**

March 2010

Vol. 25 No. 3

ISSN 1054-4887

The ACES Journal is abstracted in INSPEC, in Engineering Index, DTIC, Science Citation Index Expanded, the Research Alert, and to Current Contents/Engineering, Computing & Technology.

The first, fourth, and sixth illustrations on the front cover have been obtained from the Department of Electrical Engineering at the University of Mississippi.

The third and fifth illustrations on the front cover have been obtained from Lawrence Livermore National Laboratory.

The second illustration on the front cover has been obtained from FLUX2D software, CEDRAT S.S. France, MAGSOFT Corporation, New York.

THE APPLIED COMPUTATIONAL ELECTROMAGNETICS SOCIETY
<http://aces.ee.olemiss.edu>

ACES JOURNAL EDITOR-IN-CHIEF

Atef Elsherbeni
University of Mississippi, EE Dept.
University, MS 38677, USA

ACES JOURNAL ASSOCIATE EDITORS-IN-CHIEF

Sami Barmada
University of Pisa, EE Dept.
Pisa, Italy, 56126

Fan Yang
University of Mississippi, EE Dept.
University, MS 38677, USA

ACES JOURNAL EDITORIAL ASSISTANTS

Matthew J. Inman
University of Mississippi, EE Dept.
University, MS 38677, USA

Mohamed Al Sharkawy
Arab Academy for Science and Technology
ECE Dept.
Alexandria, Egypt

ACES JOURNAL EMERITUS EDITORS-IN-CHIEF

Duncan C. Baker
EE Dept. U. of Pretoria
0002 Pretoria, South Africa

Allen Glisson
University of Mississippi, EE Dept.
University, MS 38677, USA

David E. Stein
USAF Scientific Advisory Board
Washington, DC 20330, USA

Robert M. Bevensee
Box 812
Alamo, CA 94507-0516, USA

Ahmed Kishk
University of Mississippi, EE Dept.
University, MS 38677, USA

ACES JOURNAL EMERITUS ASSOCIATE EDITORS-IN-CHIEF

Alexander Yakovlev
University of Mississippi, EE Dept.
University, MS 38677, USA

Erdem Topsakal
Mississippi State University, EE Dept.
Mississippi State, MS 39762, USA

MARCH 2010 REVIEWERS

Mohamed Bakr
Rajeev Bansal
Fatma El-Hefnawi

Kwok Leung
C. Reddy
Lauri Sydänheimo

Leena Ukkonen
Fan Yang

THE APPLIED COMPUTATIONAL ELECTROMAGNETICS SOCIETY
JOURNAL

Vol. 25 No. 3

March 2010

TABLE OF CONTENTS

“Logo-Antenna Based RFID Tags for Advertising Application” K. ElMahgoub, T. Elsherbeni, F. Yang, A. Z. Elsherbeni, L. Sydänheimo, and L. Ukkonen.....	174
“Bidirectional Radiated Circularly Polarized Annular-Ring Slot Antenna for Portable RFID Reader” Y. Lin, Y. Kao, S. Pan, and H. Chen	182
“Low-profile Normal-Mode Helical Antenna for Use in Proximity to Metal” W. Hong, N. Michishita and Y. Yamada	190
“New Antennas Based on Triangular Patch as a Solution for RFID Application” A. Ferchichi, N. Sboui, A. Gharsallah, and H. Baudrand.....	199
“The Effect of Curvature on the Performance and Readability of Passive UHF RFID Tags” D. D. Arumugam, D. W. Engels, and M. H. Mickle.....	206
“Advanced Carbon-Fiber Composite Materials for RFID Tag Antenna Applications” A. Mehdipour, I. D. Rosca, A. Sebak, C. W. Trueman, and S. V. Hoa.....	218
“Green Technologies and RFID: Present and Future” G. Orecchini, L. Yang, A. Rida, F. Alimenti, M. M. Tentzeris, and L. Roselli.....	230
“Collision Resolution in ISO 18000-6c Passive RFID” Y. Sun, P. J. Hawrylak, Z. Mao, and M. H. Mickle	239
“RFID-Network Planning by Particle Swarm Optimization” E. Di Giampaolo, F. Fornì, and G. Marrocco.....	263
“RFID-Based System for Pilgrims Identification and Tracking” M. Mohandes.....	273

Logo-Antenna Based RFID Tags for Advertising Application

Khaled ElMahgoub¹, Tamer Elsherbeni¹, Fan Yang¹, Atef Z. Elsherbeni¹, Lauri Sydänheimo², Leena Ukkonen²

¹ Center of Applied Electromagnetic System Research (CAESR), Department of Electrical Engineering, University of Mississippi, University, MS 38677-1848, USA
kelmahgo@olemiss.edu, taelsheri@olemiss.edu, fyang@olemiss.edu, atef@olemiss.edu

² Rauma Research Unit, Institute of Electronics, Tampere University of Technology, Kalliokatu 2, Rauma 26100, Finland
lauri.sydanheimo@tut.fi, leena.ukkonen@tut.fi

Abstract— In this paper we provide the basis of using radio frequency identification (RFID) tags for advertisement. Two RFID tags that apply to the 866 MHz and 915 MHz operating frequencies, respectively, were designed based on the logos of two universities participating in this project. Several fabrication methods were used to build the RFID tags on different substrates. The experimental results exhibited favorable read ranges and radiation patterns. This work demonstrates the applicability and design flexibility of RFID tags for many advertising applications.

Index Terms— Radio Frequency Identification (RFID), advertising applications, active radiation pattern measurements, tag read range.

I. INTRODUCTION

The sales of company products thrive off innovative advertising propagation. Thus, the purpose of Logo-RFID tags is to stimulate an emotional reaction and generate a favorable response towards a company by representing their advanced capabilities. Therefore, Logo-RFID tags are an immense asset for companies because of their new perspective for advertising that has never been used in marketing.

Radio Frequency Identification (RFID) is a technology which uses RF signals for automatic identification of objects. RFID tags are used for many applications in various areas such as electronic toll collection, asset identification, retail item management, access tracking systems and

many others. An RFID system consists of two basic parts: a reader (interrogator) and a tag (transponder). An RFID tag can either be an active tag which has a battery or a passive tag which is battery-less. A passive tag consists of an antenna and an application specific integrated circuit (ASIC) known as a chip. A passive back-scattered RFID system operates as follows: the reader transmits modulated signal with periods of unmodulated radio frequency (RF) carrier, which is received by the tag antenna. The RF voltage developed on the antenna terminal during unmodulated period is converted to DC. This voltage powers up the chip, which sends back the information by varying its complex RF input impedance. The impedance typically changes between two different states, a conjugate match impedance and a mismatched impedance, effectively modulating the back-scattered signal [1].

The idea of using text as a meander line antenna in RFID tags has been discussed before in [2]. In this paper the idea of using logo-antenna based passive RFID tags for both identification and advertising purposes is investigated. RFID tags consisting of logos from two universities were designed, simulated, fabricated on different substrates, and measured. The implemented substrates included paper, thin transparent film, polyethylene terephthalate (PET) and fabrics which are popularly used in the advertising industry. The measured tags gave desirable performance and read a range of nearly 12m at both 866MHz and 915MHz, the European and US frequencies. While

the RFID tags were activated, their radiation patterns were measured for both bandwidths.

II. LOGO ANTENNA DESIGN

An RFID tag consists of two parts, an antenna and a chip. For maximum performance the antenna input impedance must be the conjugate match of the chip's impedance [3] which is usually capacitive impedance and depends on both the operation frequency and received power level [4]. To compensate for the capacitive part of the chip's impedance, a matching loop is needed in tag antenna designs [5].

Generally, during the design of an efficient RFID tag several parameters must be determined, (1) the operation frequency and required bandwidth [6], (2) the type of chip and its impedance, (3) the chip's minimum operating power, (4) the substrate parameters according to the fabrication process [7]. These issues will be presented in the following design procedure.

A. The Logo Tag Design

Our design process started by combining the logos of two universities, The University of Mississippi (UM) and Tampere University of Technology (TUT). To design a symmetric antenna, "TUT" was aligned horizontally and "UM" was positioned vertically, as shown in Fig. 1. The main controlling parameter in our RFID tag was the letter 'M' which had an inductive loop for the tag design. By controlling the shape of 'M' the input impedance of the antenna could be matched to the conjugate of the chip's impedance.

The design was simulated using Ansoft HFSS (high frequency structural simulator) [8]. The tag was designed on a substrate with $\epsilon_r = 2.33$, thickness 0.1 mm, copper with $\sigma = 5.8 \text{ MS/m}$ and thickness $17 \mu\text{m}$. The type of chip used for our RFID tag was the Alien gen2 and the chip impedance is $17-135j\Omega$ at 866MHz and -11dBm power level. Two final designs corresponding to the US and

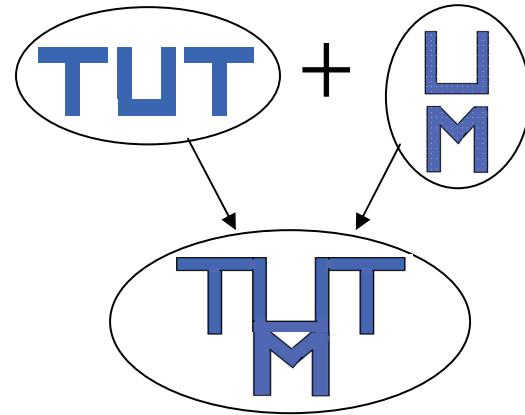


Fig. 1. The logo-RFID tag for the University of Mississippi (UM) and Tampere University of Technology.

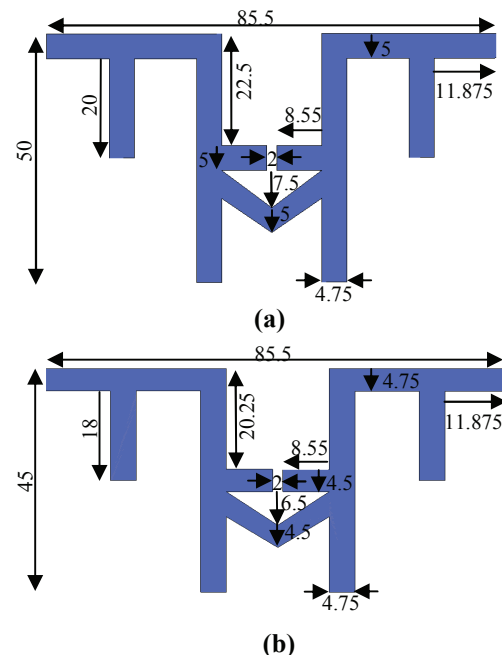


Fig. 2. The final designs for (a) 866MHz and (b) 915MHz, respectively all dimensions are in (mm).

European frequencies were developed and their dimensions are shown in Fig. 2.

These designs were achieved by conducting parametric studies to determine good initial values for optimization. Quasi Newton optimization was used to determine the final values.

To match the input impedance of the antenna to the conjugate of the chip's impedance, the size of the letter 'M' was decreased to get the needed induction. Design

(b) is obtained from shrinking design (a) and modifying the letter ‘M’ to operate at a higher frequency.

B. Simulated Results of Power Reflection Coefficient and Input Impedance

The power reflection coefficient and the input impedance of the antenna were calculated, as shown in Fig. 3 and Fig. 4. The power reflection coefficient was calculated using the following equation:

$$|\Gamma|^2 = \left| \frac{Z_c - Z_a^*}{Z_c + Z_a} \right|^2 \quad (1)$$

where Z_c is the chip impedance and Z_a is the antenna impedance. This is a general formula used for complex nominal impedance; the scattering parameters for complex nominal impedance were proved in [9] to be as follows:

$$a = \frac{1}{2\sqrt{R_a}}(V + Z_a I), b = \frac{1}{2\sqrt{R_a}}(V - Z_a^* I) \quad (2)$$

The normal power reflection coefficient formula can't be used while the nominal impedance is complex, because this might lead to having the magnitude of the reflection coefficient greater than 1.

The center frequency for design (a) was 857MHz and for design (b) was 898 MHz while the -10dB bandwidth for design (a) was 2.89% and for design (b) was 3.37%.

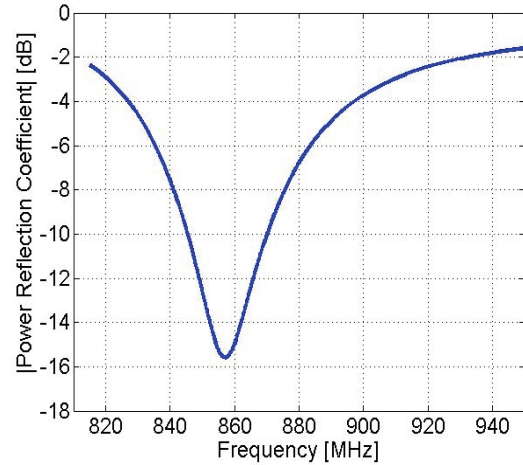
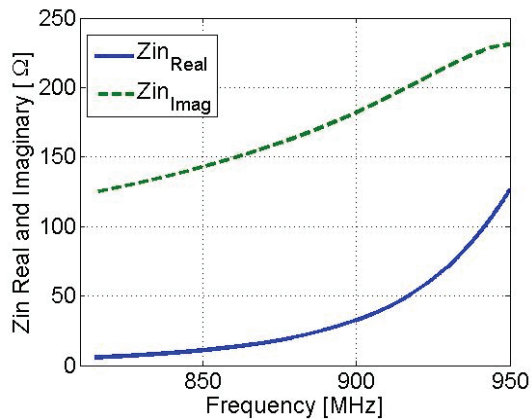


Fig. 3. The input impedance and power reflection coefficient for design 1 shown in Fig. 2(a).

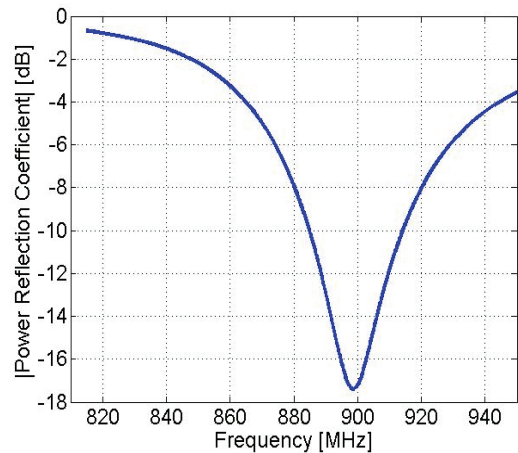
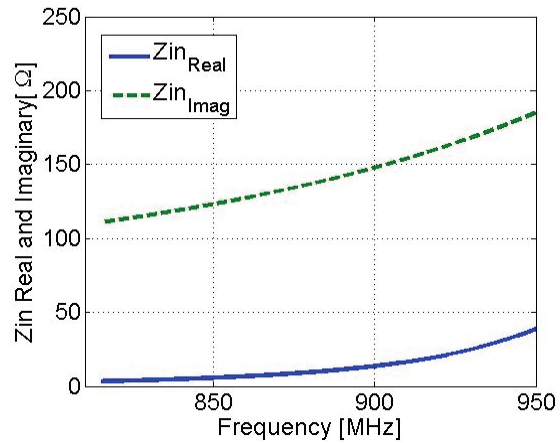


Fig. 4. The input impedance and power reflection coefficient for design 2 shown in Fig. 2 (b).

C. Measurements Results

All measurements were conducted using the Tagformance device [10]. The measurements were based on an electromagnetic threshold technique, in which the frequency was changed from 830 MHz to 990 MHz in a step of 1 MHz. At each frequency the transmitted power was increased by 0.1dB until the tag was activated and properly responded. The minimum transmitted power to activate the tag was measured at each frequency. The device can calculate the read range by using free space Friis formula [11] and taking into account the path and cable losses and also the antenna gains. The read range is calculated using the following equation:

$$r_{\max}(f) = \sqrt{\frac{EIRP}{P_{tmin}LG_t}} \quad (3)$$

Where $EIRP$ is the effective isotropic radiated power, P_{tmin} is the minimum transmitted power to activate the tag and it is measured by the device, L is a factor taking in consideration the cable and path loss, and G_t is the transmitting antenna gain [4].

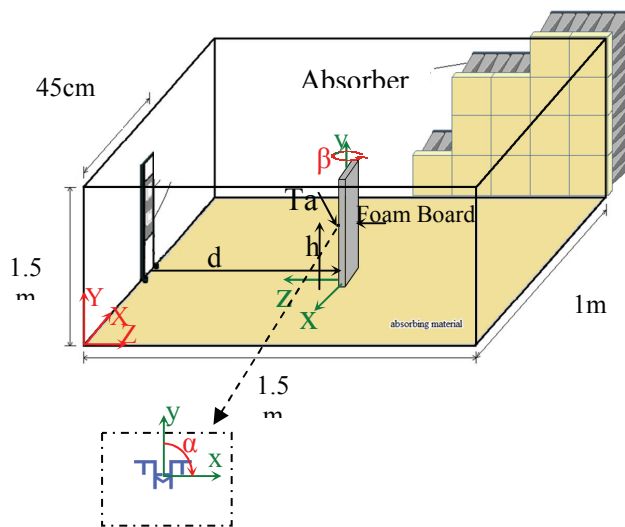


Fig. 5. The measurement setup for RFID tags.

Figure 5 shows the measurement setup. The tag was mounted over a foam board at height $h = 1\text{m}$ and at distance $d = 1\text{m}$ from the Tagformance antennas the ground and side wall were covered by absorbers. To measure the radiation patterns for the tag while it is operating the following procedures were used: For the x-z plane, horizontal polarized reader antennas were used and the foam board was rotated around the y-axis in x-z plane by changing the ' β ' angle by a step of 15 degrees as shown in Fig. 5. For the y-z plane, vertical polarized reader antennas were used and the tag was rotated so that its x-axis became the vertical axis. The board was rotated along the x-axis, by changing the ' β ' angle by a step of 15 degrees.

The Tagformance measured the minimum transmitted power to activate the tag. These values were used at each angle to plot the measured radiation pattern in each plane.

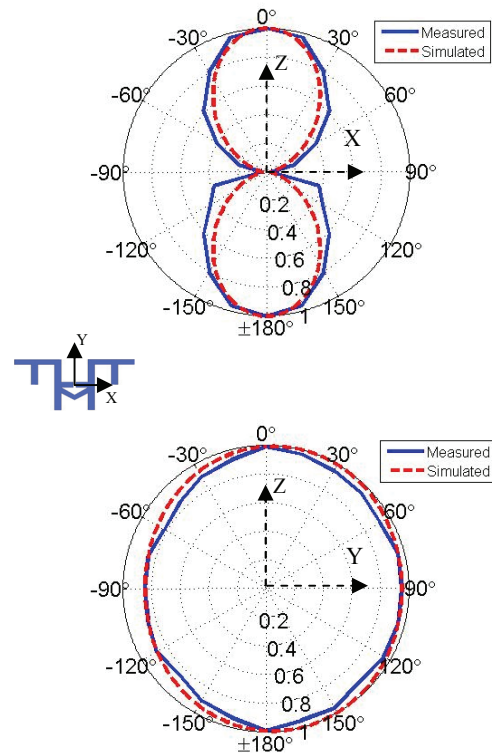


Fig. 6. The measured and simulated radiation pattern for different plane cuts at 866 MHz.

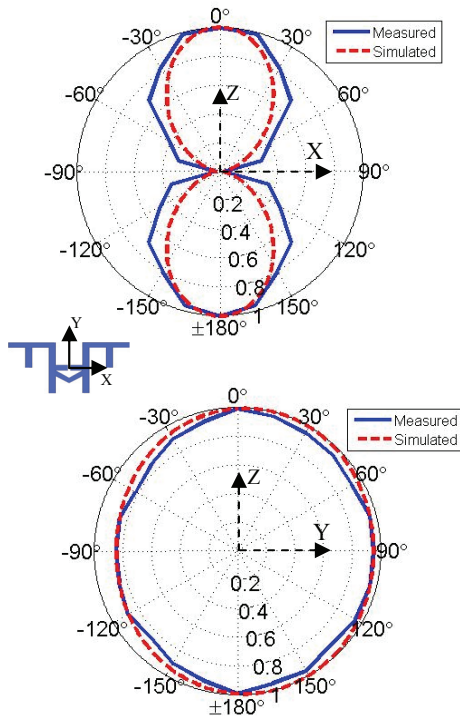


Fig. 7. The measured and simulated radiation pattern for different plane cuts at 915 MHz.

Figs. 6 and 7 compare the measured data to the simulated radiation patterns based on HFSS simulation in both frequencies, and it can be noticed that the measured and the simulated data are in good agreement. Differences could have occurred due to the resolution of the measurement device by increasing the transmitted power (0.1dB), and the 15 degree increment tag rotation.

D. Using Different Substrates in Fabrication Process

The RFID tags were fabricated using three different techniques: manual cutting using copper tape, etching using aluminum and copper, and screen printing using silver conductive ink. Each method was used on four different substrates: paper thin transparent film, PET and fabric. The components of the fabricated tags are shown in Table 1. The multiple substrates and conducting materials were used to prove the flexibility of the logo design for advertising applications. More than

40 tags were fabricated and measured. The best tags for each substrate and conductive material were chosen as prototypes if mass production is needed. Their read ranges are recorded and compared in Table 1.

Table 1. Tags with different substrates and conductive materials.

Tag No.	Substrate	Conductive Material	Fabrication process	Read Range[m]	Frequency of operation[MHz]
1	PET	Copper	Etching	12	866
2	Thin film	Sliver Ink	Screen Printing	9.5	866
3	Thin film	Sliver Ink	Screen Printing	6	915
4	Thin film	Copper	Manual cutting	10	866
5	Thin film	Copper	Manual cutting	9.5	915
6	Thin film	Aluminum	Etching	9	866
7	Paper	Sliver Ink	Screen Printing	9	866
8	Fabric	Sliver Ink	Screen Printing	11.2	866
9	Fabric	Sliver Ink	Screen Printing	7	915

III. CONCLUSION

In this paper the technique of using the RFID tags for advertising application was confirmed. An example of this application was implemented by a sample logo tag. The tags were simulated and fabricated using different substrates such as fabric and printing paper and different conducting materials which are widely used in advertising applications. The performance of these tags were measured and compared well with simulation results. The tag was originally designed using PET and copper as conducting material which is the reason for producing the highest performance (longest read range). Future designs can be modified for different substrates and conducting materials to obtain better results. This paper provides substantial proof that RFID logo tags could be used for both identification and advertising applications.

ACKNOWLEDGMENT

The Authors would like to thank Alien Technology Company for providing the Chips and Voyantic Company for providing the Tagformance device.

REFERENCES

- [1] K. V. S. Rao, P. V. Nikitin, and S. F. Lam, "Antenna Design for UHF RFID Tags: A Review and a Practical Application", *IEEE Transaction on Antennas and Propagation*, Vol. 53, No. 12, Dec. 2005.
- [2] M. Keskilammi, and M. Kivikoski, "Using Text as a Meander Line for RFID Transponder Antennas", *IEEE Antennas and Wireless Propagation Letters*, Vol. 3, 2004.
- [3] K., Kurokawa, "Power waves and the scattering matrix," *IEEE Trans. Microwave Theory and Techniques*, MTT-13, No. 3, pp. 194-202, Mar. 1965.
- [4] C. Loo, K. ElMahgoub, F. Yang, A. Elsherbeni, D. Kajfez, A. Kishk, T. Elsherbeni, L. Ukkonen, L. Sydänheimo, M. Kivikoski, S. Merilampi, and P. Ruuskanen, "Chip Impedance Matching for UHF RFID Tag Antenna Design", *Progress In Electromagnetics Research*, PIER 81, pp. 359-370, 2008.
- [5] P. V. Nikitin, K. V. S. Rao, S. F. Lam, V. Pillai, R. Martinez, and H. Heinrich, "Power Reflection Coefficient Analysis for Complex Impedances in RFID Tag Design" *IEEE Trans. Microwave Theory and Techniques*, Vol. 53, No. 9, pp. 2721-2725, Sept. 2005.
- [6] J. R. Sanford, "Antenna Design Considerations for RFID Applications" Sept. 7, 2005, <http://www.rfglobalnet.com/>.
- [7] C.A. Balanis, *Antenna Theory and Design*, 2nd edition, USA: John Wiley & Sons, 1997.
- [8] Ansoft corporation, <http://www.ansoft.com/products/hf/hfss/>.
- [9] D. C. Youla, "On Scattering Matrices Normalized to Complex Port Numbers," *Proc. IRE*, Vol. 49, p. 1221, Jul. 1961.
- [10] Voyantic TagformanceTM Lite, <http://www.voyantic.com>.
- [11] H. T. Friis, "A note on a simple transmission formula," *Proc. IRE*, vol. 34, No. 5, pp. 254-256, May 1946.



Khaled ElMahgoub received the B.Sc. and M.Sc. degrees in electronics and electrical communications engineering from Cairo University, Egypt, in 2001 and 2006, respectively. Currently, he is working

towards the Ph.D. degree in the Department of Electrical Engineering at the University of Mississippi, USA. His current research interests include RFID systems, FDTD, Antenna design and Numerical techniques for electromagnetics. Mr. ElMahgoub is a member of IEEE and ACES society.

From 2001 to 2006, he has been teacher assistant at Cairo University, and since 2007, he is a research assistant at the University of Mississippi.



Tamer Elsherbeni currently working towards his B. Sc. in Electrical Engineering with RF/Wireless emphasis at the University of Mississippi. He was selected to participate in the NSF Research Experience for Undergraduates (REU) program at The College of Optics and Photonics at University of Central Florida in the summer of 2009. He also received the Science, Mathematics, And Research for Transformation Program (SMART) scholarship in 2009. His current research interests include RFID systems, measurements and fabrication techniques for electromagnetic application, wireless power and infrared systems.



Fan Yang received the B.S. and M.S. degrees from Tsinghua University in 1997 and 1999, and the Ph.D. degree from University of California, Los Angeles (UCLA) in 2002. From 1994 to 1999, he was a Research Assistant in the State Key

Laboratory of Microwave and Digital Communications, Tsinghua University, China. From 1999 to 2002, he was a Graduate Student Researcher in the Antenna Lab, UCLA. From 2002 to 2004, he was a Post-doc Research Engineer and Instructor in the Electrical Engineering Department, UCLA. In August 2004, he joined the Electrical Engineering Department, The University of Mississippi as an Assistant Professor and was promoted to Associate Professor in 2009.

Dr. Yang's research interests include antenna theory, designs, and measurements, electromagnetic band gap (EBG) structures and their applications, computational electromagnetics and optimization techniques, and applied electromagnetic systems such as the radio frequency identification (RFID) system and concentrating solar energy system. He has published over 100 technical journal articles and conference papers, five book chapters, and two books entitled *Electromagnetic Band Gap Structures in Antenna Engineering* and *Electromagnetics and Antenna Optimization Using Taguchi's Method*.

Dr. Yang is a Senior Member of IEEE and was Secretary of IEEE AP Society, Los Angeles chapter. He is also a Full Member of URSI/USNC. Dr. Yang serves as the Associate Editor-in-Chief of the Applied Computational Electromagnetics Society (ACES) Journal. He is also a frequent reviewer for over twenty scientific journals and book publishers, and has chaired numerous technical sessions in various international symposiums. Dr. Yang was a Faculty Senator at The University of Mississippi, and currently is a Member of the University Assessment Committee.

For his contributions, Dr. Yang has received several prestigious awards and recognitions. In 2004, he received the *Certificate for Exceptional Accomplishment in Research and Professional Development Award* from UCLA. Dr. Yang was the recipient of *Young Scientist Award* in the 2005 URSI General Assembly and in the 2007 International Symposium on Electromagnetic Theory. He was also appointed as The University of Mississippi *Faculty Research Fellow* in year 2005 and 2006. In 2008, Dr. Yang received the *Junior Faculty Research Award* from The University of Mississippi. In 2009, he received the

inaugural IEEE Donald G. Dudley Jr. Undergraduate Teaching Award.



Atef Elsherbeni received an honor B.Sc. degree in Electronics and Communications, an honor B.Sc. degree in Applied Physics, and a M.Eng. degree in Electrical Engineering, all from Cairo University, Cairo, Egypt, in 1976, 1979, and 1982, respectively, and a Ph.D. degree in Electrical Engineering from Manitoba University, Winnipeg, Manitoba, Canada, in 1987. He was a part time Software and System Design Engineer from March 1980 to December 1982 at the Automated Data System Center, Cairo, Egypt. From January to August 1987, he was a Post Doctoral Fellow at Manitoba University. Dr. Elsherbeni joined the faculty at the University of Mississippi in August 1987 as an Assistant Professor of Electrical Engineering. He advanced to the rank of Associate Professor on July 1991, and to the rank of Professor on July 1997. On August 2002 he became the director of The School of Engineering CAD Lab, and the associate director of The Center for Applied Electromagnetic Systems Research (CAESR) at The University of Mississippi. He was appointed as Adjunct Professor, at The Department of Electrical Engineering and Computer Science of the L.C. Smith College of Engineering and Computer Science at Syracuse University on January 2004. He spent a sabbatical term in 1996 at the Electrical Engineering Department, University of California at Los Angeles (UCLA) and was a visiting Professor at Magdeburg University during the summer of 2005 and at Tampere University of Technology in Finland during the summer of 2007. In 2009 he was appointed as Finland Distinguished Professor by the Academy of Finland and TEKES.

Dr. Elsherbeni received the 2006 School of Engineering Senior Faculty Research Award for Outstanding Performance in research, the 2005 School of Engineering Faculty Service Award for Outstanding Performance in Service, The 2004 Valued Service Award from the Applied Computational Electromagnetics Society (ACES)

for Outstanding Service as 2003 ACES Symposium Chair, the Mississippi Academy of Science 2003 Outstanding Contribution to Science Award, the 2002 IEEE Region 3 Outstanding Engineering Educator Award, the 2002 School of Engineering Outstanding Engineering Faculty Member of the Year Award, the 2001 ACES Exemplary Service Award for leadership and contributions as Electronic Publishing Managing Editor 1999-2001, the 2001 Researcher/Scholar of the year award in the Department of Electrical Engineering, The University of Mississippi, and the 1996 Outstanding Engineering Educator of the IEEE Memphis Section.

Over the last 23 years, Dr. Elsherbeni participated in acquiring over 10 million dollars to support his research dealing with scattering and diffraction by dielectric and metal objects, finite difference time domain analysis of passive and active microwave devices including planar transmission lines, field visualization and software development for EM education, interactions of electromagnetic waves with human body, sensors development for monitoring soil moisture, airports noise levels, air quality including haze and humidity, reflector and printed antennas and antenna arrays for radars, UAV, and personal communication systems, antennas for wideband applications, and antenna and material properties measurements. He has co-authored 102 technical journal articles, 25 book chapters, and contributed to over 300 professional presentations, offered 20 short courses and 24 invited seminars. He is the coauthor of the book entitled "The Finite Difference Time Domain Method for Electromagnetics with Matlab Simulations", Scitech, 2009, the coauthor of the book entitled "Antenna Design and Visualization Using Matlab", Scitech, 2006, the book entitled "MATLAB Simulations for Radar Systems Design", CRC Press, 2003, the book entitled "Electromagnetic Scattering Using the Iterative Multiregion Technique", Morgan & Claypool, 2007, the book entitled "Electromagnetics and Antenna Optimization using Taguchi's Method", Morgan & Claypool, 2007, and the main author of the chapters "Handheld Antennas" and "The Finite Difference Time Domain Technique for Microstrip Antennas" in Handbook of Antennas in Wireless Communications, CRC Press, 2001. He

was the main advisor for 33 MS and 9 PhD students.

Dr. Elsherbeni is a Fellow member of the Institute of Electrical and Electronics Engineers (IEEE) and a fellow member of The Applied Computational Electromagnetic Society (ACES). He is the Editor-in-Chief for ACES Journal, and an Associate Editor to the Radio Science Journal. He serves on the editorial board of the Book Series on Progress in Electromagnetic Research, the Electromagnetic Waves and Applications Journal, and the Computer Applications in Engineering Education Journal. He was the Chair of the Engineering and Physics Division of the Mississippi Academy of Science and was the Chair of the Educational Activity Committee for the IEEE Region 3 Section.



Lauri Sydänheimo received the M.Sc. and Ph.D. degrees in electrical engineering from Tampere University of Technology (TUT). He is currently a Professor with the Department of Electronics, TUT, and works as the Research Director of Tampere

University of Technology's Rauma Research Unit. He has authored over 120 publications in the field of RFID tag and reader antenna design and RFID system performance improvement.

His research interests are focused on wireless data communication and radio frequency identification (RFID).

Leena Ukkonen received the M.Sc. and Ph.D. degrees in electrical engineering from Tampere University of Technology (TUT) in 2003 and 2006, respectively. She is currently working at the TUT,



Department of Electronics as Senior Research Scientist leading the RFID research group. She has authored over 60 publications in the field of RFID antenna design and industrial RFID applications.

Her research interests are focused on passive UHF radio frequency identification (RFID) antenna development for tags and readers.

Bidirectional Radiated Circularly Polarized Annular-Ring Slot Antenna for Portable RFID Reader

¹Yi-Fang Lin, ¹Yu-Chang Kao, ²Shan-Cheng Pan, and ¹Hua-Ming Chen

¹Institute of Photonics and Communications,
National Kaohsiung University of Applied Sciences, Kaohsiung 807, Taiwan
hmchen@cc.kuas.edu.tw; linyf@cc.kuas.edu.tw

²Department of Computer and Communication,
Shu-Te University, Yen Chau, Kaohsiung 824, Taiwan

Abstract— A novel single-layer, microstrip-to-slotline transition technique for coupling a circularly polarized annular-ring slot antenna in the UHF band is presented. In the proposed design, circular polarization is generated using a proper asymmetry within the annular-ring slot structure and feeding the annular-ring slot using a slotline feed at 135° from the asymmetry. The direct slotline feed is used which is coupled to a $50\text{-}\Omega$ microstrip line on the opposite side of the substrate. The asymmetry in the proposed design is a meandered-slot section and the proposed CP design is achieved by the two orthogonal linear modes of the annular-ring slot. Simulated and measured results indicate that the proposed structure can achieve good CP radiation performances, and an impedance bandwidth and a 3-dB axial-ratio bandwidth obtained for the design are about 17.6% and 3.72%, respectively.

Index Terms— Annular-ring slot antenna, circular polarization (CP), microstrip-to-slotline transition, RFID reader.

I. INTRODUCTION

Radio frequency identification (RFID) system in the ultra-high frequency (UHF) band has gained much interest in several service industries, purchasing and distribution logistics, manufacturing companies and goods flow system [1]. The RFID system generally consists of the reader and the tag, and the UHF RFID system

operates at the bands of North America (902-928 MHz), Taiwan (920-928 MHz) and Europe (865-867 MHz). The reader can be a read device that uses an antenna which sends a radio frequency signal to a tag. The RFID reader antenna is one of the important components in RFID system and has been designed with CP operation. Circularly polarized antennas can reduce the loss caused by the multi-path effects between the reader and the tag antenna. A CP antenna with a low profile, small size, and light weight is required in portable RFID reader.

A typical technique for generating circular polarization radiation is to excite two orthogonal degenerate resonant modes with a 90° phase difference. Single-fed circularly polarized annular-ring, square and circular patch antennas with symmetrical or asymmetrical perturbation elements are reported [2-5]. Using perturbation cuts or strips to suitably differentiate the two orthogonal modes at resonant frequency, the antenna can easily radiate CP wave. However, these antennas provide small impedance bandwidth and narrow axial ratio (AR) bandwidth. To enhance an AR bandwidth, a single-fed slot-coupled microstrip antenna for circular polarization operation is preferred [6-8]. The CP antenna is achieved by using an inclined nonlinear coupling slot or unequal arm of cross-slot. However, a common slot coupling patch antenna in its basic structure consists of two substrates separated by a ground plane. Two substrates

increase the volume of the antenna and the complexity of fabrication. Another drawback is that a multi-layered substrate with the coupling slot on the ground plane can result in coupled surface-wave modes, which will lead to distorted radiation patterns.

To improve the operating bandwidth and not increase the antenna size, using the printed slot antenna is a possible method. Since the printed slot antenna is a dual of the microstrip antenna, it is also possible that by introducing some perturbations to the slot antenna, CP radiation of slot antenna can be achieved. However, the single-layer slot antenna with circular polarization has a few studied up to now. The CP radiation can be obtained by the introducing of some symmetrical or asymmetrical perturbation elements into a single-feed slot antenna, and the bandwidth is greater than that of a conventional circularly polarized microstrip antenna operated in the fundamental mode [9-12].

In this paper, a novel and single-layer annular-ring slot antenna has been proposed to obtain circularly polarized radiation. The proposed antenna has a simple narrow annular-ring slot with asymmetry and is fed from the microstrip line coupling to the slotline, as shown in Fig. 1. The proposed asymmetry has a simple structure of a meandered slot section. Additionally, the antenna operates at its fundamental orthogonal modes for the UHF band, and the two near-degenerated resonant modes for circularly polarization of an annular-ring slot antenna are generated by etching diagonal asymmetrical meandered-slot to the annular-ring slot. Details of the antenna design and the obtained experimental results of the antenna performance are presented and discussed.

II. ANTENNA CONFIGURATION

The configuration of the proposed antenna is shown in Fig. 1, in which an annular-ring slot antenna with a meandered slot section is etched on the ground plane ($100 \times 100 \text{ mm}^2$) of FR4 substrate with thickness $h = 1.6 \text{ mm}$ and relative permittivity 4.4. The outer and inner radii of the annular-ring slot radiator are R_1 and R_2 , respectively, and the slot width W is $R_1 - R_2$. The meandered slot section is a U-shaped slot, which is placed at the annular-ring slot edge with an angle

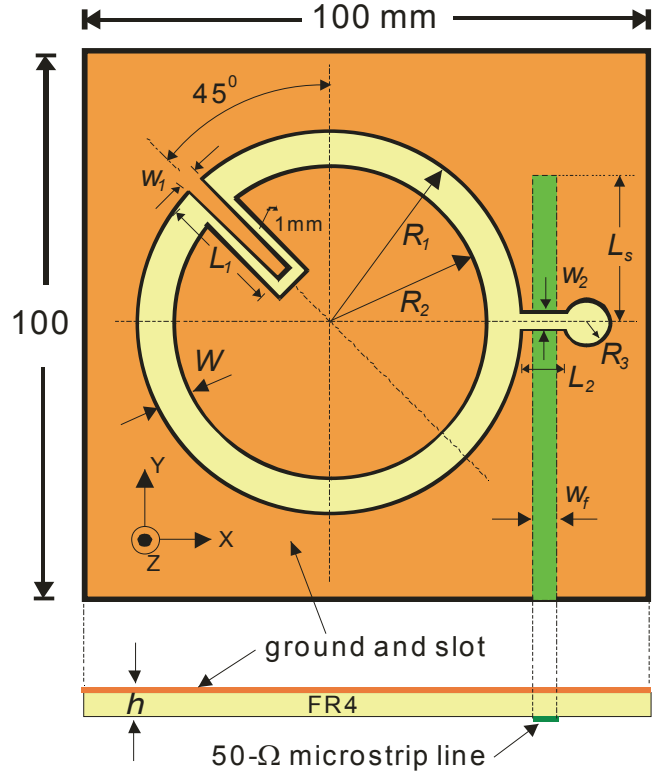


Fig. 1. Geometry of the single-layer circularly polarized annular-ring slot antenna.

of 45° from the y-axis. The U-shaped slot has a side length of L_1 , a gap distance of W_1 and a fixed uniform width of 1 mm. In addition, the annular-ring slot is fed by a simple slotline on the same side of the substrate, which energy is coupled from the 50- Ω microstrip feed line. The simple slotline consists of a narrow rectangular slot with dimensions $L_2 \times W_2$ and a circular slot of radius R_3 for open stub. A 50- Ω microstrip feed line with a width $W_f = 3.0 \text{ mm}$ is printed on the opposite side of the FR4 substrate. The microstrip line is extended beyond the center of the slotline by a length $L_s = 0.16\lambda_g$ (25 mm) for the tuning stub, where λ_g is the feed line wavelength at 915 MHz. The tuning stub has improved the impedance matching of the proposed antenna. The field in the annular-ring slot antenna is excited from the feed line through the slotline. Therefore, radiation from the annular-ring slot can be enabled.

In order to reduce experimental cut-and-try design cycles, the simulation software HFSS is used to guide fabrication. For conventional annular-ring slot antennas, the fundamental

resonant mode (TE₁₁ mode) occurs at a frequency whose wavelength in the ring-slot approximately corresponds to the mean circumference of the ring-slot [13]. That is,

$$f = \frac{c}{\pi(R_1 + R_2)\sqrt{\epsilon_{eff}}} \quad (1)$$

$$\epsilon_{eff} = 1 + q(\epsilon_r - 1) \quad (2)$$

where c is the speed of light in free space, f is the fundamental frequency of the conventional annular-ring slot antenna, $\pi(R_1 + R_2)$ is the mean circumference of the annular-ring slot, ϵ_{eff} is the effective dielectric constant and q is the correction factor considering the presence of the different dielectric material on the two sides of the annular-ring slot. In this study, slot width of $W = R_1 - R_2$ and dielectric constant of substrate $\epsilon_r = 4.4$ were used in all measurements and the value of q is obtained from many simulations for the narrow slot width. It can be found that the effective dielectric constant decreases when the slot width W is increased. In this study, it has to be noted that the q factor of 0.082 in equation (2) is an average value for the narrow annular-ring slot with a width of 2 mm to 6 mm, and then the calculated resonance frequency of the fundamental TE₁₁ mode is approximately 1207 MHz for slot width of 4 mm.

With the introduced meandered slot section (U-shaped slot), the symmetry of the annular-ring slot antenna is perturbed and the fundamental resonant mode can be split into two orthogonal degenerate resonant modes with equal amplitudes and a 90° phase difference required for the generation of circular polarization. One of the resonant lengths of the degenerate modes is left perimeter of annular-ring slot from the diagonal line and the other resonant length is right perimeter, which operates at its fundamental mode and corresponds to about half guided wavelength of the center frequency.

III. PARAMETRIC STUDY

To achieve optimum performance, a parametric study by using commercial EM software HFSS 10.0 is carried out to investigate the characteristics of the proposed annular-ring slot antenna. The antenna's initial values, unless

otherwise stated, are fixed at $R_1 = 37$ mm, $R_2 = 33$ mm, $W_f = 3$ mm, $L_s = 25$ mm, $L_1 = 21$ mm, $W_1 = 3$ mm, $L_2 = 4.8$ mm, $W_2 = 1$ mm and $R_3 = 3$ mm.

A. Operational Mechanism of CP Radiation

In Fig. 1, a U-shaped slot with an angle 45° from the y-axis is etched on the edge of the annular-ring slot, and a horizontal slotline segment terminated by a small circular slot, as a tuning stub, is centrally fed by a microstrip line for coupling the electromagnetic energy to the annular-ring slot. In this antenna configuration, it was shown that by introducing the U-shaped slot in the annular-ring slot located at 45° with respect to the y-axis circular polarization can be excited. In order to check this operating mechanism, Fig. 2 shows the simulated electric current flow and distribution on the annular-ring slot antenna. It can be observed that the null currents are located at the diagonal line with azimuth angle ϕ of 45° and 225°, respectively; that is, one of the resonant current lengths of the degenerate modes is the perimeter of annular-ring slot from A-C-B line and the other resonant length is the perimeter of A-D-B line, which operates at its fundamental mode and corresponds to about half guided wavelength of the center frequency. That is,

$$f_a \approx \frac{c}{2[\pi(R_1 + R_2)/2 + 2(L_1 - W/2) - W_1 + 1]\sqrt{\epsilon_{eff}}} \quad (3)$$

$$f_b \approx \frac{c}{2[\pi(R_1 + R_2)/2 + 2L_2 + 2\pi R_3 - 2W_2]\sqrt{\epsilon_{eff}}} \quad (4)$$

$$\epsilon_{eff} = 1 + 0.082(\epsilon_r - 1)$$

the q factor of effective dielectric constant can be approximately expressed as 0.082 in equation (2). The total resonant length, from point A through point C, then to point B, is about 149.9 mm ($\pi(R_1 + R_2)/2 + 2(L_1 - W/2) - W_1 + 1$) which is about $0.5\lambda_s$ at $f_a = 884$ MHz. The other current flow from points A and D to point B can also generate a half wavelength mode at $f_b = 930$ MHz, which resonant length is about 142.6 mm ($\pi(R_1 + R_2)/2 + 2L_2 + 2\pi R_3 - 2W_2$). Note that the right-handed circularly polarized (RHCP) wave is obtained because the higher frequency f_b leads the lower frequency f_a by phase difference 90°.

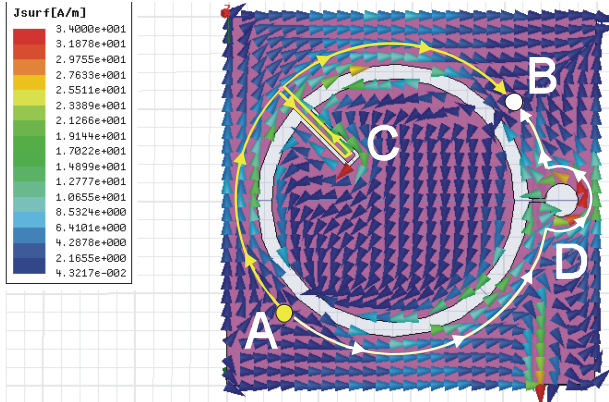


Fig. 2. Simulated current flow and distribution of the proposed antenna at 915 MHz.

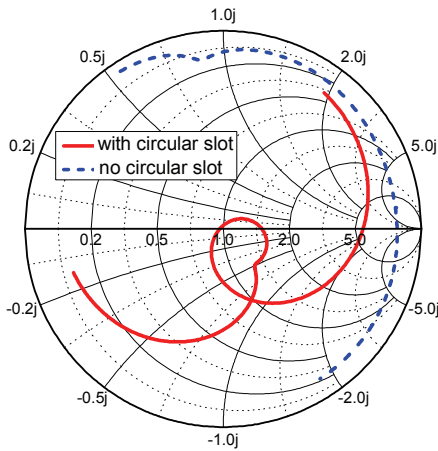


Fig. 3. Simulated Smith Chart for different circular slot radii (R_3).

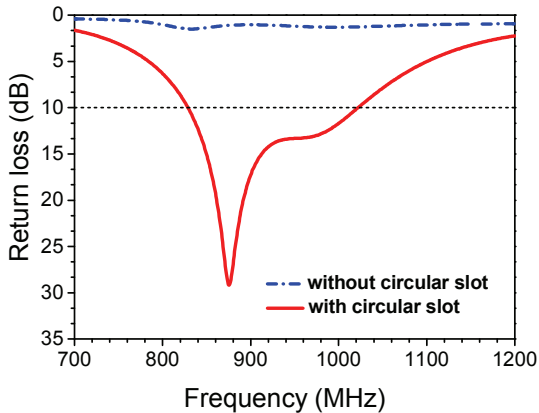


Fig. 4. Simulated return loss for different circular slot radii (R_3).

B. Effects of Circular Slot Radius

The radius (R_3) of the circular slot on the end of the slotline is a major design parameter for the

antenna, and it determines the phase difference of the two degenerate modes of the proposed antenna and the impedance matching. Figs. 3 and 4 show the simulated input impedance on the Smith Chart and the simulated return loss for various radii (R_3). It is first noted that a small loop can be obtained in the impedance loci for the CP operation and it can be tuned to obtain an optimum axial ratio after the impedance matching is achieved. For $R_3 = 0$ mm (no circular slot), there are no loop in the impedance loci and it has larger inductive impedance, i.e. without the circular slot did not excite the CP radiation. Observing the results in Fig. 4, no CP radiation is occurred without the presence of circular slot. A good CP performance in terms of the loop and good impedance matching is achieved when $R_3 = 4.0$ mm.

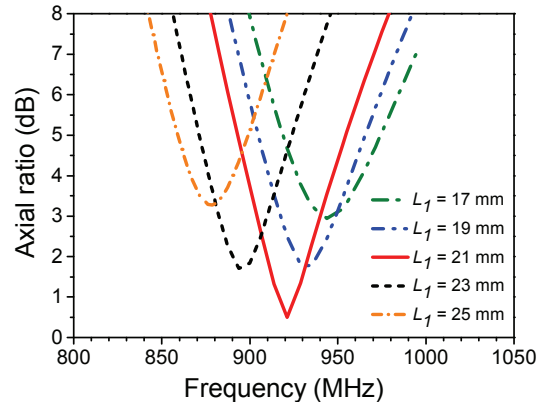


Fig. 5. Simulated axial ratio for different lengths of meandered slot section (L_1).

C. Effects of Meandered Slot Section

For the annular-ring slot antenna, the proposed CP design procedure can be applied to different size of meandered slot section. Figure 5 shows the simulated axial ratio with different length L_1 . As expected, the CP center frequency decreases when the length L_1 is increased. Fig. 6 shows the simulation return loss for the different width W_1 with a fixed length of $L_1 = 21$ mm. Also as expected in equation (3), there are no significantly effects for the various width of W_1 .

D. Effects of Inner Radius of Annular-Ring Slot

Fig. 7 shows the simulated axial ratio versus frequency for different inner radius R_2 . It can be find that a good axial ratio for different R_2 is

obtained. Additionally, the CP center frequency decreases when the radius R_2 is increased. As expected in equation (1), the CP center frequency decreases with increasing the mean circumference of the annular-ring slot ($\pi(R_1+R_2)$).

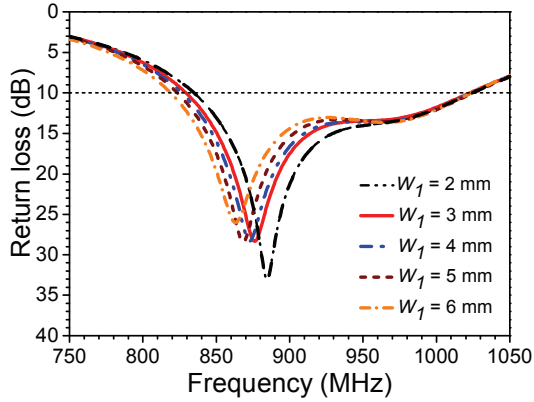


Fig. 6. Simulated return loss for different widths of meandered slot section (W_1).

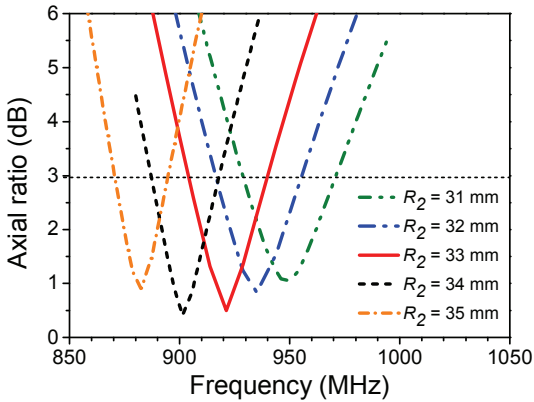


Fig. 7. Simulated axial ratio versus frequency for different inner radii (R_2).

IV. EXPERIMENTAL RESULTS

The proposed CP antenna is designed to operate at the center frequency of about 915 MHz in the UHF band for RFID reader. The return loss is measured using an Agilent N5230A vector network analyzer, and axial ratio and radiation patterns are evaluated in anechoic chamber with an NSI-800F10 antenna measurement system. Fig. 8 shows the simulated and measured return loss of the proposed antenna. The measured impedance

bandwidth for 10 dB return loss is 17.6%, ranging from 830 to 990 MHz, and agrees well with the HFSS simulated results (829-1021 MHz). Fig. 9 shows the simulated phase diagram for the proposed antenna. It can be found that the operational principle of this circularly polarized antenna is based on the fact that the generated mode can be separated into two orthogonal modes ($f_a = 884$ MHz and $f_b = 930$ MHz) of equal amplitude and about 89° phase difference and resulted in a good RHCP radiation. In addition, the measured axial ratio in the broadside direction versus frequency is also presented in Fig. 10. The 3-dB axial-ratio CP bandwidth is about 34 MHz or 3.71% around the center frequency at 915 MHz. Note that the minimum axial-ratio value is about 0.52 dB at the frequency (920 MHz), indicating that the circular polarization is pure.

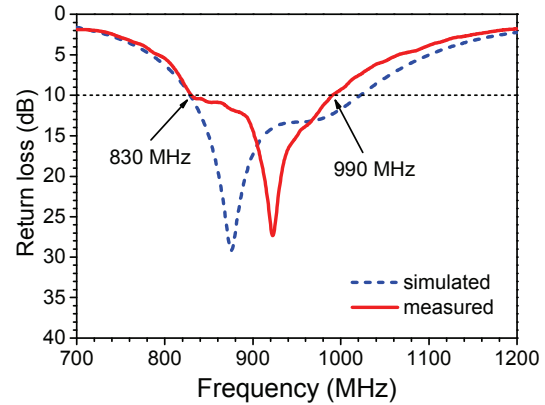


Fig. 8. Measured and simulated return loss of the proposed antenna.

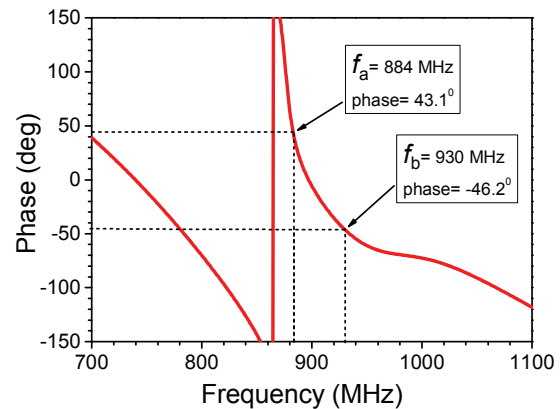


Fig. 9. Simulated phase diagram versus frequency for the proposed antenna.

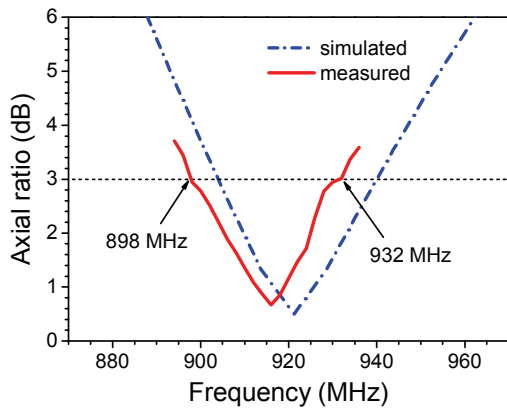


Fig. 10. Measured and simulated axial ratios of the proposed antenna.

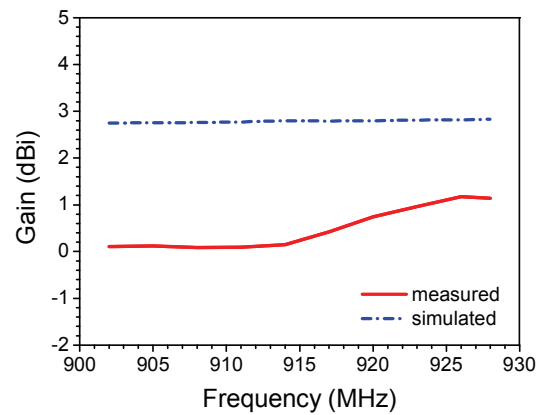


Fig. 12. Measured and simulated antenna gains versus frequency for the proposed antenna.

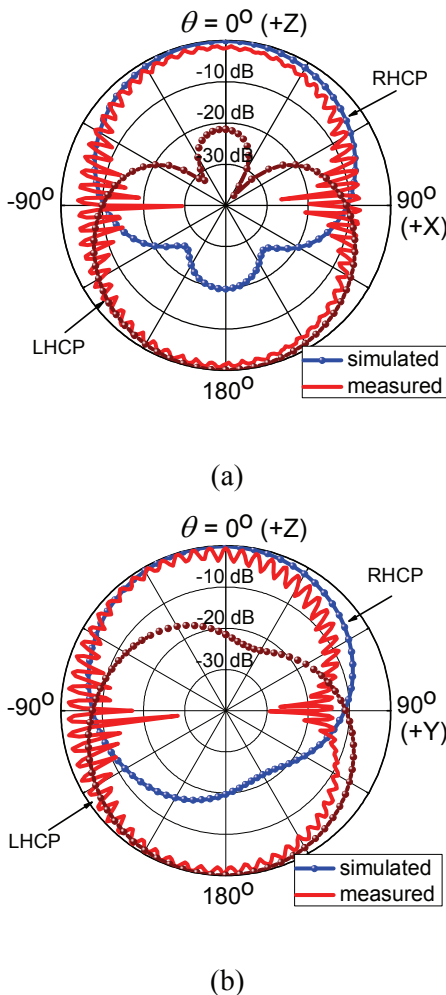


Fig. 11. Measured and simulated normalized RHCP/LHCP radiation patterns of the proposed antenna at 915 MHz. (a) x-z; (b) y-z plane.

The measured and simulated RHCP/LHCP radiation pattern at 915 MHz is plotted in Fig. 11, and good symmetry of bidirectional radiation has been observed. Note that a CP slot antenna without a reflector radiates a bidirectional wave, and the radiation patterns in both sides of the slot antenna are about the same with contrary circular polarization; that is, the front-side radiates RHCP while back-side radiates LHCP. Also, it can be observed from the pattern that the 3-dB beam widths are about 96° ($-50^\circ \sim 46^\circ$) with symmetry in the x-z plane and 98° ($-55^\circ \sim 43^\circ$) beam widths with a tilt to left in the y-z plane. The measured gain was obtained using the gain transfer method where standard gain horn antenna was used as a reference. The obtained peak antenna gain is from 0 dBi to 1.5 dBi in the UHF band (902-928 MHz) owing to the small size of the antenna.

V. CONCLUSIONS

A microstrip-to-slotline feed mechanism of circularly polarized annular-ring slot antenna with an asymmetrically meandered slot section for RFID reader is designed and measured. The asymmetrically meandered slot section is used to excite two orthogonal linear polarized modes. Experimental results show that the proposed antenna can have a 3-dB CP bandwidth of about 3.71% and an impedance bandwidth of about 17.6%. In addition, the proposed antenna is compact, bidirectional radiated and easily to find application as transmitting antenna in portable

RFID reader.

ACKNOWLEDGMENTS

This work was supported by the National Science Council of Taiwan under Contract NSC 97-2221-E-151-010.

REFERENCES

- [1] K. Finkenzeller, *RFID Handbook*, 2nd Ed, New York, Wiley, 2004.
- [2] K. L. Wong and Y. F. Lin, "Circularly polarized microstrip antenna with a tuning stub," *Electron. Lett.*, vol. 34, pp. 831-832, April 30, 1998.
- [3] K. L. Wong, W. H. Hsu and C. K. Wu, "Single-feed circularly polarized microstrip antenna with a slit," *Microwave Opt. Technol. Lett.*, vol. 18, pp. 306-308, July 1998.
- [4] H. M. Chen and K. L. Wong, "On the circular polarization operation of annular-ring microstrip antennas," *IEEE Trans. Antennas Propagat.*, vol. 47, pp. 1289-1292, Aug. 1999.
- [5] J. S. Row, "Dual-frequency circularly polarized annular-ring microstrip antenna," *Electron. Lett.*, vol. 40, no. 3, Feb. 5, 2004.
- [6] J. S. Row, "Design of aperture-coupled annular-ring microstrip antennas for circular polarization," *IEEE Trans. Antennas Propagat.*, vol. 53, pp. 1779-1784, May 2005.
- [7] D. H. Hyun, J. W. Baik, and Y. S. Kim, "Compact reconfigurable circularly polarized microstrip antenna with asymmetric cross slots," *Microw. Opt. Technol. Lett.*, vol. 50, no. 8, pp. 2217-2219, 2008.
- [8] K. L. Wong, C. C. Huang, and W. S. Chen, "Printed ring slot antenna for circular polarization," *IEEE Trans. Antennas Propagat.*, vol. 50, no. 1, pp. 75-77, Jan. 2002.
- [9] J. Y. Sze, K. L. Wong, and C. C. Huang, "CPW-fed square slot antenna for broadband circularly polarizes radiating," *IEEE Trans. Antennas Propagat.*, vol. 51, no. 8, pp. 2141-2144, 2003.
- [10] Y. B. Chen, X. F. Liu, Y. C. Jiao and F. S. Zhang, "CPW-fed broadband circularly polarized square slot antenna," *Electron.*

Lett., vol. 42, no. 19, pp. 1074-1075, Sep. 2006.

- [11] C. C. Chou, K. H. Lin and H. L. Su, "Broadband circularly polarized crosspatch-loaded square slot antenna," *Electron. Lett.*, vol. 43, no. 9, pp. 485-486, 2007.
- [12] T. N. Chang, and J. M. Lin, "A novel circularly polarized patch antenna with a serial multislot type of loading," *IEEE Trans. Antennas Propagat.*, vol. 55, no. 11, pp. 3345-3348, 2007.
- [13] R. Garg, P. Bhartia, A. Bahl, and A. Ittipibon, *Microstrip Antenna Design Handbook*, Artech House, Inc., 2001.



Yi-Fang Lin received the B.S. degree in physics from National Tsing Hua University, Hsinchu, Taiwan, the M.S. degree in Institute of Electro-Optical Engineering, and the Ph.D. degree in electrical engineering from National Sun Yat-Sen University, Kaohsiung, Taiwan, in 1993, 1995, and 1998, respectively.

Since 2000 she has been with the Institute of Photonics and Communications at National Kaohsiung University of Applied Sciences, Kaohsiung, Taiwan, where she became an Associated Professor in 2009. Her current research interests include microstrip antennas, dielectric resonator antennas and small antenna design.



Yu-Chang Kao was born in Tainan, Taiwan, in 1983. He received the B.S. degree in department of physics from National Kaohsiung Normal University, Kaohsiung, Taiwan, and the M.S. degree from the Institute of Photonics and

Communications, National Kaohsiung University of Applied Sciences, Kaohsiung, Taiwan, in 2007, and 2009, respectively. He is currently working on

design of circularly polarized antenna at school. His main research interests are in circularly polarized operation and broadband operation of antenna, especially using the slot antenna for RFID applications.



Shan-Cheng Pan received the B.S. and M.S. degrees in electronic engineering from National Taiwan University of Science and Technology, Taipei, Taiwan, in 1986 and 1990, respectively, and the Ph.D. degree in electrical engineering from National

Sun Yat-Sen University, Kaohsiung, Taiwan, in 1998.

Since 2005 he has been with the Department of Computer and Communication at Shu-Te University, Kaohsiung, Taiwan, where he became an Associate Professor. He also served as Chairman of the Computer and Communication Department at the same university since 2007. His current research interests include microstrip antennas, dielectric resonator antennas and microwave circuit design.



Hua-Ming Chen (M'98-SM'06) received the B.S. degree in physics from National Tsing Hua University, Hsinchu, Taiwan, the M.S. degree in Institute of Electro-Optics from National Chiao Tung University, Hsinchu, Taiwan, and the

Ph.D. degree in electrical engineering from National Sun Yat-Sen University, Kaohsiung, Taiwan, in 1983, 1987, and 1996, respectively.

Since 1988 he has been with the Institute of Photonics and Communications at National Kaohsiung University of Applied Sciences, Kaohsiung, Taiwan, where he became a Professor in 2001. He also served as Director of Institute of Photonics and Communications at the same university from 2005 to 2008. He has published more than 110 journal and conference papers and takes out 18 patents on antenna design. Several of his antenna designs have been licensed to industry for production. His current research interests include microstrip antennas, dielectric resonator antennas, RFID antennas and microwave circuit design. Since 2009, he has been serving as the Chair of IEEE AP-S Tainan Chapter. He also served as a Technical Program Committee member of IEEE TENCON 2007 in Taiwan. He was also listed in Who's Who in Science and Engineering and Who's Who in Asia.

Low-profile Normal-Mode Helical Antenna for Use in Proximity to Metal

Wongook Hong, Naobumi Michishita and Yoshihide Yamada

Department of Electrical and Electronic Engineering
National Defense Academy
1-10-20 Hashirimizu, Yokosuka-shi, 239-8686 JAPAN
yyamada@nda.ac.jp

Abstract— To expand the applicability of UHF tags, a low-profile, small, normal-mode helical antenna (NMHA) that can be used on metallic plates was developed. This paper clarifies the design method for antenna structures for use in proximity to metal. The design data were obtained with the electromagnetic simulator FEKO. Fundamental electrical characteristics such as the antenna input impedances, self-resonance conditions, and radiation characteristics were clarified in proximity to metal. For antenna sizes of $0.03\text{--}0.05$ wavelengths, antenna gains of about -0.5 dBd were achieved. The calculated results were verified using an actual antenna (size, 0.04 wavelengths). A tap feed structure was used for impedance matching. It was shown that very precise design results could be achieved. Moreover, the developed NMHA was designed to be a tag antenna. Here, the antenna impedance was matched to the IC chip impedance. The read range of the developed tag was measured to be about 15 m.

Index Terms— Tag antenna, Normal Mmode Helical Antenna, Metal Proximity Use and Read Range.

I. INTRODUCTION

Radio-frequency identification (RFID) systems have recently attracted much interest for use in efficiently tracking and identifying objects in various supply chains [1]. An RFID system basically consists of a reader, writer, and tag. For UHF tags, film-type half-wavelength (0.5λ) dipole antennas are used as antennas in many applications [2]. However, such tag antennas cannot be mounted on metallic objects or bottles full of liquids because the antenna characteristics are seriously degraded by the resulting change in antenna impedance [3]. For

these applications, some designs for patch antennas [4] and slot antennas [5] were proposed. Nevertheless, although these antennas were sufficiently thin—some less than 4 mm—they were about 80 mm in size, which limited them to specialized applications. This limitation was overcome in the design of a small, normal-mode helical antenna (NMHA) that could be used on metallic plates [6]. An antenna gain of -0.4 dBd was achieved by an antenna that was 0.035λ (11 mm) in size in proximity to metal. However, the antenna thickness was as large as 9 mm. This must be reduced to increase user convenience.

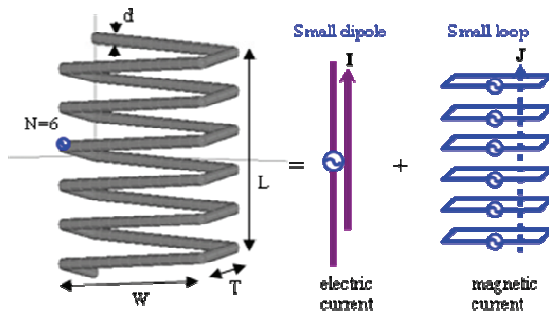
In this study, projection was reduced by using a rectangular cross section for the NMHA. This rectangular NMHA was designed using the commercial electromagnetic simulator FEKO Suite 5.4 [7]. The simulation parameters were verified to ensure precise calculations, and the fundamental electrical performance characteristics such as the antenna input impedances, self-resonance condition, and radiation characteristics were calculated in proximity to metal. For antenna sizes of $0.03\text{--}0.05\lambda$, antenna gains of about -0.5 dBd were achieved. The calculated results were confirmed using an actual antenna with the size 0.04λ . A tap feed structure was designed for impedance matching. It was shown that very precise design results could be achieved. Moreover, the developed NMHA was designed to be a tag antenna. Here, the antenna impedance was matched to the IC chip impedance. The read range of the developed tag was measured to be about 15 m.

II. FEATURES OF THE RECTANGULAR NMHA

The configuration of the rectangular NMHA is

shown in Fig. 1(a). L and W represent the antenna length and width, respectively. The number of turns in the helix is represented by N . The antenna wire has the diameter d . The NMHA has a rectangular cross section. The projection from the metal is expressed by T . This projection was decreased sufficiently.

Electrically, the proposed NMHA is equivalent to the small dipole and loops shown in Fig. 1(b). And because the capacitance of the small dipole is cancelled out by the inductance of the loops—a condition called self-resonance—a purely resistive input impedance can be achieved. This is very important for effective radiation. When this antenna is placed near a metal plate, although the performance of the small dipole is degraded, the performance of the loop antenna is enhanced. Therefore, this antenna works well even in proximity to metal.



(a) Perspective view (b) Electrical equivalent configuration

Fig. 1. Configuration of the rectangular NMHA.

III. SIMULATION CONDITIONS

In order to calculate precisely, the simulation parameters were studied. The commercial electromagnetic simulator FEKO was employed. A simulation example is shown in Fig. 2. The antenna was placed on a metal plate with a 1 mm spacing. The most important parameter to obtain for exact results was the segment size (ΔS) of the metal plate near the antenna, as shown by the red frame. Table 1 gives the simulation parameters. Because the antenna length was very small, such as about $\lambda/25$, the antenna segment size was set at $\lambda/500$. As for the metal plate mesh sizes, $\lambda/20$ was used outside the red frame. Inside the red frame, the mesh sizes were varied from $\lambda/10$ to $\lambda/80$ so as to check the convergence of the calculated results. Other calculation data for the

memory size and calculation time showed that the computational load was very light.

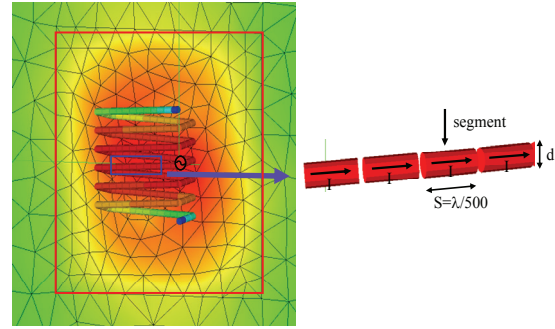


Fig. 2. Current distributions of NMHA structure.

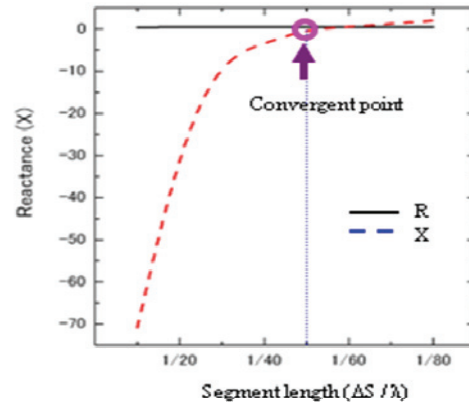


Fig. 3. Convergence of the input impedance.

Table 1: Simulation parameters.

Computer	CPU	2.8 GHz
	Memory	7.9 GByte
Simulator	MOM of FEKO	
Frequency	953 MHz	
Segment size	Antenna	$\lambda/500$
	Metal plate (near the ant.)	$\lambda/10$ to $\lambda/80$
	Metal plate (far from the ant.)	$\lambda/20$
Number of segments	Antenna	348
	Metal plate	5,448
Calculation memory size	Antenna	696 KByte
	Metal plate	120 MByte
Calculation time (seconds)	Antenna	0.94
	Metal plate	139

Fig. 3 shows the convergence of the input impedance calculations. This antenna was designed to satisfy the self-resonant condition. Consequently, the reactance of the input impedance should become zero. At a segment size of $\lambda/50$, the reactance approached zero. Hence, a mesh size of $\lambda/50$ was used in the red frame area. The input resistance was not affected by the segment size.

IV. CALCULATED DESIGN DATA

The simulation configuration is shown in Fig. 4. The antenna thickness is expressed by T . The size of the metal plate is expressed by M . The spacing between the antenna and the metal plate is expressed by S . The equivalent electric and magnetic currents are indicated by I and J , respectively. As for the radiation components, E_θ and E_ϕ correspond to the radiation from the electric and magnetic currents, respectively.

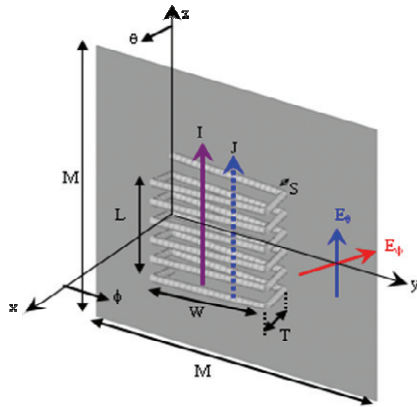


Fig. 4. Simulation configuration.

In the antenna configuration design, the most important design subject is the self-resonance condition. In the self-resonance condition, the capacitance and inductance of the input impedance are cancelled out. The antenna length L determines the input capacitance ($-X_D$) of the short dipole. The cross-sectional area of the antenna, given by the antenna width W and the thickness T , determines the input inductance (X_L). The total input inductance can be found by multiplying by the number of turns N . So, for a given L , combinations of W , T , and N were determined. The relations of these parameters are shown in Fig. 5. In this case, T and N are given as variable parameters. Other parameters,

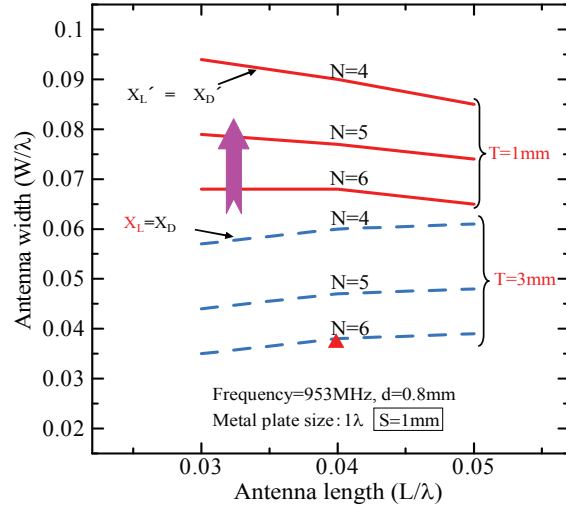


Fig. 5. Self-resonance for various T .

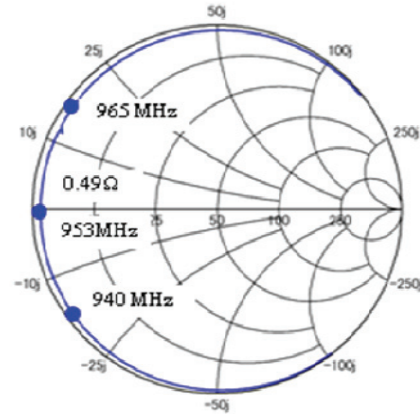


Fig. 6. Input impedances.

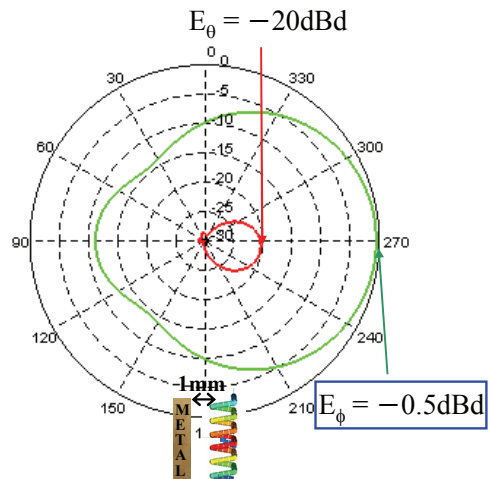


Fig. 7. Radiation patterns.

such as the wire diameter (d), spacing (S), and metal size (M) are shown in the figure. For smaller values of T , larger W values were needed in order to maintain the cross-sectional area. For

smaller values of N , larger W values were needed in order to increase the individual inductances of the cross-sectional areas. It is remarkable that all of the curves were almost unaffected by a change in L .

An example of the input impedance at the structure indicated by the triangular mark at $T = 3$ mm is shown in Fig. 6. At 953 MHz, the input impedance became a pure resistance of 0.49Ω . Because the antenna had a very small length of 0.04λ , the input resistance became very small. The radiation characteristics are shown in Fig. 7. In order to estimate the radiation level conveniently, the input impedance mismatch was ignored by utilizing a “no mismatch” calculation condition. The dominant radiation component became E_ϕ , which corresponded to

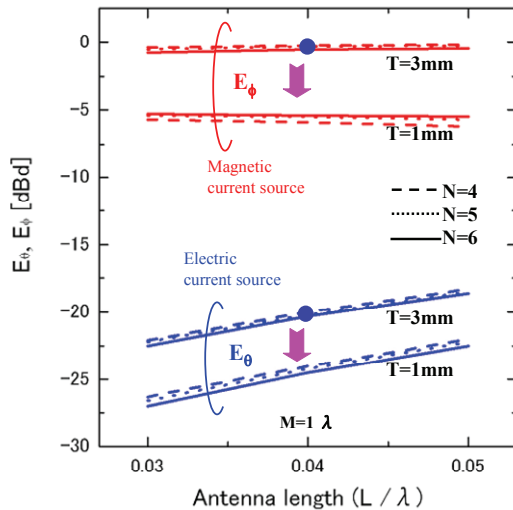


Fig. 8. Gain for various T .

the magnetic current source. It was surprising that an antenna gain of -0.5 dBd was obtained, which was comparable to a 0.5λ dipole antenna. Here, the unit dBd represents the antenna gain normalized by that of the 0.5λ dipole antenna. The high gain is due to the adequate ohmic resistance (R_o) in relation to the radiation resistance (R_r). R_o is determined by the antenna wire length and diameter (d). Here, because R_r is 0.24Ω , R_o should be smaller than R_r . To achieve a very small resistance, the wire diameter should be as large as possible. For $d = 0.8$ mm, $R_o = 0.25 \Omega$. Then, the antenna radiation efficiency is about 50%. This confirms the practicality of this small rectangular NMHA when used in proximity to metal.

The important antenna gain characteristics under the self-resonance condition are shown in Fig. 8. It is remarkable that the E_ϕ components were dominant. The E_θ components became less than -20 dBd. As for N changes, no antenna gain differences were observed. For larger T values, high gains were achieved. For $T = 3$ mm, antenna gains comparable to that of a 0.5λ dipole antenna are expected. One more feature was that the antenna gains remained constant for different L . Hence, it is expected that excellent antenna gains are probable for very small antenna sizes such as 0.03λ .

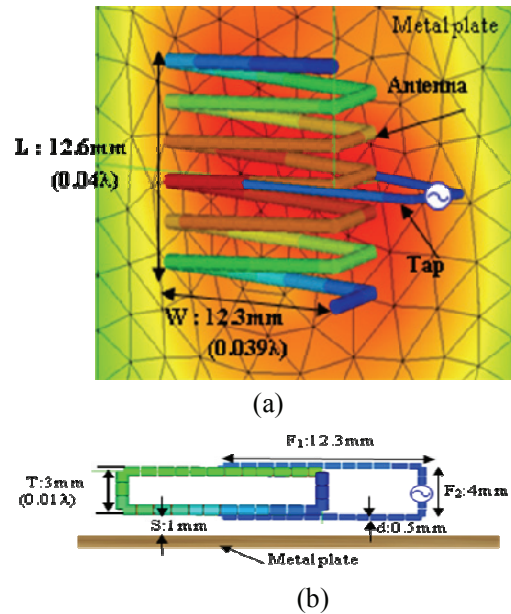


Fig. 9. (a) Perspective view and (b) cross-sectional view of the experimental NMHA structure.

V. PRACTICAL ANTENNA DESIGN

The previous section showed that high antenna gains can be expected in the very small NMHA. However, because the input resistance is very small, an antenna impedance matching structure is needed for practical application. This section shows how such a matching structure can be achieved. A tap type matching structure [8] was employed, as shown in Fig. 9(a) and (b). The tap was composed of a single U shaped wire. One end of the wire was connected to the antenna conductor. A feed point was placed at the other end. Wire diameters of 0.8 mm and 0.5 mm were selected for the antenna and the tap, respectively. Fig. 9(b) shows that the tap arms were placed

between the antenna wires in order to avoid increasing the antenna thickness [9]. Because the spacing between the antenna and the metal plate was very small (1 mm), the arrangement of the tap arms was very important.

The actual parameters are shown in Fig. 9. In order to verify the electrical performance characteristics of the antenna through measurements, the antenna input impedance was matched to the coaxial cable impedance of 50 Ω. The tap structure of this case is considered to be rather simple.

The fabricated antenna and feed cable are shown in Fig. 10. The tap arms were soldered to the antenna wire. A coaxial cable was used as a feed line. A sperrtopf balun was attached to the coaxial cable to suppress the leak currents on the coaxial cable. Fig. 11 shows the measured and calculated antenna impedances. The measured and calculated results agreed very well with and without tap feeds. When the tap feed was employed, the antenna impedance became exactly 50 Ω. The effectiveness of the tap feed was thus verified. The bandwidth characteristics are shown in Fig. 12. A 3.5 MHz bandwidth was obtained when VSWR < 2. This bandwidth corresponded to 0.4% of the center frequency.

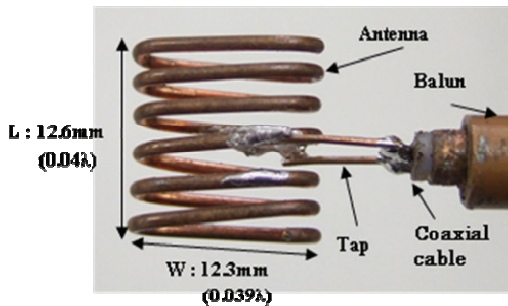


Fig. 10. Photograph of the fabricated antenna.

The radiation characteristics were verified through measurements. Fig. 13 shows the data for the case without the metal plate. The measured and calculated results agreed very well. Therefore, the achievement of the designed results was verified. In this case, the E_θ component corresponding to the electric current source became dominant. An antenna gain of about -2.9 dBd was achieved. By taking into account the small antenna size of 0.04λ , this antenna gain seems surprisingly large. However, the E_ϕ component, which corresponded to the magnetic current source, became small, such as -11 dBd.

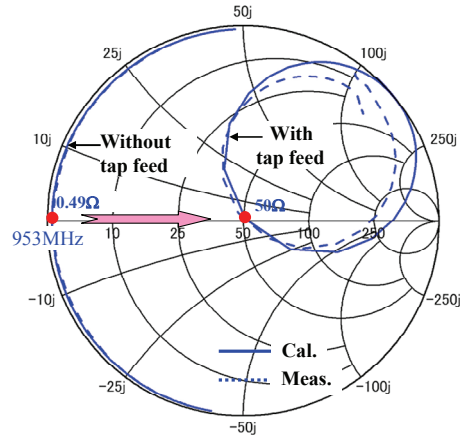


Fig. 11. Input impedances with and without tap feed.

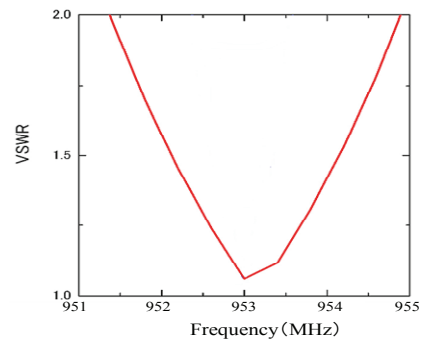


Fig. 12. The characteristics of the VSWR.

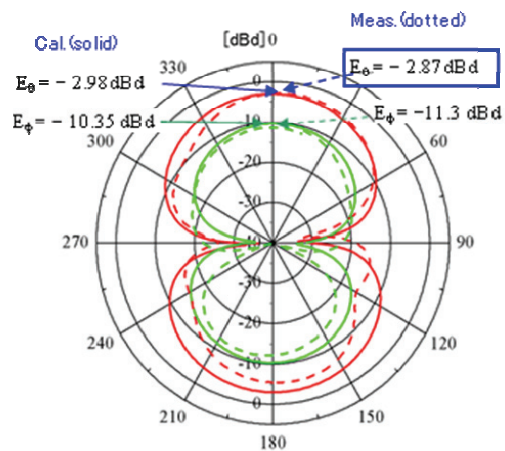


Fig. 13. Radiation patterns without metal plate.

The important radiation characteristics with a metal plate are shown in Fig. 14. In this case, the antenna was placed on the metal plate with $S = 1$ mm. A square metal plate with a size of 0.5λ was employed. The E_ϕ component became dominant in the case of metal proximity. A very

high antenna gain of -0.5 dBd was achieved. The E_ϕ level was increased by about 10 dB compared to the case without the metal plate. The usefulness of the NMHA in a metal proximity application was verified. At the same time, the intensity of the E_θ component decreased to -11 dBd. This showed that the electrical current source no longer worked well in proximity to the metal.

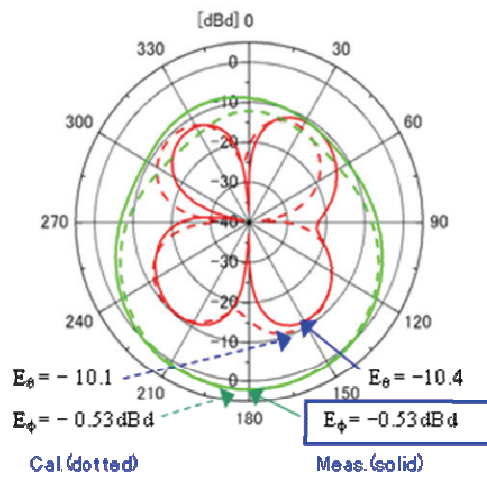


Fig. 14. Radiation patterns with metal plate.

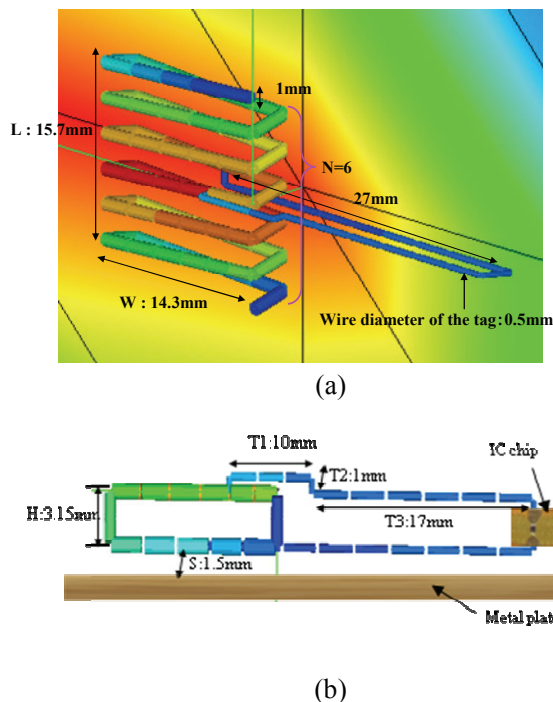


Fig. 15. (a) Perspective view and (b) cross-sectional view of the antenna structure matching IC chip.

VI. TAG ANTENNA DESIGN

In order to use the rectangular NMHA as a tag antenna, the antenna input impedance had to be matched to the IC chip impedance of $Z_{IC} = 25 - j95 \Omega$. Therefore, the antenna size and tap size were modified as shown in Fig. 15. The tap length was elongated in order to produce the inductance that was needed to achieve conjugate matching to the IC chip capacitance. The spacing between the antenna and the metal plate was set to 1.5 mm. As for the metal plate, a 0.5λ square plate was employed.

The impedance matching process is shown in Fig. 16. It was recognized that the tap length (T_3) was very important in the matching to the IC chip. Almost complete conjugate matching could be achieved at $T_3 = 17$ mm.

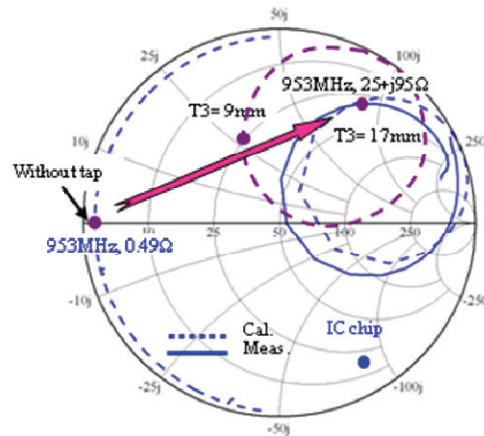


Fig. 16. Input impedances.

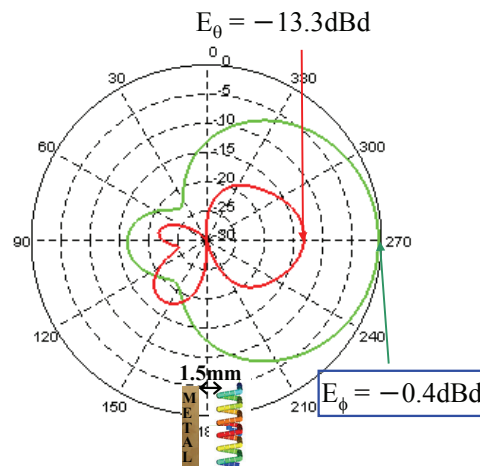
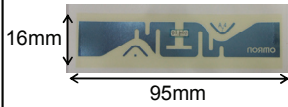
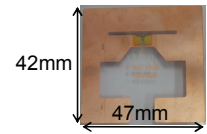
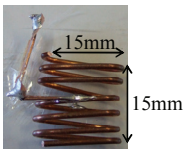
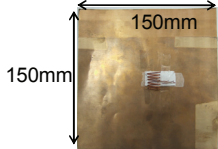


Fig. 17. Estimated radiation patterns.

Table 2: Measured read ranges.

	Antenna alone	Read range	Antenna alone	Read range
Current Antenna		9m		9m
Low profile NMHA		6m	Metal plate (150mm × 150mm)	15m
				

In order to estimate the antenna gain of this structure, the radiation characteristics were calculated, and the results are shown in Fig. 17. In this case, the antenna input impedance was designed to be $Z_{ANT} = 25 + j95 \Omega$. In order to easily calculate the radiation intensity, the input impedance mismatch was ignored by utilizing the “no mismatch” calculation condition. An antenna gain of -0.4 dBd was obtained. Therefore, an electrical performance comparable to conventional tags can be expected.

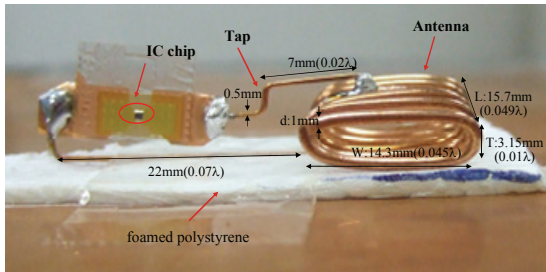


Fig. 18. The RFID tag structure using the NMHA.

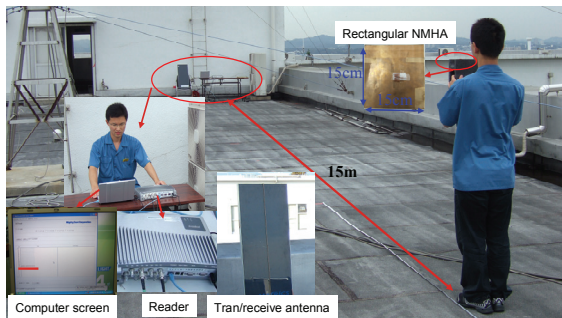


Fig. 19. Read range measurement.

VII. READ RANGE

The final estimation of the electrical performance of a tag is the read range. The tag configuration of the rectangular NMHA is shown in Fig. 18. The IC chip was inserted in the tap arm. The antenna and IC chip were placed on a piece of polystyrene foam attached to the metal plate. The thickness of the foam was 1.5 mm. The size of the metal plate was 0.5λ square. The read range was measured with the setup shown in Fig. 19. A commercial reader antenna was used for transmitting and receiving. This reader antenna was connected to a reader unit and a computer. When the tag information was read, the tag number was indicated on the computer screen.

Read range measurement were conducted by changing the distance between the reader antenna and the tag. The distance where the tag number disappeared was considered the read range. These read ranges might be affected by the height pattern at the measurement site. So, in every case, the height of the tag was selected so as to obtain the highest electrical strength.

The measured read ranges of some types of tags are summarized in Table 2. In the case of conventional antennas, read ranges of 9 m are obtained. In the case of the NMHA, read ranges of 6 m and 15 m were obtained without and with metal plate proximity, respectively. The effectiveness of the developed tag was verified through this read range measurement

VIII. CONCLUSIONS

A low profile, small NMHA was developed

for use on the surface of a metal plate. Important design data were obtained through simulations using the electromagnetic simulator FEKO. The following novel technical results were obtained.

- (1) The structural conditions for $0.03\text{--}0.05\lambda$ antennas were obtained.
- (2) The antenna gain design data for metal proximity applications were obtained. A nearly -0.5 dBd gain was shown.
- (3) In order to fabricate a practical antenna, a tap type matching structure was designed to match the antenna impedance to a $50\ \Omega$ cable or IC chip impedance.
- (4) The read range characteristics of the NMHA tag were obtained through measurements. A read range of about 15 m was verified.

ACKNOWLEDGMENT

The authors would like to thank the president, K. Kabumoto, and the executive director, T. Hiarano, of Mighty Card Co-op. for their continuous support of this study.

REFERENCES

- [1] RFID-related presentations, Special sessions at *IEEE AP-S International Symposium*, Honolulu, HI, June 2007.
- [2] H.W. Son, G. Y. Choi, and C. S. Pyo, "Open-Ended Two Strip Meander-Line Antenna for RFID Tags," *ETRI Journal*, vol. 28, no. 3, pp. 383-385, June 2006.
- [3] L. Ukkonen, M. Schaffrath, L. Sydanheimo and M. Kivikoski, "Analysis of integrated slot-type tag antenna for passive UHF RFID," *IEEE AP-S International Symposium*, pp. 1343-1346, July 2006.
- [4] M. L. Ng, et al, "Design and Miniaturization of an RFID Tag Using a Simple Rectangular Patch Antenna for Metallic Object Identification," *IEEE AP-S International Symposium*, pp. 1741-1744, June 2007.
- [5] X. Zeng, et al, "Slots in Metallic Label as RFID Tag Antenna," *IEEE AP-S International Symposium*, pp. 1749-1752, June 2007.
- [6] W. G. Hong, W. H. Jung, Y. Yamada and N. Michishita, "High Performance Normal Mode Helical Antenna for RFID Tags," *IEEE AP-S International Symposium*, pp. 6023-6026, June 2007.
- [7] www.feko.info
- [8] C. A. Balanis, "Antenna Theory Analysis and Design, Second Edition", John Wiley & Sons Inc., Ch. 9, pp. 472-480, 1997.
- [9] W. G. Hong, Y. Yamada and N. Michishita, "Design of a simple tap structure for low profile small normal mode helical antenna," *IEEE AP-S International Symposium*, no. 229, vol. 5, July 2008.



Won Gook Hong was born in Pusan, Korea on June 23, 1976. He enlisted in the Republic of Korea Army in 1999. He began as a platoon leader. Now he is a Captain. He entered the master course for

Electronics Engineering at the National Defense Academy, Kanagawa, in 2007. His current research interests include tag antennas and reader antennas for RFID.



Naobumi Michishita received the B.E., M.E., and D.E. degrees in Electrical and Computer Engineering from Yokohama National University in 1999, 2001, and 2004, respectively. He

joined the Department of Electrical and Electronic Engineering, National Defense Academy, as a research associate in 2004. He was a visiting scholar at the University of California, Los Angeles from 2006 to 2007. He received the Young Engineer Award from the IEEE AP-S Japan Chapter and IEICE in 2004 and 2005, respectively. His current research interests include metamaterial antennas and electromagnetic analysis. He is a member of IEEE.

**Yoshihide Yamada**

graduated from the Nagoya Institute of Technology and received the BS and MS degrees in electronics in 1971 and 1973, respectively. He received the DE degree from the Tokyo Institute of Technology in 1989. In 1973, he joined the Electrical Communication Laboratories of the Nippon Telegraph and Telephone Corporation (NTT). Until 1984, he was engaged in research and development related to reflector antennas for terrestrial and satellite communications. Beginning in 1985, he engaged in R&D for base station antennas for mobile radio systems. In 1993, he moved to the NTT Mobile Communications Network Inc. (NTT DoCoMo). In 1995, he was temporarily transferred to the YRP Mobile Telecommunications Key Technology Research Laboratories Co., Ltd. At the same time, he was a guest professor at the cooperative research center of Niigata University, and a lecturer at the Science University of Tokyo, both from 1996. In 1998, he took a position as a professor at the National Defense Academy. At present, he is interested in very small RFID antennas, shaped dielectric lens antennas, and electromagnetic simulations of large objects.

He is a member of the IEICE and JSST of Japan and an IEEE society member of AP, VT, and COMM.

New Antennas Based on Triangular Patch as a Solution for RFID Application

A. Ferchichi¹, N. Sboui¹, A. Gharsallah¹, H. Baudrand²

¹Laboratoire d'Electronique,
Faculté des sciences de Tunis, 2092 El Manar Tunisia
noureddine.sboui@fst.rnu.tn

²Laboratoire d'Electronique EN SEEIHT de Toulouse France

Abstract — This paper covers the design of a new antenna for RFID applications at microwave frequencies. Five antennas are studied. The first three structures are inspired from a triangular patch, whereas the fourth and the fifth are inspired from a Sierpensi fractal antenna. The size reduction is more than 80%, which explains the utility of the proposed antennas.

Index Terms— Radio Frequency Identification (RFID), interrogator, bow tie, fractal antennas, Sierpensi.

I. INTRODUCTION

Radio Frequency Identification RFID is one of several technologies where the goal is to automatically identify goods with as little human intervention as possible. Auto-ID technologies tend to become more flexible, enabling data to be collected anywhere, anytime and without human involvement [1]. This technology, which is often presented as the next generation of barcodes, is now used in many fields such as transport (access control), libraries, animal tracking, and security.

An RFID system consists of three major components: a transponder, a reader and a computer with an RFID application. The RFID TAG contains an antenna and an integrated circuit chip, or IC. The reader (Interrogator) includes an antenna which communicates with the TAG [2]. When choosing the antenna we should take some points into consideration: the antenna type, its characteristics and performance in RF frequencies.

Firstly, in order to obtain a small TAG, we must reduce the size since it is the main component of the TAG. Reducing its size leads automatically to reducing the TAG size. Secondly, one of the important characteristics of the RFID system is the readable range R_r which is the

maximum distance that the Interrogator can read from the TAG. This readable range depends on antenna gain [3].

Many works are interested in developing new small antennas for RFID systems with an acceptable parameter. Many works are based on replied dipole as in [4] where Galehdar, Thiel, and O'Keefe propose a new meander line dipole where they apply three methods to calculate the efficiency of electrically small wire antennas. Secondly, in [5], Morocco proposes a new meander line antenna and optimises the gain and the size by using a genetic algorithm. Thirdly, in [6], Tedjini, Vuong and Berouille used the fractal technique to reduce antenna size. Lastly, in [7], Asniza et al. present a compact antenna based on the Hilbert curve fractal for RFID application.

In this paper, we will present a new compact antenna based on triangular and fractal antenna as a solution to RFID reader. The basic antennas are designed at 2.45 GHz, which is one of the frequencies used in RFID applications.

This paper is organized as follows: Section II deals with some characteristics of triangular patch and proposes its model; this patch represents the main component of the second and the third structure. In Section III, a Sierpensi antenna will be the main basis of our fractal structure. In the Section IV, the results will be discussed and analyzed, followed by a brief conclusion.

II. A TRIANGULAR ANTENNA FOR RFID SYSTEMS

1. Design of the patch antenna

Figure 1 shows the geometry of an equilateral triangular patch deposited on a dielectric substrate with a ground plan.

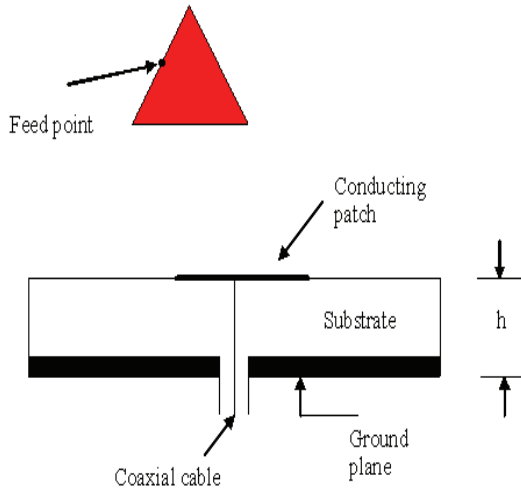


Fig. 1. Antenna structure (triangular patch).

The use of triangular patch provides the possibility of a multi resonator antenna which can be useful for an RFID reader to communicate with more than one TAG [8]. The resonance frequency is calculated using the equation (1) [9].

$$f_r = \frac{2c}{3a\sqrt{\epsilon_r}} \sqrt{m^2 + mn + n^2} \quad (1)$$

For the fundamental mode, $m=1, n=0$, 'a' is the length of triangle, 'c' is the velocity of light and ϵ_r is the relative dielectric constant.

Concerning our work, the antenna is designed to resonate at 2.45 GHz and it is mounted on a substrate material with a thickness $h = 3.6\text{mm}$, a relative dielectric constant $\epsilon_r = 2,6$, loss tangent ($\text{tang } \delta$) = 0.002 and 'a' = 50mm. The patch is excited by a coaxial line at the middle of the right side Fig. 1.

The structure is simulated by ADS which uses the Momentum method. The method of moments is a frequency domain technique. It is used in the electromagnetic analysis of structures by solving the integral equations. The method consists of dividing the antenna structure into wires or metal plates. Then each piece is subdivided to a number of segments that are small enough compared to the frequency's wavelength so that we can assume they have constant current. With the current then the electric and magnetic fields can be derived and important parameters such as impedance, return loss, gain, and directivity will be calculated.

One of the strengths of this method is that it is very intuitive, due to of its conceptual simplicity. Another advantage is that if only analyzing one frequency, it provides the results very quickly.

However, its weakness is that if a large range of frequencies is to be analyzed then the computations will take a long time.

To study this structure, an electrical model is developed. The electrical model is useful for parametric analysis not to design of the antenna. It is useful to know what has occurred to the input impedance when modifying antenna characteristics: geometry, parameters, feeding point. This model is derived from the cavity model of rectangular patch where the parameters are calculated from the input impedance [10]. The triangular patch is replaced by its equivalent rectangular patch [11]. This one is modelled by a resonant parallel RLC circuit, and the coaxial line is considered as an inductive reactance X_L , Fig. 2.

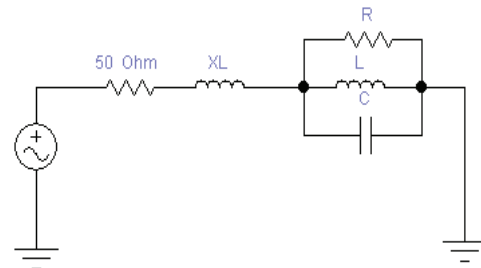


Fig. 2. Electrical model with $C=0.168 \text{ nF}$, $L=25.11 \text{ pH}$, $R=66.66 \text{ Ohm}$, $X_L = 1\text{nH}$ (triangular patch).

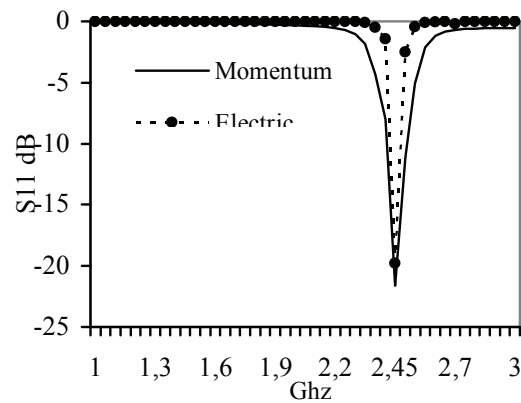


Fig. 3. Return loss for both physical and model patch.

As demonstrated by Fig. 3, a good agreement has been achieved between the electrical model and Momentum. The band width differs by about 50Hz.

2. A multiple triangular patch

a. First Example:

In the second structure, we use four triangle patches which are excited in the middle as shown in Fig. 4. Every triangle patch is an equilateral with an edge $a = 7\text{mm}$, then the antenna dimensions are $14\text{mm} \times 13.9\text{mm}$ which is mounted on a dielectric with a thickness $h = 0.65\text{mm}$ and $\epsilon_r = 2.3$.

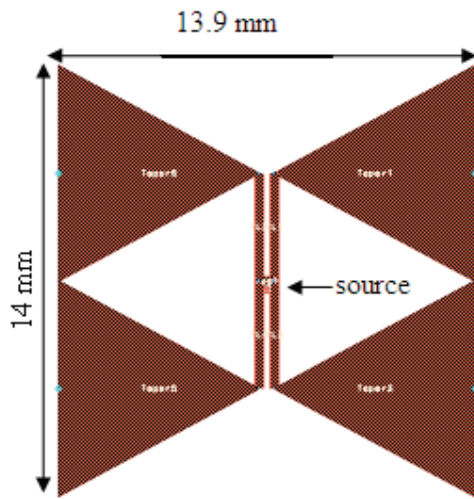


Fig. 4. Antenna structure (first structure).

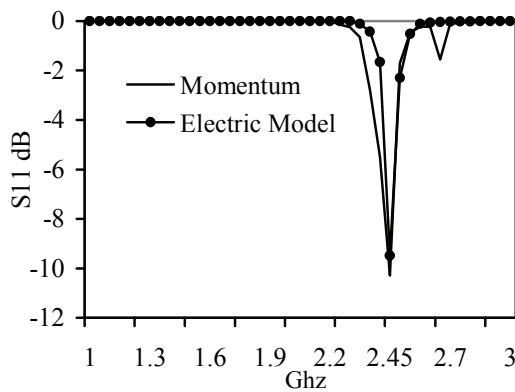


Fig. 5. Return loss of both physical and model patch (first structure).

Compared to the initial triangular antenna, the reduction size of the new structure is more than 70%. Besides the simulation of the S parameters gives the resonant frequency a gain of 1.6 dB and directivity is 4.5 dB and the band width is equal 80Hz which are good parameters for RFID system, Fig. 5.

b. Second Example

The proposed patch is composed by four triangles, shown in Fig. 6. This structure is inspired by a bow tie patch antenna. Only one transmission line links the four triangles. We keep the same dielectric thickness and permittivity of last example.

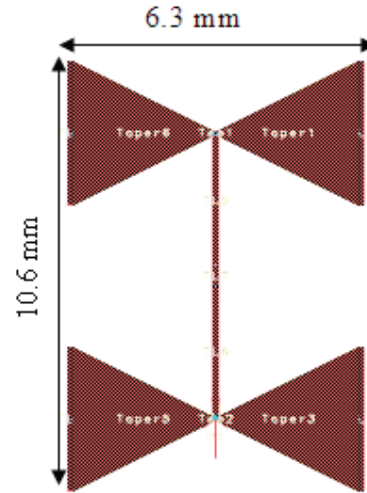


Fig. 6. Antenna structure (second structure).

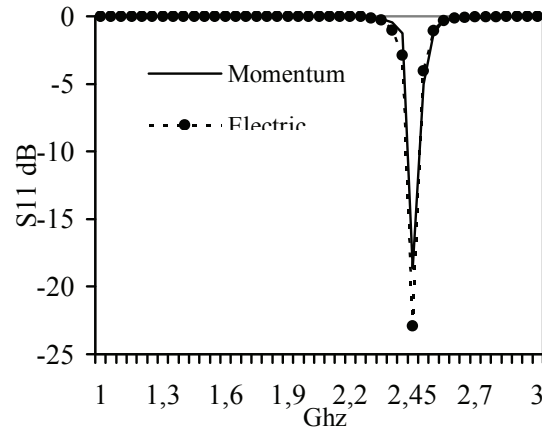


Fig. 7. Return loss of both physical and model patch (second structure).

The dimensions of the present antenna are about $10.6\text{mm} \times 6.3\text{mm}$ which means that the dimensions of antennas are reduced more than 80%. We used the same technique to calculate the parameters of the model. The return loss is shown in Fig. 7. The resonant frequency is 2.45 GHz and the band width is 80 Hz for both approaches. The gain and the directivity are 1.62dB and 4.87dB, respectively.

III. FRACTAL ANTENNA FOR RFID SYSTEM

1. A monopole Sierpinski

The fractal technique is used to obtain a special antenna as in RFID systems. The main geometric characteristics of fractal antenna are an infinite perimeter, a finite surface and a fractal dimension D .

The general concept of fractals can be applied to develop various antenna elements. The fractal technique allows as obtaining smaller and multiband frequencies antennas. Furthermore, the dimension and geometries can be defined through Euclidean dimension and self-similarity dimension [12]. For this reason, fractal antennas have been a recent topic of interest.

In this section, we will present a different fractal antenna based on the Sierpinski microstrip antenna and a novel fractal antenna which is simulated with our model. The obtained results are compared to Momentum data.

The Sierpinski gasket has the geometry described by Sierpinski in [13]. It is constructed by subtracting a central inverted triangle from the main triangle. This procedure is repeated every iteration. The triangles number is noted N_n , the triangles length is noted L_n and the fractional area is A_n ; they are calculated after every iteration [14]:

$$N_n = 3^n \tag{2}$$

$$L_n = \frac{1}{2^n} \tag{3}$$

$$A_n = L_n^2 N_n = \left(\frac{3}{4}\right)^n \tag{4}$$

Figure 8 shows the first three iterations of Sierpinski antenna which are mounted on substrate material with a dielectric constant $\epsilon_r = 2,52$ and loss tangent ($\text{tang } \delta$) = 0.002 and a thickness $h=3.2\text{mm}$. The patch is exited by a coaxial feed line at the middle of the right side.

The simulated return loss is shown in Fig. 9. As can be seen, after three iterations, the resonant frequency is reduced by more than 51%. This implies that the resonant length of the antenna can be reduced by more than 51%.

This change is very important in reducing RFID system size. But as can be seen in Table 1, the main performances of the antenna are conserved until the second iteration with a high gain and directivity and a comparative return loss

but after the third iteration the antenna performances decrease.

When looking at the radiation pattern of the first iteration of the Sierpinski gasket antenna, we can say that the radiations are virtually unchanged with the original structure, and as for the second iteration, it's clear that the antenna is less omnidirectional due to fractal effect, Fig. 10.

2. A multiple Sierpinski microstrip antenna

The fourth antenna is composed of Sierpinski gasket patches. The four triangles are connected by two microstrip lines and exited by a coaxial line at the middle, Fig. 11. The antenna is deposited on a dielectric substrate with thickness $h = 0.65\text{mm}$ and $\epsilon_r = 2.3$. The dimensions are $13.4\text{mm} \times 13.9\text{mm}$ whereas the original dimensions are $50\text{mm} \times 43\text{mm}$, thus the size is reduced by more than 72%.



Fig. 8. First three iterations of Sierpinski antenna.

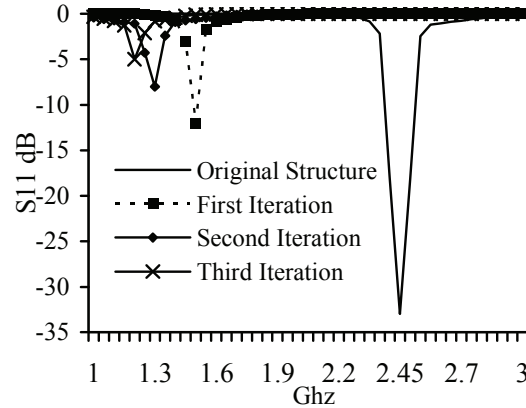


Fig. 9. Return loss of Sierpinski antenna.

Table 1: Performance of the three first iterations of Sierpinski antenna.

	f_r (GHz)	S_{11} (dB)	G(dB)	D(dB)	reduction %
original structure	2.45	-33	6.41	7.87	0
first iteration	1.5	-12	3.95	4.62	38
second iteration	1.25	-8	2.92	4.80	49
third iteration	1.2	-5	1.85	4.81	51

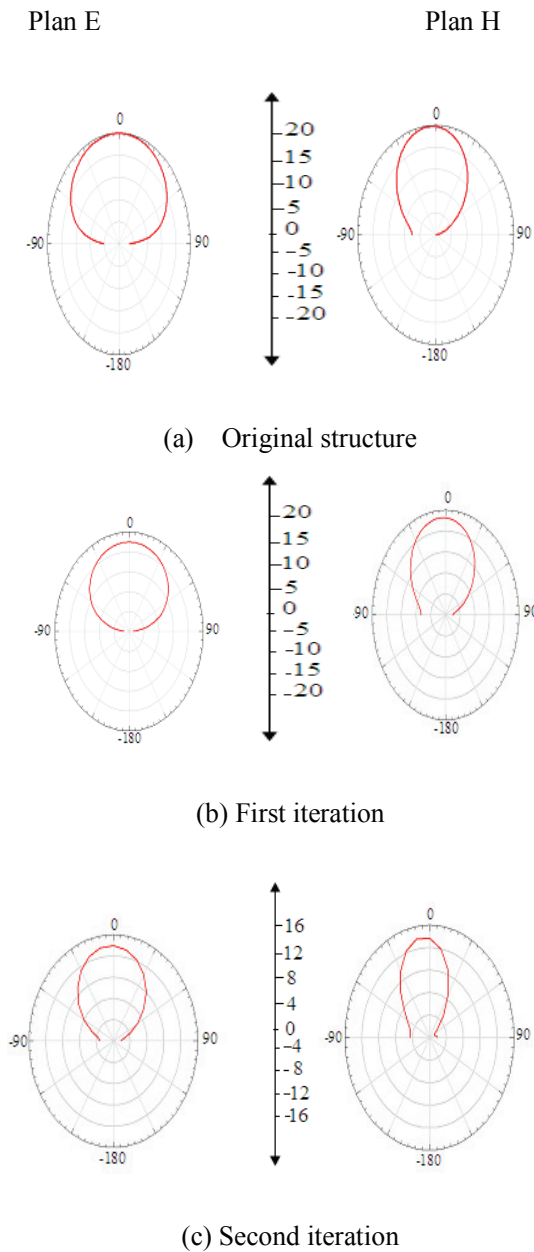


Fig. 10. Radiation pattern (E_{total}) of triangular and Sierpinski patch.

The return loss for this antenna is shown in Fig. 12. We can see that the resonant frequency is about 2.45 GHz, the gain and directivity are 1.7dB and 4.81dB respectively which are a good performances for the RFID system.

The principal advantage of the proposed fractal antenna is the size reduction percentage (more than 72%). As for the radiation pattern, this antenna is less omnidirectional due to its small size but it is still acceptable in RFID applications where the readable range in which the reader can

identify the TAG is very short (about 1m), Fig. 13.

Finally, as it is clearly demonstrated in the results, the examples of multi triangular patch, and the multi Sierpinski micro strip antenna are very useful for RFID systems because they are very small and they present a suitable gain, directivity and band width. In addition to the simplicity of realization, we think also that the first example of

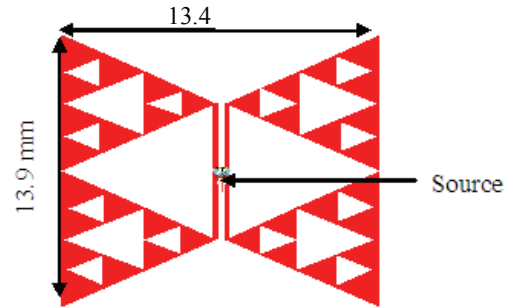


Fig. 11. Antenna structure (multiple Sierpinski antennas).

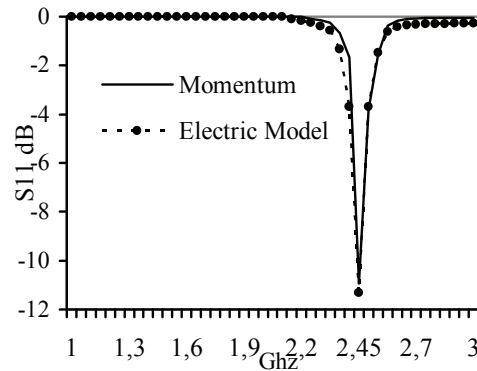


Fig. 12. Return loss of physical, first and second model antenna (multiple Sierpinski antenna).

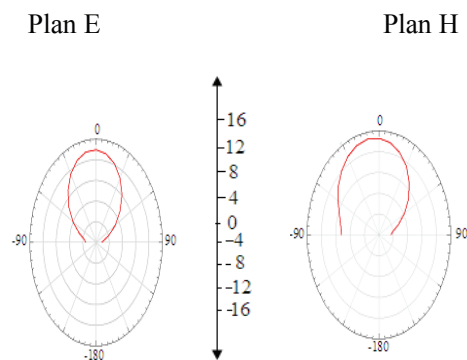


Fig. 13. Radiation pattern (E_{total}) of multiple Sierpinski patch.

multi triangular patch presents a dimension much reduced compared to the other antenna with similar parameters (Table 2). Moreover, the monopole triangular patch and the monopole Sierpensi present a good gain and directivity but they are not small enough.

Table 2: Performances of new antennas.

	Dimension W/L (mm)	BW_{-3dB}	G(dB)	D(dB)
1	50*43	100	6.41	7.81
2	24*20.6	100	2.83	4.81
3	13.9*14.1	80	1.6	4.5
4	10.6*6.3	80	1.62	4.87
5	13.9*13.4	100	1.7	4.81

Where:

- 1: Monopole Triangular patch
- 2: The third iteration of Sierpensi antenna
- 3: The first model of multi triangular patch
- 4: The second model of multi triangular patch
- 5: The multi Sierpensi micro strip antenna

IV. CONCLUSION

In this paper, two approaches are used to reduce the size of a RFID antenna. The first one is based on a multiple triangular patch whereas the second one is based on using fractal technique. The height reduction, the simplicity of realization, and its acceptable characteristic give our antennas a great interest in RFID system.

REFERENCES

- [1] G. Marrocco, "The art of UHF RFID antenna design: impedance matching and size-reduction techniques," *IEEE Antenna Wireless Propagation Letters*, Vol. 6, pp. 156-159, 2007.
- [2] G. Wang, J. Siden, P. Jonsson, and T. Olsson, "RFID Antenna Investigation," *Rapport serie FSCN Mid Sweden University*, 2002.
- [3] K. Finkenzeller, "RFID Handbook," 2nd Edition, 2003.
- [4] A. Galehdar, D. V. Thiel, and S. G. O'Keefe, "Antenna Efficiency Calculations for Electrically Small, RFID Antennas," *IEEE Antenna Wireless Propagation Letters*, Vol. 6, pp. 156-159, 2007.
- [5] G. Marrocco, "Gain-Optimized Self-Resonant Meander Line Antennas for RFID Applications," *IEEE Antenna Wireless Propagation Letters*, Vol. 2, pp. 302-305, 2003.
- [6] S. Tedjini, T.-P. Vuong and V. Beroulle, "Antennas for RFID tags," *Joint sOc-EUSAI Conference*, October 2005.
- [7] N. Asniza Murad, M. Eza, M. Fairus Mohd Yusoff and S. Hajer and A. Ali "Hilbert Curve Fractal Antenna for RFID Application", *International RF and Microwave Conference Proceeding*, Sept. 2006.
- [8] M. Biswas, J. Y. Siddiqui and D. Guha "Computer aided design of triangular microstrip patch antenna in multilayered media," *URSI GA*, October 2005.
- [9] K. F. Lee, K. M. Luk and J. S. Dahele "Characteristics of the Equilateral Triangular Patch Antenna", *IEEE Antenna and Propagation*, Vol. 36, 1988.
- [10] C. Yildiz, K. Güney, "Simple model for the impedance of rectangular microstrip antenna", *Journal of Engineering Sciences*, pp. 733-738, 1998.
- [11] Nasimuddin and A. K. V. Amir, "Fast and accurate model for analysis of equilateral triangular patch antenna," *Journal of Microwaves and Optoelectronics*, Vol. 3, pp. 99-110, April 2004.
- [12] J. Parron, J. Romeu, J. M. Rius, J. R. Mosig "Method of Moments Enhancement Technique for the Analysis of Sierpinski Pre-Fractal Antennas", *IEEE Transactions on Antennas and Propagation*, Vol. 51, No. 8, August 2003.
- [13] M. K. A. Rahim, A. S. Jaafar, and M. Z. A. Abdul Aziz "Sierpensi Gasket Monopole Antenna Design", *Asia Pacific Conference on Applied Electromagnetic Proceedings*, 2005.
- [14] D. H. Werner, R. L. Haupt, and P. L. Wernej, "Fractal Antenna Engineering: The Theory and Design of Fractal Antenna Arrays", *IEEE Antenna and Propagation Magazine*, pp. 37-57, 1999.



Ferchichi Abdelhak received a Masters degree in electronic systems from The Faculty des Sciences de Tunis in 2006. He is currently working toward his Ph.D.



Noureddine Sboui is a Doctor of electrical engineering. Since 2002 he has been with the Faculte des Sciences de Tunis. His current research interests include numerical method for electromagnetic field problems and advanced microwave circuits and components



Ali Gharsallah is a professor of electrical engineering. Since 1991 he has been with the Faculte des Sciences de Tunis. His current research interests include antennas, multilayered structures and microwave integrated circuits.



Henry Baudrand, Professor at the Ecole Superieure d'Electronique lectrotechnique Informatique, ENSEEIHT, of Toulouse, France. His current research interests include the modelling of passive and active circuits and antennas. He co-signed over 100 publications in journals and 250 communications in international conferences. He is a Fellow of the IEEE Society, Member of the "Electromagnetism Academy" and Senior Member of IEE society. He was President of URSI France commission B for 6 years (1993–1999), and President of the IEEE MTT- ED French chapter. He was awarded Officier des Palmes académiques, and Director Honoris causa of Iasi University.

The Effect of Curvature on the Performance and Readability of Passive UHF RFID Tags

Darindra D. Arumugam¹, Daniel W. Engels², and Marlin H. Mickle³

¹ Department of Electrical and Computer Engineering
Carnegie Mellon University, Pittsburgh, PA 15213, USA
darumugam@cmu.edu

² Department of Electrical Engineering
University of Texas at Arlington, Arlington, TX 76019, USA
dengels@uta.edu

³ Department of Electrical and Computer Engineering
University of Pittsburgh, Pittsburgh, PA 15261, USA
mickle@pitt.edu

Abstract— In this paper, the effect of curvature on the passive UHF RFID tag is studied. Maxwell's equations are used to depict the typical curved passive tag and are used to study the theoretical limitations of a tag operating under curvatures at its normal axes. This theoretical framework is then used to analyze the typical tag for various curvatures. Here, the analysis is conducted to derive the effect of curvature on the optimal impedances for ASIC load matching, as well as gain. This analytical evaluation is also generalized to describe the shift in center frequency of the tag operation due to tag curvatures. The results derived from this theoretical study on commercially available passive UHF RFID tags are verified with experimental results. It is shown that the curvature of passive UHF RFID tags have a significant impact on the performance and readability at values of $K > \pi/\lambda$, and reaches a breakdown on conformity at curvature values of $K = 4\pi/\lambda$.

Index Terms— Passive UHF RFID, curvature.

I. INTRODUCTION

Recently there has been significant interest in the characterization of passive UHF Radio Frequency Identification (RFID) tags [1-8]. The interest in this area is predominantly spurred by the need to understand the implications that the environment has on the performance of these passive tags. Previous studies have concentrated

on internal [9-14], as well as external [15-17] environmental factors, but have often times neglected some of the more obvious details involved in the use of passive tags in the industry. These passive tags operate in the Industrial Science and Medical (ISM) band of 902 MHz to 928 MHz within the U.S., and are governed by the Federal Communications Commission (FCC) for frequency selectivity, power levels, and other requirements. The characteristics of passive tags as studied previously have involved many types of analysis such as the backscatter [9, 10], antenna designs [11-13], as well as the application specific integrated circuits (ASIC) studies. Published works citing curvature in antenna designs have not been put in context of passive RFID tags [18-20], while those that have, concentrate on inductively coupled (HF) antennas [21], or lack clear conclusions regarding the effects of curvature on the performance of passive UHF RFID tags globally [22-25].

This paper is organized as follows: a background on tag curvatures and fundamental electromagnetism is presented in Section II. Section III presents the theory of electromagnetism for the specific case of a curved passive RFID tag in free space. The comprehensive general theory and curvature limitations of passive RFID tags are presented in Section IV along with the theory of general propagation. Here, the results of the theoretical analysis are presented to illuminate the impedance

mismatching, as well as gain variation and operational frequency shifting. An experimental analysis is presented in Section V for RFID tags with various curvature values. In Section VI, the effects of the segmentation process and segment density is discussed on the characterization of passive UHF RFID tags in CEM tools. Finally, a comprehensive conclusion is presented in Section VII.

II. BACKGROUND

The typical passive UHF RFID tag is composed of an antenna and an ASIC, that are connected to each other using a conductive glue or solder, as well as a substrate made of a dielectric material such as PET upon which the antenna and ASIC are affixed (as shown in Fig. 1) and packaged for the complete tag. From an RF standpoint, the radiation elements of this tag antenna are the antenna traces.

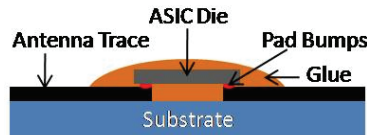


Fig. 1. The typical passive UHF RFID tag with a substrate supporting the antenna and ASIC.

The electrical evaluation for the structure in Figure 1 can be simplified using the assumption that the characteristics of the tag radiation pattern (including frequency selectivity) is dependent predominantly on the tag antenna structure and its matching to the ASIC input terminals [4, 5]. This assumption is further generalized by the fact that the ASIC mis-match is also a static property that would be dynamic in curvature studies, only with respect to the antenna structure. These assumptions allow us to simplify the setup as depicted in Fig. 1, into the traditional antenna studies. Typical commercially available UHF RFID tags tend to have somewhat complex (non-simplistic) current densities. These current variations are an important part of defining the far-field response of the tag itself, as can be viewed from the derived electric far field of Equations 1-3 for the case of a center-fed infinitesimal dipole antenna system with spherical (surface) coordinates.

$$E_r = \eta \frac{I_0 l \cos \theta}{2\pi r^2} \left[1 + \frac{1}{jkr} \right] e^{-jkr} \quad (1)$$

$$E_\theta = j\eta \frac{kI_0 l \sin \theta}{4\pi r} \left[1 + \frac{1}{jkr} - \frac{1}{(kr)^2} \right] e^{-jkr} \quad (2)$$

$$E_\phi = 0 \quad (3)$$

Equations 1-3 describe the electric field at every instance in space except at the source itself [26], and are an accurate method for determining the power density and radiation resistance of the tag antenna itself. This system is depicted in Fig. 2, where the tag is considered as a center-fed dipole with a wire length much shorter than the wavelength ($l \ll \lambda$) and is very thin, such that the diameter of the wire is much lesser than the wavelength of the radiated wave ($a \ll \lambda$).

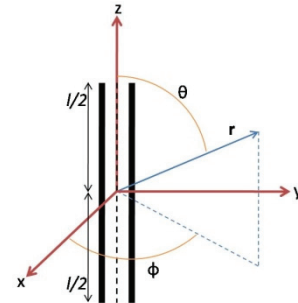


Fig. 2. Geometrical system of the infinitesimal dipole antenna system.

From Fig. 2 and wire antenna theory, we know that the current distribution of the dipole through the entire length of the structure is described using a $\sin \theta$ function, and that depending on the termination at both ends, this function could be altered into a linear (constant slope) function for the short dipole, which allows a simplification that arrives to Equations 1-2. This simplification exists for cases where $l \leq \lambda/50$, which allows us to determine the vector potential with the assumptions that the phase errors are negligible [26, 27] and does not affect the radiation characteristics of the antenna system. Using this justification and assumptions, we can perform the appropriate integration to derive the vector potential using that used by the infinitesimal case in Equation 4.

$$\mathbf{A}(x, y, z) = \hat{\mathbf{a}}_z \frac{\mu I_0}{4\pi r} e^{-jkr} \int_{-l/2}^{l/2} dz' = \hat{\mathbf{a}}_z \frac{\mu I_0 l}{4\pi r} e^{-jkr} \quad (4)$$

The results of this integration are as depicted in Equation 5, where the vector potential is shown to be one half of that shown in Equation 4, and is increasingly accurate as $kr \rightarrow \infty$ due to the far field region of the system. Note that the results of this system require that we assume that the current is zero on either ends of the short dipole, and is maximum at the center.

$$\mathbf{A}(x, y, z) = \hat{\mathbf{a}}_z A_z = \hat{\mathbf{a}}_z \frac{1}{2} \left[\frac{\mu_0 I_0 l}{4\pi r} e^{-jkr} \right]. \quad (5)$$

Using Equation 5, we can rewrite Equations 1-3 into Equations 6 and 7, for values of $kr \gg 1$. Here, we see that the approximate simplifications allow us to notice that the fields are half the previous field equations of the infinitesimal dipole as well.

$$E_\theta \approx j\eta \frac{kI_0 l}{8\pi r} e^{-jkr} \sin \theta \quad (6)$$

$$E_r \approx E_\phi = 0. \quad (7)$$

Note that since the directivity is a function of pattern or shape, the directivity and hence the maximum effective capture area of the short dipole is similar to that of the infinitesimal dipole [26, 27]. Following this, the radiation resistance of the short dipole is (squared) one fourth of that of the infinitesimal dipole, and is given in Equation 8. Note that this value is strictly dependent on the length of the dipole as well as the wavelength of the radiated wave.

$$R_r = \frac{2P_{rad}}{|I_0|^2} = 20\pi^2 \left(\frac{l}{\lambda} \right)^2. \quad (8)$$

III. MATHEMATICAL ANALYSIS OF TAG CURVATURES

From the derivations so far, we notice that the two major changes during curvature are due to the fact that the current distribution would be altered tremendously, and that the geometrical setup would also alter significantly. Curvature can be described effectively using the radius of curvature. This radius of curvature can be depicted using an analogy similar to Fig. 3, where curvature (K) is determined using the radius (R), where $K = 1/R$. From this definition, we can classify curvatures

involved in the dipole system to depict the changes as a sum of bent short dipoles.



Fig. 3. Radius of curvature of a wire.

Considering the scenario described by the summation of partially bent short dipoles, it is easily noticed that the current distribution would change drastically as we navigate from one short dipole to the next.

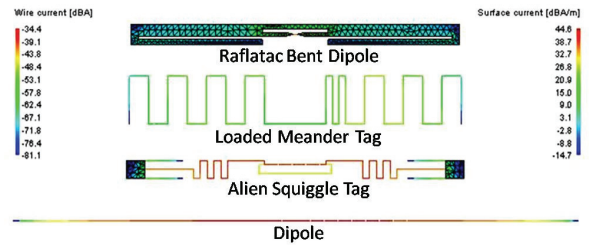


Fig. 4. Current distribution of commercial RFID tags as compared to the typical dipole antenna.

To further explore this condition, Fig.4 depicts the current distribution for three commercially available passive UHF RFID tags as compared to the typical dipole illustrated in Fig. 2, and derived in Equations 1-8.

From Fig. 4, we notice that bends do typically change the current distribution, since they tend to be the radiation echo sites. However, we notice that the linear or log in Fig. 4 (due to dB measure) current distribution patterns for the dipole antenna is best used for the purpose of a generalized theory. In order to model the current distribution, we first depict the scenario under which a curved tag (curved dipole tag antenna) will exist in Fig. 5.

The tag curvature along the radius of curvature (which is equal to the radius of the circle) involves complex manipulations of angles due to the bent short dipoles. In order to properly describe the curvature, we must introduce the angles θ'_i , α_i , and β_i as depicted in Fig. 5. These angles are used to depict the study of each dipole with respect to the original short dipole. Note that the use of the summation of short dipoles is similar to that used

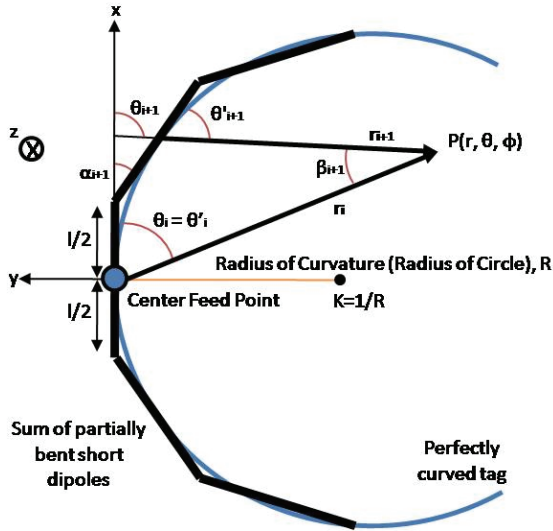


Fig. 5. Geometrical setup of a typical passive UHF RFID tag undergoing z-axial curvature.

in the segmentation process in the methods of moments. From Fig. 5, we can further analyze the triangular nature of the first β angle by utilizing geometrical calculus as depicted in Fig. 6.

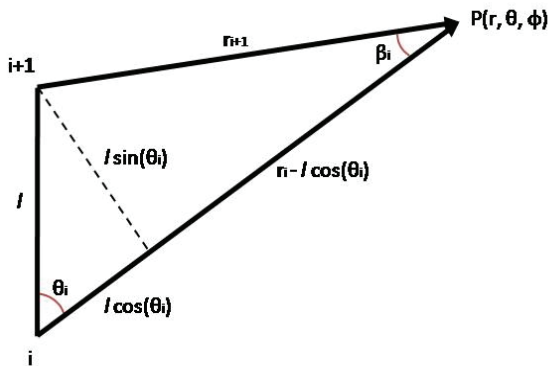


Fig. 6. Geometrical analysis of the far-field pattern angle, β .

From Figure 6, we notice that the first β angle can be defined by Equation 9, which describes the far-field pattern angle as a subsection of the deployment angle (θ), and the length of each segment during the segmentation process (l). Note that this derivation would be similar to the analysis using computational electromagnetic (CEM) methods. The results of these computational electromagnetic (CEM) methods will be depicted in subsequent sections.

$$\beta_i = \tan^{-1} \left\{ \frac{l \sin \theta_i}{r_i - l \cos \theta_i} \right\} . \quad (9)$$

Comparing the results obtained in Equation 9 through analysis with Figs. 5 and 6, we notice that the deployment angle of each segment in the curved tag problem can be defined as described in Equation 10, where α is the differential angle between the (i)th segment and the ($i + 1$)th segment as depicted in Fig. 5.

$$\theta'_i = \theta'_{i-1} - \alpha_{i-1} + \beta_{i-1} . \quad (10)$$

Using the electric far-field derivation in Equations 6 and 7, we can substitute Equation 10 to arrive at the partial solution for the curvature problem. Equations 11 and 12 present the modified field equations that describe the curvature effects on the geometrical nature of the tag antenna.

$$E_\theta \approx j\eta \frac{kl_0 l}{8\pi r_i} e^{-jkr} \sin \theta'_i \quad (11)$$

$$E_r \approx E_\phi = 0 . \quad (12)$$

From Equations 11 and 12, we see that the field equations are complete in terms of the curvature of the system. However, notice that the system still emphasizes a linear current distribution for the entire curved body. This current distribution is non-conformal to the concept of multiple bent short dipoles, and must be modified to depict the current distribution of a set of segments as depicted in Fig. 5. In order to

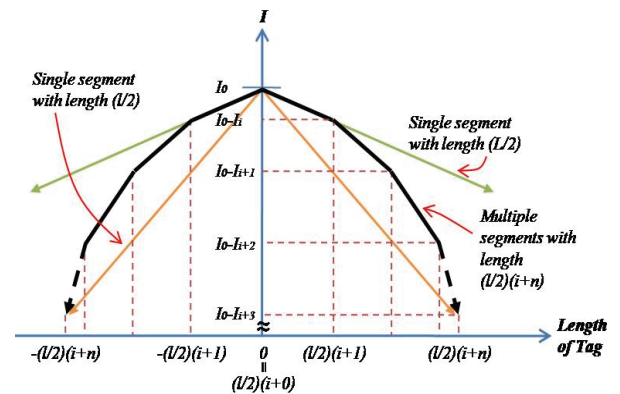


Fig. 7. Current distribution of tag antenna depending on the number of segments and length.

do so, we first review the current distribution of a single dipole element as compared to multiple dipole elements. Fig. 7 shows the current distribution of the single element as compared to the same length dipole with multiple elements.

From Fig. 7, we notice that the current I_0 needs to be modified such that it varies linearly based on the segment number. Here we also see that the current is the same at the either end due to symmetry, and that the current at the end points always approach zero. From this conceptual diagram, Equations 11 and 12 can be effectively modified to resemble Equation 13 and 14, where the current modification as well as the segment length (li) adjustments are considered.

$$E_\theta \approx j\eta \frac{k(I_0 - I_i)li}{8\pi r_i} e^{-jkr} \sin \theta'_i \quad (13)$$

$$E_r \approx E_\phi = 0. \quad (14)$$

From Equation 13, we can see that the complexities that exist due to curvature in the far-field can be effectively modeled using geometrical analysis as well as modifications to the current distributions. In the following section, these modifications are used to describe the relevance to propagation, as well as impedance mismatches, gain variations and operational frequency shifting.

IV. CHARACTERISTICS OF CURVED TAGS

In order to study the curvature of the tag, we notice that an explicit simplification is made to the generalized definition of curvature itself. Curvature of the typical tag can be described using $K = 1/R$, where R is the radius of curvature of the entire system. It is easily noticeable, that curvature of the typical passive tag as discussed throughout this paper would be directly related to the differential angle between each segment (α_i) in Fig. 5. To understand the simplification that exist, we must first study the relationship between the effective tag length (L_e) and the radius (R), which can be described using the simple geometry of an arc on a circle as noted in Equation 15.

$$\frac{L_e}{2} = \frac{\theta}{360} 2\pi R. \quad (15)$$

Substituting R for the curvature (K), we can rewrite Equation 15 in the form as depicted by Equation 16.

$$\theta = \frac{360L_eK}{4\pi}. \quad (16)$$

From Fig. 8, we see that the angle describing the maxima of the arc for the tag effective length is actually described by the deployment angle itself, such that $\theta \equiv \alpha_i$.

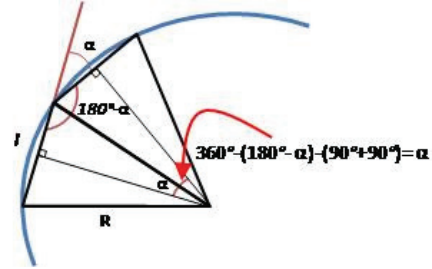


Fig. 8. Relationship between tag effective length (L_e) and differential deployment angle (α).

Assuming that the deployment angle is constant such that the radius of curvature is constant (the tag is constantly curved, rather than dynamically curved), then we note that $\theta \equiv \alpha$, since $\alpha = \alpha_i = \alpha_{i+1} = \alpha_{i+n}$. This assumption allows us to rewrite θ as a direct substitution of α in Equation 16. Substituting the modified Equation 16 into Equation 10, we get Equation 17.

$$\theta'_i = \theta'_{i-1} - \frac{360L_eK}{4\pi} + \beta_{i-1}. \quad (17)$$

Finally, substituting Equation 17 into the expanded Equation 13, we derive the complete electric far field relationship for the tag curvature in Equations 18 and 19.

$$E_{\theta'_i} \approx j\eta \frac{k(I_0 - I_i)li}{8\pi r_i} e^{-jkr} \sin \left(\theta'_{i-1} - \frac{360L_eK}{4\pi} + \beta_{i-1} \right) \quad (18)$$

$$E_r \approx E_\phi = 0. \quad (19)$$

In order to understand the implications of the modified field equations, we find the average radiated power in Equation 20 using Equations 18 and 19 [26].

$$W_{rad}(r, \theta'_i, \varphi) = \hat{a}_r \frac{1}{2} \times \left[\eta \left| j \frac{k(l_0 - l_i) l_i}{8\pi r_i} e^{-jkr} \sin \left(\theta'_{i-1} - \frac{360L_e K}{4\pi} + \beta_{i-1} \right) \right|^2 \right]. \quad (20)$$

Declaring the radiated power, we use the average radiated power of Equation 20 to define the directivity ($D(\theta'_i, \varphi)$) in Equation 21. This is then used to define the radiation and input resistance, as well as the maximum effective area in Equations 21 through to 23 respectively [26].

$$D(\theta'_i, \varphi) = \frac{4\pi r_i^2 W_{rad}(r, \theta'_i, \varphi)}{\int_0^{2\pi} \int_0^\pi W_{rad}(r, \theta'_i, \varphi) r_i^2 \sin \theta'_i d\theta'_i d\varphi} \quad (21)$$

$$R_r = \frac{2 \int_0^{2\pi} \int_0^\pi W_{rad}(r, \theta'_i, \varphi) r_i^2 \sin \theta'_i d\theta'_i d\varphi}{|I_0 - I_i|^2}, \quad R_{in} = \frac{R_r}{\sin^2 \left(\frac{Kl}{2} \right)} \quad (22)$$

$$A_{em} = \frac{\lambda^2}{4\pi} D_{max}. \quad (23)$$

Using these equations, it is clear that the short dipole moments create changes in both the input resistance, as well as radiated resistance. The modification that exists however, do not significantly change the directivity of the curved antenna, and therefore will not change the maximum effective area of the antenna itself. This proposition is a very interesting conceptual idea which proposes that the tag would have the same directivity measure as would, say a typical dipole under no curvature ($K = 0$). The theory also predicts that the effective capture area would not change drastically, thus the power radiated by the tag would also remain relatively constant. Since the radiation resistances change due to curvatures, it is probable to suggest that the operation of the tag would be dependent on these changes. For the typical passive UHF RFID tag, changes in the input resistance would create a mismatch with the tag ASIC load, which would detune the operational frequency of the tag. This act would effectively hover the typical tag away from its' operational frequency band of 902 MHz through to 928 MHz in the US. The effect of tag detuning is an analysis that is well known in passive tags, and has been previously discussed in relation to a metallic environment [4, 13], as well as in a moist environment [28]. In order to verify the results of the theory, simulations are conducted in FEKO 5.3, which is a CEM tool utilizing a hybrid FEM/MoM method. The meshing guidelines used

here require that the segment radius equals to 10^{-4} m, and that the segment length equals to $\lambda/90$ m, which allows for the vastly assumed regions for the short dipole concepts of $< \lambda/50$ m.

Fig. 9 presents the test setup used in the simulation environment. Note that the values of curvature (K) is varied starting from $K = 0$ ($R = \infty$), up to $K = 4\pi/\lambda$, where the typical quarter wave dipole becomes a complete loop.

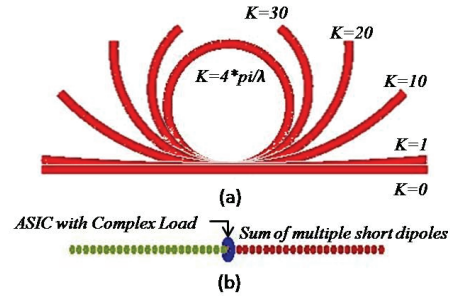


Fig. 9. Test setup of the curvature of a center-fed dipole: (a) showing the variation of curvature (K); (b) the tag composed of a summation of cylindrical parts and a complex load.

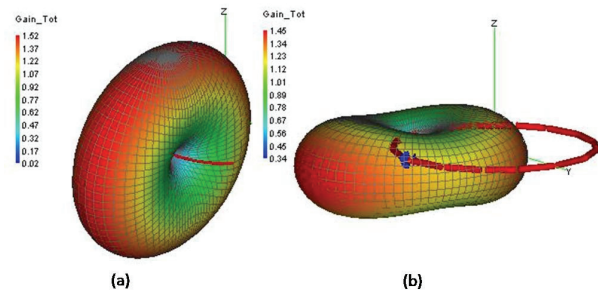


Fig. 10. 3D pattern of the tag gain: (a) during curvature values of $K < 4\pi/\lambda$; (b) at $K = 4\pi/\lambda$.

In Fig. 9b, we notice that the mathematical model utilized for the dipole involves a summation of cylindrical short dipoles, while the center feed point is an ASIC. In the simulation, the feed point is designed to be a sinusoidal voltage with a maximum value of 1V, and the point source is modeled using a complex load (real and imaginary parts). The values of the complex load are varied to achieve the optimal load for matching purposes. This process is repeated for each tag antenna design utilized in this paper (Alien Squiggle and Raflatac Bent Dipole). Fig. 10 depicts the 3D radiation patten of the curved dipole tag at normal curvature (close to the regular straight dipole

antenna), and at the extreme curvature (where the dipole becomes a loop antenna). Since the theory is designed to handle a dipole antenna (Equations 1 to 3), it is not sufficiently accurate at the maximum curvatures, and therefore is theoretically unsuited to accommodate loop like structures.

From Fig. 10, we notice that the tag maintains a dipole like pattern throughout various types of curvature, but transforms from an isotropic-x (or -y) into an isotropic-z as the tag approaches the maxima curvatures of $K = 4\pi/\lambda$. Fig. 11 presents the results indicating the effect of the curvature at different frequencies (using a frequency sweep). Here we notice that curvature (K) of a typical dipole has an impact on the frequency of operation of the tag. There is a skewing effect on the optimal operational frequency that seems to slide off to higher frequencies as the tag curvatures increase ($K \rightarrow 4\pi/\lambda$). However, at the maxima curvatures of $K = 4\pi/\lambda$, it is seen (yellow) that the tag offers very poor values of reflection coefficients (S_{11}), which could be related to due to the high voltage standing wave ratio (VSWR) when contact is made between each end of the tag.

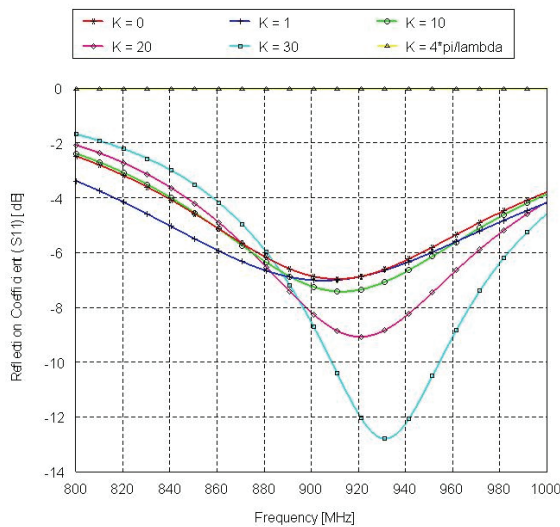


Fig. 11. Effect of curvature (K) at different frequencies.

Fig. 12 presents the effect of curvature on the optimal value of the imaginary load impedance. The imaginary load is varied for negative values of 1 through to 1000 Ω . From the logarithmic (x-axis) scale it is noticed that the imaginary part is well suited (for lowest S_{11} values) at values of approximately -50Ω (for all values of curvatures,

K). Note that throughout this paper, the real part of the complex load is affixed at 50Ω . Using these values ($[50 - j50] \Omega$) for the analytical evaluation, Fig. 14 is derived to depict the effect of curvature on the fundamental RF parameters in the tag.

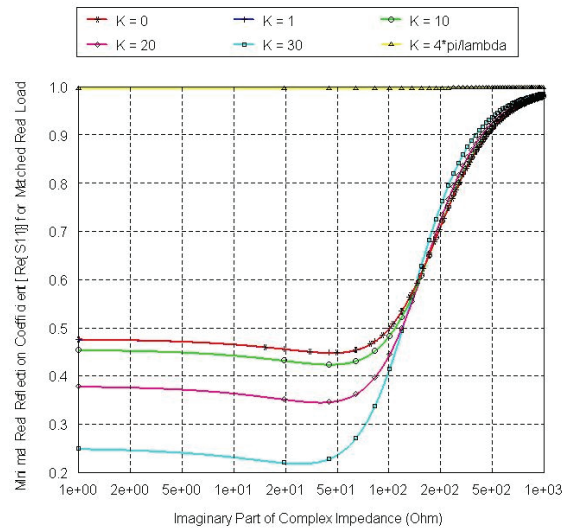


Fig. 12. Effect of curvature (K) on the optimal value for the imaginary part of the complex impedance of the load.

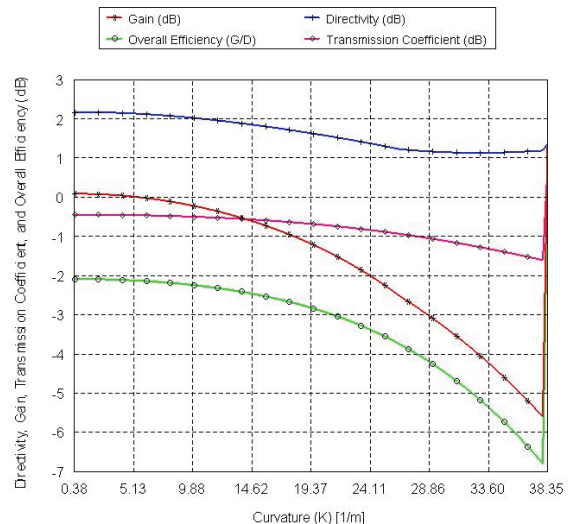


Fig. 13. Effect of curvature (K) on the directivity, gain, overall efficiency, and transmission coefficient of a center-fed dipole tag at 915 MHz.

The parameters derived from this analysis are the gain, directivity, overall efficiency, and transmission coefficient. Notice that the gain and

the directivity values are different (not the same) for tag curvatures above $K > 0$. This is an interesting idea when considering the definition of gain and directivity which often times reflects their similarities under the assumptions of a perfect match and no ohmic losses. However, the finer interest that lie in the differences here are the fact that the differences are in variation with respect to the curvature itself. This distorted case is what is of most interested, and can be easily described using the harmonized definition of gain and directivity as detailed in Equation 24.

$$G_T = (1 - |\Gamma|^2) \cdot D_T . \quad (24)$$

Using this refined definition, we notice that the transmission coefficient ($|\Gamma|$) is in fact frequency dependent, and as depicted in Fig. 14 plays a crucial role in the manipulation of the tag overall efficiency, a factor that changes the gain to be much lower than the directivity of the tag antenna itself. Fig. 15 compares the results of the transmission coefficient in Fig. 14 against values of the reflection coefficients, return loss, and VSWR. Here we see that as $|\Gamma|$ decreases with the curvature of a tag, the theory predicts that the return loss would also increase.

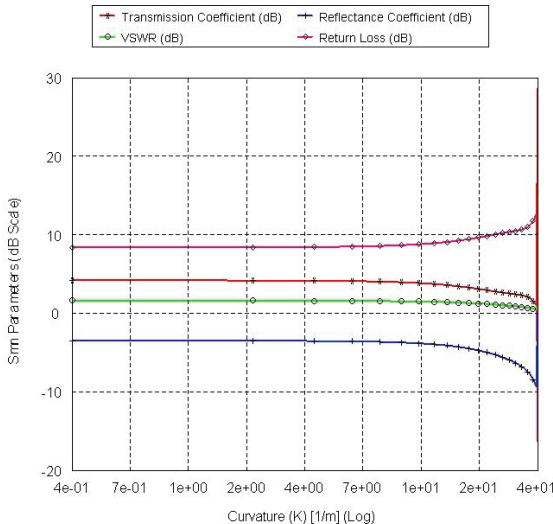


Fig. 14. Effect of curvature (K) on the reflectance coefficient, voltage standing wave ratio, and return loss as compared to the transmission coefficient for a center-fed dipole tag at 915 MHz.

In understanding the implications of these results, we must draw attention to the fact that the

range ratio of the passive tag can be effectively characterized using Equation 25.

$$\frac{R'}{R} = \sqrt{(1 - |\Gamma|^2) \frac{D'}{D}} . \quad (25)$$

Considering the fact that at values of $K < \pi/\lambda$ the change in directivity is negligible, we can generalize that the range ratio is dependent only on the values of the overall efficiency (e_{cd}) at these values as described by Equation 26.

$$\frac{R'}{R} = \sqrt{e_{cd}} . \quad (26)$$

It is seen that there exist an exponential account on the performance degradation of passive tags after this cutoff point, which contributes directly (through equation 26) to the readability of these tags.

V. EXPERIMENTAL ANALYSIS

The experimental analysis of curvature effects on the Alien Squiggle is conducted in free space (indoor). Fig. 15 depicts the test setup for the curvature analysis conducted in this section.

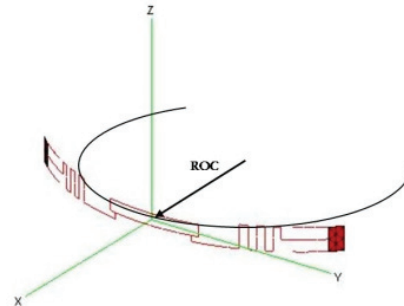


Fig. 15. Curvature setup of the Alien Squiggle tag for a given radius of curvature (ROC).

The analysis is first conducted to derive the optimal imaginary part of the tag, which is then compared with the bent dipole tag by Raflatac in Fig. 16. From this figure, we notice that the imaginary part of the Alien Squiggle is perfectly matched (the real part is 50Ω) when the complex load is approximately $([50 - j508.3]\Omega)$. This value is also much lesser than that required for perfect matching (under the same conditions) of the Raflatac bent dipole at 915 MHz. Using the same simulation environment, Fig. 17 plots the effect of curvatures on the reflection coefficient (in dB) from 800 MHz through to 1000 MHz.

Here it is noticeable that there is a trend for the skew towards higher frequencies and higher reflection losses as the curvature of the tag increases. Fig. 18 presents the analysis conducted in free space using the actual tag.

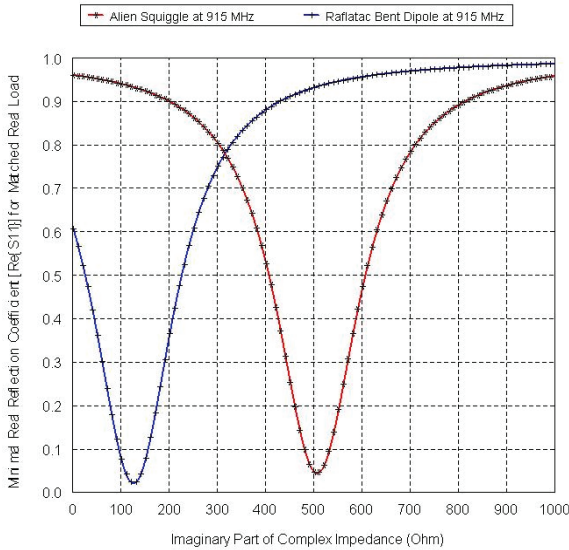


Fig. 16. Optimal value for the imaginary part of the complex load of the Alien Squiggle tag compared with the Raflatac bent dipole.

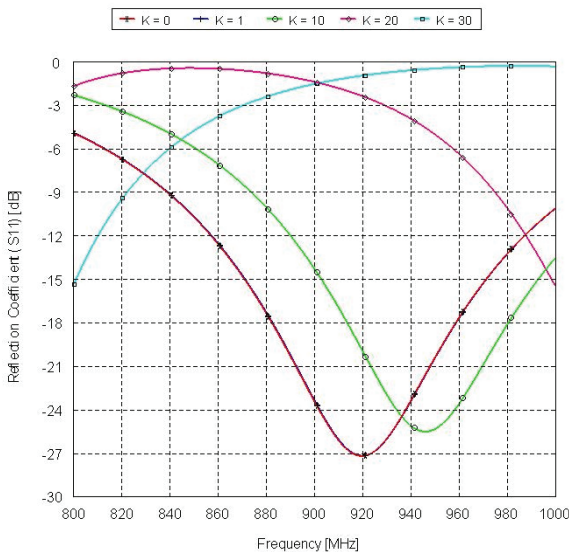


Fig. 17. Effects of curvature on variations of the reflection coefficient for the perfectly matched (at 915 MHz) Alien Squiggle tag from 800 MHz through to 1000 MHz.

It is seen that the fitted polynomial curves (darker lines) show that frequency skewing is less of a real issue, while losses are much more

prevalent. The testing was conducted in open lab space without obstacles, and that a repeatability test was conducted to determine the extent of the noise and its' occurrences, which proved to be negligible. The global minima of the curves indicate the tuning of the tag which is compared to the reflection coefficient plots in Fig. 17, while the change in transmitted power required is related to the impedance mis-match due to the constant curvature of the tag. The test is conducted with heights of 1m from the ground for both the tag and reader antenna, and for a separation of 1m from each other. The ripples in the measured curves are a result of multi-path which is present in the testing environment.

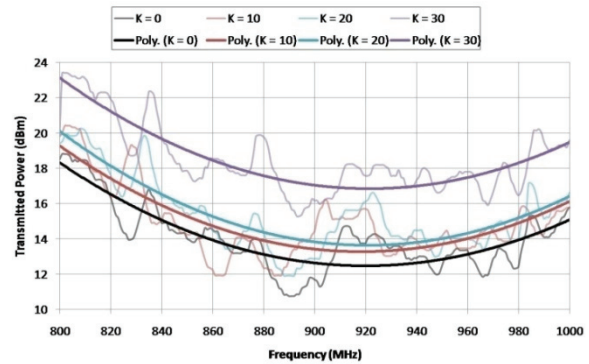


Fig. 18. Experimental analysis and polynomial curve fitting of the results for curvatures of the Alien Squiggle tag from 800-1000 MHz.

VI. EFFECTS OF THE SEGMENTATION PROCESS IN CEM TOOLS

It is shown that the current profile plays the most crucial role in the field equations, an occurrence that is studied in Fig. 7 in general, and detailed in Fig. 19 numerically.

As the number of segments (#) increases (lambda/#) in the theory, the normalized current becomes more sinusoidal in nature, which contributes to the accuracy of the theory. Increases in the curvature would definitely increase the effect that the segments play in the calculation of the field equations.

Fig. 20 shows that for a damp segmentation process (with higher segment counts), the breakdown begins at $K > 3\pi/\lambda$, and (from the previous sections) occurs at $K = 4\pi/\lambda$. In addition to these factors, we also predict that readability and performance is not effected (in

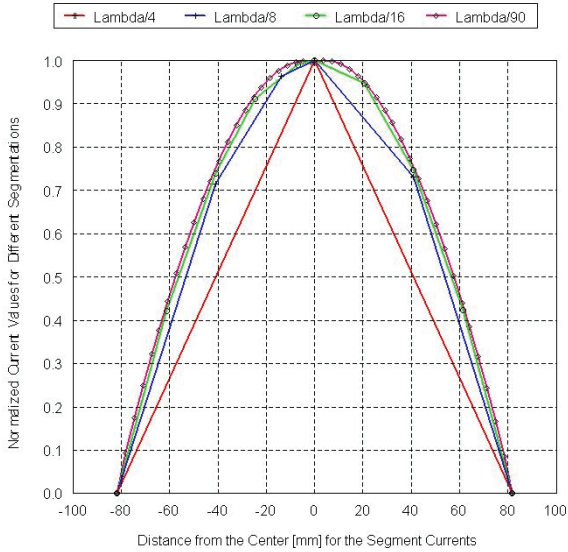


Fig. 19. Effect of the segmentation process and meshing guidelines on the segment currents.

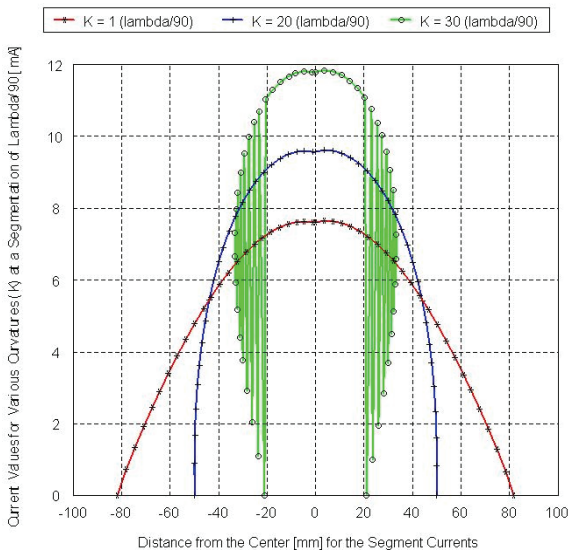


Fig. 20. Effect of the tag curvature on the segment currents for damp meshing guidelines (dense segmentation process).

ideal conditions) until $K > \pi/\lambda$ for a typical dipole-like passive UHF RFID tag antenna, where λ is the wave-length referred to the self-resonance of the antennas, rather than the frequency of operation of the tag. This is true since it is common to design passive UHF RFID tags away from the self resonance of the antenna, and due to the fact that K is related to the antenna directly.

VII. CONCLUSION

In this paper, a theoretical framework is presented to describe the effects of curvature on the passive RFID tag. Maxwell's equations are used to describe the curvature of the typical tag by using the center-fed dipole as a standard tag antenna. The equations are derived to present a general theory describing curvature in passive UHF RFID tags. Analytical evaluations are conducted to study the variation of gain, impedance mismatching, as well as operational frequency shifting of the passive UHF RFID tag. Experimental evaluations of curvature in commercially existing passive UHF RFID tags are conducted. The results of this study show that there exist significant impacts on the performance of the typical RFID tag at curvature values of $K > \pi/\lambda$. Furthermore, it is shown that a breakdown (non-conformity to typical operation) occurs at $K = 4\pi/\lambda$.

REFERENCES

- [1] H. Vogt, "Efficient Object Identification with Passive RFID Tags", *Int. Conf. on Pervasive Computing*, No. 2424, pp. 98-113, 2002.
- [2] R. Glidden, "Design of ultra-low-cost UHF RFID tags for supply chain applications", *IEEE Communication Magazine*, Vol. 42, No. 8, pp. 140-151, 2004.
- [3] P. V. Nikitin, K. V. S. Rao, and R. D. Martinez, "Differential RCS of RFID tag", *Electronics Letters*, Vol. 43, No. 8, pp. 431-432, 2007.
- [4] D. D. Arumugam, D.W. Engels, and A. Modi, "Environmental and performance analysis of SAW-based RFID systems", *Int. J. Radio Frequency Identification Technology and Applications*, Vol. 1, No. 2, pp. 203-235, 2007.
- [5] D. D. Arumugam, A. Vijayakrishnan, D. W. Engels, and A. Modi, "2D localisation using SAW-based RFID systems: a single antenna approach", *Int. J. Radio Frequency Identification Technology and Applications*, Vol. 1, No. 4, pp. 417-438, 2007.
- [6] D. D. Arumugam, and D. W. Engels, "Characterization of RF Propagation in Helical and Toroidal Metal Pipes for Passive RFID Systems", *IEEE Int. Conf. on RFID*, Vol. 39, No. 1, pp. 61-62, 2008.

- [7] D. D. Arumugam and D. W. Engels, "Characterisation of RF Propagation in Metal Pipes for Passive RFID Systems", *Int. J. Radio Frequency Identification Technology and Applications*, Vol. 1, No. 3, pp. 303-343, 2007.
- [8] D. D. Arumugam and D. W. Engels, "Characterisation of RF Propagation in Rectangular Metal Pipes for Passive RFID Systems", *Int. J. Radio Frequency Identification Technology and Applications*, Vol. 1, No. 4, pp. 345-362, 2007.
- [9] P. V. Nikitin and K. V. S. Rao, "Theory and measurement of backscattering from RFID tags", *IEEE Trans. on Antennas and Propagation*, Vol. 48, No. 6, pp. 212-218, 2006.
- [10] K. V. S. Rao, "An overview of backscattered radio frequency identification system (RFID)", *Asia Pacific Microwave Conference*, Vol. 3, pp. 746-749, 1999.
- [11] K. V. S. Rao, P.V. Nikitin, and S.F. Lam, "Antenna design for UHF RFID tags: A review and a practical application", *IEEE Trans. on Antennas and Propagation*, Vol. 53, No. 12, pp. 3870-3876, 2005.
- [12] M. E. Schaffrath, L. Ukkonen, L. T. Sydanheimo, and M. A. Kivikoski, "RFID Antenna Designs for Paper Industry Applications: Passive Bow-Tie-Transponder Performance Analysis", *IASTED Int. Conf. on Antennas, Radar, and Wave Propagation*, pp. 348-353, 2005.
- [13] L. Sydanheimo, L. T. Ukkonen, and M. Kivikoski, "Effects of Size and Shape of Metallic Objects on Performance of Passive Radio Frequency Identification", *IEEE/ACES Int. Conf. on Wireless Communications and Applied Computational Electromagnetics*, pp. 178-181, 2006.
- [14] G. Kumar and K. P. Ray, *Broadband Microstrip Antennas*, Artech House, 2003.
- [15] K. D. Laakmann and W. H. Steier, "Waveguides: Characteristic Modes of Hollow Rectangular Dielectric Waveguides," *Applied Optics*, Vol. 15, pp. 1334-1340, 1976.
- [16] J. M. Molina-Garcia-Pardo, M. Lienard, P. Degauque, D. G. Dudley and L. Juan-Llacer, "MIMO Channel Characteristics in Rectangular Tunnels from Modal Theory," *IEEE Transactions on Vehicular Technology*, 2006.
- [17] S. F. Mahmoud and J. R. Wait, "Guided Electromagnetic Waves in a Curved Rectangular Mine Tunnel," *Radio Science*, Vol. 9, pp. 567-572, 1974.
- [18] M. A. K. Hamid, W. M. Boerner, L. Shafai, S. J. Towaij, W. P. Alsip, and G. J. Wilson, "Radiation Characteristics of Bent-Wire Antennas", *Electromagnetic Compatibility, IEEE Transactions on*, Vol. 12, No. 3, pp. 106-111, Aug. 1970.
- [19] G. Burrell, "Propagation of current on bent wire antennas-an experimental study", *Antennas and Propagation, IEEE Transactions on*, Vol. 26, No. 3, pp. 427-434, May 1978.
- [20] S. Egashira, M. Taguchi, and A. Sakitani, "Consideration on the measurement of current distribution on bent wire antennas", *Antennas and Propagation, IEEE Transactions on*, Vol. 36, No. 7, pp. 918-926, July 1988.
- [21] S. Y. Y. Leung and D. C. C. Lam, "Performance of Printed Polymer-Based RFID Antenna on Curvilinear Surface", *Electronics Packaging Manufacturing, IEEE Transactions on*, Vol. 30, No. 3, pp. 200-205, July 2007
- [22] X. Zhou and G. Wang, "Study on the influence of curving of tag antennas on performance of RFID system," *4th International Conference on Microwave and Millimeter Wave Technology Proceedings (IEEE Cat. No.04EX827)*, pp. 122-125, 2004.
- [23] H.-T. Hsu, H.-T. Chou, and W.-W. Lee, "Performance degradation of RFID system due to curving in tag antenna through Radar Cross Section (RCS) analysis," *2007 IEEE Antennas and Propagation Society International Symposium*, pp. 1197-2000, 2008.
- [24] Y. Tikhov and J. H. Won, "Impedance-matching arrangement for microwave transponder operating over plurality of bent installations of antenna," *Electronics Letters*, Vol. 40, No. 10, pp. 574-575, May 2004.
- [25] J. Siden, P. Jonsson, T. Olsson, and G. Wang, "Performance degradation of RFID system due to the distortion in RFID tag antenna", *Microwave and Telecommunication Technology, 11th International Conference on*, pp. 371-373, 2001.

- [26] C. A. Balanis, *Antenna Theory: Analysis and Design*, John-Wiley and Sons Publishing Company, 2005.
- [27] D. K. Cheng, *Fundamentals of Engineering Electromagnetics*, Addison-Wesley Publishing Company, 1993.
- [28] R. Fletcher, U. P. Marti, and R. Redemske, "Study of UHF RFID signal propagation through complex media", *IEEE Int. Symp. on Antennas and Propagation Society*, Vol. 1B, pp. 747-750, 2005.



Darmindra D. Arumugam is a Researcher and a Ph.D. Candidate in the Department of Electrical & Computer Engineering at Carnegie Mellon University. He received a BSc and MSc in Electrical Engineering at the University of Texas at

Arlington in 2005 and 2007. His current research is in the area of applied physics and electromagnetism concentrating on radiation theory and propagation characteristics, applications of smart objects and sensors, energy harvesting, wireless sensor networks and intelligent objects. Mr. Arumugam has authored over 30 peer reviewed international journal and conference publications, and has been invited to speak at numerous technical events.



Daniel W. Engels is the Director of the Texas Radio Frequency Innovation and Technology Center and an Associate Professor at the University of Texas at Arlington. Dr. Engels is the former Director of Research of the Auto-ID Labs at MIT

and is an original member of the research team started in 1998 that founded the Auto-ID Center at MIT. Dr. Engels is one of the principal architects of the Networked Physical World EPC System, the foundation of the Internet of Things, developed under the Auto-ID Center and licensed to EPCglobal Inc. Dr. Engels received his Ph.D. from the Massachusetts Institute of Technology. He has

over 50 peer reviewed publications in RFID, RFID applications, security, embedded computing, and computer-aided design.



Marlin H. Mickle is Nickolas A. DeCecco Professor in Electrical and Computer Engineering (Primary), Professor of Computer Engineering, Telecommunications, and Industrial Engineering at the University of

Pittsburgh. He is the Director of the RFID Center of Excellence. He received the B.S.E.E., M.S.E.E., and the Ph.D. University of Pittsburgh in 1961, 1963, and 1967. Marlin received the Carnegie Science Center Award for Excellence in Corporate Innovation - 2005; he has 21 patents and received the Pitt Innovator Award 2005, 2006, 2007 and 2008; 1988 Recipient of the Systems Research and Cybernetics Award of the IIASSRC, a member of the AIDC100, and he is a Life Fellow of the IEEE.

Advanced Carbon-Fiber Composite Materials for RFID Tag Antenna Applications

Aidin Mehdipour¹, Iosif D. Rosca², Abdel-Razik Sebak¹, Christopher W. Trueman¹,
and Suong V. Hoa²

¹Department of Electrical and Computer Engineering,
Concordia University, Montreal, Quebec, H3G 2W1, Canada
a_meh@ece.concordia.ca, abdo@ece.concordia.ca, trueman@ece.concordia.ca

²Department of Mechanical and Industrial Engineering,
Concordia University, Montreal, Quebec, H3G 2W1, Canada
rosca_iosif@yahoo.com, hoasuon@alcor.concordia.ca

Abstract— In this paper we explore the use of carbon fiber composites (CFC) in radio-frequency identification (RFID) antenna applications both numerically and experimentally. For this purpose, we use two kinds of CFC materials as the radiating element. We consider two types of RFID antennas: the T-match bowtie antenna, and the meander line antenna. The electromagnetic (EM) model of CFC antennas is developed using the Microwave Studio software for numerical analysis. By characterizing samples of CFC material an accurate model of the composite is obtained to be used in the antenna simulation. The composite RFID antenna performance is investigated and compared with a metal antenna. The performance of the antenna can be controlled using the anisotropic property of reinforced continuous carbon fiber composite material. The bandwidth, radiation resistance, and gain/read-range of the RFID antenna can be adjusted by changing the thickness, conductivity, and fiber orientation of the composite material. Because the CFC antenna has a much higher bandwidth, it can be more effective than a metal antenna in RFID.

Index Terms— Antenna, carbon-fiber composites (CFC), radiating element, radio-frequency identification (RFID).

I. INTRODUCTION

Radio-frequency identification (RFID) is extensively used in tracking and identifying objects in many applications [1-7]. The most-used RFID frequency bands are the UHF RFID band (902–928 MHz in North America, 866–869 MHz in Europe and 950–956 MHz in Japan) and the unlicensed wireless bands (2.4-2.484 GHz and 5.15-5.875 GHz). The main part of an RFID system is the antenna tag, which should be inexpensive, light, and easy to fabricate. An antenna with good corrosion resistance is desirable in some applications in harsh environments.

Metals such as copper or aluminum are commonly used for the radiating element of an RFID tag. However, cost, fabrication procedure, and weight are some of the important parameters which limit the use of metals. In harsh environments corrosion resistance and the adhesion between radiating element and substrate are major issues. Some recent studies have used various composite materials as replacements for metals [8-12]. In [8], a conducting-polymer patch antenna is proposed. A conductive textile coated with carbon nanotubes (CNTs) and gold is used to fabricate a patch antenna in [9]. Silver nanoparticle ink [10, 11] and the metallo-organic conductive ink [12] are used to prepare the high-conductive material as a replacement of metal for RFID tag antennas.

Advanced carbon-fiber composite (CFC) materials are being used widely in the aerospace industry as a good replacement for metal because of their higher

strength, lower weight, and lower cost [13-21]. CFCs have lower electrical conductivity than metals, and so the shielding effectiveness is of concern when electromagnetic compatibility (EMC) must be maintained [15-19]. There are two types of highly-conductive CFCs, namely the reinforced continuous carbon fiber (RCCF) [16-18] and the CNT composites [19-24]. In one-layer unidirectional RCCF composites, the carbon fibers run in one direction only so that the conductivity is anisotropic, being high along the direction of the fibers, but low in the perpendicular direction. The effective anisotropic conductivity tensor of one-layer composite depends on the thickness of layer, the fiber diameter, the separation distance between fibers and the conductivity of the fibers [17]. CNT composites can be made using single-wall nanotubes (SWCNT) [24] or multi-wall carbon nanotubes (MWCNT) [21] to obtain conductivity. The electrical conductivity of CNT composites highly depends on the properties and loading of the CNTs, the aspect ratio of the CNTs, and the characteristics of the conductive network throughout the matrix. Unlike RCCF composites, the CNT composite material is an isotropic medium because the CNTs are randomly oriented throughout the material.

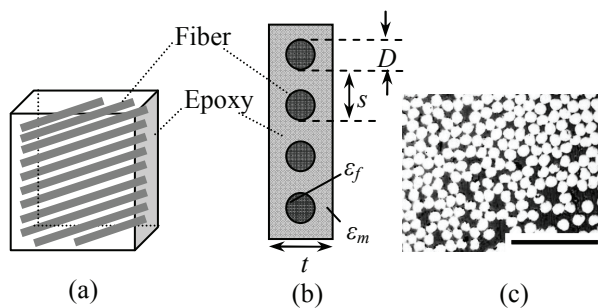


Fig. 1. (a) RCCF composite, (b) Cross-view, (c) Optical micrograph of RCCF Composite (scale bar 50 μm).

In [26], we used numerical modeling to investigate RCCF and braided-tissue carbon-fiber materials for the radiating element of an RFID antenna.

In this paper, we explore in detail using RCCF and SWCNT composites for RFID antenna applications. Two types of RFID antennas, namely the T-match bowtie [11] and the meander line [7], are considered for analysis. Both numerical and experimental results are provided. The organization of the paper is as follows. The composite materials properties and

fabrication process are explained in Section II. The antenna performance using RCCF and SWCNT composites as the material of radiating element is carefully investigated in Section III. The fabrication of SWCNT antennas and the experimental results are presented in Section IV. Finally, Section V contains conclusions and ideas for future work.

II. CARBON-FIBER COMPOSITE MATERIALS

In this section, the structure of RCCF and SWCNT composite materials and the method of fabrication are explained. The composite samples are produced in Concordia Center for Composites (CONCOM) [27]. To develop a model of composite material for use in computer simulations of RFID antennas, we characterize the composite material over the frequency range of interest by using standard measurement setups, namely a coaxial fixture below 1.6 GHz, and waveguide setups at higher frequencies. Each measurement setup is modeled using Microwave Studio (MWS) [28, 29]. By minimizing the difference between the simulated and measured scattering parameters over a frequency range, the complex permittivity tensor can be extracted [21, 30].

A. Single-Layer RCCF Composite and Method of Preparation

Fig. 1 shows a typical RCCF composite material. The carbon fibers are embedded in epoxy resin and are all oriented in a specific direction. The effective permittivity tensor of one layer of this composite depends on the thickness of layer (t), the diameter (D) of the fibers, the separation distance between fibers

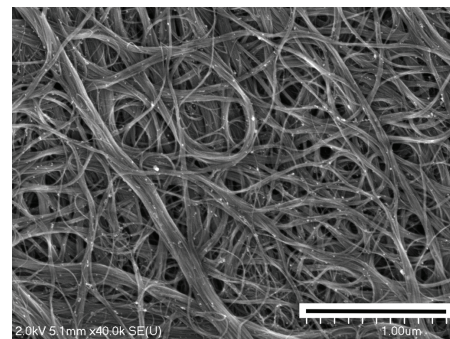


Fig. 2. SEM micrograph of bucky-paper made of SWCNTs (scale bar 1 μm).

(s) and the permittivity of the fibers of the fibers and the host medium (ϵ_f , ϵ_m). The effective tensor of homogenized model of RCCF is given by [17]

$$\epsilon_z^{-1} = (1-g)\epsilon_m^{-1} + g\epsilon_f^{-1} \quad (1)$$

$$\epsilon_{x'} = \epsilon_{y'} = (1-g)\epsilon_m + g\epsilon_f \quad (2)$$

where g is a coefficient which depends on the volume fraction of fibers inside host medium. Compared to metals, the conductivity of RCCF is anisotropic, being high along the direction of fibers, but low in the perpendicular direction. This is an important characteristic of RCCF composites which should be accounted for and can be taken advantage of in antenna design. We should extract the conductivity of composite sample for both directions. The proper measurement setup for this purpose is standard waveguide using the dominant TE_{10} mode, with the electric field oriented parallel to the short wall of the guide. We can obtain the conductivity tensor by using two sample orientations: with the fibers parallel to the electric field vector, and with the fibers perpendicular.

An RCCF sample is fabricated by co-author Rosca using the following procedure. The epoxy resin Epon 862 and the curing agent Epikure W are produced by Hexion Specialty Chemicals [31]. The unidirectional carbon cloth (T300) is purchased from MF Composites [32]. The mixture of resin and the curing agent (26.4 wt%) is degassed in a vacuum oven at 90 °C for 30 min. Next, one ply of unidirectional carbon cloth is impregnated with the mixture and placed between two aluminum plates coated with demolding agent. Finally, the plates are tightened together by bolt joints, and the composite is cured at 120°C for 6 hours.

Because the electrical properties of RCCF are not noticeably frequency-dependant [17, 18], the RCCF sample was characterized using a G -band waveguide setup and the conductivity values were used at the lower frequencies of the RFID bands. The RCCF composite conductivity is found to be 3500 S/m along fiber direction and 10 S/m perpendicular to the fibers.

B. SWCNT Thin-Film Composite and Method of Preparation

A SWCNT thin-film composite is sometimes called a “bucky paper” and is shown in Fig. 2. Since the SWCNT composite has an isotropic conductivity, the standard coaxial cable fixture is used for sample

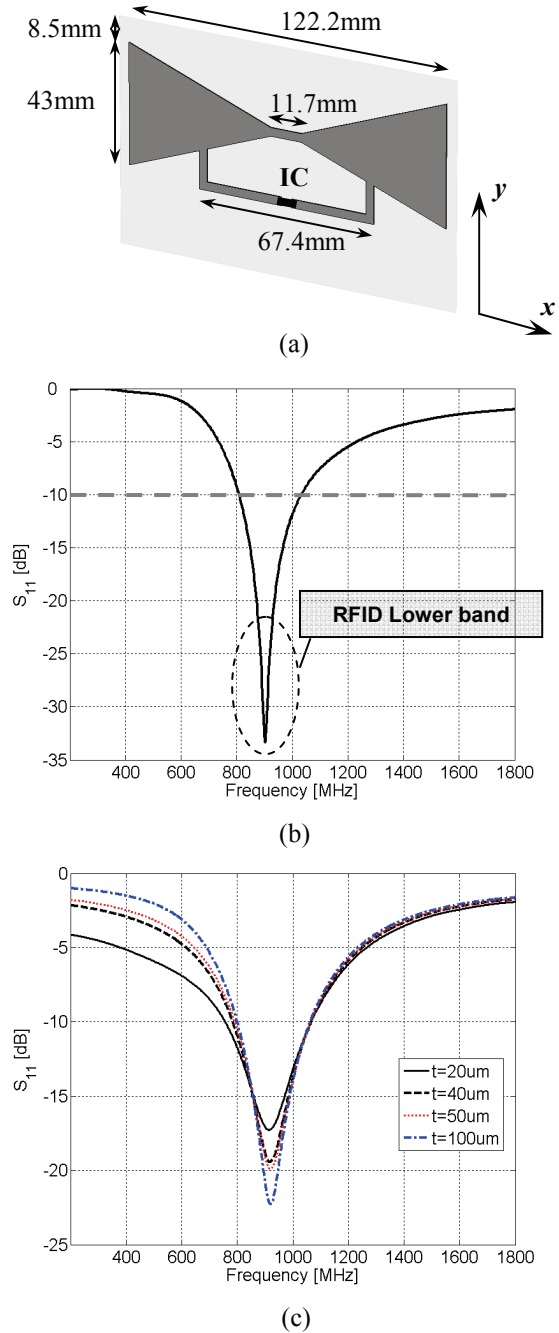


Fig. 3. (a) T-match folded bow-tie RFID antenna, (b) Return loss of the antenna with radiation element made of copper. (c) Return loss with radiation element made of SWCNT.

characterization.

Thin film devices made of SWCNT exhibit high conductivity and sufficient mechanical strength that there is no need for a binder. For the standard coaxial setup, bucky papers were prepared by a filtration

technique. First a given amount of SWCNTs (Nikkiso Co. [33]) is dispersed by sonication (Misonix 3000) in N, N-dimethyl formamide (DMF) for 30 minutes at 27W sonication power. Next, the SWCNT suspension is filtered on a polyamide membrane filter with diameter and pore-size of 90 mm and 45 μm respectively. The solvent is evaporated in a vacuum oven at 120 $^{\circ}\text{C}$ for 6 hours. The dried bucky paper of $\sim 40 \mu\text{m}$ thickness is easily detached from the filter membrane and glued to an epoxy plate of 0.5 mm to ensure sufficient rigidity.

By characterizing the fabricated composite sample using the coaxial setup, the dielectric constant and conductivity in the RFID frequency band are obtained as $\epsilon_r = 5$ and $\sigma = 25000 \text{ S/m}$, respectively.

III. COMPOSITE RFID ANTENNA PERFORMANCE

In what follows, two well-known types of RFID antennas, namely the T-match bow-tie antenna and the meander line antenna (MLA), are considered. The return loss, radiation efficiency, gain, and bandwidth of each antenna are compared with the radiating element made of composite and of metal. The antennas are modeled with MWS, which uses the finite integration technique (FIT) to solve the discretized Maxwell equations. The details of FIT can be found in [29], [34-36]. The composite material is characterized using the permittivity and conductivity obtained above.

A. T-Match Bow-Tie Antenna

The T-match folded bow-tie RFID antenna is shown in Fig. 3 (a). The antenna is excited by a lumped port between arms of the T. The input impedance of the RFID microchip (TI RI-UHF-Strap-08 IC) [37] at the port is chosen as 380Ω . The radiation element is placed on a $130 \text{ mm} \times 80 \text{ mm}$ substrate with dielectric constant $\epsilon_r = 3.4$ and thickness 0.26 mm. The return loss of the antenna with a copper radiation element is shown in Fig. 3 (b). The gain and radiation efficiency of the antenna are 2.4 dB and 97%, respectively.

1) SWCNT Composite Antenna

The radiation element was then changed to the SWCNT composite material, modeled using its equivalent permittivity and conductivity. The return

loss of the RFID antenna for different thicknesses of composite material is shown in Fig. 3 (c). The resonant frequency of the RFID antenna with the composite radiating element is not much different from that with the metal element.

Due to the much lower conductivity of composites compared to metals, the ohmic loss (R_{Loss}) of an antenna with composite radiating element is higher. Therefore, the gain and radiation efficiency (η) of

Table 1: Radiation efficiency of the nanotube composite antenna ($f = 921 \text{ MHz}$).

Thickness (μm)	$\sigma = 10\text{K}$ (S/m)	$\sigma = 15\text{K}$ (S/m)	$\sigma = 20\text{K}$ (S/m)	$\sigma = 25\text{K}$ (S/m)
20	37.83 %	46.94 %	54.25 %	59.35 %
40	55.78 %	62 %	68.57 %	72.34 %
50	59.4 %	67 %	74.3 %	76 %
100	72.42 %	79.15 %	82.8 %	85.2 %

Table 2: Maximum gain of the nanotube composite antenna.

Thickness (μm)	$\sigma = 10\text{K}$ (S/m)	$\sigma = 15\text{K}$ (S/m)	$\sigma = 20\text{K}$ (S/m)	$\sigma = 25\text{K}$ (S/m)
20	-1.94 dB	-0.61 dB	-0.01 dB	0.37 dB
40	0.005 dB	0.63 dB	0.97 dB	1.19 dB
50	0.37 dB	0.9 dB	0.92 dB	1.4 dB
100	1.2 dB	1.57 dB	1.76 dB	1.88 dB

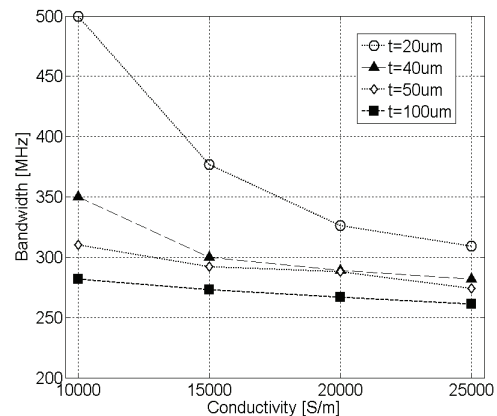


Fig. 4. The bandwidth of SWCNT antenna versus conductivity ($f = 921 \text{ MHz}$).

composite antenna are lower than for a metal antenna. The ohmic loss of a conductive box with effective

conductivity of σ_{eff} can be expressed as

$$R_{loss} = \frac{L}{\sigma_{eff} A_{eff}} \quad (3)$$

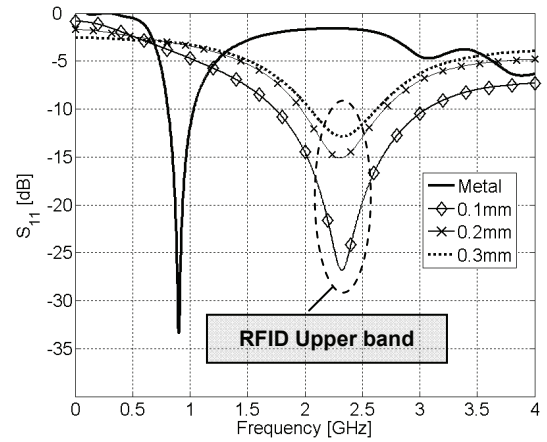
where A_{eff} is the effective area along a current path of length L . Since for a composite antenna the current flows inside the volume of radiating element, A_{eff} can be controlled by changing the thickness (t) of radiating element and skin depth of composite through the conductivity. Therefore, the gain of the composite antenna can be adjusted by changing both t and σ_{eff} . Tables 1 and 2 show the effect of the thickness and the conductivity on the composite antenna's performance, computed using the MWS model. The values can be compared with the copper antenna's gain of 2.4 dB and efficiency of 97%. Note that using the parameters of the sample described in Section II, $t = 40 \mu\text{m}$ and $\sigma = 25000 \text{ S/m}$, the radiation efficiency and gain are 72.34% and 1.19dB, respectively.

The tables show that as the conductivity and thickness of the composite increases, both the gain and the efficiency increase to approach the values for the metal antenna of 2.4 dB and 97%. However, as shown in Fig. 4, the bandwidth of the antenna for a return loss better than -10 dB is reduced by decreasing the antenna loss. In resonant circuits, as the ohmic loss decreases, the bandwidth decreases and the Q -factor increases, and the composite antenna shows this behavior. The -10dB bandwidth of the antenna with a metal radiating element is 822 to 1053 MHz, or 231 MHz, which is lower than the composite antenna. For example, the composite antenna with thicknesses of 20 μm and 40 μm is 310 MHz, and 270 MHz bandwidth, respectively. It is seen that more flexibility of design is attained by using composite material instead of metal.

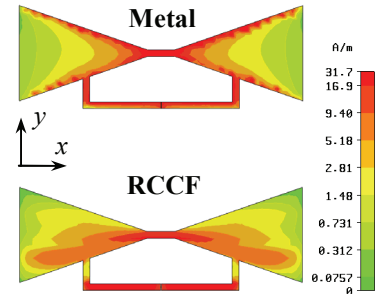
The maximum read-range (d_{max}) of an RFID antenna is obtained from [4]

$$d_{max} = \frac{\lambda}{4\pi} \sqrt{\frac{G_{tag} \cdot EIRP_t}{P_{chip}}} \quad (4)$$

where G_{tag} , $EIRP_t$ and P_{chip} are the gain of RFID tag, the effective isotropic radiated power of the reader and the sensitivity power level of RFID IC, respectively. With $EIRP_t = 0.5 \text{ W}$, the maximum allowed value, and $P_{chip} = 1 \text{ mW}$ [3], d_{max} of antenna with metal and fabricated-SWCNT radiating element are 76.52 cm and 66.54 cm, respectively.



(a)



(b)

Fig. 5. (a) Return loss of RCCF antenna, (b) Current distribution on the radiation element at resonant frequency ($f = 2330 \text{ MHz}$).

2) RCCF Composite Antenna

The second composite material we have chosen for study is RCCF composite. The direction of fibers determines the direction in which the anisotropic conductivity is large. MWS enables us to model anisotropic materials using the permittivity tensor. Using the tensor permittivity values for the fabricated RCCF sample, two antennas were modeled: one having the fibers oriented in the x direction of Fig. 3(a), and the other with the fibers in the y direction. It was observed that the current distribution on the antenna with the fibers oriented in the x direction flows from one arm to the other of bow-tie and then the antenna radiates effectively. The return loss of the RCCF antenna with x -directed fibers is shown in Fig. 5 (a) for different thicknesses of composite. Compared to the metal antenna, the resonant frequency is shifted upwards to about 2450 MHz in the RFID upper band. The reason for this shift can be explained by comparing the current flow on the

composite radiating element in Fig. 5 (b) with that on the metal antenna. The current flow on the metal antenna resembles that on a dipole, using the full length of the antenna, corresponding to resonance in the lower RFID band. However, the current flow on the composite antenna is confined to the section of the antenna adjacent to the T-match, and the behavior is more like that of a short dipole antenna, with a correspondingly higher resonant frequency. The current flow at the ends of the T-match section is quite small.

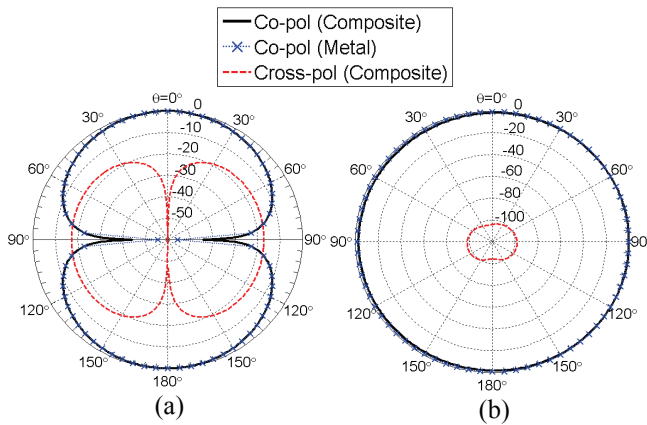


Fig. 6. Normalized radiation pattern of bow-tie antenna, (a) *E*-plane, (b) *H*-plane.

Table 3: Radiation efficiency and -10dB BW of the RCCF composite antenna.

Thickness (mm)	η (%)	BW (MHz)
0.1	35.17	1320
0.2	39.27	730
0.3	40.1	581

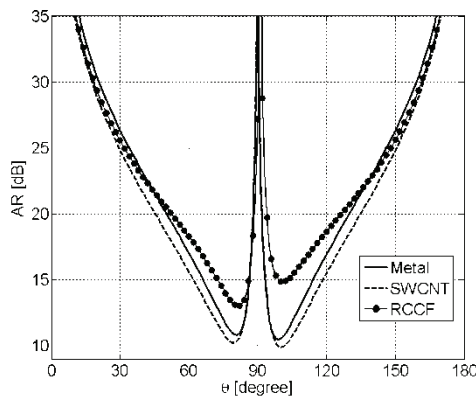


Fig. 7. *E*-plane axial ratio of bow-tie antenna with different radiating element.

The normalized radiation pattern in both *E*- and *H*-plane at the frequency of resonance, 2330 MHz, is shown in Fig. 6. It is observed that using RCCF composite instead of metal changes the radiation pattern very little. However, the polarization property of the RCCF antenna would be affected due to the anisotropic property of RCCF material. Fig. 7 shows the axial ratio (AR) of bow-tie antenna at *E*-plane. It is observed that the polarization purity of RCCF composite antenna is improved compared to the metal and SWCNT antennas.

The radiation efficiency and gain of the antenna made of 0.2 mm-thick RCCF are computed at resonant frequency as 39.27% and -0.2 dB, respectively. Using (4), the maximum read-range of RCCF antenna is obtained as $d_{max} = 21.3$ cm. The radiation efficiency and -10dB bandwidth of the antenna for different thicknesses is reported in Table 3. Although the gain/read-range of the composite antenna is relatively low compared to the metal antenna, it should be noted that the antenna covers the microwave RFID frequency band centered at 2.45 GHz along with a wide bandwidth (BW = 1.32 GHz) due to the interesting properties of RCCF composite material.

B. Meander Line Antenna (MLA)

Figure 8 shows a meander-line antenna (MLA). Due to its small size and space-filling geometry, the MLA is one of the most desirable antennas for RFID applications [7], [38-40]. In the MLA design, a straight dipole is bent to take less length on the substrate, and this also lowers the resonant frequency. In addition, the radiation resistance is changed,

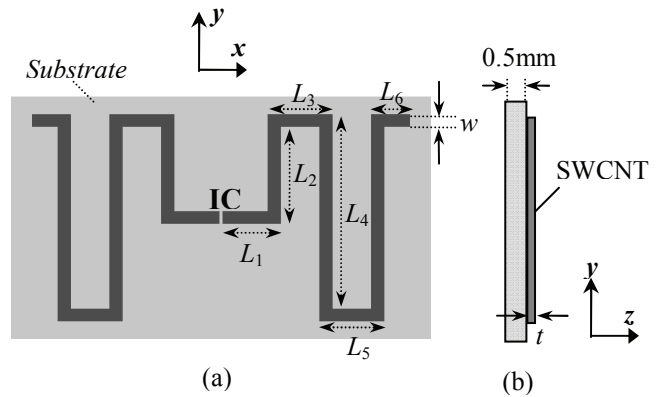


Fig. 8. (a) MLA structure, (b) Cross-view.

which should be taken into account for matching-circuit design. The planar MLA of Fig. 8 with dimensions $L_1 = 9\text{mm}$, $L_2 = 15.25\text{mm}$, $L_3 = 10\text{mm}$, $L_4 = 30.5\text{mm}$, $L_5 = 10\text{mm}$, $L_6 = 6\text{mm}$, and $w = 2\text{mm}$ resonates in the RFID lower frequency band around 950 MHz. The substrate is 0.5mm-thick epoxy with $\epsilon_r = 3$ and loss tangent $\tan\delta = 0.0013$. The gain, radiation resistance and d_{max} of MLA with a copper radiating element are given in Table 4. The -10 dB bandwidth of maximum 24 MHz is achieved.

Table 5 gives the performance of the MLA when the radiating element is SWCNT composite, with a width of 2 mm, for various thicknesses of the SWCNT material. It is observed that the bandwidth for 30 μm thickness is much wider than the bandwidth of 24 MHz of the metal antenna. The bandwidth decreases with increasing thickness of the composite as the resistance per unit length of the arms of the antenna decreases. However, the gain is low compared to the metal antenna. The input impedance of the MLA is quite different from the RFID IC's impedance of 380 ohms, needing a matching circuit between antenna and IC. The 30 μm composite antenna has a resistance of 106 ohms, much closer to the IC's 380 ohms than the resistance of the metal antenna of 12 to 15 ohms, hence the matching circuit could be simplified. The input impedance can also be adjusted by using composites with different values of conductivity, to get closer to 380 ohms. Therefore composites provide more flexibility in the design. The center frequency of resonance for nanotube antenna can be adjusted by tuning the length of the MLA.

The ohmic loss of nanotube MLA can be controlled by varying the width of the line (w) and the conductivity (σ) of composite, as well as the thickness of line. The effect of w and σ on the gain and bandwidth of MLA is shown in Fig. 9. The gain could be improved considerably by using thicker and wider MLA. However, it can be seen that one may compromise between the gain and bandwidth.

IV. EXPERIMENTAL RESULTS

In order to investigate the composite antennas performance experimentally and to verify simulation results, we fabricated the monopole configuration of the SWCNT dipole bow-tie and MLA antennas as shown in Fig. 10. For SWCNT antenna fabrication, the same procedure explained in Section II-B is used.

Table 4: MLA performance with a copper radiating element ($t = 40\ \mu\text{m}$).

w (mm)	f_0 (MHz)	η (%)	Gain (dB)	R_r (Ω)	d_{max} (cm)
1	873	96.71	1.84	12.51	75.57
2	914	97.94	1.86	14.82	72.35
3	959	98.22	1.87	15.3	69

Table 5: MLA performance with an SWCNT radiating element ($w = 2\text{mm}$).

Thickness (μm)	f_0 (MHz)	η (%)	Gain (dB)	R_r (Ω)	BW (MHz)	d_{max} (cm)
30	966.5	15.24	-6.21	106	239	27
40	954.6	18.7	-5.32	81.5	162	30.3
50	950.4	22	-4.6	67.61	149.3	33
100	976.35	37.12	-2.35	43.58	93	42

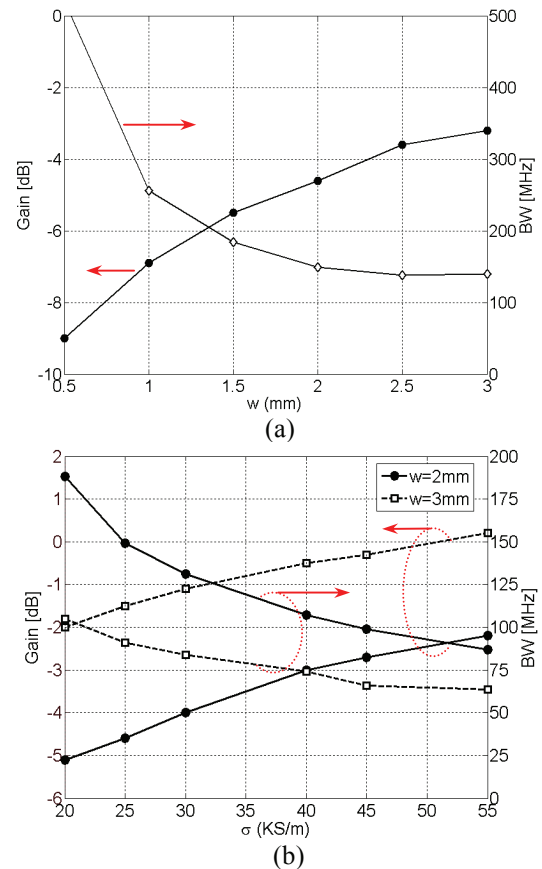


Fig. 9. Gain-bandwidth diagram of SWCNT MLA versus (a) w ($\sigma = 25\text{KS/m}$, $t = 50\ \mu\text{m}$, $f = 950.4\text{MHz}$), (b) σ ($t = 100\ \mu\text{m}$, $f = 976.35\text{MHz}$).

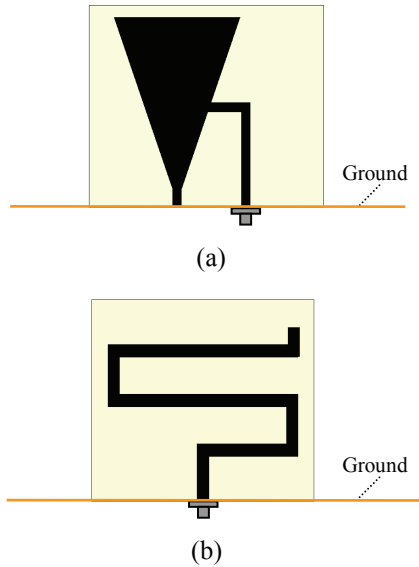


Fig. 10. Monopole configuration of SWCNT composite antennas, (a) T-match bow-tie, and (b) MLA.

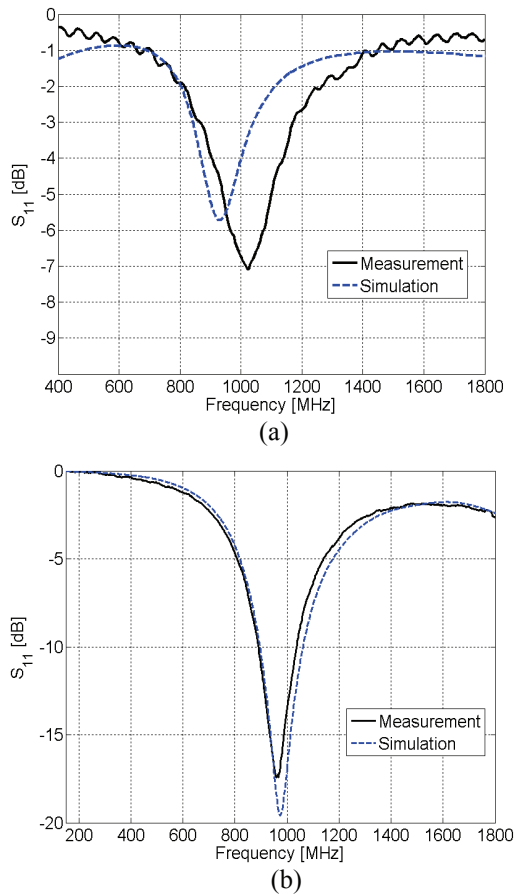


Fig. 11. Return loss of SWCNT composite antenna, (a) T-match bow-tie, and (b) MLA.

Table 6: Simulation and measurement results for the SWCNT bow-tie antenna and MLA antenna.

Type of Antenna		f_o (MHz)	R_r (Ω)
Bow-tie	Simulation	930	157
	Measurement	1013	130.7
MLA	Simulation	963	40.2
	Measurement	965	54.3

However, in this case the filter membrane was covered by a mask of silicon rubber that allowed the nanotube to accumulate in the shape of the antenna. The monopole composite antenna mounted on a ground plane is fed through a 50-ohm SMA connector from the bottom. The size of ground plane for the bow-tie antenna is $120\text{mm} \times 160\text{mm}$, and for the MLA antenna is $100\text{mm} \times 100\text{mm}$. The composite material thickness is $40\ \mu\text{m}$. The dimensions of the bow-tie are as reported in Fig. 3(a). The MLA parameters are $L_1 = 8.5\ \text{mm}$, $L_2 = 15\ \text{mm}$, $L_3 = 10\ \text{mm}$, $L_4 = 30.2\ \text{mm}$, $L_5 = 10\ \text{mm}$, and $L_6 = 3\ \text{mm}$, and $w = 2\ \text{mm}$.

Using HP8720 network analyzer, the return loss of composite antennas is measured as shown in Fig. 11. Satisfactory agreement is seen between the MWS simulation and the measurement. The small shift of measured resonance frequency can be explained by material and manufacturing tolerance. The resonant frequency and radiation resistance of both composite antennas are reported in Table VI.

V. CONCLUSION

The use of continuous carbon fiber composite and carbon nanotube composite is investigated numerically and experimentally for building antennas for RFID applications. The metal is replaced with CFC in a T-match bow-tie antenna and a meander-line antenna. In addition to low cost, low weight, ease of fabrication and good corrosion resistance, the composite antennas are shown to have promising characteristics compared to a metal antenna. Although the gain and the read-range of composite antennas are lower than those of metal antennas, the bandwidth is improved considerably for both the RCCF and the CNT antennas. Furthermore, the matching between input impedances of the RFID IC chip and the antenna can be controlled by using composite

materials with different values of conductivity and thickness. It is observed that new antenna designs can be developed using the RCCF composites. One may also control the direction of current flow using the anisotropic conductivity of continuous carbon fiber composite, and this suggests many possibilities for new antenna configurations. Studying the composite antenna performance carefully, we show that CFCs can be efficiently used instead of metal as the material for fabricating the radiating element.

ACKNOWLEDGMENT

The authors would like to thank Natural Sciences and Engineering Research Council of Canada (NSERC), Bell Helicopter Textron Canada Ltd., Delastek Ltd. and Consortium for Research an Innovation in Aerospace in Quebec (CRIAQ) for supporting this work.

The SWCNT samples were generously offered by Nikkiso Co.

REFERENCES

- [1] S.-L. Chen, and K.-H. Lin, "A slim RFID tag antenna design for metallic object applications," *IEEE Antennas and Wireless Propagat. Lett.*, vol. 7, pp. 729-732, 2008.
- [2] G. Marrocco, "The art of UHF RFID antenna design: impedance-matching and size-reduction techniques," *IEEE Antennas and Propagat. Magazine*, vol. 50, pp. 66-79, 2008.
- [3] K. Finkenzeller, *RFID Handbook*, 2nd ed. New York: Wiley, 2003.
- [4] P. V. Nikitin, K. V. S. Rao, S. F. Lam, V. Pillai, R. Martinez, and H. Heinrich, "Power reflection coefficient analysis for complex impedances in RFID tag design," *IEEE Trans. Microw. Theory Tech.*, vol. 53, pp. 2721-2715, 2005.
- [5] M. Hirvonen, K. Jaakkola, P. Pursula, and J. Säily, "Dual-band platform tolerant antennas for radio-frequency identification," *IEEE Trans. Antenna Propagat.* vol. 54, pp. 2632-2637, 2006.
- [6] K. V. Seshagiri Rao, P. V. Nikitin, and S. F. Lam, "Antenna design for UHF RFID tags: a review and a practical application," *IEEE Trans. Antenna Propagat.* vol. 53, pp. 3870-3876, 2005.
- [7] G. Marrocco, "Gain-Optimized self-resonant meander line antennas for RFID applications," *IEEE Antennas and Wireless Propagat. Lett.*, vol. 2, pp. 302-305, 2003.
- [8] H. Rmili, J.-L. Miane, H. Zangar, and T. Olinga, "Design of microstrip-fed proximity-coupled conducting polymer patch antenna," *Microw. Opt. Technol. Lett.*, vol. 48, pp. 655-660, 2006.
- [9] Y. Bayram, Y. Zhou, J. L. Volakis, B.-S. Shim and N. A. Kotov, "Conductive textiles and polymer-ceramic composites for novel load bearing antennas," *Proc. of IEEE Antenna and Propagation Symposium*, July 2008.
- [10] P. V. Nikitin, S. Lam, and K. V. S. Rao, "Low cost silver ink RFID tag antennas," in *Proc. IEEE Antennas Propag. Society Int. Symp.*, pp. 353-356, 2005.
- [11] L. Yang, A. Rida, R. Vyas, and M. M. Tentzeris, "RFID tag and RF structures on a paper substrate using inkjet-printing technology," *IEEE Trans. Microw. Theory Tech.*, vol. 55, pp. 2894-2901, 2007.
- [12] S. Ludmerer, "Conductive Inks for RFID Antenna: the low cost high speed route to RFID labels," Parelec. Inc. www.parelec.com.
- [13] R. A. Tellakula, V. K. Varadan, T. C. Shamy, and G. N. Mathur, "Carbon fiber and nanotube based composites with polypyrrole fabric as electromagnetic absorbers," *Smart Mater. Struct.*, vol. 13, pp. 1040-1044, 2004.
- [14] M. H. Choi, B. H. Jeon, and I. J. Chung, "The effect of coupling agent on electrical and mechanical properties of carbon fiber/phenolic resin composites," *Polymer*, vol. 41, pp. 3243-3252, 2000.
- [15] M. De Rosa, F. Sarasini, M. S. Sarto, and A. Tamburrano, "EMC impact of advanced carbon fiber/carbon nanotube reinforced composites for next-generation aerospace applications," *IEEE Trans. Electromagn. Compat.*, vol. 50, pp. 556-563, 2008.
- [16] C. Buccella, "Quasi-Stationary analysis of the electric field in anisotropic laminated composites," *IEEE Trans. Industry App.*, vol. 35, pp. 1296-1305, 1999.

- [17] C. L. Holloway, M. S. Sarto, and M. Johansson, "Analyzing Carbon-Fiber Composite Materials with Equivalent-Layer Models," *IEEE Trans. on Electromagn. Compatibility*, vol. 47, no. 4, pp. 833-844, 2005.
- [18] Mehdipour, C. W. Trueman, A. R. Sebak, I. D. Rosca, and S. V. Hoa, "Shielding effectiveness analysis of multilayer carbon-fiber composite materials," *Proc. of General Assembly of the International Union of Radio Science (URSI)*, 2008.
- [19] M. S. Sarto, and C. L. Holloway, "Effective boundary conditions for the time-domain analysis of the EMC performances of fiber composites", *Proc. of IEEE International Symposium on Electromagn. Compat.*, pp. 462-467, 1999.
- [20] W. Bauhofer, and J. Z. Kovacs, "A review and analysis of electrical percolation in carbon nanotube polymer composites", *Compos. Sci. Technol.*, 2008.
- [21] R. K. Challa, D. Kajfez, V. Demir, J. R. Gladden, and A. Z. Elsherbeni, "Characterization of multiwalled carbon nanotube (MWCNT) composites in a waveguide of square cross section," *IEEE Microwave and Wireless Components Lett.*, vol. 18, no. 3, pp. 161-163, 2008.
- [22] F. H. Gojny, M. H. G. Wichmann, B. Fiedler, and K. Schulte, "Influence of different carbon nanotubes on the mechanical properties of epoxy matrix composites - A comparative study," *Compos. Sci. Technol.*, vol. 65, pp. 2300-2313, 2005.
- [23] B. Hornbostela, U. Leuteb, P. Potschkec, J. Kotza, D. Kornfelda, P.-W. Chiud, and S. Rotha, "Attenuation of electromagnetic waves by carbon nanotube composites," *Physica E*, vol. 40, pp. 2425-2429, 2008.
- [24] Y. Huang, N. Li, Y. Ma, F. Du, F. Li, X. He, X. Lin, H. Gao, and Y. Chen, "The influence of single-walled carbon nanotube structure on the electromagnetic interference shielding efficiency of its epoxy composites," *Carbon*, vol. 45, pp. 1614-1621, 2007.
- [25] Z. Liu, G. Bai, Y. Huang, Y. Ma, F. Du, F. Li, T. Guo, and Y. Chen, "Reflection and absorption contributions to the electromagnetic interference shielding of single-walled carbon nanotube/polyurethane composites," *Carbon*, vol. 45, pp. 821-827, 2007.
- [26] Mehdipour, A.-R. Sebak and C. W. Trueman, and S. V. Hoa "Carbon-Fiber composite T-match folded bow-tie antenna for RFID applications," to be presented in *IEEE Antenna and Propagation Symposium*, 2009.
- [27] *Concordia Center for Composites (CONCOM)*, Concordia University, QC, Canada, <http://concom.encs.concordia.ca>, 1979.
- [28] *CST – Microwave Studio*, Computer Simulation Technology, 2009.
- [29] CST of America, "Efficient, accurate, reliable EM simulation tool", *Microwave Journal*, Oct. 2008.
- [30] R. K. Challa, D. Kajfez, J. R. Gladden, and A. Z. Elsherbeni, "Permittivity measurement with a non-standard waveguide by using TRL calibration and fractional linear data fitting," *Progress In Electromagnetics Research B*, vol. 2, pp. 1-13, 2008.
- [31] Hexion Specially Chemicals Inc., Columbus, OH, 2006.
- [32] Freeman Mfg. & Supply Co., Columbus, OH, 2001.
- [33] *Composite Tech. Unit.*, Nikkiso Co., Ltd., Tokyo, Japan, 2000.
- [34] Munteanu, and T. Weiland, *RF & microwave simulation with the finite integration technique – from component to system design*, Springer Berlin Heidelberg, 2007.
- [35] M. Clemens and T. Weiland, "Discrete electromagnetism with the finite integration technique," *Progress In Electromagnetics Research, PIER* 32, pp. 65-87, 2001.
- [36] R. Potthast, and L. Kuhn, "On the convergence of the finite integration technique for the anisotropic boundary value problem of magnetic tomography," *Mathematical Methods in the Applied Sciences*, vol. 26, pp. 739-757, 2003.
- [37] *UHF Frequency ICs*, Texas Instrument Inc., Dallas, TX, <http://focus.ti.com/docs/prod/folders/print/ri-uhf-strap-08.html>, 2006.
- [38] C. T. Rodenbeck, "Planar miniature RFID antennas suitable for integration with batteries," *IEEE Trans. Antenna Propagat.* vol. 54, pp. 302-305, 2006.

- [39] J. Rashed, and C. T. Tai, "A new class of resonant antennas," *IEEE Trans. on Antennas and Propagat.*, vol. 39, pp. 1428-1430, 1991.
- [40] T. J. Warnagiris and T. J. Minardo, "Performance of a meandered line as an electrically small transmitting antenna," *IEEE Trans. on Antennas and Propagat.*, vol. 46, pp. 1797-1801, 1998.



Aidin Mehdipour received the B.S. degree from Amirkabir University of Technology, Tehran, Iran, in 2003 and the M.S. degree from University of Tehran, in 2006, both in electrical engineering. He is currently working toward the Ph.D. degree at Concordia University, Montreal, Canada. His main research interests include advanced carbon fiber composites electromagnetic analysis, novel material development for shielding and antenna applications, small antenna design, RFID and wideband/ultrawideband antennas. In 2006, he was a senior research engineer of the Iran Telecommunication Research Center (ITRC) in a project on ultra-wideband antenna design. He serves as a reviewer for the *IEEE Transactions on Electromagnetic Compatibility*. He has authored and co-authored over more than 20 papers in referred journals and conference proceedings. Mr. Mehdipour is the recipient of the David J. Azrieli Graduate Fellowship, as the highest ranking Concordia University fellowship award, and the France and André Desmarais Graduate Fellowship for the 2009-2010 academic years.



Iosif Daniel Rosca received his engineer diploma in Polymer Science and Technology from Polytechnic University of Bucharest, Romania. He earned his Ph.D. in Chemistry with Prof. J.M. Vergnaud at Jean Monnet University, Saint-Etienne, France. He is associated professor of Polymer Science and Technology at the Polytechnic University of Bucharest, Romania. Rosca spent 2 years as JSPS Postdoctoral Fellow at Hokkaido

University, Japan. He is currently a Research Associate with Prof. S. V. Hoa at Concordia University, Canada. His present research focuses on fabrication and application of polymer composites based on carbon nanomaterials.



Abdel-Razik Sebak received the B.Sc. degree (with honors) in Electrical Engineering from Cairo University, Egypt, in 1976 and the B.Sc. degree in Applied Mathematics from Ein Shams University, Egypt, in 1978. He received the M.Eng. and Ph.D. degrees from the University of Manitoba, Winnipeg, MB, Canada, in 1982 and 1984, respectively, both in electrical engineering. From 1984 to 1986, he was with the Canadian Marconi Company, Kanata, Ontario, working on the design of microstrip phased array antennas. From 1987 to 2002, he was a Professor in the Electrical and Computer Engineering Department, University of Manitoba, Winnipeg. He is currently a Professor of Electrical and Computer Engineering, Concordia University, Montreal. His current research interests include phased array antennas, computational electromagnetics, integrated antennas, electromagnetic theory, interaction of EM waves with new materials and bio-electromagnetics. Dr. Sebak received the 2007-2008 Faculty of Engineering, Concordia University double Merit Award for outstanding Teaching and Research. He has also received the 2000 and 1992 University of Manitoba Merit Award for outstanding Teaching and Research, the 1994 Rh Award for Outstanding Contributions to Scholarship and Research in the Applied Sciences category, and the 1996 Faculty of Engineering Superior Academic Performance. Dr. Sebak has served as Chair for the IEEE Canada Awards and Recognition Committee (2002-2004) and IEEE Canada CONAC (1999-2001). He has also served as Chair of the IEEE Winnipeg Section (1996-97). He was the Technical Program Co-Chair (2006) and served as the Treasurer (1992, 1996, and 2000) and Publicity Chair (1994) for the Symposium on Antenna Technology and Applied Electromagnetics (ANTEM). Dr. Sebak has also served as Chair (1991-92) of the joint IEEE AP/MTT/VT Winnipeg Chapter. He received, as the Chapter Chair, the 1992 IEEE Antennas and Propagation Society Best Chapter

Award. He is a Senior Member of the IEEE, and a member of the International Union of Radio Science Commission B.



Christopher W. Trueman

received his Ph.D. from McGill University in 1979. He has applied the methods of computational electromagnetics to problems such as aircraft antenna performance, antenna-to-antenna coupling and EMC on aircraft,

aircraft and ship radar cross-section at HF frequencies, suppression of scattering of the signal of a commercial radio station from power lines, dielectric resonators, unconditionally-stable formulations for the finite-difference time-domain method, and the fields of portable radios such as cellular phones held against the head. Recently, his research has investigated the radar cross-section of ships at VHF frequencies, composite materials for aircraft, indoor propagation, and EMC issues between portable radios and medical equipment. Dr. Trueman is currently the Associate Dean for Academic Affairs in the Faculty of Engineering and Computer Science at Concordia University.



Dr. Suong Van Hoa is a professor in the Department of Mechanical and Industrial Engineering at Concordia University, Montreal, Quebec, Canada. He is also Director of Concordia Center for Composites. He has been working

on composites materials and structures since 1979 and on polymer nanocomposites since 2000. He has worked on the incorporation of nanoparticles such as nanoclays, carbon nanotubes into composites materials. He has also developed self healing composite materials using microcapsules. He has published more than 500 articles in scientific journals and conferences, and many patents. Dr. Hoa is the recipient of the NanoAcademia prize from Nanoquebec in 2008.

Green Technologies and RFID: Present and Future

Giulia Orecchini¹, Li Yang², Amin Rida², Federico Alimenti¹,
Manos M. Tentzeris², Luca Roselli¹

¹ Department of Electrical Engineering
University of Perugia, Italy

² GEDC, Department of Electrical and Computer Engineering
Georgia Institute of Technology, USA

Abstract— RFID systems are proliferating in everyday applications. In this paper, the authors present a unified approach that relies on the development of novel low-cost inkjet-printed platforms with optimized metallization trace and effective integration of diodes for enhanced-discrimination capability applications. Potentially, the presented approach could set the foundation for the first generation of truly “green” RFID-based devices.

Index Terms— UHF RFID’s, inkjet-printed electronics, antennas, diode integration, multiplier.

I. INTRODUCTION

Historically speaking, the introduction of RFID took place in the defense area; it can be dated back to the 40’s and ascribed to the Identification Friend or Foe (IFF) associated to the radar systems. The first scientific contribution mentioning RFID approach is probably due to Stockman [1] where information transfer via reflected waves is theorized. First commercial applications of RFID approach are testified by several patents the first of which can be likely considered by Harris [2]. RFID’s were first used in anti theft systems and automatic opening systems (electronic keys). In the late 70’s RFID accessed the application that would have been the leading one for many years: logistics. Still in the defense area, it was in this field that the intrinsic capability of an RFID system to give information on demand was exploited in the monitoring movements of items. At the beginning it was the monitoring of

sensitive materials such as nuclear elements and weapons; afterwards, RFID monitoring accessed the civil world in the early 80’s when it was first used to monitor cows, and in particular, to control their health and recovery status. In the late 80’s both in Europe (Italy) and in the US (Oklahoma) automatic pay toll systems appeared, clearly theorized in open literature by Hauslen in 1977 [3], based on a gate reader and a car tag. In the early 90’s, due to a collaboration between IBM and Wal-Mart, massive goods’ monitoring systems based on passive, very low cost tags were implemented, constituting the first truly consumer application of RFID’s, thanks to the technology improvement and the related cost reduction that allowed the realization of tags, the cost of which was in the same order of magnitude of paper labels. Potential substitution of barcodes with RFID tags, still more expensive but much more flexible and powerful, became cost-effective and RFID entered the supply chains. Since that time, the commercial deployment of RFID applications has proliferated tremendously, including, among others: vehicle and container tracking, automated toll (parking, highway, etc.), access control (also for animals), electronic doorlock, ski-lift toll, triage patient management, laundry cycle tracking, library material tracking, sport timing, etc.

In terms of regulations, in the 90’s the following bands became available for RFID’s: low frequency (between 125 to 134 KHz), high frequency (13.56 MHz), UHF (868 to 956 MHz), and microwave (2.45 GHz). Recently the 5.9 GHz band was also freed by the FCC.

II. PRESENT AND FUTURE TRENDS

The key trend that will drive modern societies and technologies in the next decades is strongly related to cognitive intelligence and ubiquitous ad-hoc networks in a variety of applications, such as logistics, Aero-ID, anti-counterfeiting, supply-chain monitoring, space, healthcare, pharmaceutical, and military [4]. Mobility, environment, health, security and energy will be the major technology drivers of the future, further increasing the demand for low cost, robust, flexible, reliable, low power consumption and durable wireless modules and electronics.

Addressing this major goal, electronics research, and consequently RFID, moves towards the development of flexible devices based on organic/inorganic materials and substrates attempting to overcome the limitations of ceramics and silicon. Thin, light-weight, heterogeneous, flexible and environmentally friendly, combinations of new materials and cost-effective, large area production processes are the challenges that need to be tackled for the applications of the future. Current research and manufacturing incorporates a wide range of electrical components that can be produced and directly integrated in low cost reel-to-reel processes, mainly involving organic electronics with the examination of several electrically conductive and semi-conducting materials.

Organic materials can be printed and patterned using various techniques (like flexo, gravure, offset, screen, and inject.) [5,6,7], each one with its own advantages and disadvantages. Based on these materials and techniques up to now, mainly passive devices have been attempted such as low cost RFID transponders, various types of sensors, memories, photo-voltaic cells, displays or batteries while the development of active components as diodes and transistors has been demonstrated, though only in low UHF (RF) bands [8,9,10]. Trends are moving to higher speeds, resolution, and frequencies without compromises in flexibility, environmental friendliness, and low cost. In order to overcome these challenges, novel approaches to manufacture electronics and RFID systems are needed in terms both of alternative materials, processes and characteristics.

III. INKJET-PRINTED TAG

As mentioned in the previous section, inkjet printing is one of the potential and very promising solutions for the future of “green” electronics fabrication. Modern inkjet printers operate by propelling tiny droplets of liquid down to 1 pico liters (pl) which results in the accuracy that conventional methods of fabrication yield such as several microns. Not to mention that inkjet printing utilizes a method of fabrication that uses material to be printed such as conductive paste, which rapidly fabricates prototype circuits without iterations in photolithographic mask design or traditional etching techniques that have been widely used in industry. Printing is also completely controlled from the designer’s computer and utilizes artwork files such as the ones used to create masks and reads them directly, transferring them into a pattern on a substrate; hence, it does not require a clean room environment [11] and may be done in a laboratory environment. The print-head, which attaches to the materials cartridge, consists of a piezo-driven jetting device with integrated reservoir and heater [12] and is responsible for the dimensions and accuracy of the printed structures.

The savings in fabrication/prototyping time that inkjet printing brings to RF/wireless circuits is very critical to the ever changing electronics market of today, verifying its feasibility as an excellent prototyping and mass-production technology for next generation electronics, especially in RFID, wireless sensors, handheld wireless devices (e.g. 4G/4.5G cell phones), flex circuits, and even in thin-film batteries [13].

Printed electronics such as: passive circuitry (transmission lines, antennas, pads for wiring), logic, display, and power supply will have the desired characteristics of: low cost, disposability, and the potential of the familiar roll-to-roll processing currently used in printing industry.

On the other hand, several organic and low cost substrates have been identified to complement inkjet-printing technology, such as paper and liquid crystal polymer [14, 15]. [14] talks about the benefits of using paper as a substrate for high-frequency applications, reporting its very good electrical/dielectric performance up to at least 1 GHz. [15] briefly discusses the use of LCP as a flexible organic substrate that has excellent performance up to 110 GHz. For instance [14]

talks about the potential of using ink-jet printing on paper substrate for the application of passive RFID, while [16] describes how inkjet printing of an antenna along with its with pads may be utilized for the mounting of discrete devices such as sensor, micro-processor, capacitors, and battery for the interconnections of a complete wireless sensor device. A photo taken under a fiducial camera of conductive ink on paper substrate is shown in the Fig. 1 below.

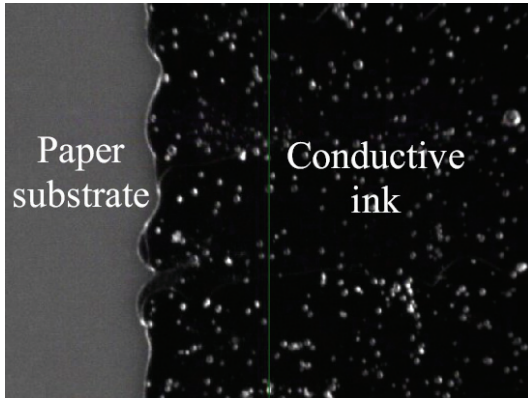


Fig. 1. Photograph of conductive ink on paper under a fiducial camera.

After introducing the paper-based substrate into the low-cost RFID tag design methodology, conductive ink has become the major cost factor of an RFID tag. Further reduction of the cost requires the optimization work on the ink’s side. Minimizing the amount of ink used per antenna will save thousands of dollars in the mass production. The investigation of minimizing the ink usage by reducing solid printed surfaces with alternative design, while maintaining the tag antenna performance is achieved in this section.

Figure 2 shows the step by step process performed to gradually reduce the amount of conductive ink utilized, starting with the first version of the “solid” dipole antenna as shown in Fig. 2a. One can clearly observe from the current distribution simulation in the figure that the highest concentration mainly occurs closest to the center of the radiating body. Based on this phenomenon, the next designs were realized. Fig. 2b shows an alternative design with thin wire grid of width 0.3 mm and resulting in a quite similar performance as depicted in Table 1. Likewise, Fig. 2c and Fig. 2d show the next steps in the antenna

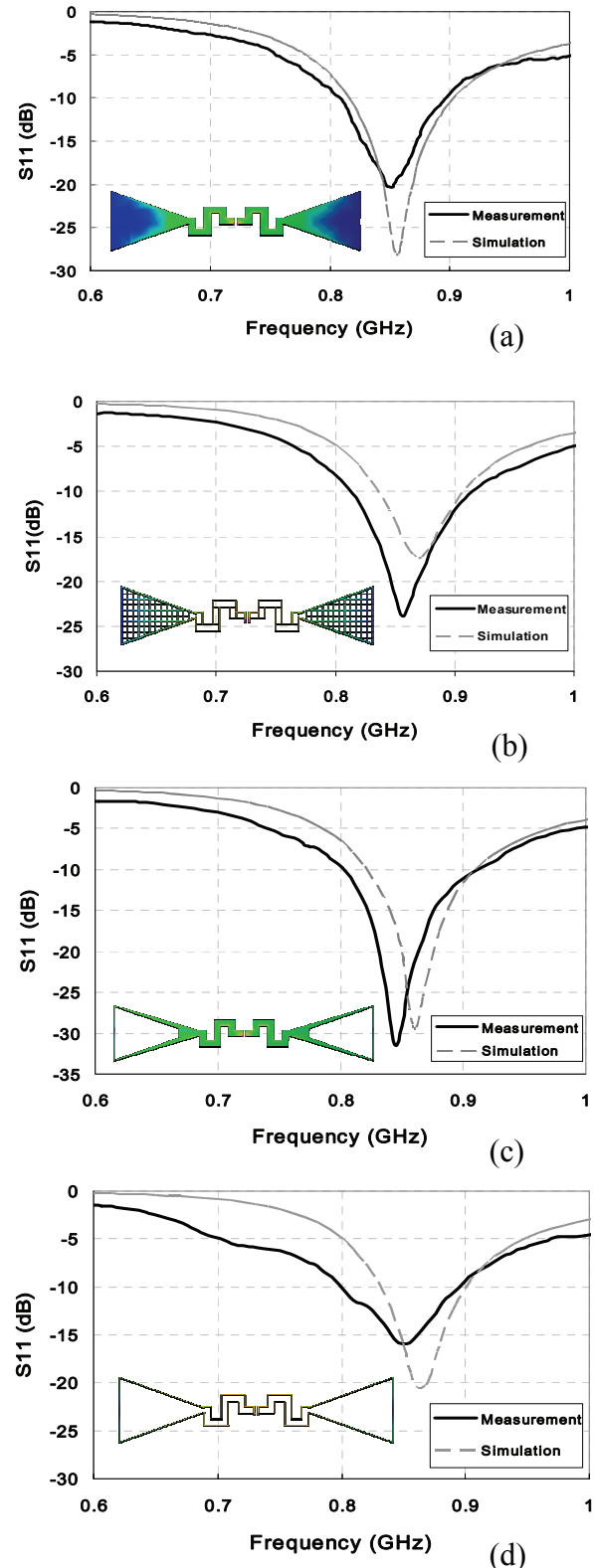


Fig. 2. Topology and return loss comparison of four inkjet-printed antenna designs at European RFID band.

Table 1: Performances comparison for the antennas shown in Fig. 2.

	<i>BW (%)</i>	<i>EFF. (%)</i>	<i>GAIN (dBi)</i>
(a)	10.1	99	1.94
(b)	8.66	91	1.61
(c)	10.3	99	2.03
(d)	7.9	89	1.66

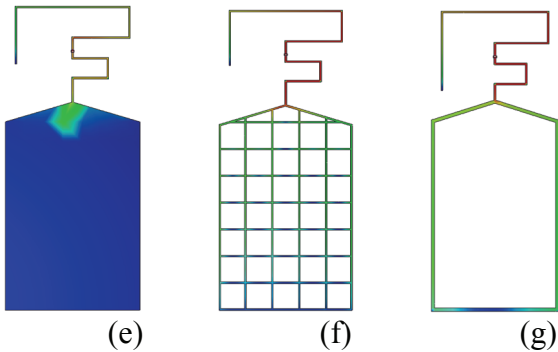


Fig. 3. Topology of inkjet-printed antenna designs of a commercial tag at US RFID band.

Table 2: Performances comparison of the antennas shown in Fig. 3.

	<i>BW (%)</i>	<i>EFF. (%)</i>	<i>GAIN (dBi)</i>
(e)	5.4	90.6	1.48
(f)	5.4	90.7	1.48
(g)	5.2	90.4	1.49

design while aiming towards optimizing and minimizing the amount of ink used as mentioned previously. It is to be noted that in all the plots (Fig. 2a through Fig. 2d), one can argue that the measurement results yield good comparison with the theoretical data. Furthermore, the performance of the final design shown in Fig. 2d features a bandwidth of 7.9% covering the European UHF RFID band.

The difference between the first and the last case, in terms of ink saved, is about 96%. As a trade off, the radiation efficiency decreases

slightly from 99% to 89% while the antenna gain from 1.94 dBi to 1.66 dBi.

The same design topology can be used to lower the cost of existing commercial RFID tags. Fig. 3 illustrates the design of a commercial RFID tag which has been widely used on toll road collection applications. The monopole ground costs a large area for the conductive ink. The gradual reduction of ink for the alternative designs can be noticed in Fig. 3. The antenna performance is listed in Table 2. The ink saved for the antenna shown in Fig. 3g is about 94% compared with the one in Fig. 3e.

IV. FREQUENCY DOUBLING RFID TAG FOR HARMONIC RADAR

This section will be devoted to address another major challenge in the RFID world, the integration of nonlinear devices in a cost and power-effective way that could be applicable in the very stringent space requirements of RFID's (potentially in the additional space created by designs similar to the one presented in the previous section). Without loss of generality, and for simplicity reasons, this section will focus on the discussion of a frequency doubling tag based on a crossed-dipole structure and UHF diodes. Such a tag is useful for harmonic radar application and seems to be a good candidate for implementation exploiting fully green processes.

One-bit RFID systems are commonly used to check and monitor the possible presence of a transponder in the interrogation zone of a reader by means of simple physical effects [17]. Among various operating principles, the generation of harmonics is reliably adopted in the microwave frequency range, leading to the harmonic radar concept [18, 19]. Such a concept has recently been exploited in avalanche rescue systems to precisely localize victims buried under the snow [20]. The harmonic radar works as follows. A tag with aerial antenna and diode bounces back to the searchers a directional radar signal. Because of the diode nonlinearity the reflected frequency is doubled with respect to that used to illuminate the tag itself. Such a signal can easily be detected by means of a microwave receiver.

In order to make this kind of rescue systems really effective, mountain walkers or climbers and skiers should be equipped with one of these frequency-doubling tags. A method could be that

of embedding the tags directly into the sky-pass cards. To this purpose both paper-based antennas [5] and organic diodes [8, 9] can be used to provide a completely green solution at very low production costs.

A structure that is particularly suited to the implementation of frequency doubling tag has already been proposed in [21]. Such a structure exploits two dipoles in a crossed configuration and four diodes and has the advantage to separate fundamental and second harmonic antennas.

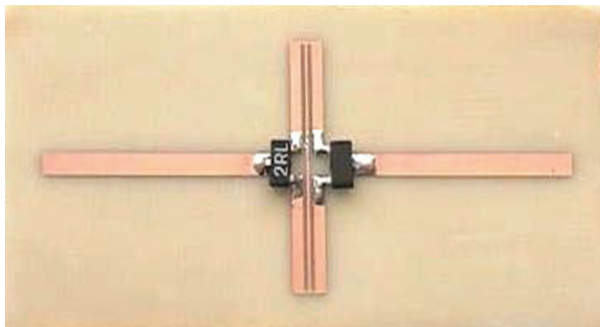


Fig. 4. Photograph of the proposed frequency doubling tag. The length of the longest l_0 dipole, corresponding to the double of the shortest one l_1 , is $l_0 = 2l_1 = 32\text{mm}$. The substrate thickness is $h = 0.8\text{mm}$ while its dielectric constant is $\epsilon_r = 3.38$.

As shown in Fig. 4, a prototype of this frequency doubling tag has been realized on plastic substrate and consists of two crossed $\lambda/2$ dipoles. The longest dipole receives the incoming power at the fundamental frequency $f_0 = 3.5\text{GHz}$, whereas the shortest dipole transmits the generated power at the doubled frequency $2f_0$ in an orthogonally polarized orientation. The multiplication is achieved by four diodes in a bridge configuration, thus forming a fully balanced multiplier bridge. Although the diodes are operating self-biased and no external DC-supply is necessary, a return for the generated DC-component must be provided for proper operation of the multiplier itself. This is done with a thin metal strip which is embedded in the short dipole connecting its outer ends. Thus a sufficient amount of inductance is provided to avoid a major disturbance of RF performances. The proposed tag was realized on a plastic substrate with $\epsilon_r = 3.38$, a value very close to that of paper ($\epsilon_r = 3.2\sim 3.8$). Moreover the layout of the crossed dipole

antennas does not present critical dimension and is completely uniplanar (no bias needed). Therefore it is suitable for paper-based implementation. The FDTD simulation of E-field patterns is shown in Fig. 5.

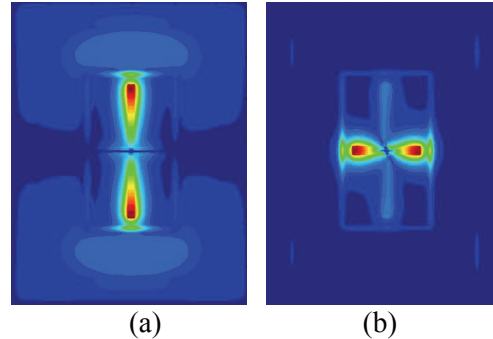


Fig. 5. FDTD simulation of E-field patterns: (a) the longest dipole is excited by a plane wave at f_0 having the E-field parallel to the dipole itself; (b) the diode quad generates a $2f_0$ frequency component which is emitted by the shortest dipole.

V. CONCLUSION

This paper introduces various new, environmentally-friendly developments in the area of UHF RFIDs. The introduction of optimal-metallization printed antennas and the effective integration of diodes could potentially lead to the first truly “green” low-cost generation of RFID-enabled devices.

REFERENCES

- [1] H. Stockman, "Communication by Means of Reflected Power", *Proceedings of the IRE*, pp. 1196-1204, October 1948.
- [2] D. B. Harris, "Radio transmission systems with modulatable passive responder", *US Patent 2,927,321*, March 1, 1960.
- [3] R. A. Hauslen, "The promise of automatic vehicle identification", *IEEE Trans. On Vehicular Technology*, Vol. 26, No. 1, pp. 30-38, Feb 1977.
- [4] J. Buckley, Final Report of the conference "From RFID to the Internet of things," ftp://ftp.cordis.europa.eu/pub/ist/docs/ka4/au_conf670306_buckley_en.pdf, Mar. 2006.
- [5] L. Yang, A. Rida, R. Vyas, and M. M. Tentzeris, "RFID tag and RF structures on a paper substrate using inkjet-printing technology," *IEEE Trans. on Microwave*

- Theory and Techniques*, Vol. 55, No. 12, pp. 2894–2901, Dec. 2007.
- [6] E. Fortunato, N. Correia, P. Barquinha, L. Pereira, G. Goncalves, and R. Martins, “High-performance flexible hybrid field-effect transistors based on cellulose fiber paper,” *IEEE Electron Device Letters*, Vol. 29, No. 9, pp. 988–990, Sep. 2008.
- [7] S. Couderc, B.J. Kim, and T. Someya, “Cellulose-based composite as a raw material for flexible and ultra-lightweight mechanical switch devices,” *22nd Int. Conferences on Micro Electro Mechanical Systems*, pp. 646–649, Jan. 2009.
- [8] S. Steudel, K. Myny, V. Arkhipov, C. Deibel, S. D. Vusser, J. Genoe, and P. Heremans, “50MHz rectifier based on an organic diode,” *Nature Materials*, Vol. 4, pp. 597–600, Aug. 2005.
- [9] S. Steudel, S. D. Vusser, K. Myny, M. Lenes, J. Genoe, and P. Heremans, “Comparison of organic diode structures regarding high-frequency rectification behavior in radio-frequency identification tags,” *Journal of Applied Physics*, Vol. 99, No. 11, June 2006.
- [10] V. Subramanian, J. M. J. Frechet, P. C. Chang, D. C. Huang, J. B. Lee, S. E. Molesa, A. R. Murphy, D. R. Redinger, and S. K. Volkman, “Progress toward development of all-printed RFID tags: Materials, processes, and devices,” *Proceedings of the IEEE*, Vol. 93, No. 7, pp. 1330–1338, July 2005.
- [11] D. Thompson, O. Tantot, H. Jallageas, G. Ponchak, M. M. Tentzeris, J. Papapolymerou, “Characterization of LCP material and transmission lines on LCP substrates from 30 to 110GHz,” *IEEE Trans. Microwave Theory and Tech.*, Vol. 52, No. 4, pp. 1343–1352, April 2004.
- [12] Fujifilm Dimatix Inc, Piezo-electric Ink-jet Print-Heads, <http://www.dimatix.com/markets/electronics.asp>.
- [13] A. Ferrer-Vidal, A. Rida, S. Basat, L. Yang, and M.M. Tentzeris, “Integration of sensors and RFIDs on ultra-low-cost paper-based substrates for wireless sensor networks applications” *IEEE Workshop on Wireless Mesh Networks*, pp. 126–128, 2006.
- [14] L. Yang, A. Rida, R. Vyas, M. M. Tentzeris, “RFID Tag and RF Structures on a Paper Substrate Using Inkjet-Printing Technology,” *Microwave Theory and Techniques, IEEE Transactions on*, Vol. 55, No. 12, Part 2, pp. 2894–2901, Dec. 2007
- [15] A. Rida, S. Nikolaou, and M. M. Tentzeris “Broadband UHF RFID/Sensor Module for Pervasive Cognition Applications”, *European Conference on Antennas and Propagation*, March 2009.
- [16] R. Vyas, A. Rida, L. Yang, M. M Tentzeris, “Design, Integration and Characterization of a Novel Paper Based Wireless Sensor Module”, *IEEE International Microwave Symposium*, June 2008.
- [17] K. Finkenzerler, *RFID Handbook: Fundamentals and Applications in Contactless Smart Cards And Identification*, John Wiley & Sons, 2003.
- [18] B. G. Colpitts, G. Boiteau, “Harmonic radar transceiver design: miniature tags for insect tracking,” *IEEE Trans. Antennas Propagation*, Vol. 52, No. 11, pp. 2825–2832, Nov. 2004.
- [19] G. L. Lovei, I. A. N. Stringer, C. D. Devine, M. Cartellieri, “Harmonic radar – a method using inexpensive tags to study invertebrate movement on land,” *New Zealand Journal of Ecology*, Vol 21, No. 2, pp. 187–193, 1997.
- [20] RECCO avalanche rescue systems, <http://recco.com>.
- [21] S. Helbing, M. Cryan, F. Alimenti, P. Mezzanotte, L. Roselli, and R. Sorrentino, “Design and verification of a novel crossed dipole structure for quasi-optical frequency doublers,” *IEEE Microwave and Guided Wave Letters*, Vol. 10, No. 3, pp. 105–107, Mar. 2000.



Giulia Orecchini received the Laurea Degree in Electronic Engineering from the University of Perugia, Italy in the summer of 2008. In autumn 2008 she started her PhD studentship under the advice of Prof. Luca Roselli. She recently joined the Georgia Institute of Technology (Atlanta, GA, U.S.) ATHENA research group under the advice of Prof. Manos Tentzeris. Her research activity is focused on the development of RFID high frequency electronic systems and technologies.



Li Yang received the B.S. and M.S. degrees in Electronic Engineering from the Tsinghua University, Beijing, China, in 2002 and 2005, respectively. He is currently pursuing his Ph.D. degree in Electrical and Computer Engineering at the Georgia Institute of

Technology.

He is a Graduate Research Assistant with the ATHENA research group at the Georgia Electronic Design Center. His research interests include Radio Frequency Identification (RFID) technology, Radio Frequency Integrated Circuit (RFIC) technology, and the design of high performance analog circuits for sensing and power scavenging applications. He was the recipient/co-recipient of the 2008 IEEE IMS Student Paper Honorary Mention Award, the 2008 IEEE APS Symposium Student Paper Honorary Mention Award, the 2007 IEEE APS Symposium Best Student Paper Award, the 2007 IEEE IMS Third Best Student Paper Award, the 2007 ISAP Poster Presentation Award, and the 2006 Asian-Pacific Microwave Conference Award.



Amin Rida received the B.S. and M.S. degree in electrical engineering from the Georgia Institute of Technology, Atlanta, in 2006 and 2009, and is currently working toward the Ph.D. degree at the Georgia Institute of Technology. He is currently

with the Georgia Electronic Design Center (GEDC), Atlanta, GA. His research interests include: design, development and packaging of electronics (Antennas, interconnects, 3D transitions, and integration) on organic, flexible, and high performance substrates for mm-wave frequencies. Other research topics focus on X-band filter design and Integration in a System on Package, characterization of organic substrates for RF applications, antenna design for RFID applications, and development of wireless transceivers for sensing and power scavenging applications. Amin received the MTT-S pre-graduate scholarship in 2006 and the Best Student Paper Award at the IEEE Antennas and

Propagation Symposium, Honolulu, HI, June 2007.



Federico Alimenti received the Laurea degree (summa cum laude) and the Ph.D. degree from the University of Perugia, Italy, in 1993 and 1997 respectively, both in electronic engineering. In 1993 he held a scholarship from Daimler Benz Aerospace, Ulm, Germany. In 1996 he was awarded as young scientist from URSI (*Union Radio-Scientifique Internationale*) and he was visiting scientist at the Lehrstuhl für Hochfrequenztechnik of the Technical University of Munich, Munich, Germany. Since 2001 Federico Alimenti has been with the Department of Electronic and Information Engineering of the University of Perugia as an assistant professor, teaching the classes of *Telecommunication Electronics*. His research interests concern the modelling, design and realization of microwave integrated circuits in CMOS and Si/SiGe BiCMOS technologies. He is an IEEE member, serving as reviewer of the following journals: IEEE Microwave and Wireless Component Letters; IEEE Transaction on Microwave Theory and Techniques; IEEE Transaction on Advanced Packaging; IEEE Transaction on Circuit and System I. Federico Alimenti belongs to the TARGET (*Top Amplifier Research Group in a European Team*) Network of Excellence. He is consultant of industries.



Manos M. Tentzeris received the Diploma Degree in Electrical and Computer Engineering from the National Technical University of Athens ("Magna Cum Laude") in Greece and the M.S. and Ph.D. degrees in Electrical Engineering and Computer

Science from the University of Michigan, Ann Arbor, MI and he is currently a Professor with School of ECE, Georgia Tech, Atlanta, GA. He has published more than 320 papers in refereed Journals and Conference Proceedings, 3 books and 17 book chapters. Dr. Tentzeris has helped

develop academic programs in Highly Integrated/Multilayer Packaging for RF and Wireless Applications using ceramic and organic flexible materials, paper-based RFID's and sensors, Microwave MEM's, SOP-integrated (UWB, multiband, conformal) antennas and Adaptive Numerical Electromagnetics (FDTD, MultiResolution Algorithms) and heads the ATHENA research group (20 researchers). He is the Georgia Electronic Design Center Associate Director for RFID/Sensors research, and he has been the Georgia Tech NSF-Packaging Research Center Associate Director for RF Research and the RF Alliance Leader from 2003-2006. He was the recipient/co-recipient of the 2007 IEEE APS Symposium Best Student Paper Award, the 2007 IEEE IMS Third Best Student Paper Award, the 2007 ISAP 2007 Poster Presentation Award, the 2006 IEEE MTT Outstanding Young Engineer Award, the 2006 Asian-Pacific Microwave Conference Award, the 2004 IEEE Transactions on Advanced Packaging Commendable Paper Award, the 2003 NASA Godfrey "Art" Anzic Collaborative Distinguished Publication Award, the 2003 IBC International Educator of the Year Award, the 2003 IEEE CPMT Outstanding Young Engineer Award, the 2002 International Conference on Microwave and Millimeter-Wave Technology Best Paper Award (Beijing, CHINA), the 2002 Georgia Tech-ECE Outstanding Junior Faculty Award, the 2001 ACES Conference Best Paper Award and the 2000 NSF CAREER Award and the 1997 Best Paper Award of the International Hybrid Microelectronics and Packaging Society. He was the TPC Chair for IEEE IMS 2008 Symposium and the Chair of the 2005 IEEE CEM-TD Workshop and he is the Vice-Chair of the RF Technical Committee (TC16) of the IEEE CPMT Society. He is the founder and chair of the RFID Technical Committee (TC24) of the IEEE MTT Society and the Secretary/Treasurer of the IEEE C-RFID. He has organized various sessions and workshops on RF/Wireless Packaging and Integration, RFID's, Numerical Techniques/Wavelets, in IEEE ECTC, IMS, VTC and APS Symposia in all of which he is a member of the Technical Program Committee in the area of "Components and RF". He is the Associate Editor of IEEE Transactions on Microwave Theory and Techniques, IEEE Transactions on Advanced Packaging and

International Journal on Antennas and Propagation. Dr. Tentzeris was a Visiting Professor with the Technical University of Munich, Germany for the summer of 2002, where he introduced a course in the area of High-Frequency Packaging. He has given more than 50 invited talks in the same area to various universities and companies in Europe, Asia and America. He is a Senior Member of IEEE, a member of URSI-Commission D, a member of MTT-15 committee, an Associate Member of EuMA, a Fellow of the Electromagnetic Academy and a member of the Technical Chamber of Greece.



Luca Roselli received the Laurea degree in electronic engineering from the University of Florence, Florence, Italy, in 1988. From 1988 to 1991 he worked at the University of Florence on SAW devices. In November 1991, he joined the Institute of Electronics at the University of Perugia, Perugia, Italy, as a Research Assistant. Since 1992 he has been an IEEE member. Since 1994 he has been teaching Electronic Devices at the same University and was the Director of works for the realization of a 35 square meters clean room 100 class at the University of Perugia. Since 1996 he has been in the reviewer list for IEEE Microwave and Guided Wave Letters (MGWL). Since 1998 he has been in the reviewer list of the IEEE Transactions on Microwave Theory and Techniques (MTT) and has been a member of the technical program committee of the Electrosoft conference, of the Microwave Theory and Techniques Symposium. Since 2000 he has been an associated professor at the University of Perugia where he teaches Microwave Electronics and High Frequency Components. Since that time he has been coordinating the research activity of the High Frequency Electronics (HFE) Lab. He founded the WiS (Wireless Solutions) Srl, a spin off company operating in the field of microwave electronic systems with which he is currently cooperating as a consultant that same year. In 2001 he was nominated IEEE senior member. Since 2003 he has been in the steering committee of CEM. In that same year he was a member of the spin off committee of the University of Perugia, in

2005 he founded a second spin off company: DiES (Digital Electronic Solutions) Srl. In 2007 he was the chairman of the VII Computational Electromagnetic in Time Domain workshop; in 2008 he was a member of the Steering Committee of the International Microwave Symposium (IMS) held in Atlanta; he was the guest editor of the special issue of the International Journal of Numerical Modelling on the VII CEM-TD; he was appointed as chairman of Sub Committee in the TPC of IMS Symposium. In the same year he was nominated as representative for Italy in the Management Committee of COST Action IC0803, RF/Microwave Communication Subsystems for Emerging Wireless Technologies (RFCSET) where he is currently operating as Work Group leader and as the responsible for Short Term Scientific Mission (STSM) selection. Again in 2008 he was the Co-PI (Principal Investigator) of the Project ADAHELI (project founded by the Italian Space Agency –ASI for the solar observation from the satellite and he has been nominated Director of the Scientific and Technology Committee of the Research center “Il Pisciello”. In 2009 he was nominated vice-chairman of the new MTT Technical Committee TC-24 “RFID-Technologies”

His research interests mainly focus on the design of high frequency electronic circuits and systems, including the development of numerical methods for electronic circuit analysis.

In these fields he has published more than 160 contributions to International reviews and peer reviewed conferences, the interest in which is testified by an ISI-HF index of 12.

Collision Resolution in ISO 18000-6c Passive RFID

Yuan Sun, Peter J. Hawrylak, Zhi-Hong Mao and Marlin H. Mickle

RFID Center of Excellence
Electrical and Computer Engineering Department
University of Pittsburgh

Abstract— According to the ISO 18000-6c passive RFID standard (EPCglobal Gen 2), in a tag intensive environment, when multiple tags receive the reader Query command and respond simultaneously, the reader may receive multiple responses giving what is termed a collision or a collision signal. This paper reports a method for resolving the two tag collision condition in real time thus not requiring any additional input by the reader. A reader has been designed using a National Instruments set of equipment which includes an FPGA-based software defined reader. The collision signal is obtained from the data acquisition system and processed by the FPGA in real time. This is a straightforward algorithm that can be implemented in silicon or programmed in a microprocessor to replace the current FPGA.

Index Terms— ISO18000-6c RFID, collision.

I. INTRODUCTION

Because passive RFID systems make use of the electromagnetic spectrum, they are relatively easy to jam using energy at the right frequency which occurs in a dense tag environment. Although this would only be an inconvenience for consumers in non critical situations (e.g. in stores with longer waits at the checkout), it could be disastrous in other environments, such as hospital emergency centers and in a military field of operation.

The collisions in UHF passive RFID communications lie in two major categories: the reader collision and the tag collision. Reader collisions occur in a reader intensive environment when the signals from two or more readers overlap in time and frequency. Tag collisions occur in a tag intensive environment when multiple tags are present in the transmitting field of the reader. In such situation, tags may respond to the reader Query command simultaneously causing the

reader to fail to decode the received signal, which is the result of collision.

This paper reports the ability to resolve the tag collision in order to improve the efficiency of ISO 18000-6c RFID systems [1]. Currently, to address the tag collision problem, multiple anti-collision protocols enabling the passive RFID tags to take turns in transmitting to a reader have been developed. Generally, there are two types of anti-collision protocols in common use based on time division multiple access (TDMA): One is the dynamic framed slotted Aloha, the other is the Binary Tree scheme [2]. ISO 18000-6c RFID systems use dynamic framed slotted Aloha. The dynamic framed slotted Aloha is a probabilistic method which can decrease the probability of collision occurrences significantly, but collisions cannot be completely avoided. Therefore, in the worst case when two or more tags in an inventory round randomly select the same time slot to respond (e.g. when the reader requests all tags to respond), the reader may receive an unrecognizable (un-decodable) mixture signal as a result of a collision. Accordingly, the reader read rates will be degraded due to this collision situation in the communication process. Therefore, it is intuitive to increase the system read rate more from pure collision avoidance by recovering the original tag signals from the collision at the reader. The philosophy of this concept is to resolve the collision after it occurs rather than trying to avoid it. It is also natural to combine the use of an anti-collision mechanism and the resolution of the collision to increase the efficiency of the reader-tag communication.

In addition, ISO 18000-6c passive RFID tags rely on limited energy harvested from the interrogator carrier wave rather than an internal power supply to perform logic functions and backscatter signals. Although this feature makes passive tags simple and inexpensive to deploy and maintain compared to active tags, the passive

RFID tags are subject to more critical communication timing constraints: A reader which fully conforms to the standard, must realize the tag inventory round including a three step handshake in order to make the tag transit into the data access states, which allows for tag memory access. The effective turn-around time between each of the three steps lies in the range of from 31.25 μ s in the worst case when the tag back link frequency (BLF) reaches 640kHz to 0.5ms in the best case when BLF is as low as 40kHz, which implies that the interrogator or any test platform conforming to the ISO 18000-6c standard must complete the signal decoding and command assembly in real time. If at least one of the tag responses can be separated and decoded in the standard specified time constraint, one inventory round including the three step handshake can be performed. Furthermore, if more than one tag response can be resolved from the collision, inventory rounds can be performed in parallel which leads to a dramatic increase in system read rates.

II. TECHNICAL BACKGROUND

A. Link Timing of ISO 18000-6c

The ISO 18000-6c standard specifies two categories of tag states: inventory states and memory access states. In order to access the memory content in the tag, a reader shall complete an inventory round to make the tag pass all the inventory states until entering the memory access state. The challenge lies in the fact that each step of the inventory round must be completed in a soft real-time, T (i.e. the Turn-around time between the tag response and the following reader command), which requires the reader to complete the decoding of the tag response and then send out the next command in the inventory round within this turnaround time. If any transition step in the inventory round fails to complete in time, T , the tag will transit back to the Ready state (the initial state after power up).

Corresponding to each state in the inventory round, there exists a three step handshake. At the first step of the handshake, the interrogator assembles and sends out a Query command; the tag chooses a random time slot to backscatter its 16-bit random number (RN16) after receiving a Query command, and then transits from the Arbitrate state to the Reply state. In the next step, the reader decodes the tag backscattered random

number and attaches it to the command header of an acknowledge command ACK, and then transmits the ACK command within the turn-around time, T . The tag receives this ACK command and responds with its ID (the tag PC and EPC number) including a 16-bit CRC code. The tag then transits into the Acknowledged state. At the last step, the interrogator receives the tag response and sends out a Req_RN command with the previous tag backscattered 16-bit random number and 16-bit CRC over the command within the same turn-around time T in Step 2 to notify the tag entering into the memory access state (Open or Secure state). The tag receives this Req_RN command and backscatters a Handle (a special 16-bit code).

B. Anti-Collision in ISO 18000-6c

To start an inventory round for the tags in the field, the reader needs to send a Query command as the first step. The anti-collision dynamic framed slotted Aloha algorithm is realized by specifying a value ranging from 0-15 to the 4-bit Q field in the Query command. Upon receiving the Query command, the matching tags pick a random number in $[0, 2^Q-1]$ to load into the slot counter. If a tag, in response to the Query command, loads its slot counter with zero initially or after counting down the original random number selected, it responds with a 16-bit random number (RN16). The tag collision occurs when multiple tags in the reader field load their slot counter with zero and thus respond to the Query command simultaneously. A form of collision control can be realized by specifying a large value for Q to reduce the probability of collisions, in the extreme case when Q equals 16 the probability for an N tag collision is $(1/65536)^{N-1}$.

C. ISO 18000-6c Tag Baseband Encoding

According to ISO 18000-6c standard [1], tags shall encode the backscattered data as either FM0 baseband or Miller modulation of a subcarrier at the data rate (BLF). The reader commands the encoding choice, and both FM0 and Miller are bi-phase space encoding. Fig. 1 shows the basis functions of FM0. FM0 inverts the baseband phase at each symbol boundary; a data-0 has an additional mid-symbol phase inversion. Fig. 2 shows the basis function of Miller encoding. Baseband Miller inverts its phase between two

data 0's in sequence. Baseband Miller also places a phase inversion in the middle of a data 1 symbol. When employing Miller encoding, the tag modulates a square wave shaped subcarrier by the Miller baseband. The Miller sequence contains exactly two, four or eight subcarrier cycles per bit [1].

Generally, the symbol of both FM0 and Miller can be categorized into formations as shown in Fig. 3. Formation 0 features an edge transition in the middle of the symbol, while there is no edge transition in the Formation 1 symbol.

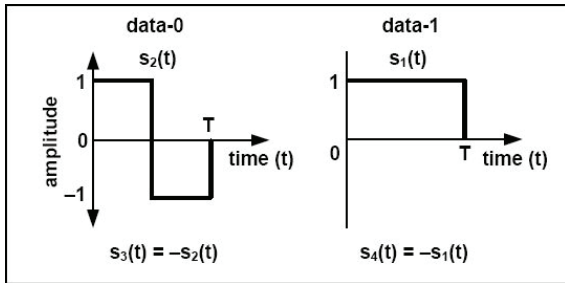


Fig. 1. FM0 baseband basis function

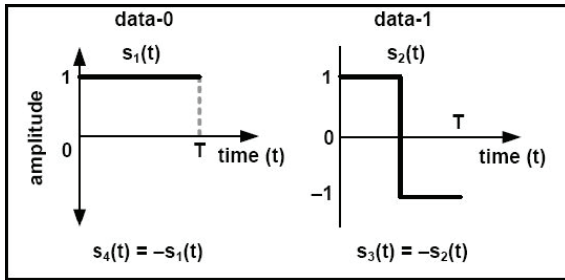


Fig. 2. Miller baseband basis function.

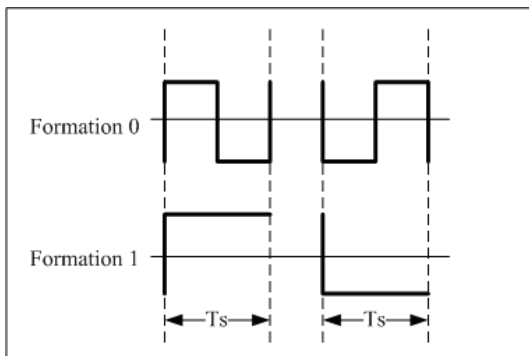


Fig. 3. Generalized tag baseband formation.

III. SOLUTION METHODOLOGY

The focus of this research is the resolution of the two tag collision situation. The collision can be forced for experimental purposes by letting the reader set the Q field in the Query command to a

value of zero, and the two tags will load 0 into their slot counters and respond with their 16-bit random numbers (RN16) simultaneously. The two tag responses are linearly superimposed forming the reader received baseband collision signal after the RF and IF down converting resulting from the superposition of the two symbol formations of either FM0 or Miller encoding as discussed in the last section. Due to the attenuation of different propagation paths and the fact that the Phase Locked Loop (PLL) in the reader receiver circuitry can only lock to one of the tag backscatter carrier waves or the reader transmitting carrier wave depending on the relative strength of the three signals, the downconverted two tag responses are normally different in magnitude. In addition, due to possible analog variations in the tag chip front ends (silicon), a phase shift (delay) exists between the two tag responses even when the two tags are from the same manufacturer. (Detailed analysis of the two tag collision waveform characteristics will be introduced later) Therefore, the resulting collision baseband signal violates the standard specified FM0 or Miller encoding, which causes the functional failure in the reader decode circuitry.

Without any collision resolution, the reader can only decode tags responding in different time slots, while two tags can share a common time slot provided their separate response can be recovered and extracted from the collision signal. For two tags in the field on a reader where $Q=4$, the probability of two tag responses colliding is $(1/16) \times (1/16)$. The probability of three tags colliding is $(1/16) \times (1/16) \times (1/16)$, which reduces the collision probability by more than an order of magnitude. Therefore, successful resolution of the two tag collision can significantly improve system data access efficiency.

As discussed in last section, the ISO 18000-6c standard mandates a real-time turnaround time specification. The collision resolution needs to be completed before this time out. Therefore, two strategies can be considered for the timing of the collision resolution as shown in Fig. 4. The first strategy starts the resolution after the complete acquisition of the collision, while the second strategy performs an on-line resolution one symbol after the other. The time available for collision resolution in the first strategy is less than the standard specified turnaround time because after

the resolution, the reader needs time to decode the recovered tag response. In comparison, the time available for the resolution equals the turnaround time plus the tag signal duration, and the reader can simultaneously decode the recovered symbols one by one. The second strategy is similar to “divide and conquer”, and thus saves processing time.

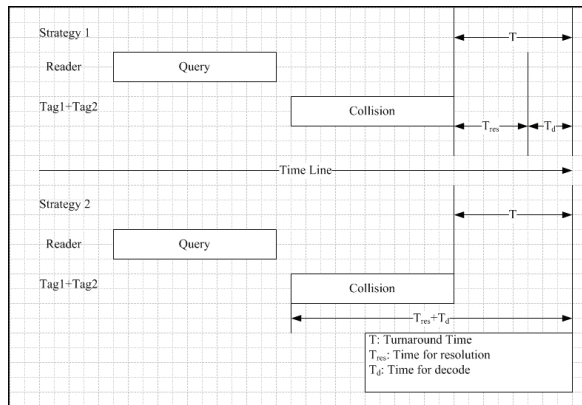


Fig. 4. Collision resolution timing strategy.

A. The Reader and Data Acquisition

An ISO 18000-6c RFID tag conformance test platform has been developed as a tool for this research. This platform is an ISO 18000-6c reader capable of, analyzing the acquired tag backscatter, and then checking the tag response baseband waveform against the standard. This platform serves as a data acquisition stage to obtain the tag response signal and the collision signal, which are the source signals in this research.

When selecting the hardware device for this platform, general purpose microprocessors and available commercial readers are both considered as candidates for ISO 18000-6c realization. General purpose microprocessors could be utilized to perform the communication, but they usually take multiple cycles to finish one instruction, and the total number of machine language instructions varies with the efficiency of user programming algorithms and the compilers. Therefore, they are difficult to time accurately and sometimes inefficient in communication timing control and thus not necessarily be the best device to be selected. Available commercial readers are alternative platforms, however their architectures are fixed at manufacture and most of those devices require users to familiarize themselves with the vendor specified command format in order to

manipulate the reader which burdens the user and degrades the RFID data access efficiency. In addition, there is no evidence that the commercial readers can provide convenient forward compatibility while the passive tags advance in technology. Upgrading those readers to support the new features of tags usually leads R&D costs if a hardware modification is required. Unlike microprocessors, FPGAs are timing accurate in their Hardware Description Language (HDL) programming. Compared to the fixed structure of commercial interrogators, a reconfigurable platform can be easily customized to perform in-depth functions. Therefore, in light of the defects of the possible solutions, it is intuitive to utilize the re-programmability of an FPGA baseband processor to build a flexible interrogator for ISO 18000-6c passive RFID tags to evaluate the proposed collision resolution algorithms. In addition, a fixed point on-line digital signal processing algorithm has been performed by the FPGA with satisfactory speed to provide signals of high quality and address the communication conflicts in a dense tag environment.

To these ends, an FPGA based software defined radio architecture is employed to implement ISO 18000-6c standard for the data conformance test platform. It features: 1) a real-time FPGA baseband, 2) a software controllable IF and RF front-end, and 3) a host PC based GUI control panel. The development tool set includes National Instruments (NI) LabVIEW 8.5 (for software programming and test front panel control), and LabVIEW FPGA module 8.5 (for FPGA baseband hardware programming). LabVIEW is distinctly suited for FPGA programming because it clearly represents parallelism and data flow. With the LabVIEW FPGA Module, custom measurement and control hardware requiring high-speed hardware reliability and tight determinism can be simulated and synthesized without low-level hardware description languages or board-level design. The LabVIEW compiler automatically translates the LabVIEW graphic code into low-level HDL code.

B. Platform Architecture

The reconfigurable software defined radio test platform consists of two major parts: The hardware, which includes the signal baseband, the intermediate frequency and the RF front end. The

software is running on a PC, which controls the hardware and analyzes the backscattered signal.

C. Platform Hardware

The architecture of the platform hardware connection is shown in Fig. 5. The 2-way signal flow includes the transmitter side and the receiver side. On the transmitter side, the software on the host PC selects and sends out the user specified command to the FPGA baseband. The baseband assembles the received binary command using PIE encoding according to the standard and then passes the data into the intermediate frequency band (IF). The IF stage consists of a DA9857 14-bit quadrature digital upconverter and a DA6654 14-bit downconverter. With the built-in Numerical Controlled Oscillator (NCO), the IF upconverter modulates the baseband data in DSB-ASK at the IF center frequency of 25MHz. The signal baseband (Xilinx Virtex-II Pro XC2VP30 FPGA) and the IF stage are together in the NI PCI-5640R Software-Defined Radio transceiver board. The 25MHz IF ASK signal is sent into the RF front end tuned to 915MHz for RF stage modulation. The RF front end consists of an NI 5610 RF upconverter and the NI5600 RF downconverter, which are connected by the NI PXI bus. On the receiver side, the tag backscattered signal passes through the 2-stage ASK demodulation in the RF and IF bands, and then enters into the baseband. For comparison purposes, an Agilent E4443A real time spectrum analyzer is employed as an auxiliary monitor of the RF communication process. The FPGA decodes the signal using FM0 or Miller encoding and sends the received signal as well as the decoded binary data back to the host PC for software offline analysis.

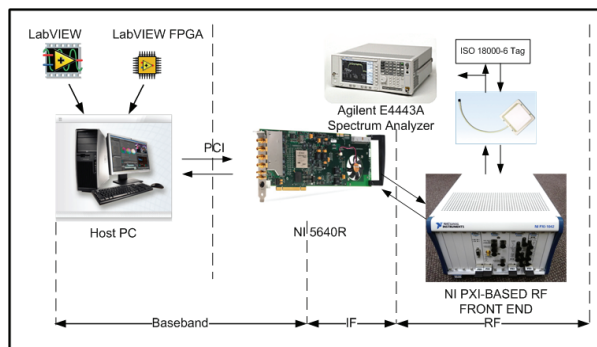


Fig. 5. Platform hardware architecture.

D. Platform Software

The platform software running on the host PC handles four major functions:

1. The test control panel: Using this panel, the user can select the command to send and set the command parameters. A set of the physical layer (PHY) features such as modulation depth, the length of Tari value, RTcal, and TRcal can be controlled by inputting values in corresponding text fields on the front panel. In addition, the IF and RF stage hardware are both conFig.d by specifying the expected center frequency, the output power level, and the sampling length/accuracy.

2. The signal analysis: The host PC software receives the demodulated baseband I/Q signals, and displays the RF envelope, I vs. Q waveform, the constellation diagram, and also calculates the spectrum.

3. The offline conformance check: The received RF envelope and calculated spectrum can be stored by the user optionally for offline conformance checking in a separate offline analysis module. The pulse width of the data stream and the integration of power in the specified bandwidth are checked against the standard.

4. The interface for remote control: By using the LabVIEW supported VISA interface, the host PC can be accessed by remote machines through the RS-232 (serial) connection or Ethernet connection in a Client-Server manner. This allows a remote terminal to send a command to the local host PC, which connects to the baseband and RF front end to perform the test.

IV. STANDARD REALIZATION AND DATA ACQUISITION

A. Standard Realization

The FPGA baseband realizes the logic function of an ISO 18000-6c conformed reader. The FPGA baseband consists of four parts to realize the ISO 18000-6c standard: the ASK modulator, the real-time DSP unit, the signal decode module for both the FM0 and the Miller encoded signal, and the processing unit for the previously mentioned three step real-time handshake.

On the transmitter side, the FPGA assembles the reader commands. It receives the binary

command from the host PC control panel, and then modulates the data stream using ASK after performing the encoding. The modulation of the ASK signal is shown in Fig. 13. The encoded data are sent into two separate quadrature channels – I and Q in the IF stage. The ASK modulation is realized by setting the magnitude multiplier in each channel as 1 when the incoming data bit is “1” in binary, and setting the multiplier as zero when the data bit is “0”. The DSB-ASK and SSB-ASK modulation manner can be selected by controlling the strobe of the Q channel.

However, the square wave shaped command bit stream generated by the FPGA contains a theoretically unlimited bandwidth. If it is passed into the IF upconverter without bandwidth limiting, the so called Gibbs phenomenon [7] occurs, resulting in significant over/under shoot at the data edges which degrades the output signal. The over/under shoots of the output command usually exceed the maximum tolerance specified in ISO 18000-6c standard and make the output command signal invalid for the tag in test. Therefore, real-time DSP work is necessary for guarantying the quality of generated interrogator signals. To eliminate the Gibbs phenomenon, a low pass filter is placed between the FPGA baseband and the IF stage in order to limit the bandwidth of the output baseband signals below the cut off frequency of the interpolation filter in IF upconverter. With the LabVIEW built-in Digital Filter Design (DFD) toolkit, the tap coefficients for an 8-order Bessel FIR low pass filter are generated and the magnitude/phase responses are displayed in Fig. 6.

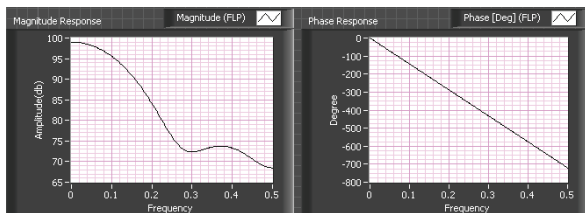


Fig. 6. FIR filter magnitude & phase responses.

As shown, the bandwidth of the baseband signal is limited to 30% of the sampling frequency, which is 10% below the cut-off frequency of the interpolation filter in the IF stage. The coefficients are selected to be symmetric to the center tap in order to ensure a linear phase response. Fig. 7 shows the realization

of the filter in the LabVIEW FPGA Module and the corresponding effect. Comparing the baseband outputs, it can be shown that the under/over shoots in command signals are significantly quenched after the smoothing.

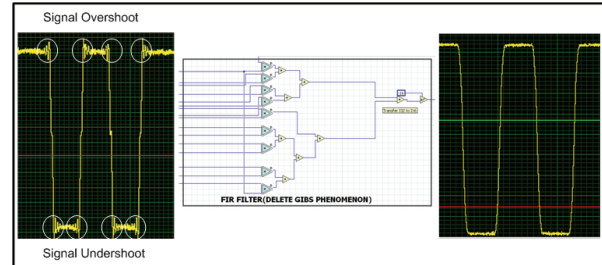


Fig. 7. Smoothing with an 8-order FIR filter.

On the receiver side, the FPGA baseband receives the IF demodulated tag backscattered signals and recovers the binary information in this FM0 or Miller encoded bit stream using a decode module. In the decode process, the clock recovery method is critical to accuracy. In light of the fact that the FM0 and Miller encoding are both self-clocking bi-phase codes, the decoding can be based on edge detection and pulse width measuring. In the decode module, the edge detector scans the data series, and sends out a notification signal as well as the distance between current and previous edges (i.e. the pulse widths) to the decode processor. The decode processor includes a 2-state Finite State Machine (FSM), which arbitrates the corresponding logic value for the data bit based on the inputs from the edge detector and the previous data bit.

The architecture of the handshake processing unit is shown in Fig. 8. In Step 1 of the three step handshake, the decode module notifies the decode module every time it detects an edge in the tag response. The decode module decodes the incoming tag response and sends out a handshake signal to the processing unit once the decode finishes for the tag backscattered random number. In Step 2, the decoded 16-bit binary random number is stored in the block memory in the FPGA and passed into an FIFO for command assembly. The ACK command header is sent into the same FIFO, and by doing this the random number gets attached to the header. The FIFO is connected to an optional delay module which allows for turn-around time adjustment. In Step 3, the assembly of the Req_RN command follows the

same procedure as in Step 2 except that the FIFO is also connected to a CRC16 generator for the CRC attachment. Handshake signals are also sent after the command assembly finishes in each step to notify the ASK modulator to modulate the assembled command for transmission. Fig. 9 shows the acquired sampling of the three step handshake.

The synthesis result of the platform provided by Xilinx XST shows that the design utilizes 86% of the total slices, 73% of the Block RAMs and 403 user I/Os among the total 556 I/O blocks of the Virtex-II Pro XC2VP30 FPGA. Consequently, the design takes reasonable advantage of the device resources.

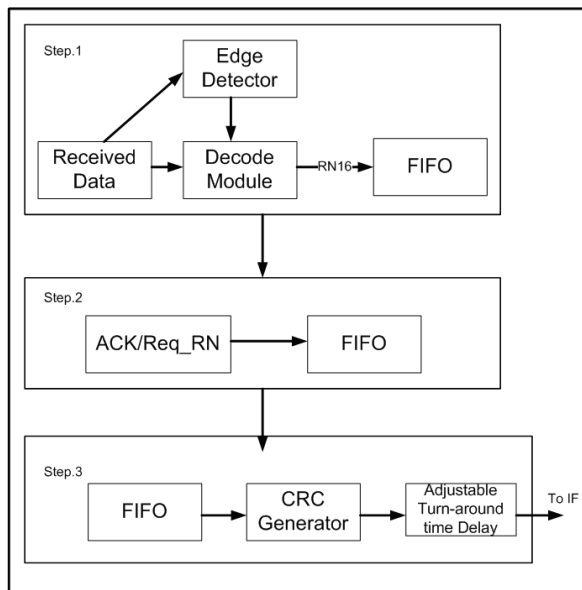


Fig. 8. Handshake processing unit.

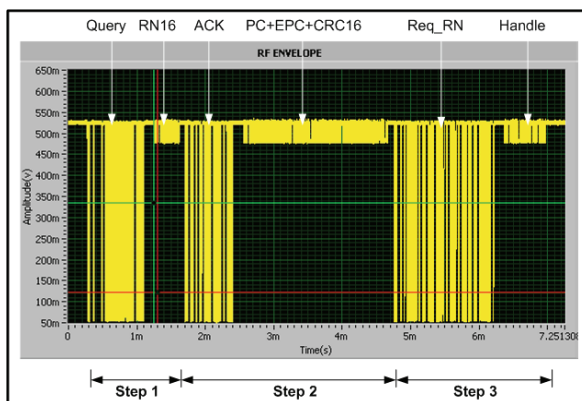


Fig. 9. Acquired inventory round.

B. Data Acquisition with the Platform

As introduced previously, the test stimulus reader command as well as hardware details can be configured by the LabVIEW Graphic User Interface (GUI) test control panel and the acquired tag response can be displayed by the signal analysis module.

In the test control panel, the user gets full control of the communication PHY and Media Access Control (MAC) configuration. The output power level and the center frequency of the RF front-end can be changed and reset by inputting the expected value in the corresponding number fields.

In addition, the center frequency of the IF stage and the ASK modulation depth can also be configured. The command Tari, TRcal, and RTcal value can be input by the user. In addition, the accuracy and length of the FPGA acquisition can be customized. The acquisition sampling rate varies from 2MHz to 25MHz (by default), which allows for a measurement resolution up to 0.04 μ s (25MHz sampling rate) in spacing between adjacent sampling points. The user can easily select the command type to send, and the corresponding pre-stored default command parameters are loaded into an editable combo box automatically. The command parameter in the command combo box can be changed if necessary to send out a customized command. Fig. 10 shows the test control panel. As shown, the RF front-end and the IF stage are tuned at 915MHz and 25MHz, separately; The Tari value is set as 25 μ s, the modulation depth is 90% and the sampling frequency is 25MHz; A Query command has been selected from the command menu, and its Q field is changed from "0000" to "0001". After clicking the "Send" button, the corresponding RF envelope of the reader command and tag response are captured by the platform hardware and displayed in the virtual oscilloscope. As shown, all the other ISO 18000-6c commands can be selected by the user from the combo box.

The waveform analysis module accepts the captured RF envelope and calculates the spectrum. The I vs. Q waveform as well as the constellation diagram are also generated from the acquired sampling data. The decoded message of the tag response is simultaneously displayed. Fig. 11 shows an excerpt of the front panel of the waveform analysis module. Accompanying the RF

envelope of the three step handshake are the decoded binary message for the RN16 after Query command, the PC+EPC+CRC after the ACK command and the Handle+CRC16 after the Req_RN command.

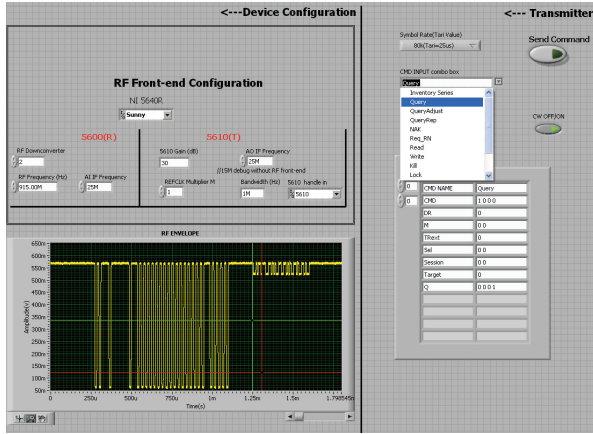


Fig. 10. Test control panel.

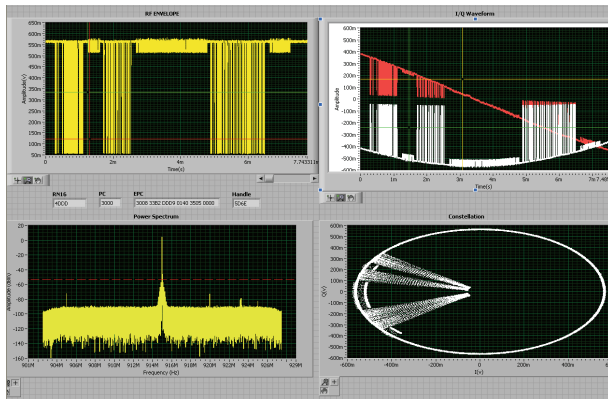


Fig. 11. Waveform analysis module.

V. TAG COLLISION ANALYSIS

Because this research focuses primarily on the resolution of two-tag collisions, the collision signal is generated from two tags from the same manufacturer in the transmitting field of the data acquisition platform as introduced previously. By configuring the command parameter, the platform sends out a Query command with its Q filed equaling zero, and thus forces the two tags in the field to respond their 16-bit random number simultaneously. The RF carrier wave frequency for the air interface is set at 915MHz, and the IF frequency of the interrogator/reader is set at 15MHz. At the receiver side, the collision signal is captured by the platform and then downconverted to the baseband signal, which is sent into the

FPGA. From the LabVIEW signal analysis module on the host PC, an acquired collision signal can be visualized as shown in Fig. 12.

Based on observation, the features of the collision signal can be summarized as follows:

The collision signal is the result of the linear superposition of tag responses, and the superposition follows a linear additive model as depicted in Fig. 13. A phase shift can also be observed in the collision signal, and the phase shift value is not fixed due to the tag BLF deviation. As can be seen, the initial phase shift is minimal, but it accumulates as the time increases.

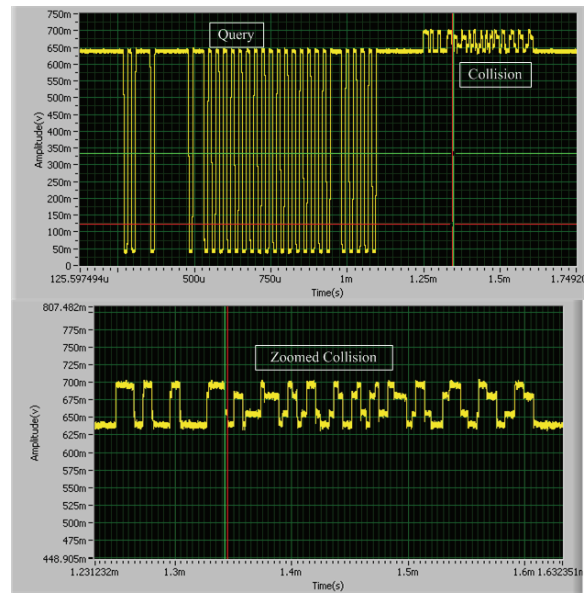


Fig. 12. Acquired collision signal.

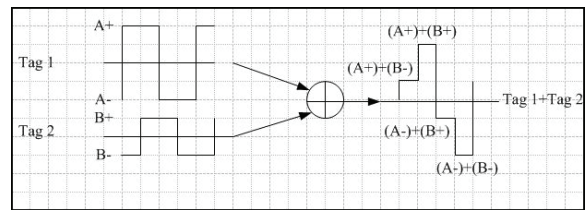


Fig. 13. Linear additive model of tag response.

The two tag responses received are likely different in magnitude. If the received two tag responses are with the same magnitude, only three possible voltage levels can be generated when they are linearly superimposed. Whereas, if they are different in magnitude, according to permutation, four possible voltage levels can be obtained from their linear superposition. The assumption is summarized in Table 2, in the left sub table, the

response of Tag 1 and Tag 2 are with the same magnitude of [A-, A+], while in the right sub table, Tag 1 is with a magnitude of [A-, A+], and Tag 2 is with a magnitude [B-, B+] (A≠B). This assumption is proven by locating the four different voltage levels in the observed collision signal. The amplitude difference in received tag responses are caused by two major facts. The first one is that the two tag responses propagate through different paths; they thus suffer from different path attenuations. The second fact is that the transmitting channel and the receiving channel of the data acquisition platform are combined by a circulator connected to one patch antenna as shown in Fig. 14. Because the transmitting power of the reader carrier wave is significantly larger than the power of the received tag response, the PLL in the RF receiving circuitry locks onto the phase of the transmitting carrier wave. In addition, due to the capacitor variation in each tag, the tags carrier waves are different in phase. Therefore, the received two tag responses suffer from different attenuation factors caused by the carrier wave being out of synchronization with the receiver's local oscillator (LO).

Table 1. Possible voltage levels in collision.

Tag1 Tag2	A+	A-		Tag1 Tag2	A+	A-
A+	(A+)+(A+)	0		B+	(A+)+(B+)	(A-)+(B+)
A-	0	(A-)+(A-)		B-	(A+)+(B-)	(A-)+(B-)

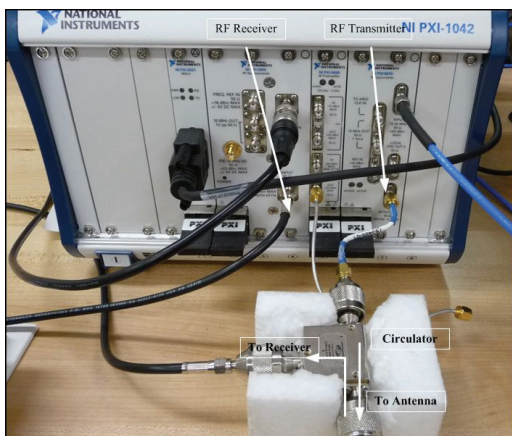


Fig. 14. RF front end connection with circulator.

The two tag responses are likely added together in the air with a phase shift (delay). The reason for this phase shift is due to two factors. First, because of physical variations of certain capacitors and antenna connections in forming the backscatter signal in each tag, the two tags respond to the reader with different speeds after receiving the Query command. In addition, the signal from each tag propagates along different paths, which are likely different in distance. The phase shift caused by the propagation path difference equals the quotient of path length difference divided by the speed of light. Because the range of passive RFID communication cannot exceed 10m normally, it is thus minimal and can be neglected in the current analysis. In sum, the observed phase shift (on average) in the collision signal is assumed to be due to the difference in the tag circuitry response characteristics.

The average phase shift is inversely proportional to the tag BLF, and cannot exceed 20% of the symbol duration. This conclusion is obtained by commanding the tags to respond at typical BLF and measuring the length of phase shift as shown in Table 3. The measurement is carried out when the two tags are placed 2.5 inches from the antenna. Table 3 lists the measurement results of the phase shift among 8 different tags from the same manufacturer. For each measurement, the tags are placed together with two in a group. The mean of the phase shift at each BLF as well as the phase shift percentage compared to the symbol duration are listed in Table 4. Figs. 15 and 16 show the data listed in Table 2 and Table 3.

In summary of the features of the collision signal, four voltage levels and a phase shift (observed as short edge transition) exist in the received collision baseband.

Table 2. Phase shift at typical tag BLF.

Measurement Number	1	2	3	4	5	6	7	8
BLF=64kHz	1.118µs	1.076µs	1.604µs	0.904µs	1.179µs	0.965µs	1.026µs	1.143µs
BLF=128kHz	0.719µs	0.573µs	0.813µs	0.53µs	0.844µs	0.639µs	0.524µs	0.862µs
BLF=256kHz	0.626µs	0.371µs	0.473µs	0.657µs	0.695µs	0.587µs	0.526µs	0.64µs
BLF=341kHz	0.206µs	0.243µs	0.301µs	0.586µs	0.527µs	0.498µs	0.276µs	0.507µs
BLF=682kHz	0.101µs	0.078µs	0.336µs	0.144µs	0.156µs	0.17µs	0.064µs	0.052µs

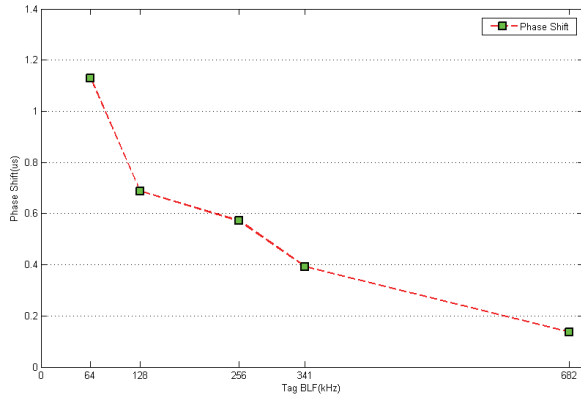


Fig. 15. Tag phase shift vs. BLF.

Table 3. Statistics of the phase shift.

	Mean(μs)	Symbol Duration(μs)	Percentage
BLF=64kHz	1.1296	15.625	7.23%
BLF=128kHz	0.6880	7.8125	8.81%
BLF=256kHz	0.5719	3.9100	14.63%
BLF=341kHz	0.3930	2.9300	13.41%
BLF=682kHz	0.1376	1.4600	9.42%

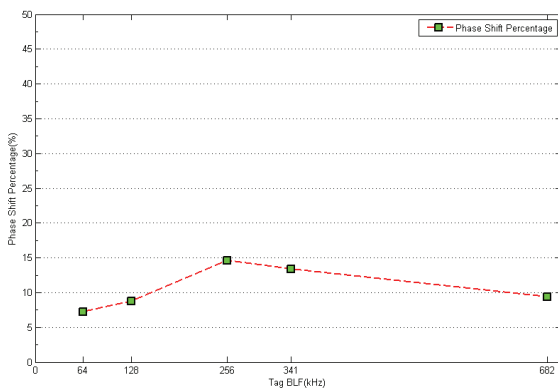


Fig. 16. Tag phase shift percentage in symbol duration vs. BLF.

VI. PROPOSED SOLUTIONS

A. The First Proposed Solution - Direct Edge Locating

Because a collision is the result of the linear superposition of each tag’s response, the formation of each tag’s response is invariant. In addition, because each tag’s response potentially arrives at the receiver side at different instants (i.e. the phase shift observed in the collision), the edge transition in each tag’s response is kept and not overlapped with each other (spaced by the phase shift). Fig. 17 illustrates the superposition of two formation-0 symbols, and the two edge transitions are maintained in the collision. Fig. 18 illustrates the superposition of two formation-1 symbols, there is

no edge transition in the collision because of the absence of edge transition in each individual tag response. Fig. 19 illustrates the superposition of one formation-0 symbol and one formation-1 symbol, only one edge transition can be observed in the collision. Therefore, although superimposed, the two tag’s responses can still be treated as being independent. Therefore, it is possible to recover the information of each tag by locating the edge transition in each symbol duration from the start of individual tag’s response. The prerequisite of this resolution method is to locate the exact position of each tag’s start in the collision signal, which will be discussed later.

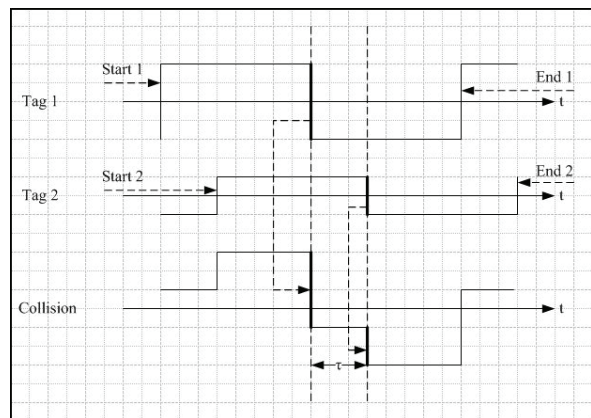


Fig. 17. Superposition of two formation-0 symbols.

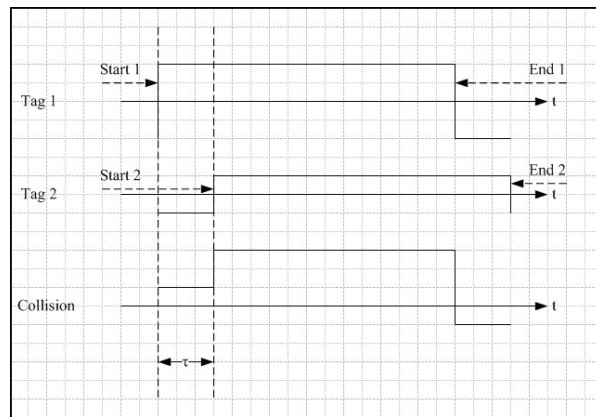


Fig. 18. Superposition of two formation-1 symbols.

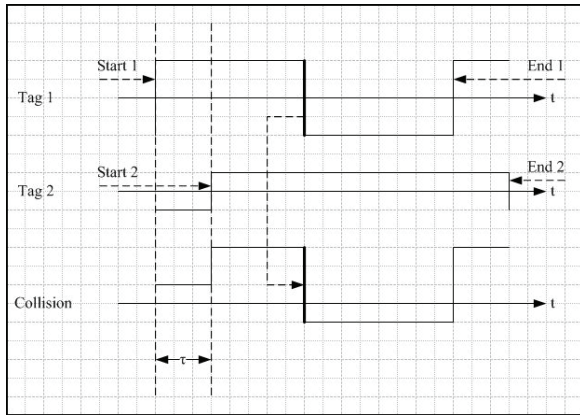


Fig. 19. Superposition of symbols.

1. Tag Response Frame Architecture

According to the ISO 18000-6c standard, when the tag responds to the reader, it shall precede its data with a preamble. Fig. 20 shows the preamble of the tag response when FM0 encoding is employed. In Fig. 21 the preamble of the tag response when FM0 encoding is employed. The parameter TRext decides whether a 12-zero pilot tone is used in the preamble. While two Tags respond the reader’s Query command with their individual RN16, the two RN16 numbers shall be preceded by the same preamble. This information can be utilized to locate the start edge of each tag’s RN16. Because once the formation of the preamble is fixed, the end of the preamble (i.e. the start of the RN16) can be located by counting to the edge number in the preamble from the start of the preamble. For example, in the FM0 encoding preamble as shown in Fig. 20, suppose no pilot tone is employed (TRext=0), there are eight edges in the preamble. The ending of the preamble can thus be located by counting 8 edges from the start edge of the preamble. In the collision signal, because the two tag responses are linearly superimposed with a phase shift, the ending of each preamble can be located by counting to the edge number in the preamble from the start of each preamble in the collision. Suppose the preamble contains N edges, the ending of the individual tag response are at the position of the (2N-1)th and the 2Nth edge in the collision signal. Fig. 22 shows an example of a collision signal consisting of two tag preambles in FM0 without pilot tone. Because each tag’s preamble has 8 edges, the ending of tag 1 and tag 2’s responses are at the 15th edge and 16th edge in the collision

signal. The ending location for Miller encoding is similar.

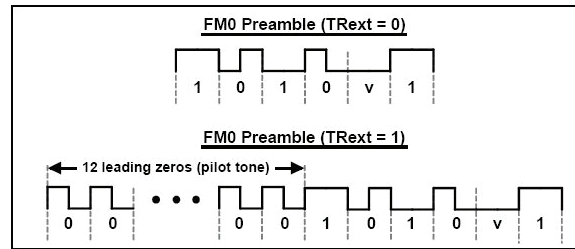


Fig. 20. Tag response preamble in FM0.

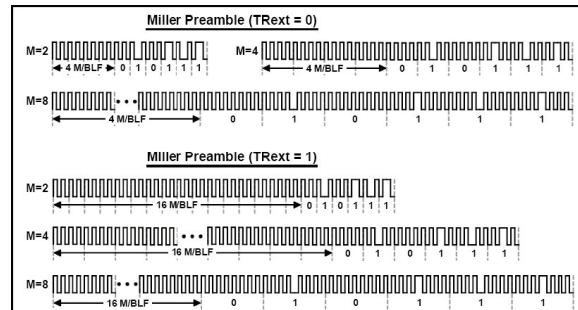


Fig. 21. Tag response preamble in Miller Subcarrier.

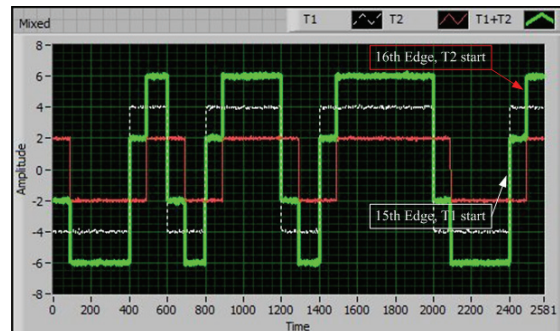


Fig. 22. Ending location of preambles in collision.

2. Algorithm Description

After locating the ending of the preamble (i.e. the starting of the RN16 in the tag responses), each bit in the RN16 of individual tag corresponding to one symbol duration can be recovered. The direct edge locating algorithm for two-tag RN16 collision resolution is listed in Table 4. This algorithm checks the collision signal one sample point at a time, and thus it is an online algorithm.

3. LabVIEW Simulation

The direct edge locating algorithm is simulated using LabVIEW on the Host PC. It is implemented by using a finite state machine (FSM) as shown in Fig. 23. The edge detector

detects each edge transition in the collision signal, and sends out handshake signals to the counter and the FSM once an edge is found. The counter records the number of the edges detected. A timer counts the elapsed time since the start of the RN16, and notifies the FSM once it reaches the middle of a symbol as specified in Table 4. The edge detector is implemented in two ways. The first method is based on calculating the running mean of the input signal as shown in Fig. 24. The edge detector keeps recording the running mean of the magnitude of the latest 5 signal sample points, and updates the average of the positive peak and the negative peak online. If the previous signal point is below the average while the current signal point is above the average, a rising edge is detected; the falling edges are found in a similar manner. The second method is to calculate the differentiation of the input signal. Because the edge is a singular point in the signal, the corresponding differentiation appears as a spike. The differentiation is calculated using Eq. 1. Because the edge transition time of the tag response normally takes no more than two sampling periods ($0.08\mu\text{s}$, 25MHz), the d_t is set as 1. Therefore, the differentiation actually equals the difference of the two adjacent sampling points in the signal. In the case when the tag edge transition takes more than two sampling periods, the edge in the collision signal corresponds to each rising edge of the obtained pulses in the differentiation Fig. 25 shows the preamble part of an FM0 collision and its corresponding differentiation.

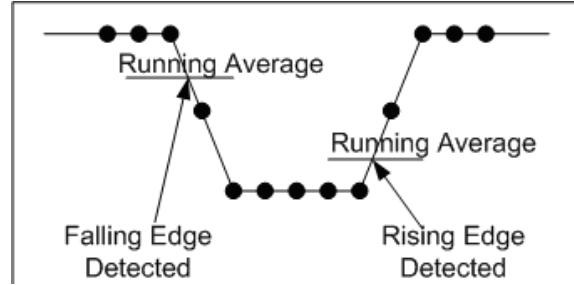


Fig. 24. The running mean calculation.

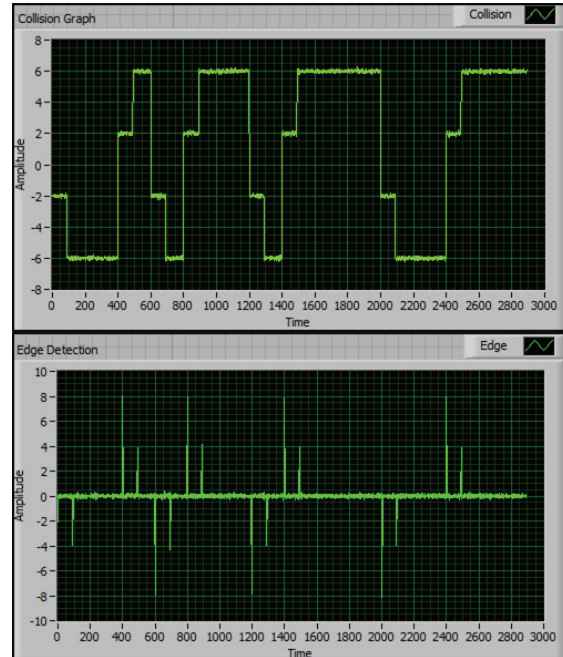


Fig. 25. The differentiation of collision signal.

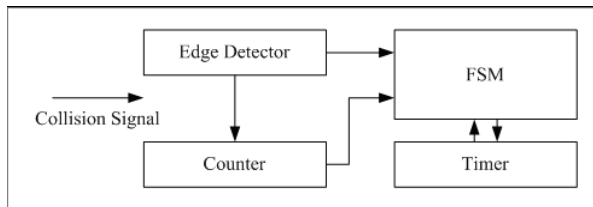


Fig. 23. FSM implementation of the algorithm.

$$\text{Differentiation} = \frac{y(t) - y(t - dt)}{dt} \quad (1)$$

Because the variation of symbol duration (BLF deviation) exists in the practical tag response, the middle symbol edge transition can appear in a range around the supposed $St+k \times T_s$ ($k=1, 3, 5, \dots, 31$) positions rather than exactly the middle of each symbol. Therefore, the FSM searches in a range around the middle of each symbol for the edge transition rather than at the exact middle position. The search range is of a length of 5% of the symbol duration centered at the middle of each symbol. Fig. 26 illustrates the searching range.

Table 4. Direct edge locating algorithm.

1. Locating the preamble ending edge of tag 1 and tag 2 separately in the collision signal, denoted as $St1$ and $St2$.
2. Start from $St1$, check the existence of edge transition at time instant $St1+k \times T_s$ ($k= 1, 3, 5, \dots, 31$), which corresponds to the middle of each symbol in tag 1's RN16 (where T_s is the symbol duration). If an edge transition is found at the specified position, the corresponding data bit in the RN16 is in formation 0. Otherwise, it is in formation 1.
3. Start from $St2$, check the existence of edge transition at time instant $St1+k \times T_s$ ($k= 1, 3, 5, \dots, 31$), which corresponds to the middle of each symbol in tag 2's RN16(where T_s is the symbol duration). If an edge transition is found at the specified position, the corresponding data bit in the RN16 is in formation 0. Otherwise, it is in formation 1.

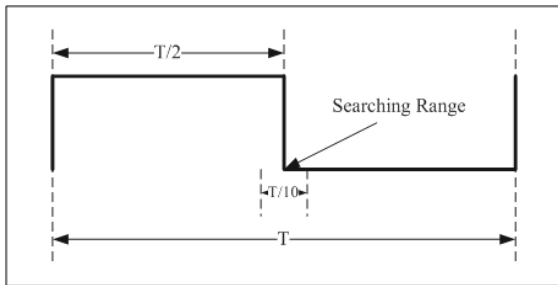


Fig. 26. Differentiation of a collision signal.

In the simulation, the symbol duration is set as 400 sample points, and the search range is thus 40 data points centered at the middle of each symbol. Two RN16 (8180h and 18FFh) encoded with FM0 are input to simulate the two tag responses separately. A Gaussian white noise with 5% of the signal strength is added to each tag response to simulate the channel noise. Fig. 27 shows the two tag responses with noise. Fig. 28 shows the collision signal and its corresponding differentiation showing the edges. The LEDs in Fig. 28 show the recovered data from the collision, the LED turned on corresponds to the formation 1 symbol while the LED turned off corresponds to the formation 0 symbol. As a comparison, the recovered data is exactly the input RN16s.

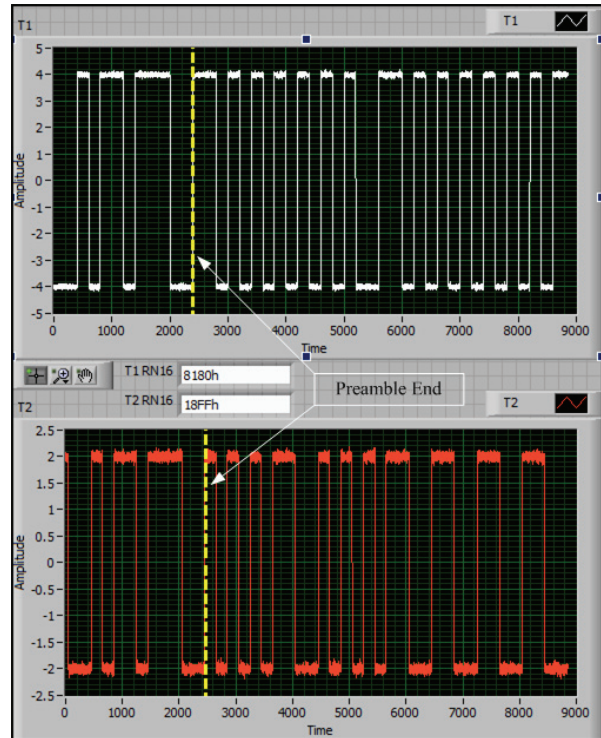


Fig. 27. Two simulated tag responses.

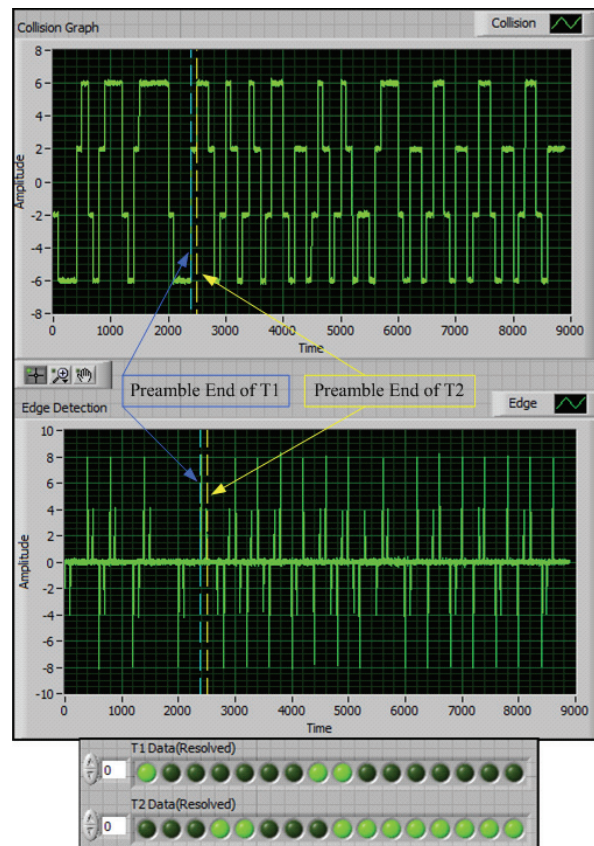


Fig. 28. Collision signal and differentiation.

There are two limitations of the algorithm:

First, as the BLF of tag increases, the phase delay decreases as shown previously, which requires the hardware timer to locate the searching range for each symbol more accurately. It is also possible that the searching range of the current symbol for each tag may overlap (as shown in Fig. 29), which requires the shrinking of the searching range.

Second, because of the variable phase shift caused by the BLF deviation, a self calibration function is required which searches for the ending edge of each data bit in the collision, and calibrates the algorithm FSM to the exact start point of the successive data bit symbol.

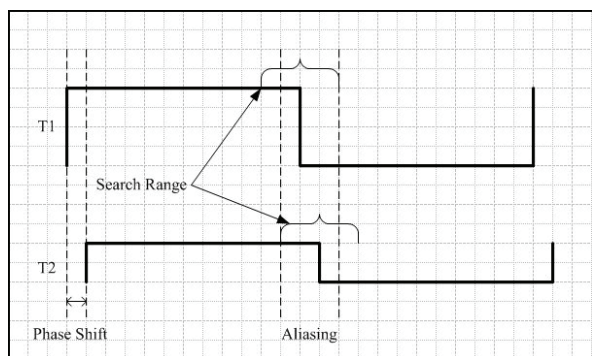


Fig. 29. Searching range overlap.

B. The Second Solution - Amplitude Mapping

As discussed previously, when the tag BLF increases, the phase shift between the two tag responses decreases. When the phase shift decreases to within the search range length, the direct edge locating method for collision resolution as described previously, does not apply because of the interference of the adjacent edge transition in each tag symbol. In the extreme case, when the phase shift shrinks to zero, an ambiguity as shown in Fig. 30 makes the direct edge locating method fail entirely when at least one tag has a formation 0 symbol appear. In Fig. 30, two tag symbols are linearly superimposed without phase shift. When one tag is responding a symbol in formation 0, while another is responding a symbol in formation 1, or when both of the tags are responding with formation 0 symbols, the observed edge transition in the middle of the symbol leads to the ambiguity when symbol arbitration. Because there is no phase shift and the

edge transitions in each tag response are completely overlapped, although an edge transition can be detected in the middle of the symbol, whether Tag 1 or Tag 2 is in transmitting formation 0 cannot be determined. However, in the case when both of the tags are transmitting formation 1 symbol, the original information can still be resolved from the collision because there is no edge transition in the middle of the symbol. Observed from Fig. 30, although all the ambiguity cases feature an edge transition in the middle of the symbol, they are different in the amplitude level positions. Therefore, it is intuitive to resolve the collision based on the relative position of the voltage levels.

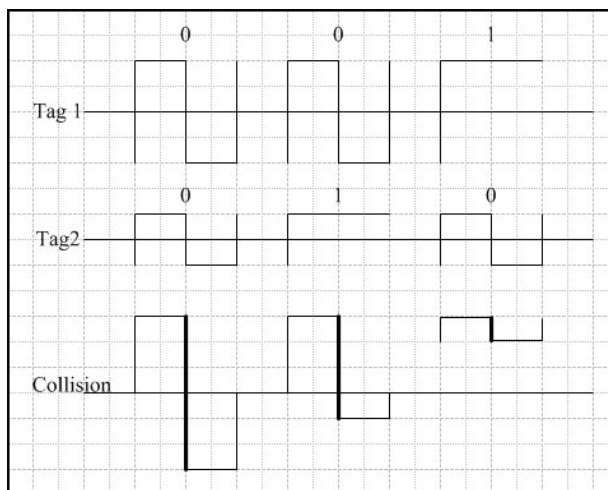


Fig. 30. Edge ambiguity.

Because there are two possible formation 0 symbols and two possible formation 1 symbols, each symbol in the tag response can have four possible shapes as shown in Fig. 31. Therefore, when the two tag responses are superimposed, there can be 16 possible shapes of the collision symbol as shown in Fig. 31. It is supposed that the amplitude of Tag 1's response is twice as the amplitude of Tag 2's response for illustration purpose. In Fig. 31, the amplitude of Tag 1's response is supposed to be twice as the amplitude of Tag 2's response for illustration purposes. The upper two portions (area 1 and area 2) correspond to the cases when both of the tag responses are same in formation, while the bottom two portions (area 3 and area 4) correspond to the cases when both of the tag responses are different in formation.

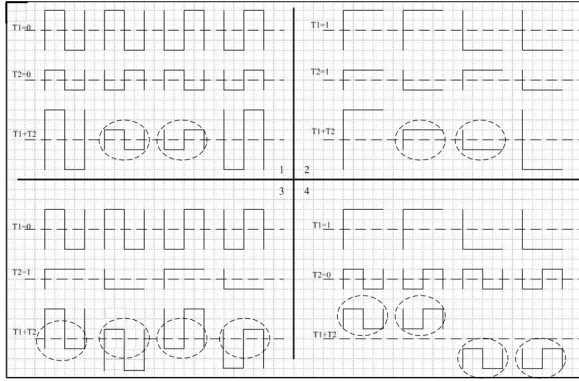


Fig. 31. Collision patterns.

The characteristics of the collision pattern can be summarized as following:

For the collision in area 1 ($T1=T2=0$): The collision signal is symmetric to the average line, and the first half symbol level and the second half symbol levels distribute at different sides of the average line.

For the collision in area 2 ($T1=T2=1$): There is no edge transition in the middle of the symbol, and the first half symbol level and the second half symbol levels distribute at the same side of the average line.

For the collision in area 3 ($T1=0, T2=1$): The collision signal is not symmetric to the average line, and the first half symbol level and the second half symbol levels distribute at different sides of the average line.

For the collision in area 4 ($T1=1, T2=0$): There is an edge transition in the middle of the symbol, and the first half symbol level and the second half symbol levels distribute at the same side of the average line.

As discussed earlier, there are four possible voltage levels in the collision signal. Because the tag responses are preceded by a common preamble, the maximum and the minimum voltage levels appear in the preamble part of the collision. The average line is calculated over the maximum and minimum voltage level. Except for the maximum and minimum voltage levels, the other two possible intermediate voltage levels, which are symmetrically distributed at the opposite side of the average line, appear when the voltage levels in the individual tag response with opposite polarization are superimposed as indicated by the circled cases in Fig. 31.

Figure 32 shows an example collision signal consisting of two tag responses in FM0 without a

phase shift. The RN16 in Tag 1 is 672Bh, and the RN16 in Tag 2 is A7CDh. To arbitrate the symmetry of the collision symbol to the average line, the average of the current symbol is compared to the average line of the collision. Two samples are taken at the first half and the second half of each collision symbol, and the symbol average is calculated as the difference of the two sample values divided by two. If the average of the current symbol voltage levels equals the collision average line, the symbol is symmetric to the average line.

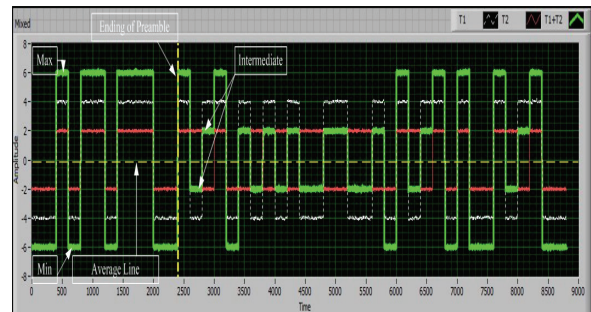


Fig. 32. Superposition of tag responses without phase shift.

1. Algorithm Description

Based on the characteristics of the collision symbol, the individual tag symbol can be resolved by scanning through the collision and mapping the collision signal to the cases as listed in Fig. 31. The algorithm is therefore named Amplitude Mapping and as listed in Table 5.

Table 5. Amplitude mapping algorithm.

1. Scan the duration of the preamble, and find the maximum/minimum value and the average line of the collision.
2. Beginning from the end of the preamble, check each symbol duration of the collided data. Calculate the average of each collide symbol.
3. Map the collided symbol to the cases as shown in Fig. 31 to decide the individual tag data.

2. LabVIEW Simulation

The amplitude mapping algorithm is simulated using LabVIEW on the Host PC. It is implemented by using a FSM as shown in Fig. 33. In each collision symbol, two sample points at 25% and

75% of the symbol duration are taken for the first half level and the second half voltage level separately as shown in Fig. 34. The timer counts the elapsed time since the start of the RN16, and notifies the FSM once it reaches the sampling points in each symbol. The comparator compares the voltage level of the sampling points in each symbol with the collision average line. A threshold is introduced in the comparator to get rid of the interference of the noise. The Arbitrator maps the collision symbols to the four cases according to the result of the comparator. In the simulation, the symbol duration is set as 400 data points, and the range for the comparator to neglect the interference of noise is set as 10% of the maximum amplitude of the collision signal. Two RN16 (672Bh and A7CDh) encoded with FM0 are input to simulate the two tag responses separately. A Gaussian white noise with 5% of the signal strength is added to each tag response to simulate the channel noise

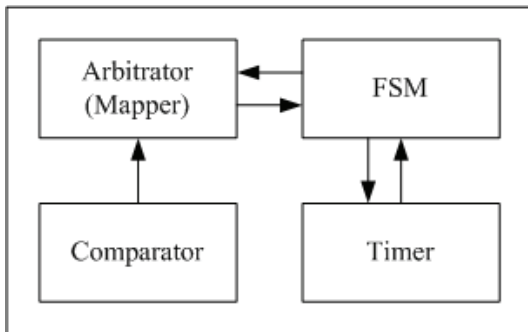


Fig. 33. FSM implementation of the algorithm.

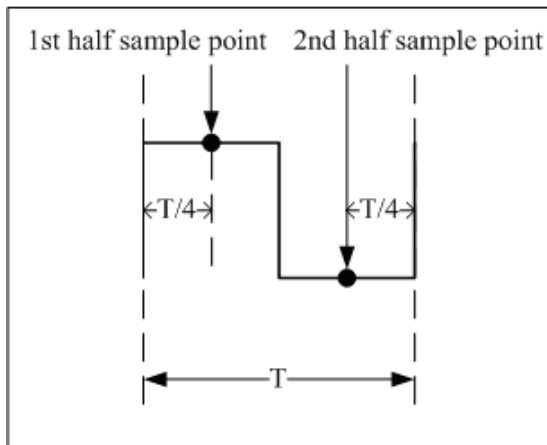


Fig. 34. Symbol sampling point.

Figure 35 shows the two tag responses with noise. Figure 36 shows the collision signal and

recovered data. The LEDs in Fig. 36 shows the recovered data from the collision, and the LED turned on corresponds to formation 1 symbol while the LED turned off corresponds to the formation 0 symbol. As a basis for comparison, the recovered data are exactly the input RN16s.

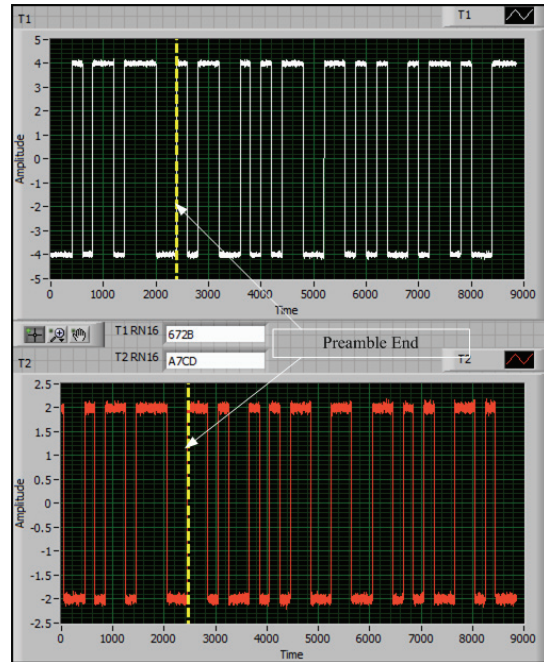


Fig. 35. Two simulated tag responses.

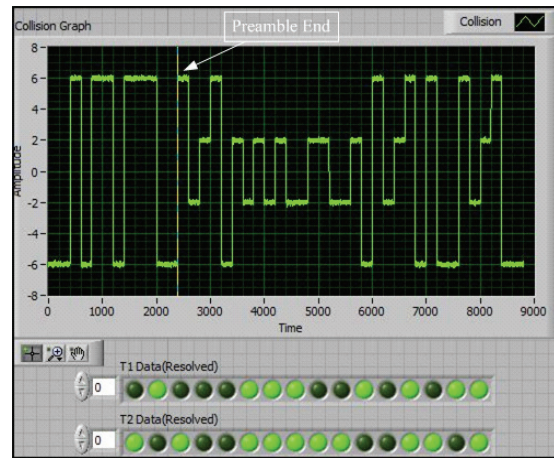


Fig. 36. Collision and resolved data.

VII. SOLUTION UNIFICATION

The solution to resolving the collision with phase shift and without shift can be unified by passing the collision signal with phase shift into a median filter. The median filter takes in N data points and outputs the median of the N data points. (N is the length of the median filter). The median

filter thus filters out the impulse in the collision signal caused by the phase shift and therefore transfers the collision with phase shift to the collision without phase shift, which can be resolved using amplitude mapping. The length of the median filter must be equal to or greater than the phase shift in order to filter out the phase shift caused impulse. In Fig. 37, a collision with phase shift of 5% symbol duration is filtered by a median filter with a length of 10% symbol duration. The impulses caused by the phase shift are circled, and in the filtered waveform they are removed.

One side benefit of the median filter is that it filters out some of the noise in the collision signal and improves the signal-to-noise ratio (SNR). As an illustration, the results of the two algorithms working on the same collision with phase shift are compared. In the simulation, the symbol duration is set 400 data points in length, and the phase shift is 20 data points (5% of T_s). The collision includes two RN16s (672Bh and A7CDh). Fig. 38 shows the resolution result. The resolution results of the two algorithms working on the same collision signal are the same.

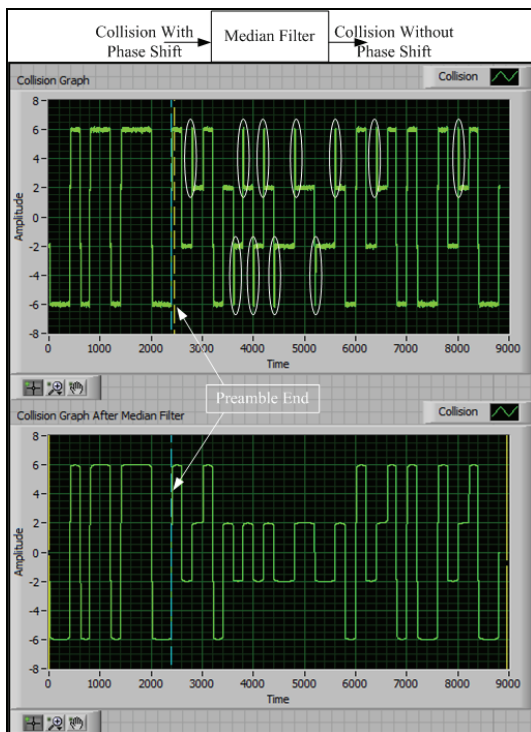


Fig. 37. The effect of median filter.

There is one limitation of the unification: the phase shift cannot exceed 25% of the symbol

duration. This is because when the phase shift exceeds 25% of the symbol duration, the impulse caused by the phase shift is greater in length than the voltage level used for amplitude mapping. Because the length of the median filter shall always be greater than the phase shift, the median filter filters out both the phase shift and part of the useful voltage level which happens to be in the shape of an impulse. Fig. 39 shows this limitation, as shown the filtered collision with a phase shift less than 25% of symbol duration(left) differentiate with the filtered collision with a phase shift of 25% of symbol duration(right). Fortunately, due to the feature of the collision signal as discussed previously, the phase shift cannot exceed 20% of the symbol duration at typical BLFs.

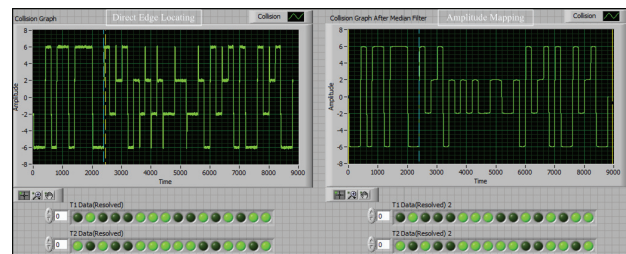


Fig. 38. Algorithm comparison.

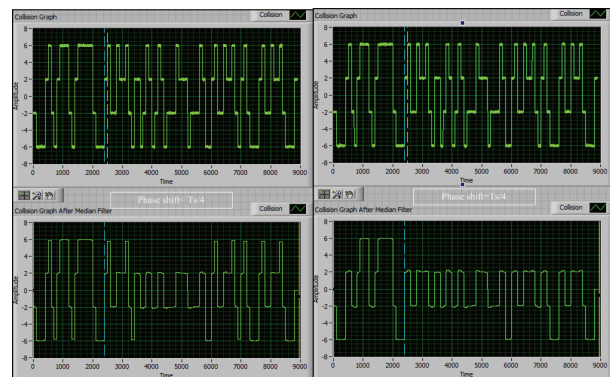


Fig. 39. The limitation of phase shift.

VIII. ALGORITHM HARDWARE IMPLEMENTATION

When simulated in LabVIEW on the host PC, both the direct edge locating algorithm and the amplitude mapping algorithm are developed and function on-line. The program reads in the collision signal and performs point-by-point processing on it. The benefit of this programming style is for a simple FPGA implementation. LabVIEW provides its FPGA compilation

environment in a LabVIEW FPGA module, which allows for direct translation of LabVIEW code into low-level HDL code. The floating-point numbers used in the host PC LabVIEW need to be transferred to fixed point numbers in LabVIEW FPGA module.

Because most of the computations involved in both algorithms are Boolean for the arbitration logic and counting for timer, the NI5640R FPGA baseband used in the data acquisition platform featuring a Xilinx Virtex-II Pro XC2VP30 FPGA is quite adequate. Two individual tag responses of typical BLF are acquired by the data acquisition platform and mixed to generate the collision signal as the test bench on Host PC. The typical BLFs are 64 kHz, 128 kHz, 256 kHz, 341 kHz and 682 kHz. Fig. 40 shows the implementation verification flow. The test bench signal is then streamed into the FPGA, and stored in the FPGA block memory for play back. The resolution result generated by the FPGA is streamed back to host PC for visualization and comparison with the original tag responses. The FPGA also generates a time stamp once it finishes the resolution, which shows the processing time. The processing time corresponding to each BLF is compared to the standard specified turnaround time to check the real time conformance of each algorithm as listed in Table 6. As shown, the implementation performs collision resolution within the required real time. Fig. 41 shows the front panel of the FPGA verification platform in LabVIEW.

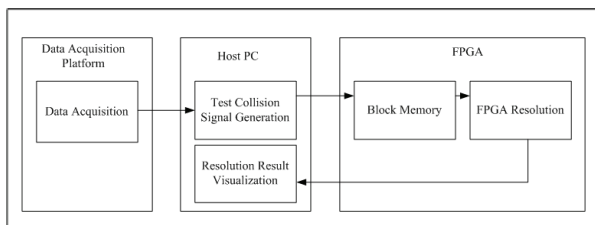


Fig. 40. Verification flow of the implementation.

Table 6. FPGA processing time of algorithms.

BLF(Hz)	Collision Length N	Processing Time(us)	Required Time(us)
64000	6256	241.96	261.4+312.5
128000	3120	121.68	124.8+156.25
256000	1568	60.92	62.72+78.125
341000	1168	46.04	46.72+62.5
682000	592	22.40	23.68+31.25

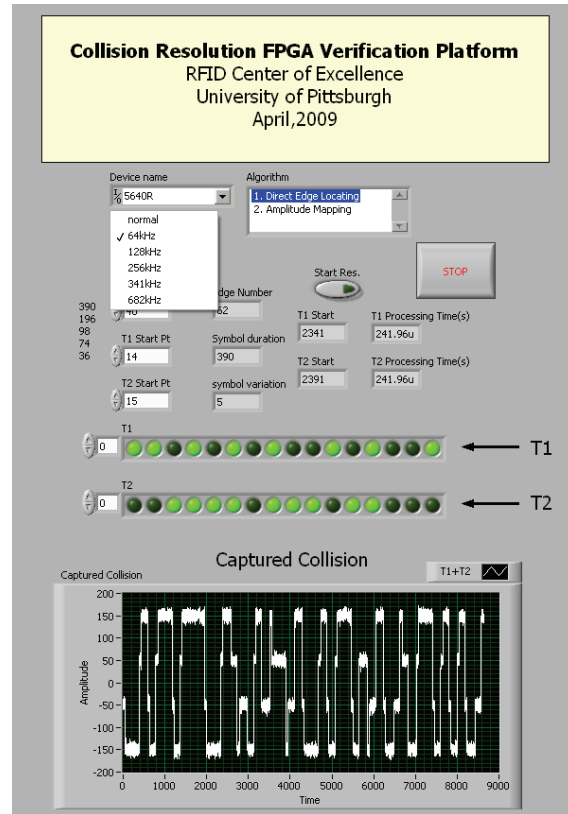


Fig. 41. Verification platform front panel.

IX. COLLISION OF MORE THAN 2 TAGS

A. Background

As discussed previously, direct edge locating can resolve two-tag collisions with phase shift, while amplitude mapping can deal with the collision without phase shift and the two methods can be unified by incorporating a median filter. However, using the direct edge locating method, as the phase shift decrease in length, the searching range of each symbol may alias and cause error; while with the unifying edge mapping method with the direct edge locating method, the phase shift cannot exceed or get close to 25% of the symbol duration, otherwise the useful edge information will be removed by the median filter. In addition, both methods require that the two tag responses are different in amplitude, which increases the probability of arbitration error when they are close in amplitude. Finally, both methods work only for two-tag collision resolution. When the number of tag collisions increases, more edge transitions may occur in one symbol duration, the probability of aliasing in the searching range

increases. The difficulty of direct edge locating will thus increase. Similarly, N^2 possible voltage levels can appear in one symbol duration for an N tag collision, which increases the logic for arbitration if using amplitude mapping. Therefore, it is intuitive to ask: is it possible to resolve multiple tag collision without the limitation of the two pre-proposed solutions?

B. Introduction to ICA

The multiple tag collision problem is similar to the "cocktail party problem", where a number of people are talking simultaneously in a room (like at a cocktail party), and one person is trying to follow one of the discussions. To resolve the collision, a Blind Source Separation (BSS) is required. BSS problems in digital signal processing are those in which several signals have been mixed together, and the objective is to find out what the original signals were. Independent Component Analysis (ICA) is one popular method for BSS. ICA is a statistical and computational technique for revealing hidden factors that underlie sets of random variables, measurements, or signals. ICA defines a generative model for the observed multivariate data, which is typically given as a large database of samples. In the model, the data variables are assumed to be linear or nonlinear mixtures of some unknown latent variables, and the mixing system is also unknown. The latent variables are assumed non-Gaussian and statistically independent as they are called the independent components of the observed data. These independent components, also called sources or factors, can be found using the ICA method. Highly successful new algorithms in ICA were introduced by several research groups, together with impressive demonstrations on problems like the cocktail-party effect, where the individual speech waveforms are found from their mixtures. ICA became one of the exciting new topics, both in the field of neural networks, especially unsupervised learning, and more generally in advanced statistics and signal processing. Reported real-world applications of ICA on biomedical signal processing, audio signal separation, telecommunications, fault diagnosis, feature extraction, financial time series analysis, and data mining are discussed in [8]. Because each tag's response with a reader command is

independent, and the statistical characteristics of the response signal are fixed and can be determined *a priori* large sample of responses, ICA can be a candidate for resolving multiple tag collisions.

ICA is a method for finding underlying factors or components from multivariate statistical data, and it looks for components that are both statistically independent, and with non-Gaussian distribution. Because the responses from each conflicting tag is a 16-bit random numbers and all the responses are driven by an independent clock signal on each tag, the reader actually receives conflicting tag responses which are statistically independent of each other. Because the baseband binary tag responses consists of only two separate logic values 0 and 1 (or +1 and -1), they are intrinsically super-Gaussian distributed characterized by two distinct peaks located near the two logic values in the probability density function (pdf) curve. Therefore, the conflicting signals satisfy both of the prerequisites of ICA. As in Eq. 2, the mixture can be represented as a vector X , where each vector variable corresponds to a received mixture; the source can be represented as a vector S , and where each vector variable corresponds to a source signal. The mixing matrix is represented as A . Assume the number of the conflicting tags (the size of the S vector in Eq. 2) is M , and the number of receiving channels (the size of the X vector in Eq. 2) is N , ICA requires that n shall be at least equal to M (i.e. There shall be no less captured/observed mixtures than the mixing sources). Therefore, in order to resolve M tag collisions, at least M receiving channels are required. If the number of the receiving channels is more than the number of conflicting tags, a preprocessing Principle Component Analysis (PCA) will be performed to extract N most significant components from the mixtures in order to make the mixing matrix A in Eq. 2 square (because only a square matrix has inverse). ICA is then performed to find the inverse of A (an N by M matrix) in an iterative manner until the algorithm converges.

$$X = AS \quad (2)$$

where $X = (x_1, x_2, \dots, x_m)'$, $S = (s_1, s_2, \dots, s_n)'$.

X. ALGORITHM DESCRIPTION

A. General

Various practical methods for employing the ICA model can be employed for the current application. Reference [8] lists several candidate methods including (1) the approach based on finding the maxima of non-Gaussianity, (2) the classic maximum likelihood estimation method, and (3) the method on minimizing the mutual information. According to [8], among the available methods, one approach based on minimizing Entropy of the collision signal in category (1) features medium computation load with reasonable separation quality. It is thus selected to be used in the ICA model for multiple tag collision resolution, which requires real time signal processing.

In information theory, Entropy H of a signal y (as described in Eq. 3) is a measure of non-Gaussianity. (Where, $P_y(y)$ is the pdf function of signal y .)

$$H(y) = - \int P_y(y) \log P_y(y) dy \quad (3)$$

According to information theory, a Gaussian signal has the largest Entropy among all random signals of equal variance. In probability theory, the central limit theorem (CLT) states conditions under which the sum of a sufficiently large number of independent random variables, each with finite mean and variance, will be approximately normally distributed [10]. According to the ICA model in Eq. 2, the mixture signal X (multiple tag collision signal) is the linear superposition of the source signal (the response of each tag), which implies that the distribution of the mixture signal approaches to normal distribution (more Gaussian) more than the source signals. Therefore, the ICA algorithm resolves the collision signal by minimizing its Entropy (Gaussianity), because once the source signals are recovered, they are with minimum Entropy compared to the collision signal. To obtain a measure of non-Gaussianity that is zero for a Gaussian variable and always nonnegative, a normalized version of differential entropy, called negentropy J as defined in Eq. 4 is used. (where y_{gauss} is a Gaussian random vector.) Negentropy is always nonnegative, and it is zero if and only if signal y has a Gaussian distribution.

$$J(y) = H(y_{\text{gauss}}) - H(y) \quad (4)$$

Although Entropy and Negentropy can be used to measure the Gaussianity, the integral in the calculation hinders computation efficiency. As an effective approximation, the Negentropy of a signal can be calculated without involving the integral as shown in Eq. 5. (Where G is a nonquadratic function):

$$J(y) \propto [E\{G(y)\} - E\{G(v)\}]^2 \quad (5)$$

Hyvärinen and Oja proposed a computation efficient algorithm FastICA [9] based on a fixed-point iteration scheme for finding a maximum of the non-Gaussianity of as measured in Eq. 5. The algorithm performs a Gaussian-Newton optimization when maximizing the Negentropy. Following Eq. 2, the source can be recovered from the collision signal X by left-multiplying the collision with a separating matrix W as shown in Eq. 6, which is the inverse of the mixing matrix X . Table 7 lists the FastICA algorithm using Negentropy maximization.

$$S = WX; \quad (6)$$

where $X = (x_1, x_2, \dots, x_n)'$, $S = (s_1, s_2, \dots, s_n)'$.

B. ICA simulation

The FastICA algorithm is simulated using LabVIEW on the Host PC. The G is selected according to Eq. 7.

$$G(u) = (1/3)u^3 \quad (7)$$

Figure 42 shows the two tag collision resolution simulation result using FastICA. Two RN16 numbers D2CCh (S_1) and 3D74h (S_2) are generated in FM0 encoding and mixed to simulate the two collisions (X_1 and X_2) captured by the two receiving channels as the upper-most waveform shows. The separated source signals from the collision are displayed in the middle and at the bottom. As shown, the recovered signals are clear enough compared to the original mixture for decoding, and they correspond to D2CCh (for recovered S_1) and 3D74h (for recovered S_2) exactly. The separating matrix W is also shown, and the result can be verified by multiplying the recovered S vector with the inverse of W , i.e.

mixing matrix A, and then comparing the products with the mixtures X (the top in Fig. 42). Because the formation of the tag response is similar to a simple bipolar square wave, the algorithm converges after only one iteration.

The FastICA as shown in Table 7 reads all the collision data points and performs the computation based on the expectation of data. This is similar to batch training rather than point-by point online training. There is the choice between on-line and batch algorithms. An on-line version of the algorithm can be obtained by substituting the expected value in the algorithm with instant data value. However, the on-line algorithm trades the accuracy for processing speed, and the algorithm may not converge well as the batch training algorithm. This problem can be alleviated by combinations of the two as shown in Fig. 43. Rather than performing the FastICA after completely receiving the collision signal, the “divide and conquer” architecture in Fig. 43 divides the collision signal into the preamble and each data bit in RN16 and then performs ICA on each section. The data portions of the collision are successively stored into a register file, and the W is successively updated: W_1 is updated based on W_0 , W_2 is updated based on W_1, \dots , etc, until the change between adjacent W becomes minimal. Once the W converges at a certain stage, ICA need not be performed thereafter, and the collisions before the converge stage are resolved by multiplying the converged W with the pre-stored data. Therefore, the computation load can be further decreased, and the resolution can be finished at the very end of the collision provided W converges before the collision end.

Table 7. FastICA algorithm.

- | |
|---|
| <ol style="list-style-type: none"> 1. Preprocessing the collision signal X by removing the mean 2. Whiten the data to Z, ($Z=(z_1, z_2, \dots, z_n)'$) 3. Initialize the w' vectors (each row) in the separating matrix W 4. $w = E\{Zg(w'Z)\} - E\{g'(w'Z)\}w$, where g is the first derivative of the G function in Eq.5. 5. Let $w = w/\ w\$ 6. If not converged. go back to step 4. |
|---|

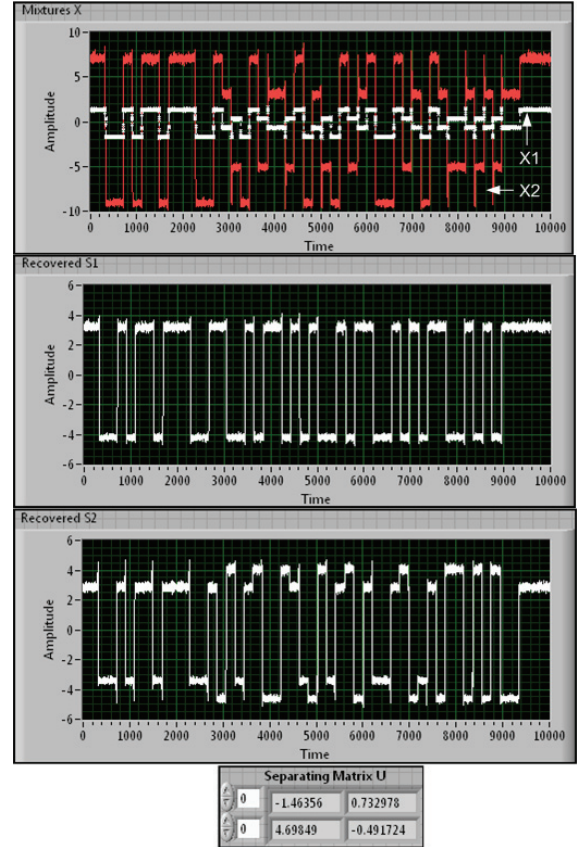


Fig. 42. ICA collision resolution result.

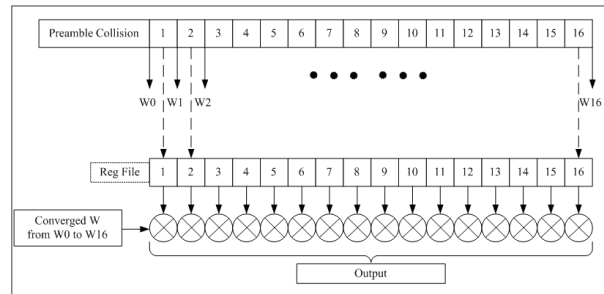


Fig. 43. Combination of batch training and online training of ICA.

XI. ICA IMPLEMENTATION

ICA treats each tag response as an independent component, and resolves the collision based on the statistical characteristics of signals rather than the phase shift information as in direct edge locating and amplitude mapping discussed earlier. Therefore, ICA performs the separation without the limitation of the previous solutions at the expense of higher computation load. The higher computation load tends to slow down of the resolution speed, which is critical in ISO 18000-6c

applications. This can be alleviated by incorporating any trade-off that can be made between the resolution accuracy and processing speed as discussed previously.

The computation load of ICA also increases linearly with the number of collided tag responses. Because the scope of this paper is limited to two-tag collision resolution, and the algorithm can be easily extended for multiple tag collision, ICA will be implemented for resolving two-tag collision for prototyping and function verification purpose.

A. Implementation Device Selection

The computation load of FastICA relates to two major parts: the update of the weight vector and the separation. Suppose the number of collided tags is two and using batch training, the computation to update weight is as shown in Eq. 8. Each function and parameter in Eq. 8 has been defined previously. Suppose the collision signal contains N data points, to calculate the first expectation in Eq. 8, it requires approximately $2N$ additions and $2N$ multiplications. To calculate the second item, it requires also approximately $2N$ additions and $2N$ multiplications. The resolution of one tag signal is shown in Eq. 9, which requires $2N$ multiplications and N additions. Therefore the total computation load for separate one tag signal from the collision of N data points is $6N$ multiplications and $5N$ additions, and it can be alleviated by using online training.

$$w = E\{Zg(w'Z)\} - E\{g'(w'Z)\}w \quad (8)$$

$$S_1 = w_1'Z \quad \text{and} \quad S_2 = w_2'Z. \quad (9)$$

Based on the analysis of the computation load, the Xilinx Virtex-5 ML506 Evaluation Platform has been selected. The development board features a XC5VSX50TFFG1136 FPGA, which is in 65nm technology and optimized for DSP and memory-intensive applications with low-power serial connectivity. It combines enhanced DSP blocks (DSP48E) for parallel processing, highest memory-to-logic ratio, and low-power serial transceivers for high I/O bandwidth. According to the Xilinx DSP48E specification [12], the multiplication speed of the target FPGA can reach 345MHz while the addition speed can reach 500MHz. Table 8 lists the expected ICA resolution speed for two tag collision resolution using the

target FPGA. Fig. 44 shows the corresponding speed at typical tag BLFs. As shown, the target FPGA can satisfy the standard specified real time limitation.

Table 8. Expected ICA speed using FPGA vs. maximum time allowed.

BLF(Hz)	Collision Length N	Processing Time(us)	Required Time(us)
64000	6256	171.36	312.5
128000	3120	85.46	156.25
256000	1568	42.95	78.125
341000	1168	31.99	62.5
682000	592	16.22	31.25

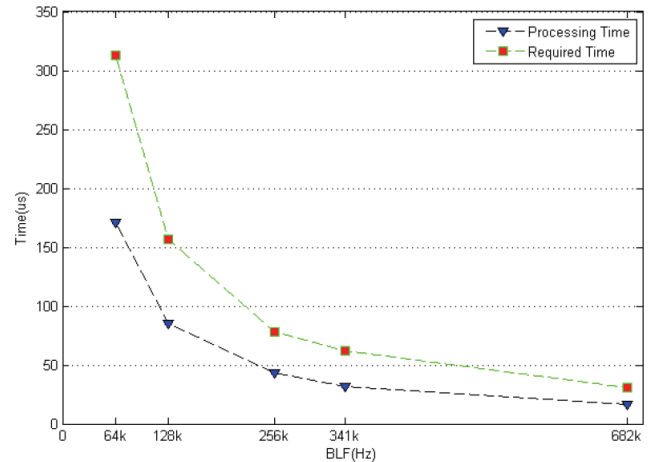


Fig. 44. Expected ICA speed using FPGA vs. required speed.

Matlab/Simulink +Xilinx System generator has been selected as the development tool chain. The FPGA design using the Xilinx System Generator is different from the typical HDL approach. Using the system generator, the FPGA is designed by first developing algorithm in Matlab/Simulink, and then the code is automatically compiled into HDL. This method can significantly reduce the hardware verification workload.

B. Experiment Setup

To resolve two-tag collision, two receiving channels are required. The experiment setup is shown in Fig. 45. Two National Instruments NI5600 RF downconverters are used as the two independent receiving channels. Collision responses of typical BLF will be acquired by the data acquisition platform. Batch training ICA and on-line training ICA will be implemented separately, and comparison on accuracy and processing speed will be reported.

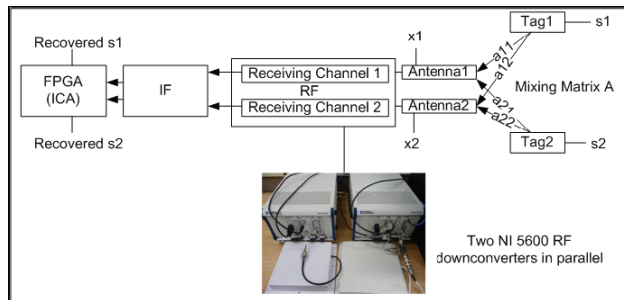


Fig. 45. ICA for two-tag collision resolution experiment configuration.

XII. SUMMARY

In this paper, the tag collision resolution into distinct readable information for ISO 18000-6c passive RFID communication has been accomplished. Two online resolution methods: direct edge locating and amplitude mapping for resolve two-tag collision has been presented. The edge locating method resolves the two-tag collision with phase shift, while the amplitude mapping method deals with the collision with very short or without phase shift. The two resolution methods are then unified by pre-processing the tag collision with a median filter. Corresponding simulations using LabVIEW on host PC were performed as preliminary work to verify the functionality of proposed algorithms. In addition, the limitation of each method is discussed separately.

To extend the resolution to multiple tag collisions, a statistic signal processing method using ICA has been introduced. The ICA method resolves two or more tag collision without the limitation of the direct edge locating and amplitude mapping at the expense of hardware cost for additional receiving channels and higher computation load. The ICA algorithm has been shown to work with both batch training and online training thus verifying the functionality.

REFERENCES

- [1] EPCglobal, "EPC Radio-Frequency Identity Protocols Class-1 Generation-2 UHF RFID Conformance Requirements V.1.0.2", <http://www.epcglobalinc.org>, 2005.
- [2] J. G. Lee, S.J. Hwang, and S. W. Kim, "Performance Study of Anti-collision Algorithms for EPC-C1 Gen2 RFID Protocol",

Proceeding of the International Conference on Information Networking, pp. 523-532, Jan. 2007.

- [3] "NI 5640R IF Transceiver User Guide," National Instruments, Austin, TX, <http://www.ni.com/pdf/manuals/374603a.pdf>, April 2007.
- [4] "NI PCI-5640R Specifications" National Instruments, Austin, TX, <http://www.ni.com/pdf/manuals/371620b.pdf>, April 2007.
- [5] "NI PXI-5670 RF Vector Signal Generator Hardware User Manual", National Instruments, Austin, TX, http://www.ni.com/pdf/manuals/rfsg_um.pdf, March 2006.
- [6] "NI 5660 RF Vector Signal Analyzer User Manual", National Instruments, Austin, TX, Aug.2004.<http://www.ni.com/pdf/manuals/371237d.pdf>.
- [7] L. Balmer, *Signals and Systems: An Introduction (2nd Edition)*, Prentice Hall, 1997.
- [8] A. Hyvärinen, J. Karhunen and E. Oja. *Independent Component Analysis*, John Wiley & Sons, 2001.
- [9] A. Hyvärinen and E. Oja., "A fast fixed-point algorithm for independent component analysis". *Neural Computation*, Vol. 9, No. 7, pp. 1483-1492, Oct. 1997.
- [10] J.A. Rice, *Mathematical Statistics and Data Analysis (Second edition)*, Duxbury Press, 1995.
- [11] P. J. Hawrylak, A. Ogirala, J. T. Cain, and M. H. Mickle. "Automated Test System for ISO 18000-7-Active RFID", *IEEE 2008 International conference on RFID*, pp. 9-18, 2008.
- [12] "Virtex-5 FPGA XtremeDSP Design Considerations", Xilinx, www.xilinx.com/support/documentation/user_guides/ug193.pdf, 2009.



Yuan Sun received his B.S. and M.S. in Electrical Engineering at Southeast University, Nanjing, China in 2004 and 2007, respectively. Currently, He is a Ph.D. candidate in Electrical Engineering and research

assistant with the RFID Center of Excellence at the University of Pittsburgh, USA. His research interests include ISO18000-6c UHF Passive RFID, high performance FPGA based digital design, embedded systems design, and network scheduling.



Peter J. Hawrylak received his B.S., in computer engineering, M.S. of electrical engineering, and Ph.D. of electrical engineering at the University of Pittsburgh, Pittsburgh, PA in 2002, 2004, and 2006 respectively. He is currently a research associate with the RFID Center of Excellence at the University of Pittsburgh, PA. His current research interests are in the areas of sensor networks, RFID, embedded system design, and system on a chip (SOC) design. Dr. Hawrylak is a member of the IEEE and IEEE Computer Society.



Zhi-Hong Mao received the dual Bachelor's degrees in automatic control and mathematics and the M.Eng. degree in intelligent control and pattern recognition from Tsinghua University, Beijing, China, in 1995 and 1998, respectively, the M.S. degree in aeronautics and astronautics from Massachusetts Institute of Technology (MIT) in 2000, and the Ph.D. degree in electrical and medical engineering from the Harvard-MIT Division of Health Sciences and Technology, Cambridge, MA, in 2005. He has been an Assistant Professor in the Department of Electrical and Computer Engineering and the Department of Bioengineering, University of Pittsburgh, Pittsburgh, PA, since 2005.



Marlin H. Mickle is Nickolas A. DeCecco Professor in Electrical and Computer Engineering (Primary), Professor of Computer Engineering, Telecommunications, and Industrial Engineering at the University of Pittsburgh. He is the Director of the RFID Center of Excellence. He received the B.S.E.E., M.S.E.E., and the Ph.D. University of Pittsburgh in 1961, 1963, and 1967. Marlin received the Carnegie Science Center Award for Excellence in Corporate Innovation - 2005; he has 21 patents and received the Pitt Innovator Award 2005, 2006, 2007 and 2008; 1988 Recipient of the Systems Research and Cybernetics Award of the IIASSRC, a member of the AIDC100, and he is a Life Fellow of the IEEE.

RFID-Network Planning by Particle Swarm Optimization

E. Di Giampaolo, F. Forni, and G. Marrocco

Dipartimento di Informatica Sistemi e Produzione,
Università di Roma 'Tor Vergata' via del Politecnico, 1 00133 Roma, Italy
digiampaolo@disp.uniroma2.it, forni@disp.uniroma2.it, marrocco@disp.uniroma2.it

Abstract— The design of an ad-hoc network of readers for RFID services in large areas may require the deployment of a significant number of interrogating antennas due to the limited range of reader-tag communication. For passive tags, the factors affecting the performance of the whole link depend on many physical and geometrical parameters. The reading region is not only related to the emitted power and the radiation patterns of reader/tag antennas, but also to the propagation environment. When a number of readers are planned in a network, mutual coverage of read-zones and mutual interference are generally undesired while safety regulation constraints have to be fulfilled in the whole area. This paper introduces simple models of the most relevant electromagnetic aspects involved in the network planning problem and considers an efficient solution based on the Particle Swarm Optimization algorithm. Numerical and experimental results show the effectiveness of the method.

Index Terms—RFID, network, propagation, Particle Swarm Optimization.

I. INTRODUCTION

Radio Frequency Identification (RFID) technology is going to be used in a number of applications involving automatic detection, location, tracking and/or identification of objects and/or people [1-4]. Passive Ultra-High Frequency (UHF: 880-960MHz) RFID technology is frequently preferred to other RFID variants due to its longer read range and low cost [5]. A basic UHF passive RFID consists of a reader (i.e. a radio-scanner unit) and a number of remote transponders called tags which extract their operating power from the reader signal. Due to the limited interrogation region of readers, large-scale RFID deployments often need multiple transmitters [6-7] properly placed to

cover the entire region of interest. The planning of RFID networks, however, has to comply with the possible overlapping among interrogation regions of different antennas. This effect could be a useful redundancy in some applications (localizations) or has to be instead avoided in others (inventory) since it worsens the efficiency of the coverage and produces undesired multiple readings of a same tag.

Focusing on the latter case, the planning of RFID networks is aimed to maximize the overall read region so that tags can be read anywhere within a given environment [8], while the overlapping regions are minimized. The goal of the planning is fulfilled using the minimum number of antennas in order to reduce the cost and the complexity of the network. The locations of readers' antennas is a degree of freedom of the planning process, but also the emitted power and the orientation angle of reader antennas can be exploited.

The read region of the single reader depends on the power emitted, which is upper-bounded by the regional regulations, on the tag sensitivity over the considered objects [9] and on the orientation of the antennas [10], but it is also affected by the electromagnetic scattering from the nearby scenario [11].

The planning of RFID network moves away from the planning paradigm of other wireless networks. The down-link (reader-to-tag) is in fact subjected to the severe power threshold of the tag's microchip while the up-link (tag-to-reader), being based on backscattering, involves small power levels. Line of sight between reader antenna and tag antenna is preferred since non-line of sight communications are frequently not possible owing to the poor link-budget or because it is not useful for the particular application (as in the case of localization). The deployment of network antennas can be made almost everywhere in the environment: for instance, in indoor environments reader antennas can be placed on ceiling, floor and walls but also

some furniture structures like shelves and tables can be used to host them. Thus the structure of the network is strictly related to the topography of the environment.

Planning procedures have to include fast electromagnetic tools able to handle the propagation phenomenology with a reasonable accuracy. Although a very reliable prediction of the read region is now affordable by using the state of the art electromagnetic ray tracers [12], their extensive application to this planning problem however is revealed to be time consuming. Closed-form propagation estimation, retaining the complexity of the free-space formula, is instead preferred.

The planning method, here proposed, involves a model that simplifies the electromagnetic calculations taking into account all (or most of) the system parameters of the reader-tag-environment system including the power/exposure constraints in the UHF range. The model encodes all the electromagnetic parameters into geometrical parameters, such as distance and shape, transforming the electromagnetic problem into a geometrical problem. The interrogation region is approximated by an ellipsoid, embedding the most significant effect of the environment, and hence a number of ellipsoids have to be placed into the environment in order to achieve a uniform coverage with minimum overlapping. The so formulated RFID network planning resembles a *packing problem* in Management, Computer Science, Operations Research [13], and is here handled by the Particle Swarm Optimization (PSO) algorithm. The proposed approach, useful for both indoor and outdoor scenarios is demonstrated by some numerical examples and by experimental evaluations.

II. PLANNING PROBLEM

The aim of the planning is to guarantee the reading of a tag at points of an environment Ω using a suitable deployment of a set of reader antennas $\{R_j\}$. Since each reader's antenna has a limited interrogation region (i.e. the region where the radiated power is higher than that necessary to activate the microchip of a tag), only the union of the interrogation regions of many antennas (Fig. 1) permits to cover large environments. If Ω_j is the interrogation region of R_j antenna, the whole interrogation region is

$\Omega_I = \bigcup_{j=1}^N \Omega_j$ where N is the number of antennas in the environment. This is a constrained optimization problem where constraints concern the maximum value of EIRP (upper-bounded by regional safety regulations or by other requirements), the maximum number of possible antennas N which represent an upper limit to the cost of the network, the permitted position of the antennas, and finally the maximum field strength admitted in man-populated regions of the environment, as required by the exposure limitations.

The RFID planning problem is formulated through the definition of three sets of *control points* for the readers' position, the coverage and the safety issues. The allowed position for the readers $\{L_R\}$ depends on the specific environment and on other engineering constraints. The read test points $\{L_T\}$ are introduced to quantify the read region's size corresponding to a particular network topology and emitted power. The $\{L_T\}$ are dislocated, with a rule depending on the particular finalization of the network, with the convention that each L_T belongs to the read region provided that the field strength at that point is enough to activate the tag's microchip. Finally the *safety test points* $\{L_S\}$ are assigned to check if the radiated electric field, at places populated by persons, exceeds the threshold of the regional safety regulations.

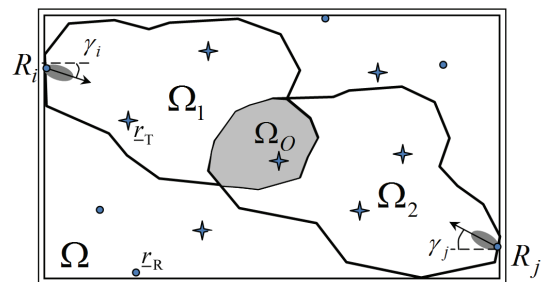


Fig. 1. Scheme of the optimization problem.

Ω region to be uniformly covered, Ω_i interrogation regions of the i th antenna R_i with tilt angle γ_i . Ω_0 is overlapping between two reading region. Dots and stars represent the allowed position of the readers and the read test point, respectively.

The extension of the interrogation region of an antenna depends on the amount of radiated power. In free-space the interrogation region is a

scaled volume of the radiation pattern of the antenna but in presence of an obstacle it is shaped by the scattering phenomena. In particular, in an indoor environment where many scattered fields contribute to the power received by the microchip, this region is not completely uniform i.e. not a path-connected space, showing jagged zones due to the interference fringes of different contributions. But jagged zones are not useful to quantify the extension of the read region because a variation of a few centimetres in the tag's position could cause an intermittent and unreliable response. Hence network evaluation has to consider a reduced path-connected subset of the interrogation region. A suitable fast electromagnetic model will be introduced in Section IV to give a simple representation of such a region by handy geometrical shapes.

The solution of the planning problem is cast as a constrained optimization aimed to maximize the following *fitness function*:

$$F = w_{COV} f_{COV} + w_{OV} f_{OV} + w_{EIRP} f_{EIRP} + w_{COST} f_{COST} + w_{SAF} f_{SAF} \quad (1)$$

where $w_{(\cdot)}$ are suitable weights ($\sum w_{(\cdot)} = 1$).

The individual contributes of F are defined as follows:

$$f_{COV} = \frac{|\{\underline{L}_R \in \Omega_I\}|}{|\{\underline{L}_R\}|} \quad (2)$$

$$f_{OV} = \frac{1}{1 + |\{\underline{L}_R \in \Omega_O\}|} \quad (3)$$

$$f_{EIRP} = \frac{1}{1 + \overline{EIRP}} \quad (4)$$

$$f_{COST} = \frac{N_{max} - N}{N_{max}} \quad (5)$$

$$f_{SAF} = \frac{1}{1 + |\{\underline{L}_S : E_T(\underline{L}_S) > E_O\}|} \quad (6)$$

where $|\{\cdot\}|$ indicates the cardinality of the included set. f_{COV} is the coverage efficiency, calculated as the number of read test points $\{\underline{L}_T\}$ included in the whole interrogation region; f_{OV} refers to the overall overlapping $\Omega_O = \bigcup_{i=1}^N (\Omega_i \cap \Omega_j)_{i \neq j}$ among all the interrogation regions; f_{EIRP} is a measure of the total power radiated by the readers' network;

$\overline{EIRP} = \frac{1}{N} \sum_{i=1}^N EIRP_i$; f_{COST} is related to the cost of

the network, e.g. it gives a measure of the readers' saving with respect to a given maximum number N_{max} ; f_{SAF} is finally an indicator of the number of safety points exposed to a total electric field E_T exceeding the limit E_O .

III. OPTIMIZATION PROCEDURE

The result of the optimization is the position (3 parameters), orientation (2 parameters), number (1 parameter), and emitted power of each allocated reader's antenna. The dimension of the problem may be huge and hence non deterministic (evolutionary) optimization algorithms are preferred to deterministic tools. The Particle Swarm Optimization (PSO) algorithm [14-15] is here applied to maximize the fitness function in (1).

PSO is a population-based method that iteratively searches the solutions space by means of a number of candidate solutions called particles. The set of particles is called a swarm. Each particle flies through the solutions space following deterministic and stochastic rules to update its position and is rated by the fitness function. At each iteration a particle takes memory of the position where it discovered the best value of the fitness function. This value is called personal best (*pbest*) solution, while the best solution among all the particles is called the global best (*gbest*). Both *pbest* and *gbest* affect the velocity and position of each particle following the update equations

$$\begin{aligned} v_{n+1} &= wv_n + c_1\rho_1(x_{pbest} - x_n) + c_2\rho_2(x_{gbest} - x_n) \\ x_{n+1} &= x_n + v_{n+1} \end{aligned} \quad (7)$$

where n is the iteration number, x and v are the position and velocity of the particle, respectively, ρ_1 and ρ_2 are random numbers uniformly distributed in (0,1), c_1 and c_2 are weighting factors while w is an inertia weight which affects the velocity of the previous iteration.

Suitable boundary conditions are required to handle particles that reach the boundary of solutions space. Here the so called invisible walls boundary conditions [14] are used together with local-best swarm topology [15].

The PSO updates the particles by means of (6) until one of the following exit condition is reached: (i) the current solution fulfils the user-defined acceptance criterion, (ii) the number of iterations exceeds a specified value, (iii) velocity updates are close to zero.

IV. FAST EVALUATION OF THE FITNESS FUNCTION

The application of the PSO requires the fitness function in (1) to be evaluated thousands of times for each particles of the swarm and for each iteration of the search. A fast but sufficiently accurate electromagnetic model is here introduced to this purpose.

The reader can be characterized by the input power P_{in} and by the radiation vector $\underline{f}_R(\theta, \phi)$ of its antenna. The field at any point of a real environment Ω , including walls or generally scattering objects, can be obtained by application of a field projector P_Ω to the reader's pattern:

$$\underline{E}(x) = \sqrt{\frac{Z_0 P_{in} G_R(\theta, \phi)}{2\pi}} P_\Omega \circ [\underline{f}_R](\theta, \phi) \quad (8)$$

where

$\hat{\underline{f}}_R(\theta, \phi) = \underline{f}_R(\theta, \phi) / |\underline{f}_R(\theta, \phi)|$ is the normalized radiation vector and G_R is the antenna gain. In case of free-space the field projector is

$$P_\Omega \circ [\hat{\underline{f}}_R](\theta, \phi) = \frac{e^{-jk_0 r}}{r} \hat{\underline{f}}_R(\theta, \phi) \quad (9)$$

The power collected by the tag's microchip is

$$P_{R \rightarrow T} = \chi \frac{\lambda^2}{(4\pi)^2} |P_\Omega \circ \hat{\underline{f}}_R|^2 P_{in} G_R(\theta, \phi) G_T(\theta, \phi) \tau \quad (10)$$

where $G_T(\theta, \phi)$ is the tag gain and χ is the polarization mismatch between the tag antenna and the incoming field. Typically, the reader emits a circular-polarized field while the tag is a linear polarized antenna and hence $\chi=0.5$ in the free space. In a complex environment the field undergoes a depolarization, but for the sake of simplicity, the average $\chi=0.5$ value is still assumed. The application of the field projector P_Ω to the reader's pattern yields the field at tag location taking account of specific propagation phenomena that could involve reflections and diffractions from walls and generally scattering objects. The *power transmission coefficient* τ

finally accounts for the impedance mismatch between tag antenna and microchip.

The power required to the tag microchip to wake up, p_C is its sensitivity, then the tag is activated when $P_{R \rightarrow T} > p_C$.

To apply equations (10) it is necessary to specify the electromagnetic model of readers and tags as well as the field projector. Moreover the region where $|P_\Omega \circ \hat{\underline{f}}_R|^2$ is path-connected needs to be quickly estimated for any combination of the optimization parameters.

A. Tag antenna modes

Since the tag's gain is not isotropic and the power collected depends on the orientation of the tag which is in general unknown, angle-averaged gain is here considered (simply G_T in the following). A macroscopic performance indicator of the tag is the *effective sensitivity* $\tilde{p}_C = p_C / (G_T \tau)$ giving the minimum radiofrequency power that such a tag has to collect to exhibit the same averaged free-space read distance of an isolated perfectly-matched isotropic tag ($G_T \tau = 1$). This variable accounts for the performance degradation of the tag due to losses of the object and to the impedance mismatch produced by that. In other words, a real tag attached over a body will performs as a reference ideal tag having a higher power threshold.

B. Reader antenna model

The angular dependence of the reader's antenna gain has to be instead preserved then starting from the consideration that the most used reader's antenna is the circularly polarized patch [16], the main beam of the radiation pattern can be approximated by an ellipsoid whose larger axis is half the maximum gain, while the smaller axis is related to the antenna beamwidths over the principal planes. In this hypothesis it is assumed that the interrogation region be approximated by an ellipsoid

$$\frac{(x - a_x)^2}{a_x^2} + \frac{y^2}{a_y^2} + \frac{z^2}{a_z^2} = 1 \quad (11)$$

where the antenna, placed at $x=0$, radiates toward $x>0$. The ellipsoid axes are related to the RFID system parameters, such as the emitted EIRP, the tag sensitivity and the reader's antenna half-power beamwidths on the principal planes (BW_{xy} and BW_{xz}). In particular, with

reference to the geometrical construction in Fig. 2, the larger axis is

$$a_x = \frac{r_R(\theta_0, \phi_0)}{2} \quad (12)$$

being $r_R(\theta, \varphi) = \frac{\lambda}{4\pi} \sqrt{\chi P_{in} G_R(\theta, \phi) / \tilde{p}_C}$ the maximum read range in the free-space, i.e. the distance from reader's antenna where $P_{R \rightarrow T} = P_C$.

(θ_0, ϕ_0) is the maximum gain direction of the reader's antenna occurring at the broadside direction (i.e. $\phi_0 = 0^\circ, \theta_0 = 90^\circ$ in the case of the considered antenna families).

Minor axes are determined enforcing the half-power beam-width point A (Fig. 2) to belong to the ellipsoid:

$$a_{y(z)} = a_x \sqrt{\tan \frac{BW_{xy(z)}}{2} \frac{\sin \frac{BW_{xy(z)}}{2}}{\sqrt{2} - \cos \frac{BW_{xy(z)}}{2}}} \quad (13)$$

Moreover, for typical reader's antennas with circular polarization, the radiation pattern exhibits a rotational symmetry and hence $a_y = a_z$.

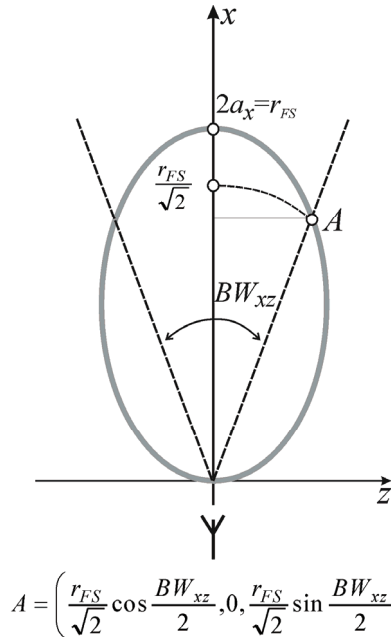


Fig. 2. Geometrical construction for the determination of the axes of the ellipsoid approximating the free-space read zone.

In a real environment the path-connected interrogation region (Ω_U) may be smaller than that in free-space owing to the interference of the radiated field with that scattered by walls and objects inside the environment. As the

interrogation range is quite short (i.e. the order of few meters) the most important interactions happen with objects placed in the neighborhood of the antenna [17]. In particular, objects placed in front of the antenna give a greater contribution to the interference in comparison with those placed laterally (floor or ceiling) owing to the directivity of the antenna. For this reason it is assumed that among all the possible contributions, only that coming from the main object in front of the antenna is dominant.

To further simplify the model, a flat obstacle is considered (as in the case of a wall) placed at distance D in front of the reader's antenna (Fig. 3). Then a simple two-ray model is able to estimate how much the useful region Ω_U is reduced. In particular, along the shortest line joining the antenna location to the object (i.e. the line perpendicular to the object surface), the *two-rays* field projector can be written as:

$$P_{\Omega} \circ [\hat{f}_{-R, \phi}] = \left(\frac{1}{r} + \frac{g}{2D-r} e^{-jk2(D-r)} \right) e^{-jkr} \quad (14)$$

where r is an abscissa along that line and g is the Fresnel's reflection coefficient of the object. When the tag moves along this line, the power collected by the tag's microchip is oscillating due to the interference of the direct and reflected ray. The distance r_{2rays} , at which the minimum power collected by the tag equals the effective microchip sensitivity, can be estimated using (9) with the field projector in (14), by solving the following equation

$$\tilde{p}_C = \chi \frac{EIRP}{(4\pi)^2} \lambda^2 \left| \frac{1}{r_{2rays}} - \frac{\Gamma}{2D-r_{2rays}} \right|^2 \quad (15)$$

where $\Gamma = |g|$ and the direction of the reader's maximum gain (θ_0, ϕ_0) is assumed perpendicular to the object surface (Fig. 3.a). Then, r_{2rays} gives the maximum distance for tag interrogation.

The function inside "[.]" in the above equation is always positive or zero for $0 < r_{2rays} < \frac{2D}{1+\Gamma}$, and hence that equation can be reduced, in this condition, to a second order polynomial

$$r_{2rays}^2 - [2D + (1+\Gamma)r_{FS}]r_{2rays} + 2Dr_{FS} = 0 \quad (16)$$

which has two solutions. One of the two solutions is not included in $(0, \frac{2D}{1+\Gamma})$ and hence it is dropped. For the particular case of perfect

conductor wall ($\Gamma=1$) the maximum read distance predicted by the two-rays model simply reduces to

$$r_{2rays} = D + r_{FS} - \sqrt{D^2 + r_{FS}^2} \quad (17)$$

Once r_{2rays} has been determined, a new ellipsoid approximating the interrogation region in real environment is obtained by setting $a_x = r_{2rays} / 2$ in equations (12).

When the reader's antenna is tilted by an angle γ (Fig. 3.b) the two-rays model can be again applied replacing D with $R = D/\cos\gamma$ because for small $\delta\gamma$ the path $r_1 + r_2 \approx 2R - r$.

In short, the ellipsoid model merges together the antenna model and the propagation model and results from a trade-off between the simplicity of the free-space approach and the accuracy of a fully (time-consuming) ray-tracer. In case of obstacles the ellipsoid extension is smaller than that of free-space model.

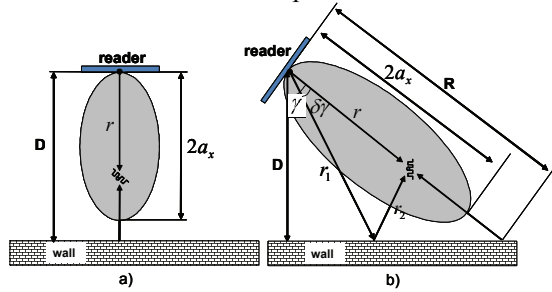


Fig. 3. Ellipsoid model of radiation pattern of readers antenna in front of a wall, a) orthogonal incidence, b) oblique incidence.

C. Experimental evaluation of the electromagnetic model

The ellipsoidal model of the read region has been experimental evaluated for a (CAEN-A948) reader whose antenna is pointing toward the ground at distance $D=2.25\text{m}$ from it. The reader's antenna has 67° beamwidth (in both the planes) and maximum gain $G_{max}=8\text{dB}$. The reader region is referred to $\tilde{p}_C = 56\mu\text{W}$ commercial meander-line tags (EPC 1 GEN2 LAB-ID UH100) replicated along a 2m -long wooden leg, with 10 cm space steps. The leg is then translated in the environment along a line with the purpose to produce a rectangular grid of measurement points. Measurement consists in recording reading and non reading tags. The reader emits 1.2 W EIRP .

A comparison between free-space model, two-ray model, full ray-tracing and measurements is shown in Fig. 4. The ray-tracing prediction is shown by the grey region wherein it is possible to observe the fringes zone owing to the interference with the ground reflected field. Continuous line ellipse concerns the two-rays model while the dotted line ellipse refers to the free-space model. Measurements are shown by means of circle and cross markers, respectively indicating responding and non-responding tags. It is noticeable the improvement of the two-ray model with respect to the free-space model.

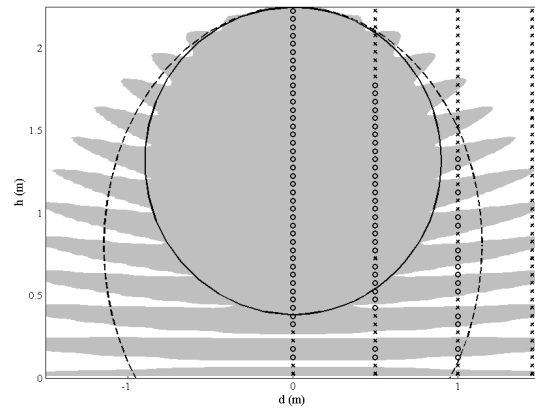


Fig. 4. Interrogation region prediction in case of the reader's antenna pointing toward the ground. Comparison between free-space model (continuous line ellipse), two-rays model (dotted line ellipse), full ray-tracing (grey region) and measurements shown by means of circle and cross markers. Circles concern reading locations, crosses non-reading locations. Reader power: 1.2 W EIRP .

V. EXAMPLES OF APPLICATION

Two optimization examples are here reported, concerning a rectangular and L-shaped room.

A. Rectangular room

The planning method has been first applied to a simple scenario shown in Fig. 5 consisting of a small hall at the entrance of a building with four doors. Reader's antennas are desired to be placed so that a uniform interrogation region is achieved on the vertical cross-section of the hall (Fig. 5.B). Antennas can be placed on side walls and ceiling and they are required to radiate the minimum possible power. The allowed reader position $\{L_R\}$ are uniformly deployed on the

ceiling and walls starting at $1m$ from the floor, with a step of $0.3m$. $\{L_T\}$ are spread on the cross-section area with a uniform $0.6 \times 0.3m^2$ grid. Safety test points $\{L_S\}$ are not been taken into consideration being this a place where people pass through. The magnitude of the reflection coefficient of both walls and ceiling has been set to $\Gamma = 0.5$. Reader's and tag's features are the same of the previous section. The allowed maximum number of antennas is four, while the allowed maximum value of EIRP is $3.2W$.

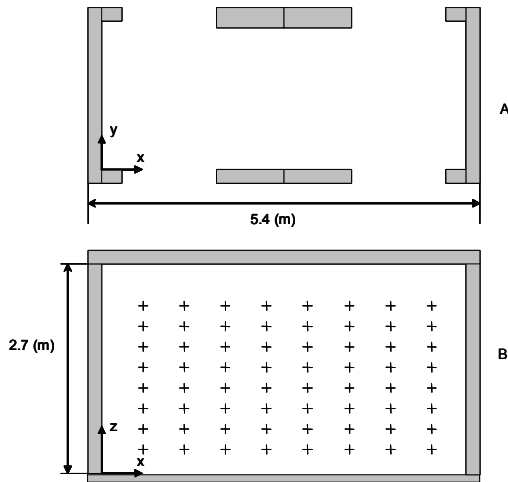


Fig. 5. Horizontal (A) and vertical (B) section of the hall used for experiment. Crosses indicate the read test points $\{L_T\}$.

The optimization parameters in (6) and in (7) are: $c_1=c_2=1.49$, $w=0.726$, $v_{max}=3.2$; $w_{COV}=0.6$, $w_{OV}=0.15$, $w_{EIRP}=0.05$, $w_{COST}=0.2$, $w_{SAF}=0.0$.

The Particle Swarm optimization results are summarized in Table 2 while the resulting ellipses of uniform reading zones are shown in Fig. 6 where it can be appreciated that only two antennas are enough to cover the 92% of the $\{L_T\}$.

The obtained planning result has been put into practice and measurements have been performed to test the reliability of the optimization. The measurement grid consist of $19 \times 25 = 475$ points laying on the vertical $y=1.5m$ plane at steps of $0.3m$ along the x axis and $0.1m$ along the z axis.

Results are shown in Fig. 7 by means of dot and cross markers which refer to reading and non reading points, respectively. The ellipses of the planned uniform reading zones are also shown and it is possible to observe a good agreement with the measurement results. The

76.21% of the measurement points are reading points.

Table 1: Optimized parameters of the two-reader network.

Reader	Position (x,y,z) [m]	EIRP [W]	Tilt [deg]	BW [deg]
R_1	(0, 1.5, 1.0)	2.95	+30	67
R_2	(5.4, 1.5, 1.5)	1.8	-30	67

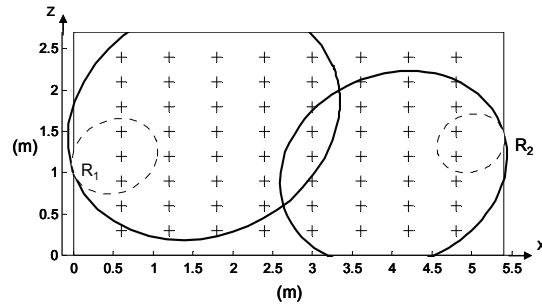


Fig. 6. Planning result on the vertical section (B) of Fig. 5. Crosses represent $\{L_T\}$ (read test points). R_1 and R_2 reader's antenna locations. Continuous line ellipses show the uniform covered zone of readers. Dotted line ellipses show the zone where the field exceeds the regional safety regulations.

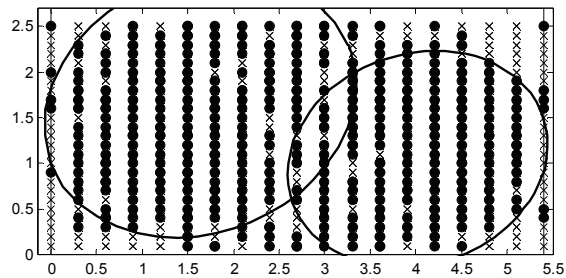


Fig. 7. Comparison between planning results and measurements. Ellipses show the planned uniform read zone as estimated by the electromagnetic two-rays tool. Crosses and dots show measured non reading and reading points, respectively.

B. L-shaped room

To highlight the ability of the optimization algorithm to reduce the cost and to enhance the coverage of the network, a more complicated topology has been considered. The scenario consists of an L-shaped environment (Fig. 8.a), wherein reader's antennas are constrained to be placed only on two side walls ($x=0m$ and $y=5m$).

Three different optimizations are presented, having gradually released the constraints on the reader's geometrical and electrical parameters. To value the benefit of the optimizations in the considered cases, the fitness function is used as an overall indicator.

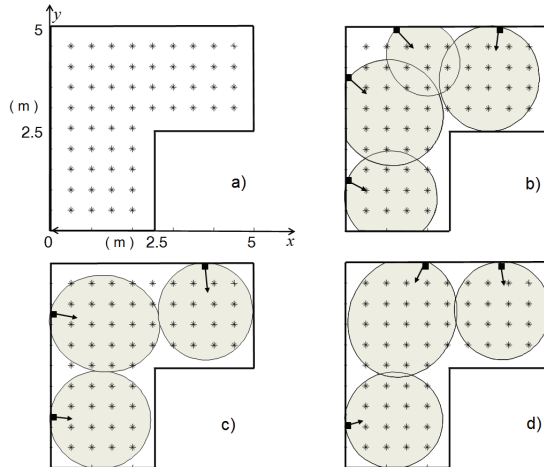


Fig. 8. L-shaped environment wherein network coverage is planned with different constraints. a) set-up with $\{L_T\}$ shown by stars; b) EIRP and antennas orientation (indicated by arrows) optimized; c) number of readers, EIRP and orientation optimized; d) complete optimization. Arrows show antennas' orientation, ellipses interrogation region.

Table 2: Result of optimization planning of the environments in Fig. 8.

	f_{COV}	f_{OV}	f_{EIRP}	f_{COST}	F
b)	0.98	0.43	0.32	0	0.67
c)	0.95	1	0.30	0.25	0.78
d)	1	0.92	0.30	0.25	0.80

At first, number and position of antennas are fixed while orientation and $EIRP \leq 3.2W$ are optimized. Starting from four antennas, the optimization process tries to reduce the overlapping regions lowering the radiated power and orienting the antennas (Fig. 8.b). Some overlapping regions are still visible however. Removing the constraint on the number of antennas, only three antennas are needed to cover the 95% of the test points (Fig. 8.c): the overall indicator is increased with respect to the previous case (Table 2) as the efficiency is enhanced and the cost and overlapping are reduced. Finally all the parameters are free to be optimized and the planning result is shown in

Fig. 8.d. The whole coverage is obtained and the overall indicator is greater than the previous cases.

VI. CONCLUSIONS

The planning of the deployment of readers in large and complex environments is a trade-off between the maximum interrogation zone, required for the particular application, and the electromagnetic and topography constraints. Simple and fast electromagnetic models have been applied in the frame of a PSO algorithm for planning in real environment.

The given numerical and experimental examples have demonstrated the effectiveness of the method and have shown that the coverage quality may be greatly improved when all the geometrical and electric options are fully exploited.

The application of the planning method to large and complex environments is expected to be computational hard because of the large number of readers, necessary to the coverage.

However, a reduction of the computational burden can be achieved by partitioning the whole optimization problem into a number of smaller sub-problems, taking advantage on the natural localization of the UHF RFID link. The environment can be subdivided into a number of subsets exploiting geometrical symmetries and the natural partition induced by walls and big objects. Fictitious reflecting surfaces, not hosting readers, may be introduced to split open space regions. The optimization process can be then applied in parallel to each subset preserving a computational complexity comparable with that of the previous examples.

ACKNOWLEDGMENT

The authors wish to thank LAB-ID to have provided UHF tags.

REFERENCES

- [1] K. Finkenzeller, *RFID Handbook*, Wiley & Son, 2000.
- [2] R. Want, "An Introduction to RFID Technology," *IEEE Pervasive Computing*, Vol.5, No.1, pp. 25-33, Jan.-March 2006.
- [3] L. M. Ni, Y. Liu, Y. C. Lau, and A. Patil, "LANDMARC: Indoor Location Sensing Using Active RFID," in *Proceeding of the first IEEE International Conference in Pervasive Computing*, 2003.

- [4] R. S. Sangwan, R. G. Qiu, and D. Jessen "Using RFID tags for tracking patients, charts and medical equipment within an integrated health delivery network", *IEEE Int. Conf. Networking Sensing and Control* 2005, pp.1070-1074, 2005.
- [5] G. Marrocco, "The art of UHF RFID antenna design: impedance-matching and size-reduction techniques", *Antennas and Propagation Magazine, IEEE*, Vol. 20, No.1, pp. 66-79, Feb. 2008.
- [6] W. James, E. Daniel, and S. Sanjay, "Colorwave: A mac for rfid reader networks", *Proc. of IEEE WCNC*, Vol. 3, pp. 1701-1704, 2003.
- [7] Z. Zhou, H. Gupta, S. R. Das, and X. Zhu, "Slotted Scheduled Tag Access in Multi-Reader RFID Systems," in *Proceeding of the fifteenth IEEE International Conference on Network Protocols (ICNP)*, 2007.
- [8] Q. Guan, Y. Liu, Y. Yang, and W. Yu, "Genetic Approach for Network Planning in the RFID Systems", *Proceedings of the Sixth International Conference on Intelligent Systems Design and Applications (ISDA'06)*, IEEE, 2006.
- [9] R. Clarke, D. Twede, J. Tazelaar, and K. Boyer, "Radio frequency identification (RFID) performance: the effect of tag orientation and package contents", *Packaging Technology and Science*, Vol. 19, No. 1, pp. 45-54, 2006.
- [10] K.V.S. Rao, D.W. Duan, and H. Heinrich, "On the read zone analysis of radio frequency identification systems with transponders oriented in arbitrary directions", *1999 IEEE Microwave Asia Pacific Conference*, Vol. 3, pp. 758-761, 1999.
- [11] R. Banerjee, R. Jesme, and R. A. Sainati, "Performance analysis of short range UHF propagation as applicable to passive RFID", *IEEE RFID Conference*, pp. 30-36, 2007.
- [12] E. Di Giampaolo and F. Bardati, "A Projective Approach to Electromagnetic Propagation in Complex Environments", *Progress In Electromagnetics Research B*, Vol. 13, pp. 357-383, 2009.
- [13] A. Donev, et al., "Improving the Density of Jammed Disordered Packings Using Ellipsoids", *Science*, Vol. 303, pp. 990-993, 2004.
- [14] J. Robinson and Y. Rahmat-Samii, "Particle Swarm Optimization in Electromagnetics", *IEEE Trans. Ant. Prop.*, Vol. 52, No. 2, 2004 .
- [15] J. Kennedy and R. Mendes, "Population Structure and Particle Swarm Performance", *Proceedings of the Evolutionary Computation 2002 Congress CEC '02*, Vol. 2, 2002.
- [16] J. M. Lee, N. S. Kim, C. S. Pyo, "A Circular Polarized Metallic Patch Antenna for RFID Reader", *Asia-Pacific Conference on Communications*, pp. 116-118, October 2005.
- [17] L. W. Mayer, M. Wrulich, and S Caban, "Measurements and channel modeling for short range indoor UHF applications", *Proceedings of The European Conference on Antennas and Propagation, (EuCAP 2006)*, November, 2006.

Emidio Di Giampaolo



received the Laurea in Electronic Engineering in 1994 and a Ph.D. in Applied Electromagnetics in 1998 both from University of L'Aquila (Italy). Since 1998 to 2004 he has been a post doctoral researcher at the

University of L'Aquila where he also taught Radio-wave propagation as a substitute. Since 2005 he has been a researcher at the University of Rome "Tor Vergata" where he teaches Industrial Microwave Applications and a laboratory class on antennas. In the spring of 2000 he was a Visiting Researcher at the European Space Research and Technology Centre (ESTEC), Noordwijk (NL).

His research interests mainly concern numerical methods for modelling radio-wave propagation in complex environments, antennas and indoor radio localization.



Fausto Forni of Siracusa (Italy) received the Laurea degree in Telecommunications Engineering from the University of Rome "Tor Vergata", Italy, in 2009. His interests include antennas, RFID systems

and evolutionary algorithms.



Gaetano Marrocco of Teramo (Italy) received the Laurea in Electronic Engineering in 1994 and a Ph.D. in Applied Electromagnetics in 1998, both from University of L'Aquila. He has been a researcher at the University of Rome "Tor Vergata" since 1997 where he currently teaches Antenna Design and Bioelectromagnetics. In the summer 1994 he was at the University of Illinois at Urbana Champaign as a post-graduate student. In the autumn 1999 he was a visiting scientist at the Imperial College in London. His research is mainly directed to the modelling and design of broad band and ultra wideband antennas and arrays as well as of miniaturized antennas for RFID applications. He has been involved in several space, avionic, naval and vehicular programs of the European Space Agency, NATO, Italian Space Agency, and the Italian Navy. He holds two patents on broadband naval antennas and one patent on sensor RFID systems. He currently serves as Associate Editor of the IEEE Antennas and Wireless Propagation Letters.

RFID-Based System for Pilgrims Identification and Tracking

Mohamed Mohandes

Department of Electrical Engineering
King Fahd University of Petroleum & Minerals
KFUPM Box 1885, Dhahran, 31261, Saudi Arabia
mohandes@kfupm.edu.sa

Abstract— This paper describes a prototype of a system developed using a *passive* RFID wristband tag for identification of pilgrims in the holy areas during Hajj. Upon presentation of the tag to a handheld reader all information related to the pilgrim holding the tag will be displayed on the screen of the reader. This way if a pilgrim gets sick, lost, or dies he can be easily identified through the tag on the spot. Officers around the holy area will have a light-weight handheld reader that can get all information from the tag without the need to burden the already overloaded communication network during the Hajj season. The developed prototype was tested on 1000 pilgrims from the country of Ivory Coast in collaboration with officials from Hajj Ministry and Development Commission of the Holy cities of Makkah and Madinah. The results of the experiment have convinced Hajj authorities to utilize this technology for all pilgrims in the future. Additionally, we have explored the possibility of tracking pilgrims using *active* RFID system. Due to the small number of working tags, experiment was performed only on 6 persons. Results of the latter experiment have shown that the system requires further development and needs to be validated with a larger number of tags.

Index Terms— Identification, tracking, crowd control, RFID.

I. INTRODUCTION

Hajj (Pilgrimage) is undoubtedly the most crowded gathering of Muslims on earth. It has unique characteristics with regard to the people who attend it (pilgrims), the place they meet in, and the kind of rituals they perform. These characteristics result in a set of challenges to the authorities and organization departments in controlling the crowd, and identifying the personalities. It is strongly believed that RFID can

be an ideal solution for crowd control and personal identification at Hajj season. In this paper a prototype system using a wristband RFID tag is developed for identification of pilgrims in the holy areas during Hajj.

RFID is an electronic tagging technology that allows an object, a place, or a person to be automatically identified at a distance using an electromagnetic charge/response exchange. Typical applications include labeling products for rapid checkout at a point-of-sale terminal, inventory tracking, animal tagging, timing marathon runners, secure automobile keys, and access control for secured facilities [1-2].

In the last few years RFID systems have experienced a surge of deployment (due to the drop in cost). Inventory tracking is now necessary on an unprecedented scale to support growing consumer markets at low operating costs. Furthermore, the components used to build the tags and tag readers have become more sophisticated as they provide greater functionality, longer reading range, and higher speed of data transfer. As a result, a number of influential organizations such as Wal-Mart, GE, U.S. Department of Immigration, and the U.S. Department of Defense, have recognized the capabilities of RFID to improve operational efficiencies [3]. Additionally, it has been used successfully during the 2008 Beijing Olympics, where 16 million RFID embedded tickets [4] were used for admission to the games.

II. CHALLENGES DURING HAJJ

While it is a great spiritual experience for all the pilgrims, at the same time it poses great challenges of all sorts for the authorities responsible for facilitating the Hajj. Despite all that is done to facilitate the Hajj, following are some of the common difficulties faced by the pilgrims and the authorities alike [5]:

- Identification of pilgrims (dead or injured)
- Medical emergencies
- Guiding lost pilgrims to their camps
- Loss of identity documents
- Crowd control

Muslims are obliged to perform Hajj once in their lifetime. Many of them love to perform it more than once. It is performed on specific days of the year (8th- 13th of the 12th Hijri month) in designated boundaries (Makkah, Mina, Muzdalifa and Arafat). The whole crowd makes the same movements at the same times doing essentially the same thing.

The authorities for Hajj try their best to limit the crowd flooding to the area by assigning quotas for pilgrims from each country, and limiting the visits of people within the Kingdom to once every five years. Yet the number of pilgrims is in the range of 2-2.5 millions every year.

The following describes some of the unique characteristics about Hajj:

A. Large Number of Elderly Pilgrims

Many Muslims decide to perform Hajj when they are old. Moreover, many countries, in attempting to adhere to the quota, give preference to the elderly. Added to the crowd and exhaustion they face, a significant number of them are exposed to falling sick or even losing their lives.

B. Language Barrier

Pilgrims in Hajj season are, literally, coming from all countries on earth, with no exception. They speak different languages. It is a serious issue when it comes to helping the lost or treating the sick.

C. Dress Code

The dress of the pilgrim consists of two pieces of garments, one is rolled around the lower part of the body and the other is put on the shoulder. There are no pockets to carry the belongings. Although pilgrims are allowed to put on a belt with small pockets, most of them do not prefer to carry valuable documents because of the fear of losing them in the crowd.

D. Identification of Pilgrims (dead or injured)

Due to the crowd, age factor and sometimes

unfortunate accidents, the death toll in Hajj season is on the high side. Many of the dead are on their own, carrying no documents. Every year at the end of Hajj season, authorities are confronted with tens of bodies of pilgrims that are never identified or claimed. This problem is not easy to solve as it is not known when and if any of these bodies will be claimed in the future.



Fig. 1. Pilgrims in Makkah during Hajj.

E. Knowing the Medical Record of Patients

Tens of thousands of pilgrims are brought to hospitals and clinics for emergency treatment. Knowing the medical record of patients, would facilitate efficient treatment and utilization of the limited resources available during this period. However, due to language barrier doctors may not be able to get basic information needed for more accurate diagnosis.

F. Guiding Lost Pilgrims to their Camps

Large numbers of pilgrims report on the hour to Help Kiosks to help them find their camps. It is not always easy to find a speaker of the lost pilgrim's native language. Without papers showing their location and contact numbers, and sometimes without a common language to communicate, it becomes almost impossible to help them. This puts a tremendous pressure on the security officers who are taking care of pilgrims.

G. Loss of Important Documents

With the special cloth of Ihram, it is highly likely that the pilgrim may lose some of his identification papers, like Passport, Residence Permit, and National ID in addition to money or

credit cards. This imposes additional burden not only on the pilgrims but also on the authorities.

H. Crowd Control

Crowd control has become a major problem with many pilgrims dying in accidents and stampedes in congested places during the Hajj. These accidents happen due to insufficient planning and management of available space as well as due to crowd behavior. The authorities have recently experimented with techniques to control the flow of the crowd to the most congested area of Al-Jamarat. The investigator is currently conducting some research on using RFID for this purpose, as well as controlling access of vehicles to the Hajj zones.

III. RFID TECHNOLOGY

An RFID system consists of the following three components as shown in Fig. 2:

- RFID tag or transponder
- RFID reader or transceiver with a scanning antenna
- Data processing subsystem that can be embedded in a handheld reader

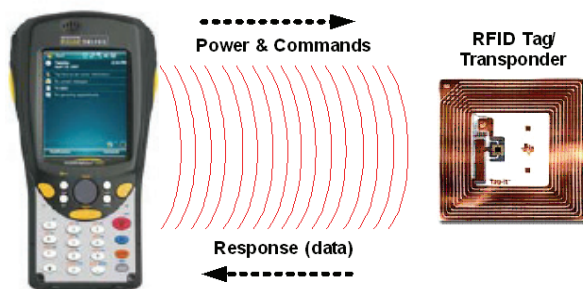


Fig. 2. A typical RFID system with handheld reader.

An RFID reader consists of an antenna, transceiver and decoder, which sends periodic signals to inquire about any tag in its vicinity. On receiving any signal from a tag it passes on that information to its embedded data processor. The scanning antenna puts out radio-frequency signals in a relatively short range. The RF radiation does two things: it provides a means of communication with the transponder tag (the RFID chip) and it provides the tag with the necessary energy to function (in the case of passive RFID tags). This is an absolutely key part of the technology; RFID tags do not need to contain batteries, and can

therefore be made simple, cheap and remain usable for very long periods of time. The scanning antennas can be permanently affixed to a surface; handheld antennas are also available. They can take whatever shape needed.

When an RFID tag passes through the field of the scanning antenna, it detects the activation signal from the antenna. That "wakes up" the RFID chip, and it transmits the information on its microchip to be picked up by the scanning antenna.

The RFID tag is composed of an antenna, a wireless transducer and an encapsulating material. These tags can be either active or passive. While the active tags have on-chip power, passive tags use the power induced by the magnetic field of the RFID reader. Thus, passive tags are cheaper but with lower range (<10m) and more sensitive to regulatory and environmental constraints, as compared to active tags. They do not have a transmitter; they simply reflect back energy (radio waves) coming from the reader antenna. Thus they do not require batteries, and can be much smaller and have a virtually unlimited life span.

Active tags have their own transmitter and power source. They broadcast a signal to transmit the information stored on the microchip.

Operating frequency is the determining factor for the type of application an RFID system is best suited for. These include high frequency (850-950 MHz and 2.4-5 GHz), intermediate frequency (10-15 MHz) and low frequency (100-500 kHz).

- **High-frequency** RFID systems are suitable for applications requiring a longer read range such as supply chain, inventory, assembly lines, toll-collection systems and railroad car and container tracking.

- **Intermediate-frequency** RFID systems are just now beginning to emerge in the financial transaction processing areas of smart card use.

- **Low-frequency** systems have short reading ranges and lower system costs. They are most commonly used in security access, asset tracking, and animal identification applications.

As you move up in frequency, tag and reader costs move up as well. Tags at 125 kHz operating frequency have ICs costing tens of cents as compared to 2.4 GHz ICs costing several dollars.

Applications of RFID systems fall into two principal categories: firstly, short range applications where the reader and the tag must be

in close proximity (such as in access control) and secondly, medium to long range applications, where the distance may be greater (such as reading across a distribution centre dock door). A sample of RFID applications includes:

- Security, ticketing and access control
- Supply chain logistics & retail
- Asset tracking and traceability
- Lifetime item identification
- Medical applications
- Animal and specimen identification
- Airline baggage handling
- Vehicle access control

IV. RFID SOLUTION FOR HAJJ

RFID offers an effective, convenient and economical solution to the Hajj problems described above. A wristband RFID tag that can be worn at all times can be provided to each pilgrim. When the tag is presented to an RFID reader the information stored in the tag can be retrieved and displayed on a handheld portable unit. The following is some of the information that can be stored in a tag:

- Personal details - like name, address, blood type, nationality, etc.
- Medical condition
- Contact information of the pilgrim's Hajj group
- E-purse that can be loaded with optional amount of money

RFID may help in crowd control by allowing the authorities to estimate the number of people at specific locations where there is a risk of accidents taking place. Combined with the efforts of the security personnel it may be possible to ease the flow of pilgrims at key points resulting in proper utilization of space. RFID readers can be installed at key entry and exit points to ping wristband RFID tags and thus get a fairly accurate estimate of people passing those points. This will help the security personnel in controlling the entry of pilgrims in high risk areas.

The utilization of the wristband can allow the pilgrims to leave their documents on safe places like hotels safe deposit boxes. Moreover, if an ID is lost, it is possible to retrieve the information needed to produce a replacement of the lost ID with the presence of wristband tag. Information

stored in the tag on the medical condition of the pilgrim can be very useful in case of a medical emergency. Having access to the medical condition of the patient in the emergency room from the tag he holds on his wrist may help save the life of the patient and improve efficiency of the medical team. The tags will also help in guiding the pilgrims who get lost - besides helping in the immediate identification of pilgrims who die during Hajj.

With the new rules that each local or external pilgrim should obtain permission to perform Hajj, the permission certificate can be the wristband itself. The presence of the tag can be detected at a distance and does not require visual reading by the security officers. For example, the officer can read tags from a distance and find out if all passengers of a car have permission to perform Hajj. This is because RFID tags do not require line of sight or contact with the reader for the information to be transferred. This would increase efficiency and deter violators in a way to achieve the objectives of Hajj authorities to control the number of pilgrims every year and make it easier for authorized pilgrims to perform their once in a life time Hajj.

Some types of RFID wristbands can't be unlocked once fixed and requires cutting the band. This will guarantee that the wristband will not get lost or disposed. There is a possibility to collect the wristbands upon finishing Hajj activities. The collected RFID tags could be re-programmed and installed in new wristbands to be used for upcoming Hajj seasons.

The wristband tag can be a real working watch; this should remove the fear and sensitivity of pilgrims and their reluctance to wear such tags. Other paper wristbands did not find the full cooperation from pilgrims in the past.

V. DEVELOPMENT OF THE PROTOTYPE SYSTEM

The developed prototype system consists of the following:

A. WorkAbout Pro S Hand-Held Computer

The WorkAbout Pro [6] is a flexible, programmable and expandable portable data collection terminal, designed for a range of data collection needs. It is available with either Windows Mobile 2003 SE or Windows CE .NET configurations. The WorkAbout Pro delivers the

performance, ruggedness and durability required for mobile data collection in an ergonomic package. The device used in the prototype has Windows Mobile 2003 as the operating system and a built-in RFID reader that supports worldwide RFID Standards in LF (125 - 134.2 KHz) or HF (13.56MHz) technologies. Based on industry standard Microsoft and Intel XScale architecture, the WorkAbout Pro ensures seamless application development and integration capabilities. Compact Flash and SD/MMC memory expansion slots combined with USB, and a 100-pin high speed expansion interface, to provide flexible radio and peripheral connectivity.

B. Psion Teklogix Mobile Devices SDK

The Psion Teklogix Mobile Devices SDK [7] for Windows Mobile 2003 SE, provides support for programming in .NET Compact Framework, C/C++ and Java. Developers are able to write flexible mobile applications to take advantage of a variety of scanners and drivers, all from the single platform. Once developed, an application can be deployed, without modification, on any Psion Teklogix mobile computer.

The Mobile Devices SDK provides a consistent set of APIs for all the Psion Teklogix Windows CE and Windows Mobile based computers. Applications built using this release of the Mobile Devices SDK are expected to be fully compliant with future software releases for the Psion Teklogix handheld computers.

C. Development Tools

- **Microsoft Visual Studio 2005**

Microsoft Visual Studio [8] is the main Integrated Development Environment (IDE) from Microsoft. It can be used to develop console and GUI applications along with Windows Forms applications, web sites, web applications, and web services in both native code as well as managed code for all platforms supported by Microsoft Windows, Windows Mobile, .NET Framework, and .NET Compact Framework [8].

- **SQL Compact Edition**

SQL Server Compact [9] is a free and easy-to-use embedded database engine that lets developers build robust mobile applications that run on all Windows platforms including Windows XP, Vista,

Pocket PC, and Smartphone.

- **Mughamrat Windows Mobile Arabic Layer**

In the Middle East market, the Arabic language support is mandatory. Hence, building Arabic C# .NET applications, running on a Pocket PC or on Windows CE is a challenging task due to the many problems related to the Arabic language specifications that developers have to cope with. To avoid these problems, Mughamrat has developed WAL (WinCE Arabic Layer) [10], which is a software development kit for developing application with an Arabic interface for mobile devices.

D. Pilgrim Information System

This software is designed to read and write pilgrims information from the data source using passive RFID tags. The purpose of the software requirement specification is to describe all the functional requirements, constraints, dependencies and the way the requirements be fulfilled. Through the use of this software the user will be able to save user information to data source, read user information using hand held device, and assign RFID tags to users. The following sections provide details about the application architecture and usage.

- **User Info Writer**

The application allows the user to input pilgrim information and assign them a tag ID. The application has been developed using C# and .NET framework. There is only one Class in this application that takes care of the required functionality. The userInfo class provides all the functions needed to store the pilgrim's info on the data source which is a SQL compact edition database. The class diagram is shown in Figure 3.

- **User Interface Screens**

Figure 4 shows the main screen of the application. It allows the user to input all the required information for the pilgrim. User can search for the required photo by clicking the Browse button. Once all the information is filled in, the user clicks the **Save** button and all the information along with the image and RFID tag number are saved to the database.



Fig. 3. UserInfo class diagram.

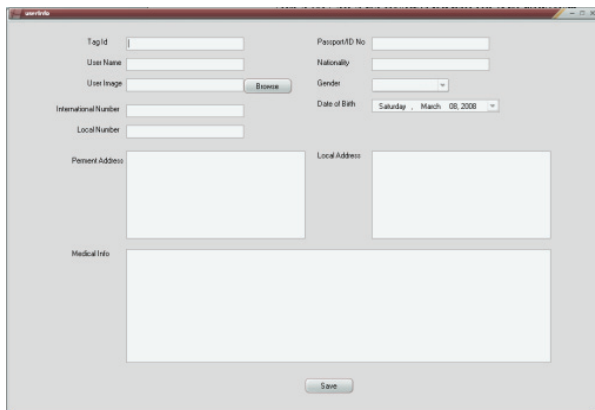


Fig. 4. Main screen of the application.

name and picture. At the bottom on the screen there are four tabs; each one displays different information regarding the pilgrim.

The second screen that is obtained when you click on the General Info tab, shows the pilgrim's gender, nationality, passport/ID number, local and international phone numbers, and blood group

The third screen that is obtained by clicking the Address tab shows the Current and Permanent addresses. The last screen which you get by clicking the Medical tab shows the medical information of the pilgrim as shown in Fig. 7.



Fig. 5. RfidTagReader class diagram.

• **Software for the Tag Reader**

This application has been developed to be deployed on a Psion Teklogix Workabout Pro S that has a built in RFID reader and Windows Mobile 2003 as the Operating System. The application will allow the user to scan any RFID tag to get the tag number and then retrieve the information related to the tag from the data source that is deployed along with the software. There is only one Class in this application that takes care of the required functionality. The class diagram is shown in Fig. 5.

• **Database Design**

There is only one database table so that the size remains small and the database doesn't have to store any relation information. tag_id is the primary key and is the tag number of the RFID. The fields used in the database are given in Table 1.

• **Handheld Reader Screens**

The first screen you see when you start the application is shown in Figure 6. It shows the tag ID when it is scanned. If the tag is assigned to a pilgrim in the database it will show the pilgrim's

Table 1: Fields of the developed database.

Column Name	Date Type	Length
user_name	nvarchar	200
tag_id (primary key)	nvarchar	100
user_pic	varbinary	8000
user_id_no	nvarchar	100
user_birth_date	datetime	8
user_gender	nvarchar	8
user_perm_address	ntext	16
user_local_address	ntext	16
user_med_info	ntext	16
user_nationality	nvarchar	100
user_inter_ph	nvarchar	20
user_local_ph	nvarchar	20

VI. PILOT PROJECT FOR PILGRIM IDENTIFICATION

A pilot project for the developed Pilgrim Identification to demonstrate the advantages of using RFID technology during the Hajj is



Fig. 6. Handheld reader screens 1 and 2.

implemented [11]. We had 1,000 tags and a single reader. Pilgrims from the country of Ivory Coast volunteered for the pilot (see Fig.8). However, the group consisted of about 4,000 pilgrims. We selected the elderly 1,000 and programmed the tags for them. An IT engineer had a complete database that includes picture, name, blood type, date of birth, and address in their back home. The medical team accompanying the group had the medical conditions of all pilgrims. Therefore, programming the tags was a simple process. Wristband tags were distributed to the pilgrims. Due to the fact that only one reader is available and not all pilgrims in the group have wristband tags limited the potential of the applications. Nonetheless, scenarios were created to show some of the possible benefits of the system. In particular, the pilot study has shown that the RFID system would help identification of pilgrims at check points, as there was no need for officer to read Hajj permit to check its validity for every person. Checking the wristband tags by the reader takes a small fraction of the time it takes to authenticate the paper permit.

At the entrance of the hotel, pilgrims with the blue wristband tags did not need to be stopped as it was clear from far that they belong to the group. The same was observed at the entrance of the camp in Mina Arafat and Muzdalipha. Queues for food and access to the buses for transportation through out the Holy areas are other occasions where RFID wristband tags would improve efficiency in checking that only authorized pilgrims use these services. Automation is necessitated further by the fact that the rituals of

Hajj are to be performed by pilgrims at the same instant of times. No manual system would perform this authorization process with ease and satisfaction. From the pilot, it was clear that participating pilgrims were identified from the unique blue wristband even without RFID reader. This indicated that in the full implementation, it is better if wristbands with a unique color are used for every group. It is even better if the wristband looks like the flag of the country from where the group of pilgrims came from. This will help drastically guiding lost pilgrims to their camps. Moreover, if tags are programmed at the country of origin before departure then information may be uploaded from the tag to the computer of immigration centre, which improves efficiency and reduces long waiting queues at the airport.



Fig. 7. Handheld reader screens 3 and 4.



Fig. 8. RFID Pilgrim Identification System.

VII. ACTIVE RFID WRISTBAND TAGS FOR PILGRIM TRACKING

Every year a significant number of violators pretend that they want to perform Hajj while their

real intention is to find jobs and stay in the country illegally. The Hajj area is limited to few squared kilometers. Therefore, if a network of RFID readers is distributed in the Holy area and an active RFID wristband is used for each pilgrim, then when a pretend pilgrim attempts to leave the area or cut the wristband an alarm is sent to security officers indicating a violator. Moreover, although short range tags proved useful for identification, a longer range would improve efficiency. At check points, officers need to check the Hajj permit of each pilgrim. Pilgrims enter the Holy area on cars or busses. Short range RFID system would require officers to bring the reader close to the tag to be able to read it. A longer range would allow pilgrims permits to be checked while pilgrims are seated in their vehicles without the need for officers to come close to read the wristband tag. Additionally, statistics about distribution of pilgrims throughout the Holy area help provide better services in future Hajj seasons. Long range RFID systems would provide such statistics without creating bottlenecks in the area. Moreover, sometimes there is a need to locate a pilgrim among the crowd. A long range RFID system with a network of readers could help locate a particular pilgrim when needed.

To develop a solution for these tasks, an off the shelf development kit is acquired from ActiveWave. Its printed specifications [12] matched our requirements reasonably well. The wristband has a replaceable 3V battery that lasts from one to three years. It's read range for receiving is up to 30 meters while for transmission is up to 85 meters. The user memory is up to 256 Kbits, which is enough to store a pilgrim's information with his picture and a finger print if needed. Anti-collision capability is also available. It sends an alarm if removed or cut. The tag is shown in Fig. 9.

The reader has three basic modes of operation: program, monitor, and call. When in programming mode, the reader configures the tags. When in monitoring mode, the reader listens to all tag activity and relays this information back to the host in real-time. When in call mode, the reader



Fig. 9. Active RFID wristband tag and reader.

wakes up specific tags, specific groups of tags, or all tags within range. The reader is shown in Fig. 9.

The development kit has been acquired that includes a reader and about 24 wristband tags. Upon testing the system, 18 tags were found not to be functional. The remaining 6 were programmed to track 6 pilgrims. The reader is placed on the ground and pilgrims were asked to start moving from about 100 meters towards the reader. It was noticed that at about 30 meters the pilgrims were detected, however, if a pilgrim occludes another, both will not be detected by the reader. The same process is observed when more pilgrims stand close to each other. The detection range is observed from all directions consistently. For the crowd in Hajj, the system as it was tested is not useful for the intended purpose of tracking. More refinement of the used frequencies, location of readers, and antennas design is needed.

For detection of passengers of cars, it was possible to detect 5 pilgrims in a passing car at a reasonable speed. This would be very helpful at check points as it allows Hajj permits to be verified while vehicles are on the move. This would improve efficiency and remove bottlenecks on the road.

VIII. CONCLUSIONS AND RECOMMENDATIONS

Hajj season poses many challenges for the authorities. The main challenges have been reviewed in this work based on official reports, interviews with key officials and the authors' personal experience. Using advanced technologies is very promising in tackling these challenges. The pilot study has demonstrated that the use of RFID technology eases some of these challenges.

We carried out a pilot project to experiment our system during Hajj 2007. The prototype RFID-based Pilgrim Identification System was tested with a group of 1000 pilgrims from Ivory Coast. This experiment proved to be very successful in demonstrating the benefits of the system. In particular, it demonstrated the effectiveness of RFID system in removing bottlenecks of the traditional authentication system. This is due to the fact that checking a wristband tag by the reader takes a small fraction of the time it takes to authenticate the paper permit.

It must be noted that the cooperation of pilgrims is very vital for the success of the system; our experiment has shown that pilgrims happily participated after enough explanation was given about the objectives of such a system and improved services it leads to future pilgrims. Moreover, it was shown that collecting the wristband tags to use them in future seasons is not practical, as most pilgrims wanted to keep the tag as a souvenir from Hajj. Pilgrims should be educated in their own countries about the system before coming for Hajj and the importance of keeping the tags as a Hajj permit and that its loss can cause them difficulties during their Hajj.

Distribution of pre-programmed tags in each pilgrim's home country makes the job of immigration officers in Jeddah easier and improves efficiency at the airport as information needs only be verified from the tags rather than inputting the information while pilgrim is waiting.

In the future, applications such as e-purse may be added to the tag, so that all what the pilgrim need to carry is his wristband tag. This saves pilgrims the worry that they may lose money or official documents.

Although 1000 pilgrims is a relatively large number for the current project, it only makes 0.04% of total pilgrims. Moreover, having only 1000 tags and one reader limited the full benefits of the RFID system for such application, especially since the group from Ivory Coast consists of about 4000 pilgrims. Therefore, it is recommended that the experiment be performed on an entire contingent of pilgrims from a country such as Malaysia which has about 14,000 pilgrims coming every year. This will help in validating the system with a relatively good sample size before deploying the system for more than 2.5 million pilgrims.

We have also investigated the use of Active RFID system to track pilgrims using a developed prototype. The system has proved to be useful for detection of Hajj permits while pilgrims are on moving vehicles. More investigation is needed for this system. Improvement of antenna design, selection of readers' location, and communication frequency are also to be tackled in future work. Wireless sensor network with GPS/RFID unit is currently under investigation for the tracking of pilgrims.

ACKNOWLEDGMENT

This work has been conducted under KFUPM Funded Project No. IN060340. The author is grateful to KFUPM for the support. The author would like to thank Usman Malik, Ahmed Abul Hussain, M. Kousa and S. Sharani for their help.

REFERENCES

- [1] K. Finkenzeller, *RFID Handbook, Radio-Frequency Identification Fundamentals and Applications*, Wiley, 1999.
- [2] D. Brown, *RFID Implementation*, McGraw-Hill, 2006.
- [3] US DOD Releases Final RFID Policy, <http://www.rfidjournal.com/article/view/1080/1/1>
- [4] "How RFID will benefit from Beijing Olympics 2008", http://www.rfid-weblog.com/50226711/how_rfid_will_benefit_from_beijing_olympics_2008.php
- [5] M. Mohandes, M. Kousa, A. Hussain, S. Shahrani, "RFID Wristband Tag for Pilgrims Identification", *KFUPM technical report*, 2008.
- [6] Workabout Pro Hand-Held Computer <http://www.psionteklogix.com/public.aspx?s=com&p=Products&pID=4391>
- [7] Psion Teklogix Mobile Devices SDK <http://www.psionteklogix.com/public.aspx?s=com&p=Products&pCat=268&pID=2390>
- [8] Microsoft Developer Network, <http://msdn.microsoft.com/en-us/default.aspx>
- [9] Microsoft SQL Server, <http://www.microsoft.com/sql/editions/compact/default.aspx>
- [10] WindowsCE Arabic Layer (WAL), <http://www.mughamrat.com/ProductsSolution/s/MobilityArabizationProducts/WindowsCEArabicLayerWAL/tabid/67/Default.aspx>

[11] M. Mohandes, "An RFID-Based Pilgrim Identification System (A Pilot Study)", 11th International Conference on Optimization of Electrical and Electronic Equipment (OPTIM'08), May 2008.

[12] ActiveWave, www.activewaveinc.com.



Dr. Mohamed Mohandes is an associate professor at King Fahd University of Petroleum and Minerals (KFUPM). He obtained his PhD from Purdue University-West Lafayette, IN, in 1993. He worked as

a senior software Engineer at Productivity Technologies Inc., Santa Clara, CA, until 1995. Then he joined The Research Center for sensor signal and information processing in Adelaide, Australia until 1997 when he joined KFUPM. He has developed several pilot RFID systems for pilgrim identification and tracking, library system, asset tracking, and vehicle access control.

2010 INSTITUTIONAL MEMBERS

DTIC-OCP LIBRARY
8725 John J. Kingman Rd, Ste 0944
Fort Belvoir, VA 22060-6218

AUSTRALIAN DEFENCE LIBRARY
Northcott Drive
Canberra, A.C.T. 2600 Australia

BEIJING BOOK CO, INC
701 E Linden Avenue
Linden, NJ 07036-2495

BUCKNELL UNIVERSITY
69 Coleman Hall Road
Lewisburg, PA 17837

ROBERT J. BURKHOLDER
OHIO STATE UNIVERSITY
1320 Kinnear Road
Columbus, OH 43212

DARTMOUTH COLLEGE
6025 Baker/Berry Library
Hanover, NH 03755-3560

DSTO EDINBURGH
AU/33851-AP, PO Box 830470
Birmingham, AL 35283

SIMEON J. EARL – BAE SYSTEMS
W432A, Warton Aerodome
Preston, Lancs., UK PR4 1AX

ELLEDIEMME
Libri Dal Mondo
PO Box 69/Poste S. Silvestro
Rome, Italy 00187

ENGINEERING INFORMATION, INC
PO Box 543
Amsterdam, Netherlands 1000 Am

ETSE TELECOMUNICACION
Biblioteca, Campus Lagoas
Vigo, 36200 Spain

OLA FORSLUND
SAAB MICROWAVE SYSTEMS
Nettovagen 6
Jarfalla, Sweden SE-17588

GEORGIA TECH LIBRARY
225 North Avenue, NW
Atlanta, GA 30332-0001

HRL LABS, RESEARCH LIBRARY
3011 Malibu Canyon
Malibu, CA 90265

IEE INSPEC
Michael Faraday House
6 Hills Way
Stevenage, Herts UK SG1 2AY

IND CANTABRIA
PO Box 830470
Birmingham, AL 35283

INSTITUTE FOR SCIENTIFIC INFO.
Publication Processing Dept.
3501 Market St.
Philadelphia, PA 19104-3302

KUWAIT UNIVERSITY
Postfach/po box 432
Basel, Switzerland 4900

LIBRARY – DRDC OTTAWA
3701 Carling Avenue
Ottawa, Ontario, Canada K1A 0Z4

LIBRARY of CONGRESS
Reg. Of Copyrights
Attn: 407 Deposits
Washington DC, 20559

LINDA HALL LIBRARY
5109 Cherry Street
Kansas City, MO 64110-2498

RAY MCKENZIE – TELESTRA
13/242 Exhibition Street
Melbourne, Vic, Australia 3000

MISSISSIPPI STATE UNIV LIBRARY
PO Box 9570
Mississippi State, MS 39762

MISSOURI S&T
400 W 14th Street
Rolla, MO 64609

MIT LINCOLN LABORATORY
Periodicals Library
244 Wood Street
Lexington, MA 02420

OSAMA MOHAMMED
FLORIDA INTERNATIONAL UNIV
10555 W Flagler Street
Miami, FL 33174

NAVAL POSTGRADUATE SCHOOL
Attn: J. Rozdal/411 Dyer Rd./ Rm 111
Monterey, CA 93943-5101

NDL KAGAKU
C/O KWE-ACCESS
PO Box 300613 (JFK A/P)
Jamaica, NY 11430-0613

OVIEDO LIBRARY
PO BOX 830679
Birmingham, AL 35283

PENN STATE UNIVERSITY
126 Paterno Library
University Park, PA 16802-1808

DAVID J. PINION
1122 E PIKE STREET #1217
SEATTLE, WA 98122

KATHERINE SIAKAVARA -
ARISTOTLE UNIV OF
THESSALONIKI
Gymnasiou 8
Thessaloniki, Greece 55236

SWETS INFORMATION SERVICES
160 Ninth Avenue, Suite A
Runnemede, NJ 08078

TIB & UNIV. BIB. HANNOVER
DE/5100/G1/0001
Welfengarten 1B
Hannover, Germany 30167

UNIV OF CENTRAL FLORIDA
4000 Central Florida Boulevard
Orlando, FL 32816-8005

UNIVERSITY OF COLORADO
1720 Pleasant Street, 184 UCB
Boulder, CO 80309-0184

UNIVERSITY OF KANSAS –
WATSON
1425 Jayhawk Blvd 210S
Lawrence, KS 66045-7594

UNIVERSITY OF MISSISSIPPI
JD Williams Library
University, MS 38677-1848

UNIVERSITY LIBRARY/HKUST
CLEAR WATER BAY ROAD
KOWLOON, HONG KONG

UNIV POLIT CARTAGENA
Serv Btca Univ,
Paseo Alfonso XIII, 48
Cartagena, Spain 30203

THOMAS WEILAND
TU DARMSTADT
Schlossgartenstrasse 8
Darmstadt, Hessen, Germany 64289

STEVEN WEISS
US ARMY RESEARCH LAB
2800 Powder Mill Road
Adelphi, MD 20783

YOSHIHIDE YAMADA
NATIONAL DEFENSE ACADEMY
1-10-20 Hashirimizu
Yokosuka, Kanagawa,
Japan 239-8686

ACES COPYRIGHT FORM

This form is intended for original, previously unpublished manuscripts submitted to ACES periodicals and conference publications. The signed form, appropriately completed, MUST ACCOMPANY any paper in order to be published by ACES. PLEASE READ REVERSE SIDE OF THIS FORM FOR FURTHER DETAILS.

TITLE OF PAPER:

RETURN FORM TO:

Dr. Atef Z. Elsherbeni
University of Mississippi
Dept. of Electrical Engineering
Anderson Hall Box 13
University, MS 38677 USA

AUTHORS(S)

PUBLICATION TITLE/DATE:

PART A - COPYRIGHT TRANSFER FORM

(NOTE: Company or other forms may not be substituted for this form. U.S. Government employees whose work is not subject to copyright may so certify by signing Part B below. Authors whose work is subject to Crown Copyright may sign Part C overleaf).

The undersigned, desiring to publish the above paper in a publication of ACES, hereby transfer their copyrights in the above paper to The Applied Computational Electromagnetics Society (ACES). The undersigned hereby represents and warrants that the paper is original and that he/she is the author of the paper or otherwise has the power and authority to make and execute this assignment.

Returned Rights: In return for these rights, ACES hereby grants to the above authors, and the employers for whom the work was performed, royalty-free permission to:

1. Retain all proprietary rights other than copyright, such as patent rights.
2. Reuse all or portions of the above paper in other works.

3. Reproduce, or have reproduced, the above paper for the author's personal use or for internal company use provided that (a) the source and ACES copyright are indicated, (b) the copies are not used in a way that implies ACES endorsement of a product or service of an employer, and (c) the copies per se are not offered for sale.

4. Make limited distribution of all or portions of the above paper prior to publication.

5. In the case of work performed under U.S. Government contract, ACES grants the U.S. Government royalty-free permission to reproduce all or portions of the above paper, and to authorize others to do so, for U.S. Government purposes only.

ACES Obligations: In exercising its rights under copyright, ACES will make all reasonable efforts to act in the interests of the authors and employers as well as in its own interest. In particular, ACES REQUIRES that:

1. The consent of the first-named author be sought as a condition in granting re-publication permission to others.
2. The consent of the undersigned employer be obtained as a condition in granting permission to others to reuse all or portions of the paper for promotion or marketing purposes.

In the event the above paper is not accepted and published by ACES or is withdrawn by the author(s) before acceptance by ACES, this agreement becomes null and void.

AUTHORIZED SIGNATURE

TITLE (IF NOT AUTHOR)

EMPLOYER FOR WHOM WORK WAS PERFORMED

DATE FORM SIGNED

Part B - U.S. GOVERNMENT EMPLOYEE CERTIFICATION

(NOTE: if your work was performed under Government contract but you are not a Government employee, sign transfer form above and see item 5 under Returned Rights).

This certifies that all authors of the above paper are employees of the U.S. Government and performed this work as part of their employment and that the paper is therefor not subject to U.S. copyright protection.

AUTHORIZED SIGNATURE

TITLE (IF NOT AUTHOR)

NAME OF GOVERNMENT ORGANIZATION

DATE FORM SIGNED

PART C - CROWN COPYRIGHT

(NOTE: ACES recognizes and will honor Crown Copyright as it does U.S. Copyright. It is understood that, in asserting Crown Copyright, ACES in no way diminishes its rights as publisher. Sign only if *ALL* authors are subject to Crown Copyright).

This certifies that all authors of the above Paper are subject to Crown Copyright. (Appropriate documentation and instructions regarding form of Crown Copyright notice may be attached).

AUTHORIZED SIGNATURE

TITLE OF SIGNEE

NAME OF GOVERNMENT BRANCH

DATE FORM SIGNED

Information to Authors

ACES POLICY

ACES distributes its technical publications throughout the world, and it may be necessary to translate and abstract its publications, and articles contained therein, for inclusion in various compendiums and similar publications, etc. When an article is submitted for publication by ACES, acceptance of the article implies that ACES has the rights to do all of the things it normally does with such an article.

In connection with its publishing activities, it is the policy of ACES to own the copyrights in its technical publications, and to the contributions contained therein, in order to protect the interests of ACES, its authors and their employers, and at the same time to facilitate the appropriate re-use of this material by others.

The new United States copyright law requires that the transfer of copyrights in each contribution from the author to ACES be confirmed in writing. It is therefore necessary that you execute either Part A-Copyright Transfer Form or Part B-U.S. Government Employee Certification or Part C-Crown Copyright on this sheet and return it to the Managing Editor (or person who supplied this sheet) as promptly as possible.

CLEARANCE OF PAPERS

ACES must of necessity assume that materials presented at its meetings or submitted to its publications is properly available for general dissemination to the audiences these activities are organized to serve. It is the responsibility of the authors, not ACES, to determine whether disclosure of their material requires the prior consent of other parties and if so, to obtain it. Furthermore, ACES must assume that, if an author uses within his/her article previously published and/or copyrighted material that permission has been obtained for such use and that any required credit lines, copyright notices, etc. are duly noted.

AUTHOR/COMPANY RIGHTS

If you are employed and you prepared your paper as a part of your job, the rights to your paper initially rest with your employer. In that case, when you sign the copyright form, we assume you are authorized to do so by your employer and that your employer has consented to all of the terms and conditions of this form. If not, it should be signed by someone so authorized.

NOTE RE RETURNED RIGHTS: Just as ACES now requires a signed copyright transfer form in order to do "business as usual", it is the intent of this form to return rights to the author and employer so that they too may do "business as usual". If further clarification is required, please contact: The Managing Editor, R. W. Adler, Naval Postgraduate School, Code EC/AB, Monterey, CA, 93943, USA (408)656-2352.

Please note that, although authors are permitted to re-use all or portions of their ACES copyrighted material in other works, this does not include granting third party requests for reprinting, republishing, or other types of re-use.

JOINT AUTHORSHIP

For jointly authored papers, only one signature is required, but we assume all authors have been advised and have consented to the terms of this form.

U.S. GOVERNMENT EMPLOYEES

Authors who are U.S. Government employees are not required to sign the Copyright Transfer Form (Part A), but any co-authors outside the Government are.

Part B of the form is to be used instead of Part A only if all authors are U.S. Government employees and prepared the paper as part of their job.

NOTE RE GOVERNMENT CONTRACT WORK: Authors whose work was performed under a U.S. Government contract but who are not Government employees are required so sign Part A-Copyright Transfer Form. However, item 5 of the form returns reproduction rights to the U. S. Government when required, even though ACES copyright policy is in effect with respect to the reuse of material by the general public.

January 2002

INFORMATION FOR AUTHORS

PUBLICATION CRITERIA

Each paper is required to manifest some relation to applied computational electromagnetics. **Papers may address general issues in applied computational electromagnetics, or they may focus on specific applications, techniques, codes, or computational issues.** While the following list is not exhaustive, each paper will generally relate to at least one of these areas:

1. **Code validation.** This is done using internal checks or experimental, analytical or other computational data. Measured data of potential utility to code validation efforts will also be considered for publication.
2. **Code performance analysis.** This usually involves identification of numerical accuracy or other limitations, solution convergence, numerical and physical modeling error, and parameter tradeoffs. However, it is also permissible to address issues such as ease-of-use, set-up time, run time, special outputs, or other special features.
3. **Computational studies of basic physics.** This involves using a code, algorithm, or computational technique to simulate reality in such a way that better, or new physical insight or understanding, is achieved.
4. **New computational techniques** or new applications for existing computational techniques or codes.
5. **“Tricks of the trade”** in selecting and applying codes and techniques.
6. **New codes, algorithms, code enhancement, and code fixes.** This category is self-explanatory, but includes significant changes to existing codes, such as applicability extensions, algorithm optimization, problem correction, limitation removal, or other performance improvement. **Note: Code (or algorithm) capability descriptions are not acceptable, unless they contain sufficient technical material to justify consideration.**
7. **Code input/output issues.** This normally involves innovations in input (such as input geometry standardization, automatic mesh generation, or computer-aided design) or in output (whether it be tabular, graphical, statistical, Fourier-transformed, or otherwise signal-processed). Material dealing with input/output database management, output interpretation, or other input/output issues will also be considered for publication.
8. **Computer hardware issues.** This is the category for analysis of hardware capabilities and limitations of various types of electromagnetics computational requirements. Vector and parallel computational techniques and implementation are of particular interest.

Applications of interest include, but are not limited to, antennas (and their electromagnetic environments), networks, static fields, radar cross section, inverse scattering, shielding, radiation hazards, biological effects, biomedical applications, electromagnetic pulse (EMP), electromagnetic interference (EMI), electromagnetic compatibility (EMC), power transmission, charge transport, dielectric, magnetic and nonlinear materials, microwave components, MEMS, RFID, and MMIC technologies, remote sensing and geometrical and physical optics, radar and communications systems, sensors, fiber optics, plasmas, particle accelerators, generators and motors, electromagnetic wave propagation, non-destructive evaluation, eddy currents, and inverse scattering.

Techniques of interest include but not limited to frequency-domain and time-domain techniques, integral equation and differential equation techniques, diffraction theories, physical and geometrical optics, method of moments, finite differences and finite element techniques, transmission line method, modal expansions, perturbation methods, and hybrid methods.

Where possible and appropriate, authors are required to provide statements of quantitative accuracy for measured and/or computed data. This issue is discussed in “Accuracy & Publication: Requiring, quantitative accuracy statements to accompany data,” by E. K. Miller, *ACES Newsletter*, Vol. 9, No. 3, pp. 23-29, 1994, ISBN 1056-9170.

SUBMITTAL PROCEDURE

All submissions should be uploaded to ACES server through ACES web site (<http://aces.ee.olemiss.edu>) by using the upload button, journal section. Only pdf files are accepted for submission. The file size should not be larger than 5MB, otherwise permission from the Editor-in-Chief should be obtained first. Automated acknowledgment of the electronic submission, after the upload process is successfully completed, will be sent to the corresponding author only. It is the responsibility of the corresponding author to keep the remaining authors, if applicable, informed. Email submission is not accepted and will not be processed.

PAPER FORMAT (INITIAL SUBMISSION)

The preferred format for initial submission manuscripts is 12 point Times Roman font, single line spacing and single column format, with 1 inch for top, bottom, left, and right margins. Manuscripts should be prepared for standard 8.5x11 inch paper.

EDITORIAL REVIEW

In order to ensure an appropriate level of quality control, papers are peer reviewed. They are reviewed both for

technical correctness and for adherence to the listed guidelines regarding information content and format.

PAPER FORMAT (FINAL SUBMISSION)

Only camera-ready electronic files are accepted for publication. The term “**camera-ready**” means that the material is neat, legible, reproducible, and in accordance with the final version format listed below.

The following requirements are in effect for the final version of an ACES Journal paper:

1. The paper title should not be placed on a separate page. The title, author(s), abstract, and (space permitting) beginning of the paper itself should all be on the first page. The title, author(s), and author affiliations should be centered (center-justified) on the first page. The title should be of font size 16 and bolded, the author names should be of font size 12 and bolded, and the author affiliation should be of font size 12 (regular font, neither italic nor bolded).
2. An abstract is required. The abstract should be a brief summary of the work described in the paper. It should state the computer codes, computational techniques, and applications discussed in the paper (as applicable) and should otherwise be usable by technical abstracting and indexing services. The word “Abstract” has to be placed at the left margin of the paper, and should be bolded and italic. It also should be followed by a hyphen (–) with the main text of the abstract starting on the same line.
3. All section titles have to be centered and all the title letters should be written in caps. The section titles need to be numbered using roman numbering (I. II.)
4. Either British English or American English spellings may be used, provided that each word is spelled consistently throughout the paper.
5. Internal consistency of references format should be maintained. As a guideline for authors, we recommend that references be given using numerical numbering in the body of the paper (with numerical listing of all references at the end of the paper). The first letter of the authors’ first name should be listed followed by a period, which in turn, followed by the authors’ complete last name. Use a coma (,) to separate between the authors’ names. Titles of papers or articles should be in quotation marks (“ ”), followed by the title of journal, which should be in italic font. The journal volume (vol.), issue number (no.), page numbering (pp.), month and year of publication should come after the journal title in the sequence listed here.
6. Internal consistency shall also be maintained for other elements of style, such as equation numbering. As a guideline for authors who have no other preference, we suggest that equation numbers be placed in parentheses at the right column margin.

7. The intent and meaning of all text must be clear. For authors who are not masters of the English language, the ACES Editorial Staff will provide assistance with grammar (subject to clarity of intent and meaning). However, this may delay the scheduled publication date.
8. Unused space should be minimized. Sections and subsections should not normally begin on a new page.

ACES reserves the right to edit any uploaded material, however, this is not generally done. It is the author(s) responsibility to provide acceptable camera-ready pdf files. Incompatible or incomplete pdf files will not be processed for publication, and authors will be requested to re-upload a revised acceptable version.

COPYRIGHTS AND RELEASES

Each primary author must sign a copyright form and obtain a release from his/her organization vesting the copyright with ACES. Copyright forms are available at ACES, web site (<http://aces.ee.olemiss.edu>). To shorten the review process time, the executed copyright form should be forwarded to the Editor-in-Chief immediately after the completion of the upload (electronic submission) process. Both the author and his/her organization are allowed to use the copyrighted material freely for their own private purposes.

Permission is granted to quote short passages and reproduce figures and tables from and ACES Journal issue provided the source is cited. Copies of ACES Journal articles may be made in accordance with usage permitted by Sections 107 or 108 of the U.S. Copyright Law. This consent does not extend to other kinds of copying, such as for general distribution, for advertising or promotional purposes, for creating new collective works, or for resale. The reproduction of multiple copies and the use of articles or extracts for commercial purposes require the consent of the author and specific permission from ACES. Institutional members are allowed to copy any ACES Journal issue for their internal distribution only.

PUBLICATION CHARGES

All authors are allowed for 8 printed pages per paper without charge. Mandatory page charges of \$75 a page apply to all pages in excess of 8 printed pages. Authors are entitled to one, free of charge, copy of the journal issue in which their paper was published. Additional reprints are available for a nominal fee by submitting a request to the managing editor or ACES Secretary.

Authors are subject to fill out a one page over-page charge form and submit it online along with the copyright form before publication of their manuscript.

ACES Journal is abstracted in INSPEC, in Engineering Index, DTIC, Science Citation Index Expanded, the Research Alert, and to Current Contents/Engineering, Computing & Technology.